N75-22560

Contract No. NAS9-13791
DRL No. T-975
Line Item No. 3
DRD No. MA-129T
ASAO-PR20056-12

SHUTTLE COMMUNICATIONS DESIGN STUDY

FINAL REPORT

March 31, 1975

Prepared for:

National Aeronautics and Space Administration
Lyndon B. Johnson Space Center
Houston, Texas 77058

Prepared by:

David E. Cartier
The Magnavox Company
Advanced Systems Analysis Office
8750 Georgia Avenue, Suite 126E
Silver Spring, Maryland 20910

Approved by: R B Myers
P. B. Myers, Director

DISTRIBUTION

NASA Lyndon B. Johnson Space Center
R&T Space Station Procurement Section
Attn: James W. Wilson, Mail Code BC761(82)
Houston, Texas 77058 (1)

NASA Lyndon B. Johnson Space Center
Technical Library Branch
Attn: Retha Shirkey, Mail Code JM6
Houston, Texas 77058 (4)

NASA Lyndon B. Johnson Space Center
Management Services Division
Attn: John T. Wheeler, Mail Code JM7
Houston, Texas 77058 (1)

NASA Lyndon B. Johnson Space Center
Avionics Systems Engineering Division
Attn: W. E. Teasdale, Mail Code EJ5
Houston, Texas 77058 (24)

ACKNOWLEDGEMENTS

The Magnavox Company would like to take this opportunity to thank the personnel at the Johnson Space Center for their help and guidance during the performance of this contract. Special thanks go to Mr. William Teasdale and Dr. Bartus Batson for "getting us on board" in the early phases of the contract. We would also like to acknowledge helpful inputs from NASA's Goddard Space Flight Center personnel.

A personal note of thanks goes to Colleen Hayes and Maria Gall for the typing and editing of this report.

LIST OF MAJOR CONTRIBUTORS

(with Section Numbers)

David E. Cartier (1.3, 1.4, 2.0, 4.0, 5.0, 8.0)

Robert M. Deffenbaugh (7.0)

Donald M. DeVito (1.1, 1.2, 6.0, 11.0)

Jhong S. Lee (8.0)

Francis L. McWhorter (5.0, 10.0)

Ke Y. Park (3.0, 9.0)

Michael J. Robusto (1.1, 6.0)

The following members of ASAO also contributed to this report.

Robert H. French

Ed McConnell

ABSTRACT

This Final Report is a compilation of the task reports which were generated during the contract period April 1, 1974, to April 1, 1975, for the Johnson Space Center of NASA in Houston, Texas. These tasks are part of the overall Shuttle communications system design and as such are many and varied. The subjects include Ku-Band satellite relay to Shuttle, phased arrays, PN acquisition, quadriplexing of direct link ranging and telemetry, communications blackout on launch and reentry, acquisition after blackout on reentry, wideband communications interface with the Ku-Band rendezvous radar, aeroflight capabilities of Shuttle, a triple multiplexing scheme equivalent to interplex, and a study of staggered quadriphase for use on Shuttle.

In the vast majority of the cases new theoretical and/or application results were created in the performance of the tasks. Each task report is a section in this report and stands alone.

TABLE OF CONTENTS

TABLE OF CONTENTS (CONT.)

TABLE OF CONTENTS (CONT.)

TABLE OF CONTENTS (CONT.)

TABLE OF CONTENTS (CONT.)

TABLE OF CONTENTS (CONT.)

LIST OF ILLUSTRATIONS

LIST OF ILLUSTRATIONS (CONT.)

LIST OF ILLUSTRATIONS (CONT.)

LIST OF ILLUSTRATIONS (CONT.)

LIST OF ILLUSTRATIONS (CONT.)

LIST OF TABLES

LIST OF TABLES (CONT.)

GENERAL INTRODUCTION AND SUMMARY

The purpose of this section is to explain the rationale used in generating, performing, and reporting the tasks together with that of writing this final report. It will be seen shortly that this document is a compilation of the individual task reports which were issued as supplements to the contractual monthly reports, and each stands alone within itself as far as content, analysis, conclusions, appendices, etc. are concerned. It was felt, then, that some sort of overall introductory material was in order.

The contract was "kicked off" in early April 1974 with a meeting between Johnson Space Center (JSC) and Magnavox Advanced Systems Analysis Office (ASAO) personnel. At that time seven full tasks were defined. They were as follows.

The baseline ranging system was to put the information on the prime carrier and the sidetone ranging on a subcarrier. The problem was whether or not this was the most efficient way of doing it. Other suggested alternatives were quadrature modulation and two separate carriers. The report studied all methods and recommended reversing the roles of the ranging and telemetry baseband with respect to the prime and subcarriers.

The second problem of interest was the blackout during launch due to the rocket flame. JSC had assumed an 18° cone of silence which produced up to 8 minutes of no communication. This problem was to be attacked by doing a first cut analysis on the flame data which would be supplied by JSC. A tolerance of 10 dB was acceptable and ultimately JSC wanted a signal level versus look angle plot as the output. The report fulfilled all objectives.

During reentry there is a 20 minute blackout due to skin heating creating a radio shield about Shuttle. JSC was interested in communicating voice and low bit rate telemetry, say, 32 kbps, or even as low as 8 kbps. The problem was to look at Ku-Band through TDRS or even S-Band if feasible. ASAO studied two major models and arrived at extrapolated results from these.

After blackout on reentry, JSC wanted to know how long it would take to reacquire and if there were any problems, such as, high doppler rates due to the high velocities and decelerations involved in Shuttle reentry. The report established that the signal-to-noise ratios were high and that Orbiter would be the pacing element for acquisition.

JSC presently has a Ku-Band pulse type radar which is of the noncoherent type as a baseline design. JSC wanted to use the 20" dish and any other parts of the radar that were feasible for an added wide-band communications link. The study showed that the baseline design was inflexible due to the near-far requirements of the radar and so only the dish could be in common with any wideband communications system add-on.

Having entered the atmosphere Shuttle will be an airplane and as such is in the Aeroflight mode. After blackout such navigational aids as TACAN and a radar altimeter will be employed. ASAO was to look at antenna coverage and review the baseline aeroflight system. The report showed only possible antenna placement problems.

Lastly there are a large number and classes of payloads to be handled by Shuttle, hence it must look like a STDN, DSN, SGLS station. How can this best be done was asked? Would "kits" determined by

the payloads be the best route to go, i.e., plug-in boxes for each payload class? How about restricted formats to get commonality? ASAO generated a usage matrix, but the task was not pursued to completion since JSC was not prepared to respond due to fluctuations in the payload philosophy.

After these initial tasks were established, the procedure for new task definition was on an "as needed" basis. As problems arose in the system the personnel at JSC would call ASAO and discuss the task. ASAO would then layout the task as we saw it and confirm the interpretation with Houston. Upon mutual agreement the study was undertaken.

There was one more facet to the interface between ASAO and JSC which was necessary, that is, the "quick look". It turned out that some problem areas needed development prior to a decision as to whether or not further effort was warranted. In other words was a problem worthy of a full task status? The initial interface was the same, however, the turnaround time and depth of study employed was less. The items were documented as appendices to the monthly reports. Several were turned into full tasks and some were dropped. This procedure worked out very well for both sides.

To complete this part of the final report we will list the other tasks and "quick looks", summarize the results, and finally briefly describe the remainder of the report.

The S-/Ku-Band TDRSS to Orbiter relay task started as a quick look and was deemed worthy of full task status. It grew out of marginal link budgets on the S-Band relay link. It was thought that advantage could be taken of the higher gain of the TDRS antenna at Ku-Band.

In the report a candidate Ku-Band relay system for the Shuttle Orbiter was studied. Link budgets were developed, the Orbiter receive system noise temperature was determined and the minimum transmit and receive antenna gains required for specific data rates were calculated. The command link was found to require directional antennas, therefore a number of them had to be used to achieve omnidirectional coverage. The high vacuum voltage breakdown in the waveguide components of the system (especially the diplexer) was recognized as a problem and was discussed in the report. An appendix to the report listed available hardware (waveguide, diplexers, rotary joints, TWT's) at Ku-Band.

The Ku-Band phased array problem started as a quick look task. It was born of a desire to phase various system antennas to improve link margins. It was soon seen, however, that the cost and complexity was too high to consider it further. It was thus dropped after the quick look report was issued as part of the fourth monthly report.

The relay PN problem is another one which started as a quick look and turned into a full task.

The relay uplink incorporates the Tracking and Data Relay Satellite System (TDRSS) to transmit uplink command and digital voice to Orbiter from the earth. In conformance with the guidelines set by the CCIR of the ITU on the maximum flux density at the earth's surface by emissions from space, the TDRSS-to-Orbiter link will be required to employ spread spectrum techniques. The study addressed the problem of acquiring and tracking a direct sequence pseudonoise (PN) code which has been phase shift keyed (PSK) onto a carrier along with the uplink data.

Several factors affect the analysis of the PN receiver. They are:

- o Up to ±60 kHz of doppler shift on the carrier
- o The use of Manchester coding on the uplink
- o The low energy per symbol
- o The length of the PN code required
- o The chip rate of the PN code required
- o The multiple bit rates to be accommodated.

The most damaging of these are the restrictions on the code. It will be seen in Section 8 that these restrictions do not allow us to take full advantage of the code properties. To be a bit more specific, the flux density requirements dictate a chip rate of at least 10 Megachips per second and a code length of at least 2047, whereas the bandwidth limitations of the system limit the chip rate to roughly 20 Megachips per second. This bounds the sync time.

Due to the desirability of having Orbiter be as autonomous as possible it was deemed necessary to be independent of any doppler correction on the ground, and so the full doppler range must be taken into account. Also Orbiter would like to receive data or not without affecting the PN acquisition scheme.

All of the above considerations severely limited the receiver design. The one chosen in Section 8 is thought to be the best compromise among all parameters.

The quick look task of multiplexing Department of Defense (DOD) data long with existing data grew out of the following considerations.

Many changes in the baseline communications system have taken place since the first proposed design. Initially the S-Band direct link was to transmit the Orbiter telemetry (192 kbps) to ground via a Manchester coded phase modulated (PM) prime carrier. Later the desirability for ranging was indicated. JSC proposed to PM the sidetone ranging onto a 1.7 MHz subcarrier which would then be low index PM'ed onto the prime. ASAO studied this configuration, found it to be adequate with adjustments in indices of modulation, but suggested that the roles of the data and ranging be reversed. The alternate was rejected by JSC for reasons of Orbiter impact.

A further modification was then suggested by JSC, namely, to quadriplex the ranging with the DOD direct link telemetry (256 kbps). This would open the possibility of eliminating the S-Band FM transmitter. The other functions of that box would be shifted to the wideband communications system and/or other boxes in the telecommunications subsystem. Specifically JSC proposed to amplitude modulate (AM) the ranging onto the in-phase subcarrier and to AM the 256 kbps data onto the quadrature subcarrier. The resultant of adding the two would then phase modulate the prime carrier along with the NASA data. ASAO was to study this new proposal for flaws and practicality among other features. The report analyzed all approaches and recommended that the DOD and NASA data be quadriphased onto the subcarrier. The ranging and this subcarrier could then be modulated onto the prime carrier.

The problem of autotracking the Orbiter high gain dish was suggested as a quick look task, but was withdrawn before any report could be issued.

In the later stages of the contract the task of devising schemes for multiplexing three asynchronous bit streams was defined. Two main approaches were studied, interplex and what we call quadriplex. Interplex required a true phase modulator and quadriplex did not, however, interplex was compatible with a hardlimiting repeater, whereas quadriplex was not. A very significant result of the study was to link the two techniques thus giving the best factors of both to the recommended system.

Lastly JSC was interested in staggered quadriphase as a method of sending relay data. ASAO was tasked to deliver a white paper on the subject. As a consequence of the study, a new result was developed, namely, it is now possible to analytically derive the power spectrum of staggered quadriphase after it has been hardlimited. The result allows the design of optimum spectrum occupation signals and gives insight into the advantages of staggered quadriphase for bandwidth conservation.

To end this section a brief rationale behind the format of this report will be given. Since most tasks had resulted in reports already, much time and effort could be saved if much of this material could be used in the final report. Also because of the "stand alone" nature of the individual studies it was felt that separate introductions, analysis, conclusions, and appendices were warranted. This philosophy was adopted in the Final Report.

TECHNICAL REPORTS

This section reports the results of the tasks stated in the General Introduction and Summary. The Quick Look results have been gathered as a section within themselves with individual subjects being subsections. The remaining part of this section reports the results of full tasks. An effort has been made to repeat all material developed under the contract whether or not it has been issued as a supplemental document previous to this final accounting.

As a preface to the sections below the reader should bear in mind that the report was done, in some cases, almost a year ago, and so should not be judged by today's Orbiter communications configuration, but by that existing at the time. The scenario and assumptions in force at the time of the studies is given in each report.

1.0 QUICK LOOK REPORTS

1.1 KU-BAND SATELLITE RELAY SYSTEM FOR SHUTTLE ORBITER

1.1.1 Introduction

It has been suggested that a Ku-Band relay capability be included in the Shuttle Orbiter in place of the baseline S-Band concept. If possible the system would utilize as much of the Ku-Band hardware associated with the rendezvous radar/wideband communication system as practicable.

A functional block diagram of the Ku-Band relay system is shown in Figure 1.1. It is assumed that the antenna system, diplexer, and receive amplifier would be mounted in the forward areas of the Orbiter, while the power amplifier, receiver, and perhaps the modem will be located in the payload area. With an omni-antenna on board the Orbiter, merely switching from S- to Ku-Band, offers no advantages. The

FIGURE 1.1 FUNCTIONAL BLOCK DIAGRAM OF KU-BAND SATELLITE RELAY CAPABILITY

increased gain of the relay satellite is offset by the increased propagation path loss. Moreover, the long waveguide run (12.2m (40 ft.) max.) from the payload area to the forward area of the Orbiter degrades system performance even further.

The solution, at first glance, appears to lie in the increased Orbiter antenna gain over that at S-Band for the same aperture dimensions. Increased gain, however, implies a corresponding decrease of beamwidth indicating the need for more Ku-Band antenna elements to be mounted at the forward area of the Orbiter.

1.1.2 Analysis

A set of link budgets and curves showing achievable data rates are presented in Tables 1.1 and 1.2 and Figures 1.2 and 1.3 for the Return and Forward links respectively. Examination of Figure 1.2 indicates that to achieve a return link data rate of 128 kbps, Orbiter EIRPs of 21 dBW and 26 dBW are required for the coded. i.e., forward error control (FEC), and non-coded transmission respectively.

To determine the minimum allowable Ku-Band antenna gain, consider the following:

Power Amplifier Output = 40 w (16 dBW)

Waveguide Length = 12.2m (40 ft.) (max.)

Waveguide Loss, L_T = 0.33 to 0.825 dB/m (0.1 to 0.25 dB/ft.)

Diplexer Loss, L_d = .5 dB

The minimum Orbiter gain required is found by the following:

$$G_{min} = EIRP_{req'd} - P_0 + L_T + L_d$$

A tabulation of G_{min} for various values of EIRP and L_T is shown in Table 1.3.

TABLE 1-1

SINGLE-ACCESS KU-BAND RETURN LINK BUDGET

PARAMETER	VALUE
Binary Error Probability	10^{-5}
User EIRP (dBW)	EIRP
Space Loss (dB)	-209.2
Pointing Loss (dB)	-0.5
Polarization Loss (dB)	-0.5
TDRS Antenna Gain (dB)	52.6 (55%)*
P_s at Output of Antenna (dBW)	-157.6 + EIRP
T_s (Antenna Output Terminals) (^oK)	710
KT_s at Output of Antenna	-200.1
Carrier-to-Noise Density, P_s/N_o, (dB-Hz)	42.5 + EIRP
Transponder Loss (dB)	-2.0
Demodulation Loss (dB)	-1.5
Residual Carrier Loss (dB)	-1.0
System Margin (dB)	-3.0
Required E_b/N_o, ΔPSK	-9.9
Achievable Data Rate (dB)	25.1 + EIRP
FEC Gain, R = 1/2, K = 7 (dB)	5.2
Achievable Data Rate (dB)	30.3 + EIRP
FEC Gain, R = 1/3, K = 7 (dB)	5.7
Achievable Data Rate (dB)	30.8 + EIRP

*On Axis

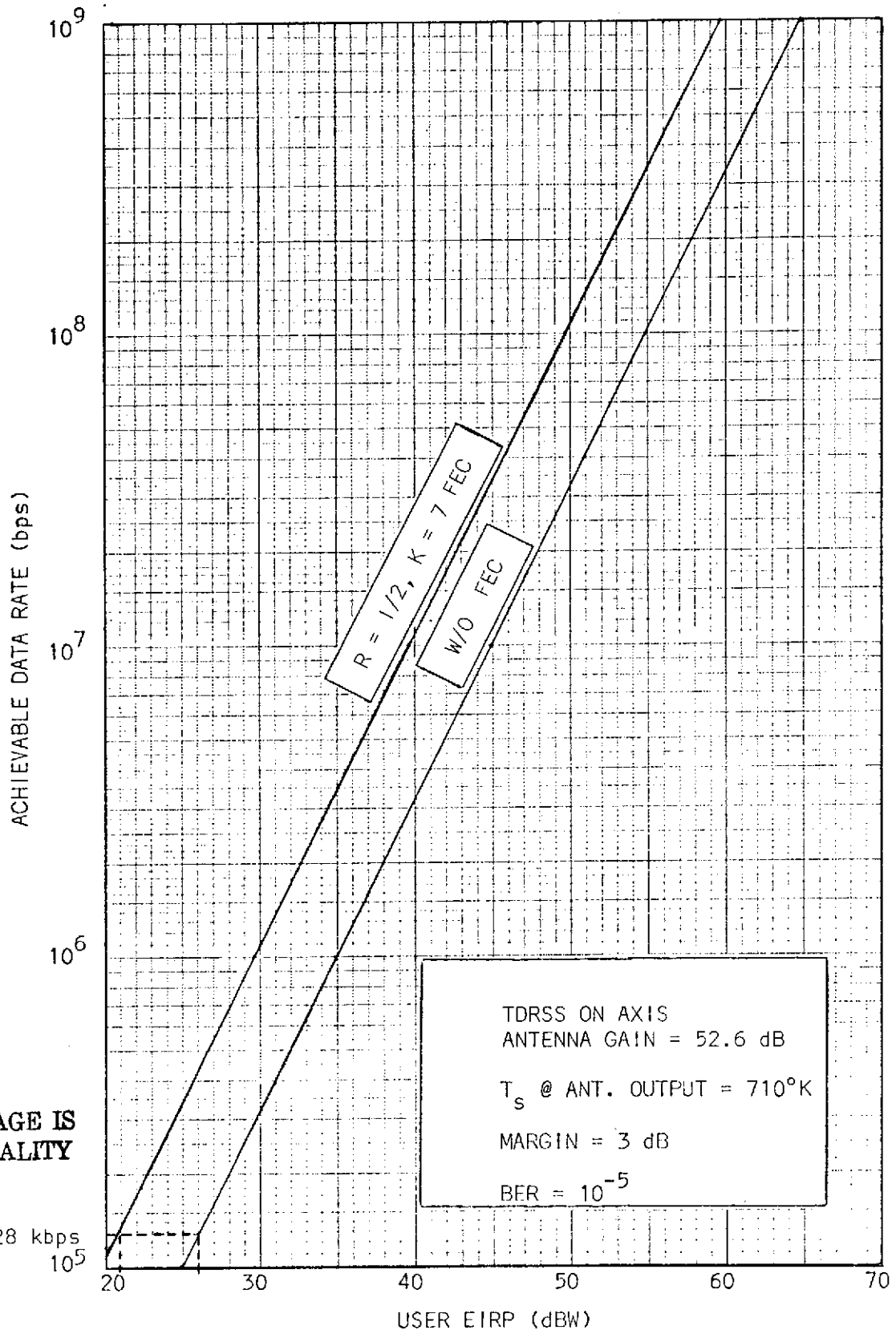

FIGURE 1.2 SINGLE-ACCESS (KU-BAND) RETURN LINK ACHIEVABLE DATA RATE vs. USER EIRP

TABLE 1-2

SINGLE-ACCESS KU-BAND FORWARD LINK BUDGET

PARAMETER	LOW POWER LINK	HIGH POWER LINK
Binary Error Probability	10^{-5}	10^{-5}
EIRP* (dBW)	29.5	49.5
Space Loss (dB)	-208.6	-208.6
User Antenna Gain (dBi)	G_u	G_u
Polarization Loss (dB)	-0.5	-0.5
P_s Out of User Antenna (dBW)	$-179.6 + G_u$	$-159.6 + G_u$
System Noise Temperature, (^oK)	T_s	T_s
Boltzmann's Constant, k, (dBW/^oK-Hz)	-228.6	-228.6
Carrier-to-Noise Density, P_s/N_o, (dB-Hz)	$49.0 + (G_u/T_s)_{dB}$	$69.0 + (G_u/T_s)_{dB}$
Transponder Loss (dB)	-1.0	-1.0
Demodulation Loss (dB)	-1.5	-1.5
PN Loss (dB)	-1.0	-1.0
Residual Carrier Loss (dB)	-1.0	-1.0
System Margin (dB)	-3.0	-3.0
Required E_b/N_o', ΔPSK (dB)	-9.9	-9.9
Achievable Data Rate (dB)	$31.6 + (G_u/T_s)_{dB}$	$51.6 + (G_u/T_s)_{dB}$
FEC Gain, R = 1/2, K = 7 (dB)	5.2	5.2
Achievable Data Rate (dB)	$36.8 + (G_u/T_s)_{dB}$	$56.8 + (G_u/T_s)_{dB}$
FEC Gain, R = 1/3, K = 7 (dB)	5.7	5.7
Achievable Data Rate (dB)	$37.3 + (G_u/T_s)_{dB}$	$57.3 + (G_u/T_s)_{dB}$

*On Axis

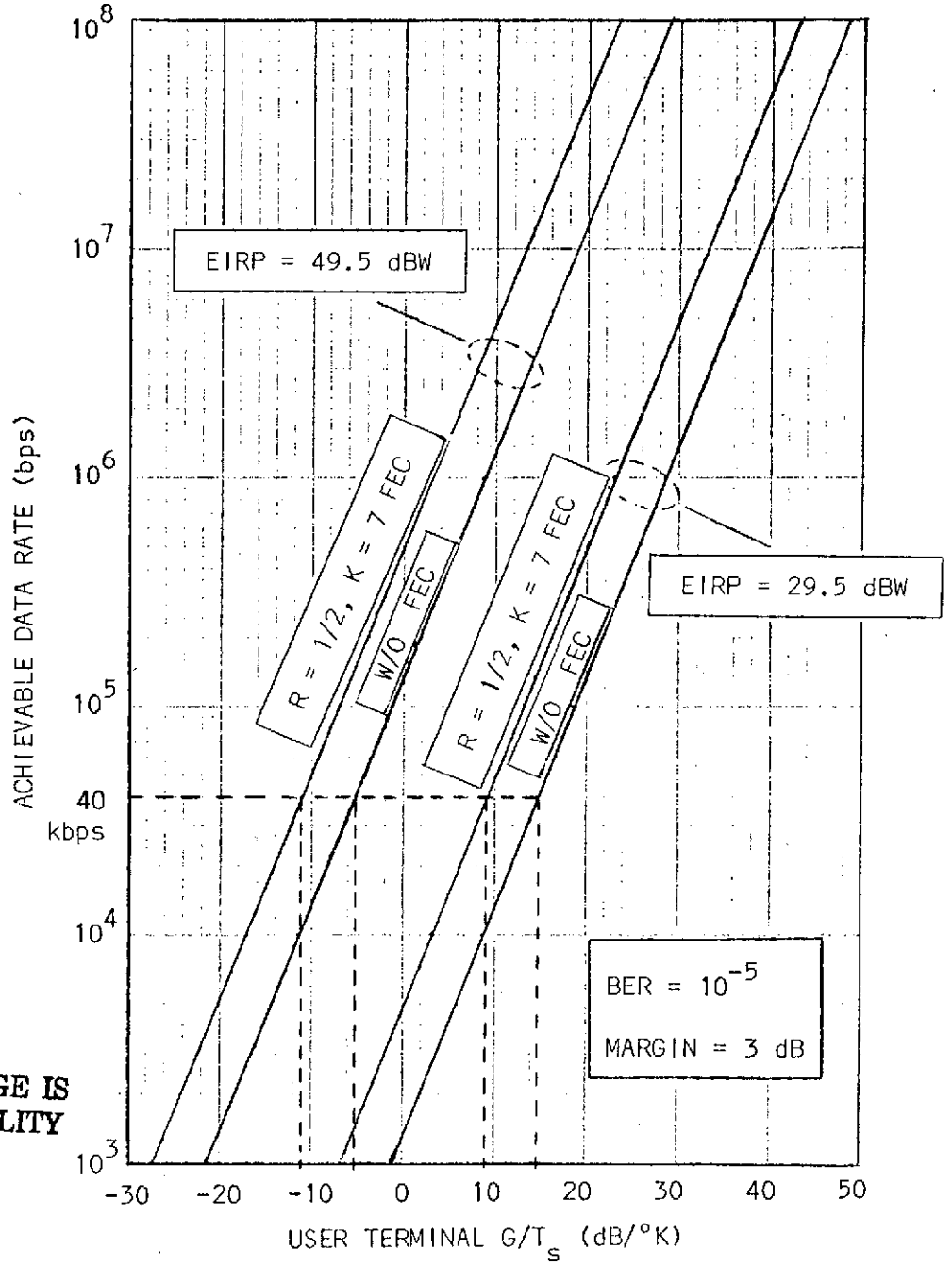

ORIGINAL PAGE IS
OF POOR QUALITY

FIGURE 1.3 SINGLE ACCESS (KU-BAND) FORWARD LINK ACHIEVABLE DATA RATE vs. USER G/T_s

TABLE 1-3

MINIMUM SHUTTLE ANTENNA GAIN (dBi)

REQUIRED TO ACHIEVE AT DATA RATE OF 128 KBPS

EIRP WITH FEC = 21 dBW		EIRP W/O FEC = 26 dBW	
L_T = 4 dB	L_T = 10 dB	L_T = 4 dB	L_T = 10 dB
9.5	15.5	14.5	20.5

TABLE 1-4

FORWARD LINK KU-BAND

SYSTEM NOISE TEMPERATURE REQUIREMENTS

SHUTTLE ANTENNA GAIN (dB)	REQUIRED SYSTEM NOISE TEMP IN dB-^{O}K FOR 40 KBPS DATA RATE			
	TDRS EIRP = +49.5 dBW		TDRS EIRP = +29.5 dBW	
	FEC	W/O FEC	FEC	W/O FEC
9.5	20.5	15.5	+.5	-4.5
15.5	26.5	21.5	6.5	+1.5
14.5	25.5	20.5	5.5	+.5
20.5	31.5	26.5	11.5	+6.5

Presented in Figure 1.3 is a set of curves indicating the required Shuttle G/T_s to support various data rates. At 40 kbps the required G/T_s varies from -11 dB/°K to +15 dB/°K depending on the TDRSS EIRP and whether or not coding is employed. Based on the minimum required antenna gains of Table 1.3, a set of system noise figure requirements has been computed and is shown in Table 1.4.

As shown in Table 1.3 the smallest antenna gain that can be "lived with" is approximately 10 dB. With the exception of arrays, there are only a few single element antennas that can practically achieve such gains, namely:

	Beam Shape	Beamwidth @ 20 dB Gain
Parabolic Dish	Symmetrical	≈18°
Parabolic Cylinder	Fanbeam	?
Horn	Broad "Flat-topped" Fanbeam	≈18°
Short Backfire	Wide; Symmetrical	≈25°

1.1.3 Conclusion

One can see that if a 360° field of view is to be covered by antennas having a beamwidth of approximately 20° then 12 such antennas must be used. This is considered by ASAO to be impractical.

1.2 GAIN ENHANCEMENT BY PHASING TWO SHUTTLE ANTENNA ELEMENTS

1.2.1 Introduction

Antenna aperatures are often times synthesized by using an array of separate antenna elements. A linear array consists of elements arranged in a straight line in one dimension. A planar array consists

of a two-dimensional array of elements arranged to lie in a plane. The relative phase and amplitude of the signals at the antenna elements are controlled to obtain the desired radiation pattern from the combined action of the elements. If one fixes the phases across the elements of the pattern the radiation pattern is also fixed.

1.2.2 Analysis

With regard to the Shuttle Orbiter it is conceivable that an additional kitted Ku-Band antenna system might be added to increase the link gain. The antenna system would consist of two directional elements each of aperature width D separated by a distance d and have an illumination pattern $\psi(x)$, as shown in Figure 1.4.

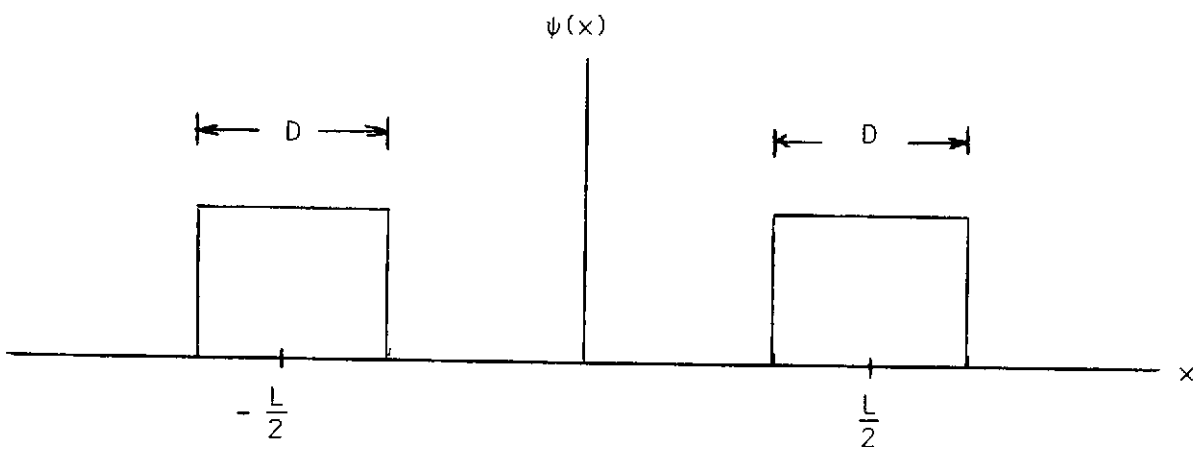

FIGURE 1.4 UNIFORM ILLUMINATION PATTERN

In reality the illumination function will be of the parabolic type, however for the consideration herein a uniform illumination is assumed. It should be noted that this two-element array is of the linear type and as such the gain increase is in one dimension only. For a corresponding increase in the other dimension a four-element planar array would be required. This could affect antenna tracking.

To obtain a broadside beam with increased gain in the main lobe the two antenna elements are summed as shown in Figure 1.5. Normally, when a array of this type is employed the antenna elements are mounted on a common gimble base so that the entire array can be steered.

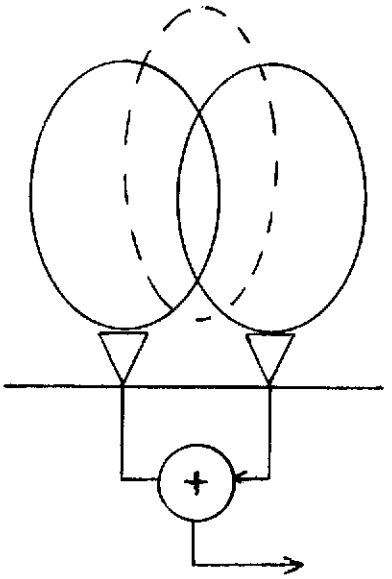

FIGURE 1.5 A BROADSIDE BEAM

This allows the synthesized aperature to remain constant regardless of the direction in which the array is pointing (see Figure 1.6a). In the case of Orbiter, however, it has been assumed that the antennas are mounted separately so that independent steering will be required, as shown in Figure 1.6b. The antenna illumination patterns in this case are no longer co-linear and the elements therefore would require some form of delay to compensate for the phase front delay.

The above rationale was under the assumption that the antennas were close enough to synthesize a new aperture from the two original ones. If they are not then the two dishes can be independently pointed and their outputs (or inputs) can be appropriately phased to achieve gain simply by coherent addition. In this case the original apertures remain

FIGURE 1.6 PHASED ARRAY GEOMETRY AND PATTERNS

separate. Independent steering as Orbiter comes in view of a TDRS, passes under it, and then travels on will cause problems. On both extremes of the TDRS view angle one or the other antennas will block the remaining one thus disrupting the aperture. Operationally it is possible to avoid this, but it is at the cost of Orbiter maneuvering.

1.2.3 Conclusion

The conclusion to the above discussion is that it is likely that the geometry of the two dish array will impose restrictions on its use and degrade the gain achievable to appreciably less than the theoretical maximum of 3 dB. This combined with the circuit losses could be intolerable.

It is recommended that an in-depth study be made to ascertain the actual degradation.

1.3 SHUTTLE PN ACQUISITION ANALYSIS

1.3.1 Introduction

The use of direct sequence pseudonoise (PN) spread spectrum on the uplink relay to Shuttle to meet international space-to-earth radiation regulations opens up a whole range of new design areas for the Orbiter communications system. Foremost among these is the requirement to acquire the transmitted code at the receiver. This report deals with that portion of the overall acquisition procedure which aligns the codes to within 1/2 chip of perfect. This is the major consideration since very low signal-to-noise ratios (SNR) are the rule and since the bulk of the overall code acquisition time is taken up by this "coarse sync" process.

The motivation for going to PN was weak links and power requirements, therefore low SNR's must be contended with as will be seen shortly. In the interest of low cost and complexity the simplest system possible was chosen by NASA for analysis by ASAO (Figure 1.7). The system basically isolates discrete power which is a function of the PN autocorrelation function.[1] If the output of the low pass filter (LPF) does not trigger the threshold detector (T.D.) then the code is "slipped a chip". If the T.D. is triggered then correlation is assumed to be sufficient ($|\tau| \leq T/2$) and the process is stopped.

In Reference 1 it is shown that the bandpass filter must be at least as wide as the data. Also if there is any doppler uncertainty, then the bandwidth must be even wider.

1.3.2 Analysis

To get a handle on the problem consider the case of no doppler and the lowest convolutionally encoded bit rate possible (command plus 1 voice) of 72 kbps. This case will indicate whether or not the scheme is worth pursuing. Since the system is not phase sensitive the PSK on the carrier can be ignored. We thus have the case of a sine wave plus noise. Note: prior to envelope detecting it is phase sensitive, however, therefore the BPF must be as wide as the information dictates.[1]

The system as it stands now is exactly the same as a radar system with 100% duty cycle and pulse spectrum given by the information stream. The following analysis and resulting curves are derived from Reference 2. Per Reference 3 the EIRP available from TDRS is 44.4 dBW (the added 2.6 dB recently gained will be used later). This translates into a SNR of

$$SNR_A = 56.2 - 1 - \hat{R}_b \text{ (dB)}, \qquad (1.3.1)$$

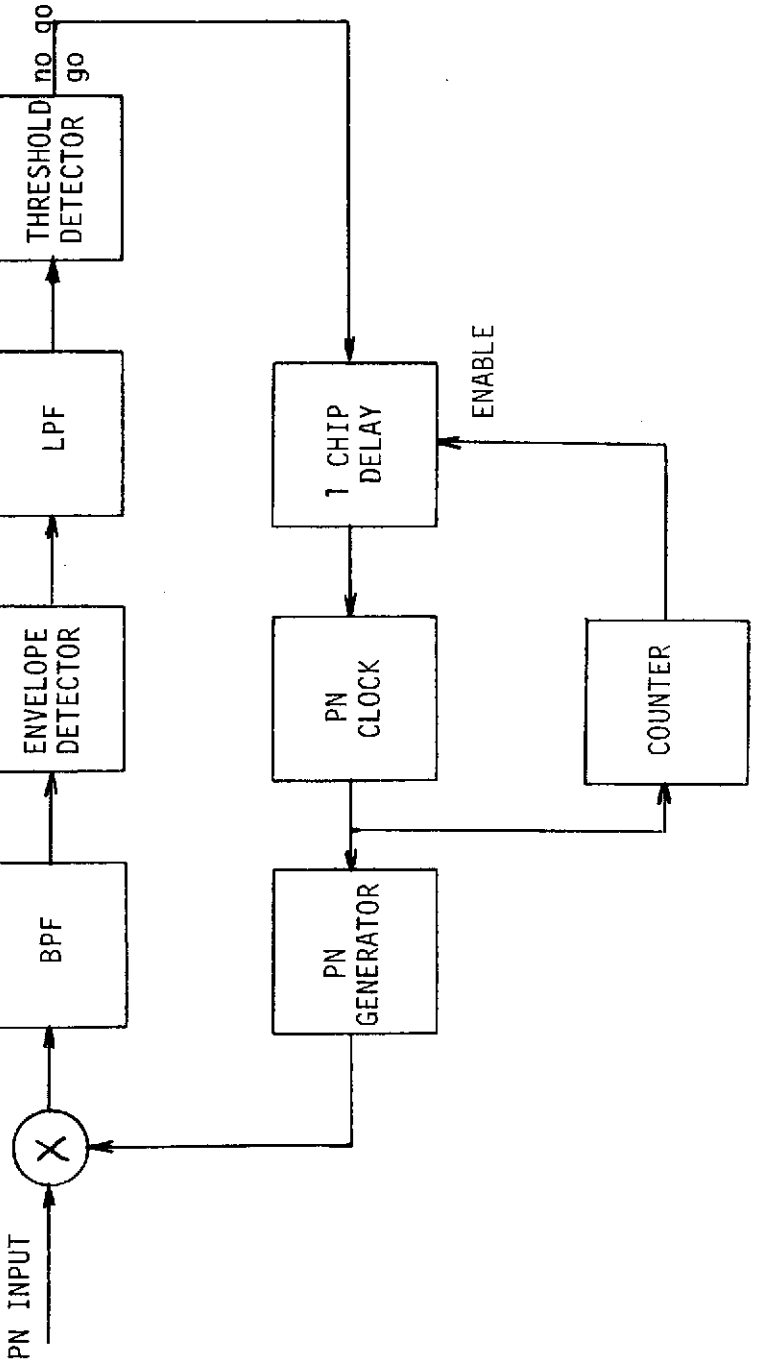

FIGURE 1.7 A NONCOHERENT PN ACQUISITION SYSTEM

where 56.2 dB is the SNR per Hertz, 1 dB is TDRS loss, $\hat{R}_b$ is the bit rate in dB. The SNR required for a false alarm probability of 10^{-5} and a detection probability of 0.99 is[2]

$$SNR_R = 14.6 + 3 + 6 + 1 \text{ (dB)}, \tag{1.3.2}$$

where 14.6 dB is needed per pulse, 3 dB is margin, 6 dB decorrelation loss is the worst case T/2 (1/2 chip) misalignment, and 1 dB reflects the use of a low pass filter to implement the post detection integration (exponential versus uniform weighting).

In the following assume a code length

$$L = 2047. \tag{1.3.3}$$

For an RC low pass filter the noise BW (B_n) is related to its time constant (τ) as follows:

$$B_n = \frac{1}{4\tau} \tag{1.3.4}$$

Assuming 4τ as the time required to let the LPF output settle before checking the threshold, and using the material on pp. 38 and 39 of Reference 2 the maximum time to lock (T_L) will be

$$T_L = 2047 \times (4\tau) = 2047/B_n. \tag{1.3.5}$$

Per Reference 2

$$R_b = \frac{4B_n \times n}{1.257} = \frac{6517n}{T_L}, \tag{1.3.6}$$

where n is the number of post detection pulses integrated.

Using "^" to indicate dB quantities, e.g., $\hat{T}_L = 10 \log T_L$,

$$\hat{R}_b = 38.1 + \hat{n} - \hat{T}_L. \tag{1.3.7}$$

Now the postdetection gain (G) curve is well described by

$$\hat{G} = 0.75\ \hat{n}, \tag{1.3.8}$$

thus using (1.3.1), (1.3.2), (1.3.7) and (1.3.8)

$$SNR_R - SNR_A = \hat{G} = 0.75\ (\hat{R}_b + \hat{T}_L - 38.1). \tag{1.3.9}$$

Solving for $\hat{R}_b$ in terms of $\hat{T}_L$ gives the desired result.

$$\hat{R}_b = 3\hat{T}_L + 8.1 \quad . \tag{1.3.10}$$

This equation is plotted as the 44.4 dBW EIRP curve in Figure 1.8.

An immediate observation is that at 72 kbps it will take about 20 seconds to lock.

1.3.3 Conclusions

The other curves in Figure 1.8 are for other EIRP's. These curves can be used to juggle various parameters to optimize performance. Let us be optimistic for a moment. Assume the following:

- o The doppler can be tracked out by the ground station.
- o The power is 47 dBW EIRP (i.e., the 2.6 dB gain is brought into the picture).
- o The bit rate is 72 kbps (one voice plus command telemetry).
- o No margin is used.

With these ground rules the effective power is 50 dBW and the curve gives 3.25 seconds maximum to lock. Remember 6 dB decorrelation loss is still in effect. This means that the system just happened to get right on the edge of the PN correlation curve. The probability of this is remote. Most likely there will be 1 or 2 dB available here.

Now lets be pessimistic.

- o The BPF must accommodate a doppler offset of roughly 72 kHz (per Reference 4 it is 56 kHz).
- o The power is 46 dB EIRP (i.e., 1 dB PN loss is assumed).
- o The bit rate is 72 kbps.
- o Full decorrelation exists (6 dB).
- o There is 3 dB margin.

This gives an effective EIRP of 43.4 dBW and the curves give a maximum acquisition time of 25 seconds.

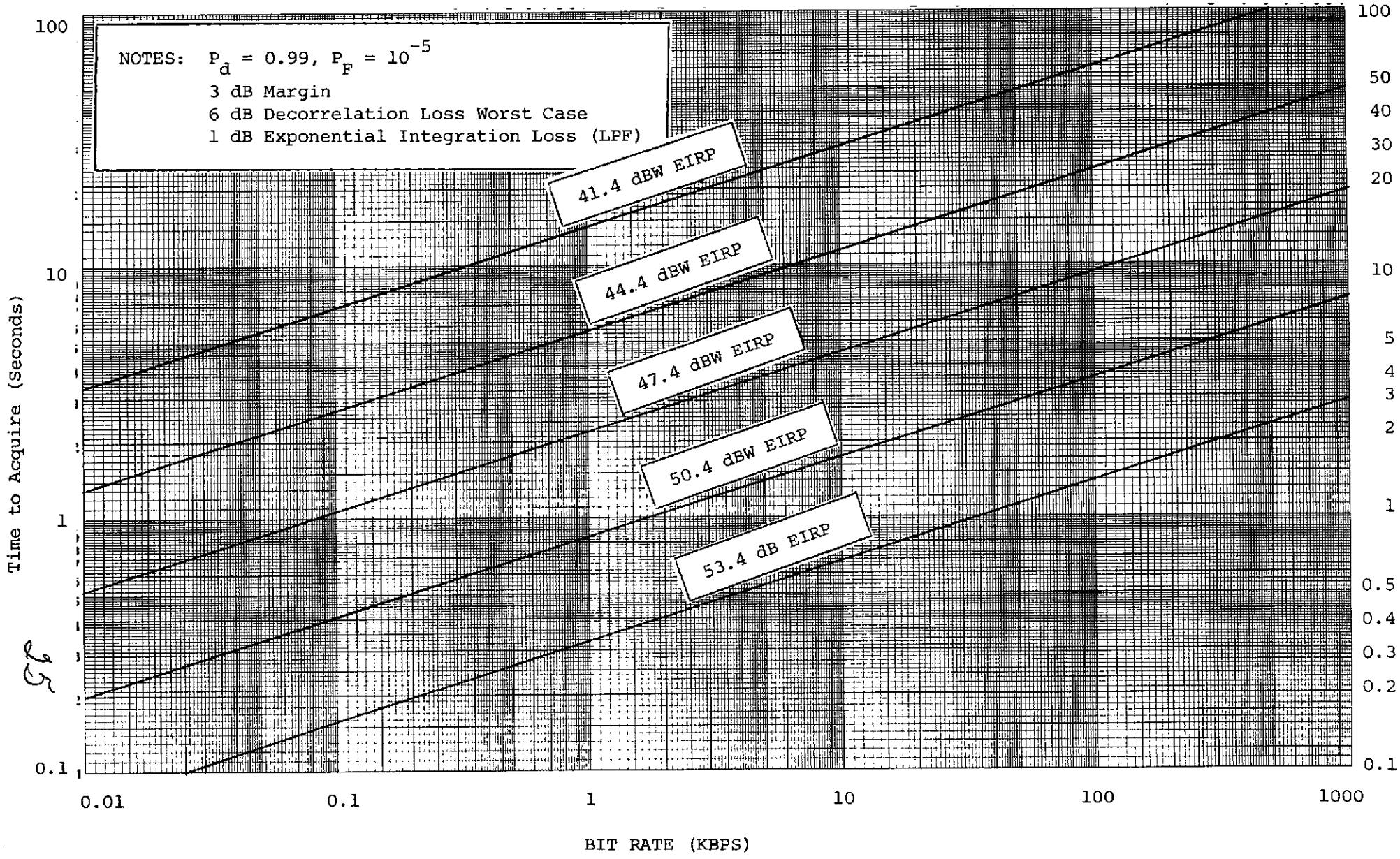

FIGURE 1.8 TIME TO ACQUIRE VERSUS BIT RATE

The conclusion is that with care the PN acquisition system will perform adequately, but a more efficient PN acquisition scheme should be used if the acquisition time is to be improved. Other techniques such as slipping less than a chip and reduced search after drop lock should be investigated. (See Section 8 of this report for an analysis of a modification to the one studied here.)

1.3.4 References

(1) D. E. Cartier, "A Frequency Domain Approach to Shuttle PN Code Acquisition," NTC'74 Conference Record, pp. 713-717.

(2) M. Skolnik, Introduction to Radar Systems, McGraw-Hill, New York, 1962.

(3) Shuttle Orbiter/GSFC Communications and Tracking Interface Control Document, ICD-0D044, NASA Lyndon B. Johnson Space Center, LEC-1161, January 1974.

(4) D. M. DeVito, M. M. Goutmann, R. C. Harper, "A Channel Simulator Design Study," Report No. ASAO-PR20022-6, Prepared for GSFC, January 1971.

1.4 DOD DIRECT LINK QUADRIPLEX

1.4.1 Introduction

Many changes in the baseline communications system have taken place since the first proposed design. Initially the S-Band direct link was to transmit the Orbiter telemetry (192 kbps) to ground via a Manchester coded phase modulated (PM) prime carrier. Later the desirability for ranging was indicated. JSC proposed to PM the sidetone ranging onto a 1.7 MHz subcarrier which would then be low index PM'ed onto the prime. ASAO studied this configuration, found it to be adequate with adjustments in indices of modulation, but suggested that the roles of the data and ranging be reversed.[1] (Reference 1 is reproduced as Section 2 of this report.) The alternate was rejected by JSC for reasons of Orbiter impact.

Recently a further modification was suggested, namely, to quadriplex the ranging with the DOD direct link telemetry (256 kbps). This would open the possibility of eliminating the S-Band FM transmitter. See Figure 1.9. The other functions of that box would be shifted to the wideband communications system and/or other boxes in the telecommunications subsystem. Specifically JSC proposed to amplitude modulate (AM) the ranging onto the in-phase subcarrier and to AM the 256 kbps data onto the quadrature subcarrier. The resultant of adding the two would then phase modulate the prime carrier along with the NASA data. ASAO was to study this new proposal for flaws and practicality among other features. The following is the result.

1.4.2 Analysis

The first item of interest is that the direct link has a 24.4 dB margin in the voice channel (without ranging) and 20.5 dB margin in the telemetry channel (again this was calculated prior to the ranging insertion).[2] The conclusion is that the link has "power to burn", thus this is not a factor.

The next item then is the interference possibility. Figure 1.10 shows that if the DOD data were split phased onto the subcarrier then there would be a considerable amount of interference. This can be seen if it is realized that 43% of the baseband split phase power is in the first sideband (86% doublesided) with 3.5% for the next, and 1% for the next sideband.[3] Thus there is significant power intermingling within the NASA and DOD data (not to mention the ranging). This brought the conclusion that an NRZ format is mandatory. Recall that separation must be sufficient for adequate filtering.

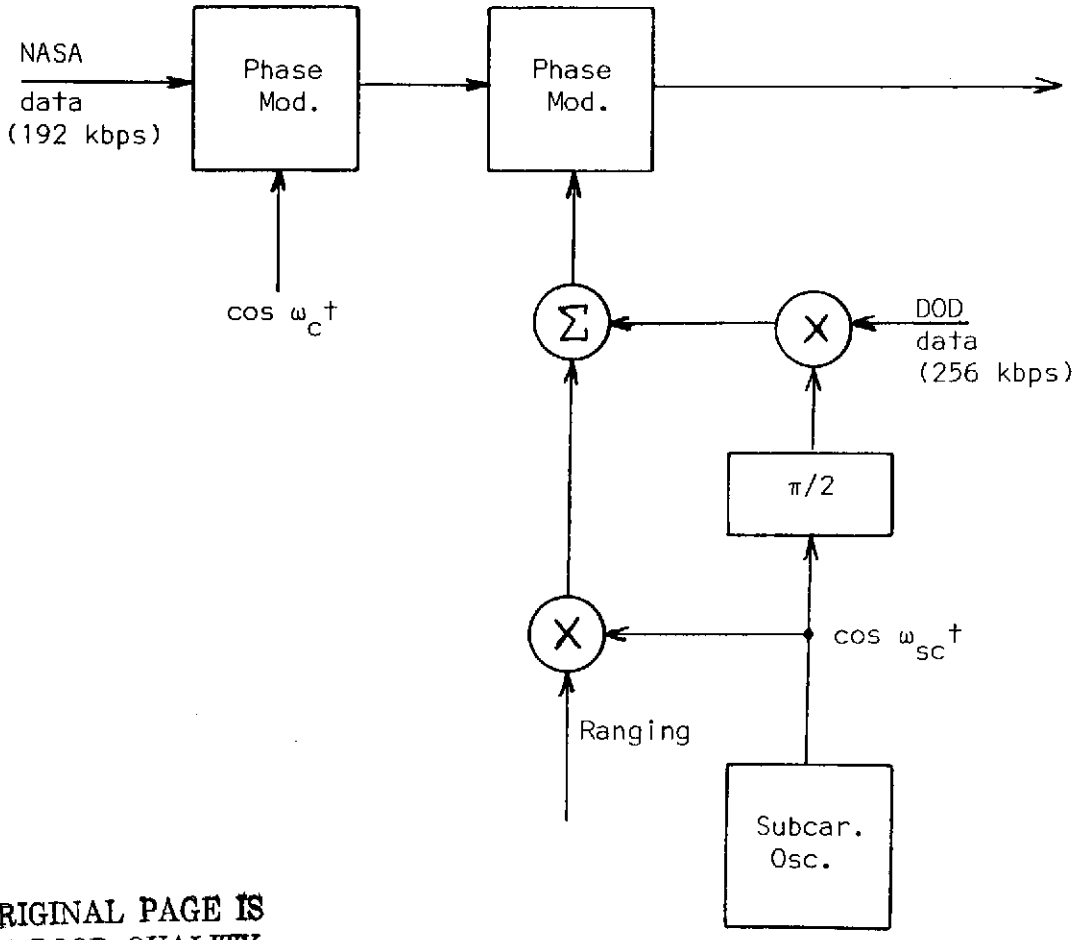

FIGURE 1.9 JSC QUADRATURE SYSTEM

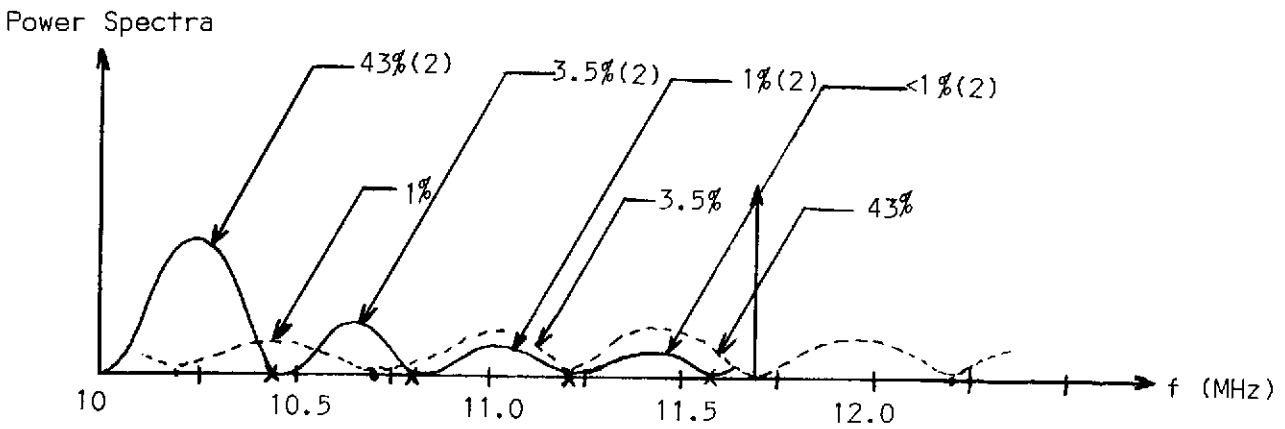

Figure 1.10 SPLIT PHASED DOD DATA CASE

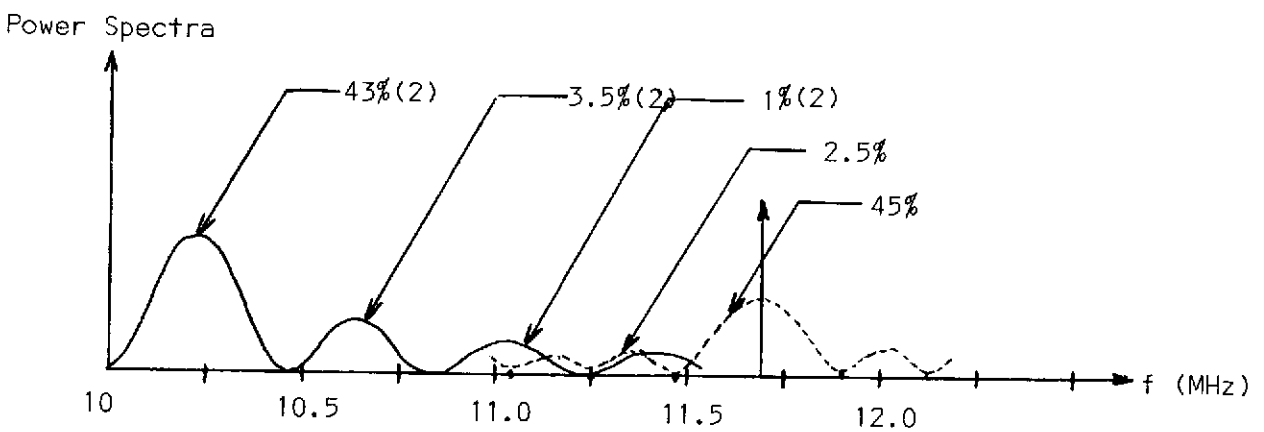

Figure 1.11 NRZ DOD DATA CASE

Figure 1.11 shows the NRZ format. The possibility now exists for proper separation. It should be noted in the above that only half the sideband power in the subcarrier interferes with the sideband power on the prime carrier since the other half is in the positive frequency direction away from the prime carrier sidebands. Both prime carrier sidebands, however, interfere with the subcarrier as can be seen readily from the figures.

The next item of interest is the balance of power among the NASA data, DOD data, and ranging. Following Lindsey[4] it can be shown that the power in the carrier, P_c, NASA data, P_d, and DOD data subcarrier plus all of its sidebands, P_e, are

$$\frac{P_c}{P} = J_0^2[\sqrt{2}\ M]\ \cos^2\tau \tag{1.4.1}$$

$$\frac{P_d}{P} = J_0^2[\sqrt{2}\ M]\ \sin^2\tau \tag{1.4.2}$$

$$\frac{P_e}{P} = 2J_1^2[\sqrt{2}\ M]\ \cos^2\tau \tag{1.4.3}$$

where P is the total direct link power, $\sqrt{2}\ M$ is the amplitude of the DOD data, τ is the peak phase deviation due to the NASA data alone, and P_r, the total ranging power, has been assumed negligible. The signal considered in the above was

$$\begin{aligned} S(t) = \sqrt{2P}\ \cos\ [&\omega_c t + \tau a_1(t) \\ &+ [\sqrt{2P_r}\ \cos\ (\omega_r t + \theta_r)]\ \cos\ (\omega_{sc} t + \theta_{sc}) \\ &+ \sqrt{2}\ M\ a_2(t)\ \sin\ (\omega_{sc} t + \theta_{sc}) + \theta_c], \end{aligned} \tag{1.4.4}$$

where ω_c is the prime carrier frequency, $a_i(t)$ is a ± 1 random bit stream, ω_r is the range tone frequency, ω_{sc} is the subcarrier frequency, and the θ_r, θ_{sc}, and θ_c are uniformly distributed random phase angles.

It should be noted that in the above the ranging was assumed to have a low peak value relative to 1. This is a good assumption since the ranging power balance is not critical, whereas the DOD and NASA power balance is critical.

Equation (1.4.1) through (1.4.3) give the following values for $\tau = 0.9$, and $\sqrt{2}\ M = 1.1$

$$\frac{P_c}{P} = 20\%, \quad \frac{P_d}{P} = 31.8\%, \quad \frac{P_e}{P} = 17.14\% \tag{1.4.5}$$

The total is 69%. The other 31% is lost in cross-modulation. Again since the link is so strong the power loss is tolerable. Further adjustment of the parameters could optimize the power balance.

As seen above in order to balance the power to suppress dominant interference by any one source, it was necessary to raise the modulation index (MI) of the DOD subcarrier. This brought with it a concommitant increase in intermodulation distortion and the loss of power. For these reasons and because the ranging system on the ground requires a phase modulated signal[5] the following alternate is proposed by ASAO. Figure 1.12 shows this system. The ranging is PM'ed onto the prime carrier. The DOD and NASA data are quadriphase (QPSK) modulated onto the 1.7 MHz subcarrier. The subcarrier then phase modulates the prime carrier. The advantages are many.

- The ranging is STDN compatible requiring only a simple filtering operation prior to injection into the range recovery system.
- There is no interference between the data channels (except through any quadrature unbalance).
- QPSK is simple to implement.
- NRZ can be used on the telemetry thereby suppressing any interference with the ranging.[1]
- The subcarrier operation is digital.
- The scheme is power efficient.

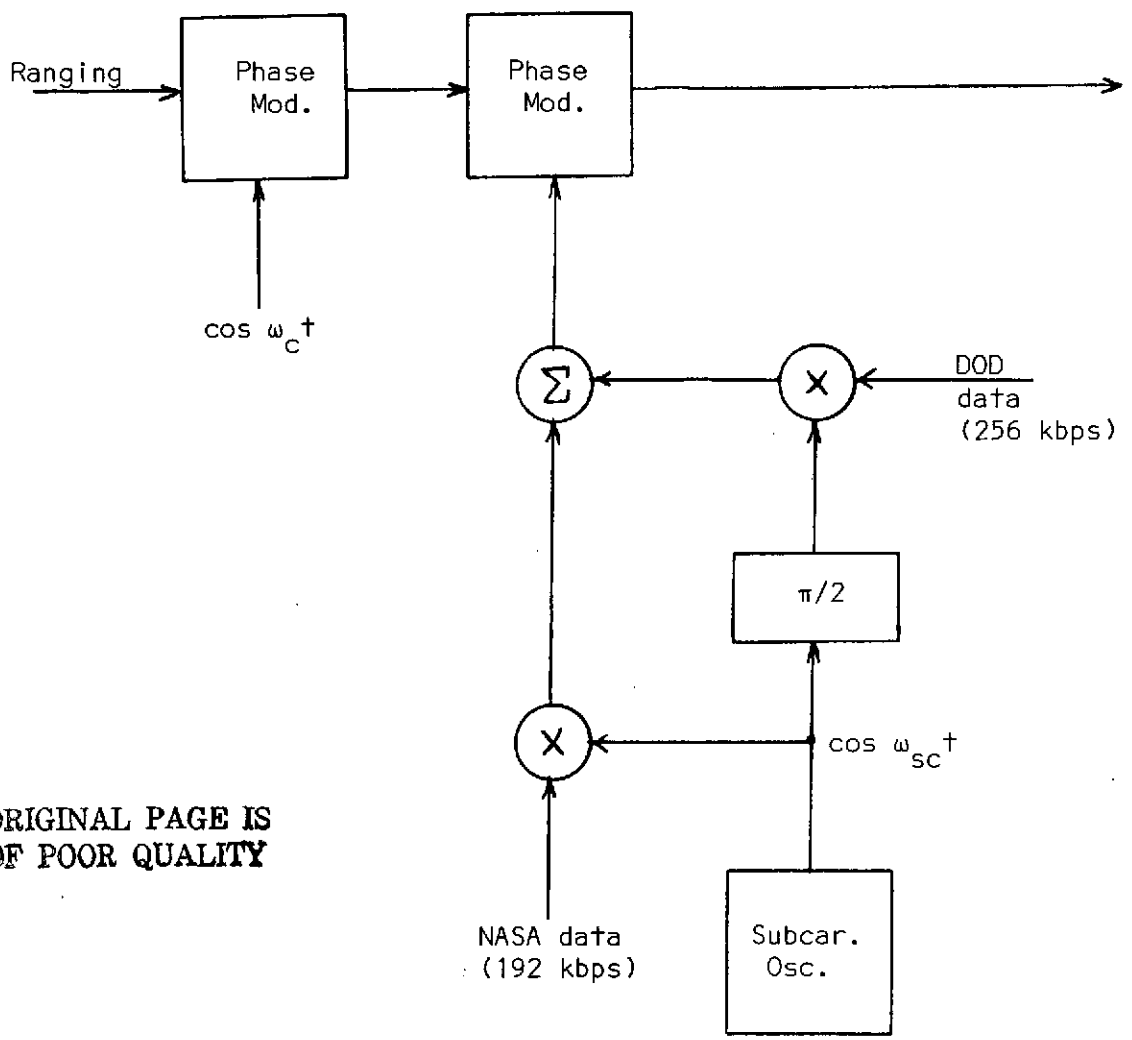

FIGURE 1.12 ASAO QUADRATURE SYSTEM

For the alternate scheme with a low index on the ranging we essentially have

$$\frac{P_c}{P} = J_0^2[\sqrt{2P_{sc}}\,] \tag{1.4.6}$$

$$\frac{P_e}{P} = 2J_1^2[\sqrt{2P_{sc}}], \tag{1.4.7}$$

where P_{sc} is the total quadriphased subcarrier power, i.e.,

$$s(t) = \sqrt{2P}\cos\left[\omega_c t + \sqrt{2P_{sc}}\cos\left(\omega_{sc}t + \phi_{sc}(t) + \phi_{sc}\right) + \phi_c\right]. \tag{1.4.8}$$

For $\sqrt{2P_{sc}} = 0.8$

$$\frac{P_c}{P} = 71.6\% \tag{1.4.9}$$

$$\frac{P_e}{P} = 27.2\%. \tag{1.4.10}$$

For an equal power split in the NASA and DOD data streams

$$P_{dNASA} = P_{dDOD} = 13.6\%. \tag{1.4.11}$$

Thus each is down only 8.7 dB from the total power. This means there is plenty of margin for all the signals. Note also that 71.6 + 27.2 = 98.8; therefore there is very little power lost in intermodulation distortion.

1.4.3 Conclusion

In conclusion then, the baseline system is marginally adequate (interference being in question). The alternate proposal is more than adequate.

1.4.4 References

(1) D. E. Cartier, "Shuttle Communications Design Study," Supplemental Report, "Direct Link Ranging/Telemetry," NAS9-13791, June 30, 1974.

(2) Shuttle Orbiter/GSFC Communications and Tracking Interface Control Document, ICD-0D044, NASA Lyndon B. Johnson Space Center, LEC-1161, January 1974.

(3) B. H. Batson, "An Analysis of the Relative Merits of Various PCM Code Formats," Internal Note No. MSC-EB-R-68-S, NASA Manned Spacecraft Center, Houston, Texas, NTIS No. N70-35709, Nov. 1, 1968.

(4) W. C. Lindsey, "Design of Block-Coded Communication Systems," IEEE Transactions on Communication Technology, Vol. COM-15, No. 4, August, 1967.

(5) GSFC Specification, Spacecraft Tracking and Data Network Ranging Equipment, S-813-P-19, Nov. 15, 1972, Rev. Aug. 2, 1973.

2.0 ORBITER DIRECT LINK RANGING/TELEMETRY STUDY

2.1 INTRODUCTION

This task grew out of a need to range on launch and reentry as well as transmit and receive telemetry and/or voice. In these situations the method of integrating doppler derived range rate is neither accurate enough nor timely enough to satisfy the system requirements. As a first cut at the problem NASA/JSC created a baseline scheme. It has the ranging (which is of the Goddard Range and Range Rate (GRARR) variety) placed on a subcarrier at 1.7 MHz away from the S-Band carrier. This carrier has been previously phase modulated by a PCM digital bit stream. This could be pure telemetry or digitized voice (via an adaptive delta modulator) or both time multiplexed together into a composite bit stream.

While the baseline scheme is simple and historically effective NASA/JSC asked Magnavox ASAO to look into the baseline as well as other possible methods for transmitting the ranging and telemetry. In the following report this is done and as an added result the modulation indices employed in the baseline design are found to create interference problems between the ranging subcarrier with its sidebands and the modulated carrier.

It is appropriate here to state these indices. They are 0.3 radians peak phase deviation on the subcarrier for the sidetone modulation, 0.3 radians peak phase deviation on the prime carrier for the subcarrier modulation, and 1.1 radians peak phase deviation on the prime carrier for the telemetry modulation.

2.2 ANALYSIS

The modulation schemes investigated were as follows.

(a) Quadrature signaling with the ranging on one orthogonal channel and the telemetry on the other.

(b) Separate Carriers.

(c) Dual Polarization.

(d) Square Wave Subcarrier.

(e) Sidetone ranging on a 1.7 MHz subcarrier with PCM telemetry on the prime carrier. (Baseline)

(f) Sidetone ranging on the prime carrier with PCM telemetry on a 1.7 MHz subcarrier.

The order of the above was chosen so as to end up with the two recommended approaches. In other words, methods (a) through (d) were rejected.

2.2.1 Quadrature Signaling

Quadrature signaling is a common modulation technique used mostly in digital communications. In the present case the ranging is analog (a sum of sine wave sidetones) and the telemetry is digital. While the modulator is straightforward, the demodulator is not simple. Also the multifunctional receiver (MFR) which will be used by the Space Tracking and Data Network (STDN) to support the Orbiter cannot handle anything other than a single channel modulation approach. A quadrature type of signal could be recovered from the wideband combiner output, however, this still leaves the problem of quadrature demodulation. Without even considering the demodulator complexity it can be concluded that this approach is wasteful of the support facilities.

The prime advantage of quadrature modulation is, of course, the bandwidth savings due to simultaneous usage of a common band by two orthogonal carriers. In the present situation bandwidth is not a problem and so the advantage is irrelevant. Other problems such as de-orthogonalization must also be considered. Any differential phase delay between the two channels results in cross-talk; thus filters would have to have good group delay properties. Due to the above discussion quadrature modulation was rejected as a means of sending simultaneous ranging and telemetry.

2.2.2 Separate Carriers

The method of using separate carriers is simple enough, but it requires two ground receivers which is again wasteful of the support facilities (as will be seen later there is a simple way of using only one receiver). There is a bandwidth savings due to no lower sideband as in the baseline design, but again the system is not bandwidth constrained.

2.2.3 Dual Polarization

The method of dual polarization is essentially an orthogonal carrier approach using the polarization properties of electromagnetic waves in place of the phase of a sine wave. Two problems arise. The first is that practical limitations on antenna and other hardware designs degrade perfect orthogonality to only about 20 dB channel to channel isolation. The second is that the MFR combines the two channels and makes no provision for individual polarization channel recovery. Implementation on the Orbiter is not overly complex, but cannot be done within the low level electronics as is most desirable. For all the reasons above and the lack of bandwidth problems, this method was rejected.

2.2.4 Square Wave Subcarrier

The next approach to be considered is the use of a square wave subcarrier for the telemetry. The idea here is to add the ranging and the telemetry together after the telemetry has been suitably processed. For example Manchester[4] (split/phase) coding the bit stream results in a space near the carrier in which the ranging may be placed (Figure 2.1). Simple filtering can, in principle, separate the two signals with the telemetry recovered with a standard bit sync. This approach was proposed for ESRO IV to send two bit stream simultaneously, one NRZ, the other split/phase.

The biggest problem with this technique is the interference possibility due to the spectral overlap. In order to work the power in the interfering part of the telemetry spectrum must be negligible. This, however, forces the signaling rate to be high with an attendant spread of the bandwidth. For split/phase a bit rate of roughly 1 MHz is required. If higher frequency subcarriers were used even more bandwidth would be needed.

Another drawback with this method is the requirement of sharp filters to separate the spectrums. Sharp filters, however, produce phase distortion with a resulting degradation in the output. This approach while very easy to implement cannot be used here. It should, however, be kept in mind if the bit rate (now at 192 kbps) is increased substantially.

2.2.5 Baseline System

The multiplexing scheme proposed originally as baseline for Orbiter is reasonably simple to implement and has been implemented enough so as to be predictable "performance-wise".

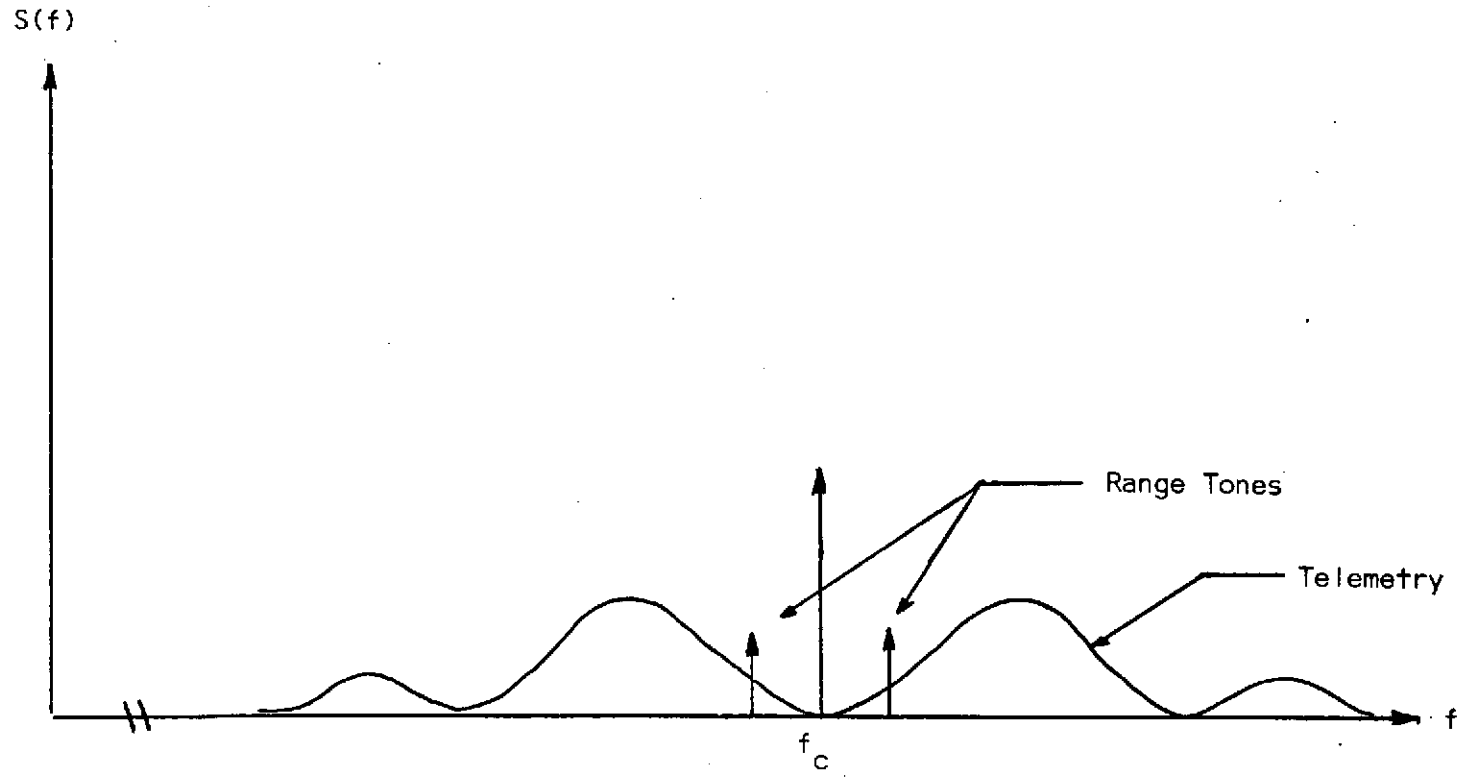

FIGURE 2.1 SQUARE WAVE SUBCARRIER MULTIPLEXING

Figure 2.2 shows the spectrum of the baseline system. The following analysis shows that the scheme is practical and the parameters can be chosen to make the performance acceptable with the ranging/telemetry interference held to a minimum.[1][2]

The signal-to-noise density available on the Orbiter to STDN link is 84.2 dB-Hz.[3] The bit rate bandwidth is 192 kHz, hence the E_b/N_o available (not considering any modulation or equipment losses) is 31.4 dB. As can be seen readily from this figure there is no problem as far as power is concerned; for example, splitting the power equally among the carrier, ranging, and telemetry, still gives 26.6 dB for the telemetry (which is more than enough to offset any equipment losses), 79.4 dB-Hz for the ranging (which is 29.4 dB more than required for acquisition and thus entirely satisfactory for ranging), and 79.4 dB-Hz for the carrier (which will allow carrier acquisition and lock with no problems at all).

The above example simply points up the fact that link margin is a secondary consideration. The prime consideration is interference, and in the final analysis the parameters which determine carrier, ranging, and telemetry power will have to be chosen so as to minimize interference. For the baseline system the telemetry being on the carrier and the STDN interface combined to require Manchester coding of the telemetry. This spreads the bandwidth over and above the normal NRZ. Rounding the 192 kbps to 200 kbps for convenience, the first null in the telemetry spectrum falls at 0.4 MHz away from the carrier. The second null is displaced 0.8 MHz and the third null at 1.2 MHz. With these values in mind it can be shown that 10% of the telemetry power falls within the

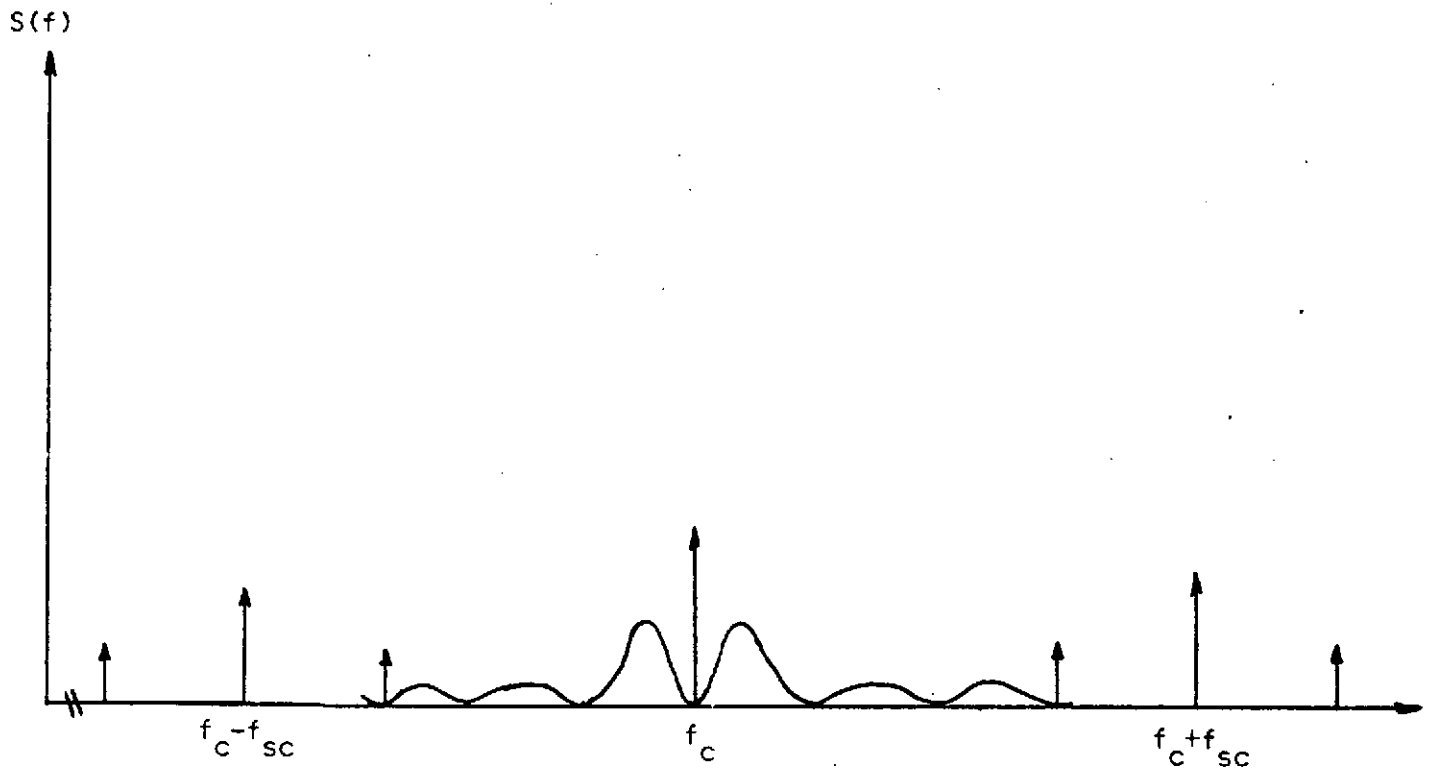

FIGURE 2.2 BASELINE POWER SPECTRUM

ranging part of the spectrum, i.e., beyond the third null.[4] The next question is the effect of filtering. Figure 2.3 should be of interest here. As a note on Figure 2.3, the IF frequency of the narrowband demodulator of the MFR is 10 MHz. Appendix 2.A states the IF filtering performance specifications of the MFR with Figure 2.4 illustrating a typical response.

Consider the effect of the ranging on telemetry recovery. The closest sidetone is at 0.5 MHz below the subcarrier and in fact falls in the third null of the split phase telemetry spectrum. The MFR bandwidths (BW) are selectable and a BW of 1 MHz will pass 86% of the telemetry power. This BW will suppress the 11.2 MHz sidetone by 20 dB and the 11.6 MHz one by 32 dB. Thus unless the ranging power is very high relative to the telemetry there will be no interference problems. To pursue this further, per Reference 5, (details may be found in Appendix 2.B)

$$P_c = P[J_0^2(m_p)\ \cos^2\tau] \tag{2.1}$$

$$P_d = P[J_0^2(m_p)\ \sin^2\tau] \tag{2.2}$$

$$P_t = P[J_1^2(m_p)\ J_1^2(m_s)\ \cos^2\tau], \tag{2.3}$$

where the signal of interest is given by

$$S(t) = \sqrt{2P}\ \sin\left[\omega_c t + \tau b(t) + m_p \cos\left(\omega_{sc} t + m_s \cos\omega_r t\right)\right], \tag{2.4}$$

P is the total power, ω_c is the prime carrier frequency, τ the amplitude of the NRZ data, b(t) is the normalized NRZ data (i.e., ± 1), m_p is the ranging mod index, ω_{sc} is the subcarrier frequency, m_s is the sidetone mod index and ω_r is the ranging sidetone (a single sidetone was chosen since this represents the worst case of most power closest to the prime carrier and is a distinct possibility in practice due to the sequential

Notes: (1) Use 1 MHz NB IF in the MFR (passes 86% of split phase power).
(2) The 11.2 MHz tone (lower subcarrier sideband) is suppressed by 20 dB.
(3) The 11.5 MHz tone (lower subcarrier sideband) is suppressed by 32 dB.
(4) The spectra and filter response are not to scale.
(5) Baseline - solid.
(6) Alternate - dotted.

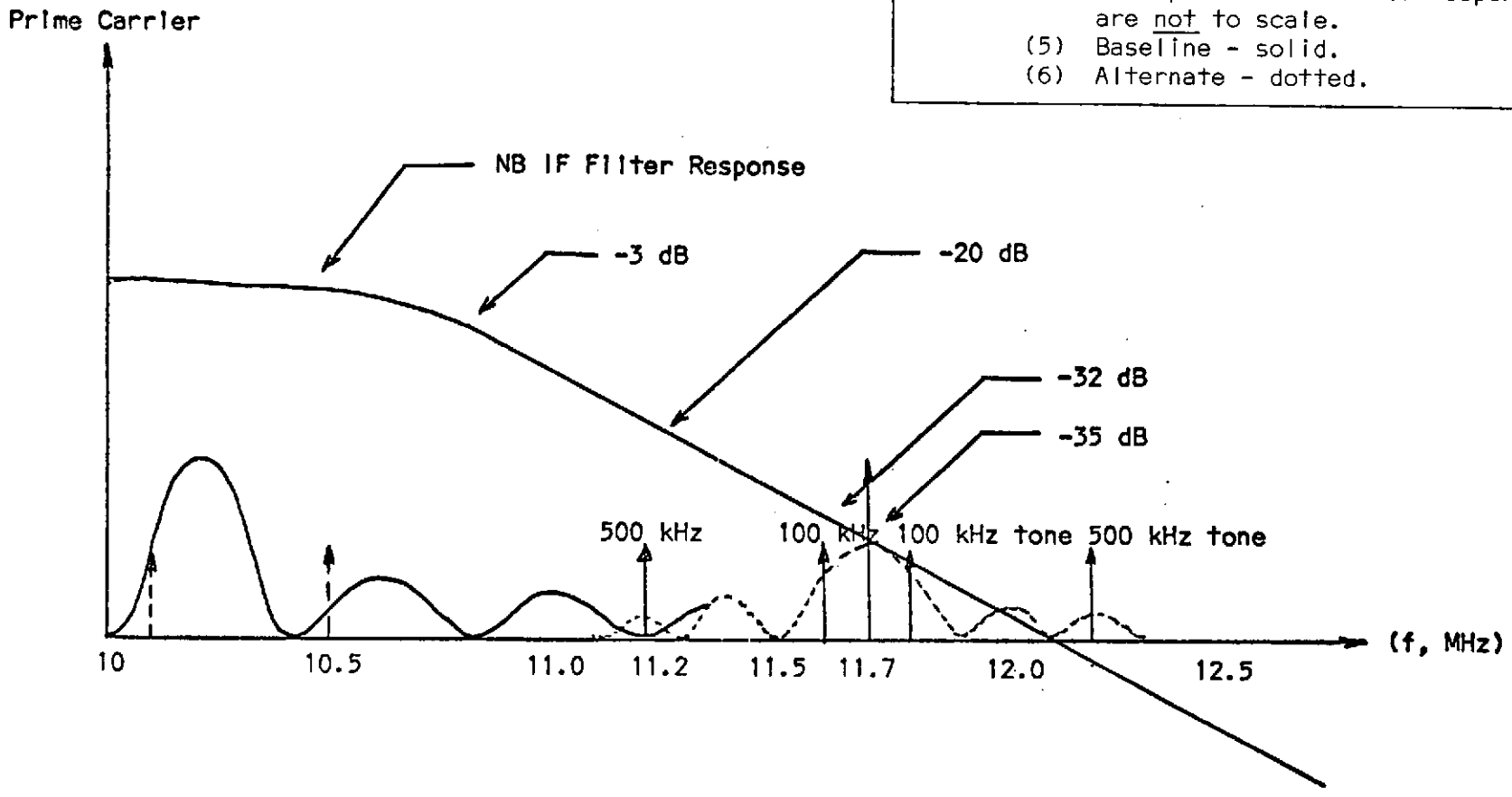

FIGURE 2.3 PERTINENT SPECTRA FOR INTERFERENCE ANALYSIS

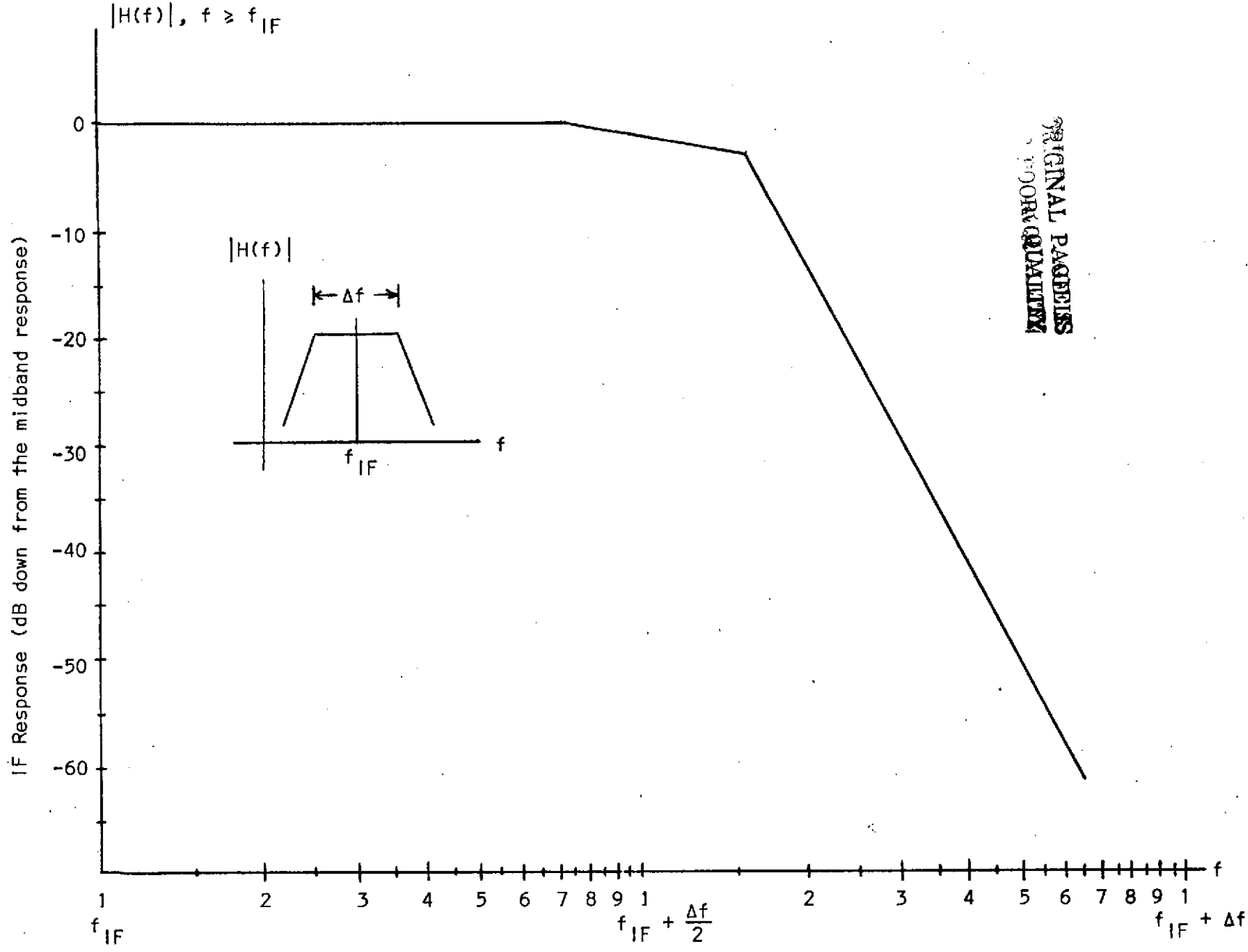

FIGURE 2.4 MFR NARROWBAND IF FILTER RESPONSE

nature of range tone application in the Goddard system), P_c is the power in the carrier, P_d is the data power (all sidebands included), and P_t is the power in one ranging tone.

For the baseline indices, namely,

$$m_p = 0.3,\ m_s = 0.3,\ \tau = 1.1, \tag{2.5}$$

$$P_c = 20\% \text{ of } P \tag{2.6}$$

$$P_d = 76\% \text{ of } P \tag{2.7}$$

$$P_t = 5 \times 10^{-3}\% \text{ of } P. \tag{2.8}$$

Clearly there is no telemetry or carrier recovery interference due to ranging even with minimal filtering. As far as the interference of the telemetry and carrier on the ranging is concerned, the system depends heavily on the filtering. Since there is so much data and carrier power and due to the closeness of the split phase spectrum to the ranging, sharp filters are required. Phase distortion can become a problem and must be a factor due to the dependence of ranging on phase measurements.

Letting P_s be the total subcarrier ranging power (subcarrier plus all the range tone sidebands)

$$\frac{P_d}{P_s} = 84 \ (19.2 \text{ dB}). \tag{2.9}$$

Thus roughly 20 dB of filtering is required just to make the powers equal which certainly is not adequate. Assuming that the MFR type filters could be used for this application only 20 dB rejection is possible at the first null of the telemetry spectrum with roughly 30 dB as the ultimate. This is not enough.

The conclusion is that the parameters should be adjusted. Note well that there will be no interference problem if this is done. The only reason there is one now is due to the large disparity between the ranging power and the remaining power. If, for example, m_p was increased from 0.3 to 1.0

$$P_s = 7.76\% \text{ of } P \tag{2.10}$$

$$P_d = 46.5\% \text{ of } P \tag{2.11}$$

$$P_c = 11.7\% \text{ of } P \tag{2.12}$$

$$\frac{P_d}{P_s} = 6 \ (7.76 \text{ dB}) \tag{2.13}$$

$$\frac{P_d + P_c}{P_s} = 7.5 \ (8.8 \text{ dB}) \tag{2.14}$$

Thus filtering could minimize the interference. Note that 11.7% of the total power in the carrier is 1.7% higher than required by the Aerospace (STDN) standards.[6]

2.2.6 Alternate System

The system that is termed the "alternate system" is to put the telemetry on the subcarrier and the ranging on the prime carrier.

Basically all we have done is switched the ranging and the telemetry roles on the carrier and subcarrier. By putting the telemetry on the subcarrier and the ranging on the carrier two advantages are gained.

(i) We can use PSK on the subcarrier and still be compatible with STDN. This narrows the spectrum required thereby decreasing the interference between the range tones and the telemetry (see Figure 2.5).

(ii) We can make more use of the Multifunctional Receiver (MFR) at STDN.

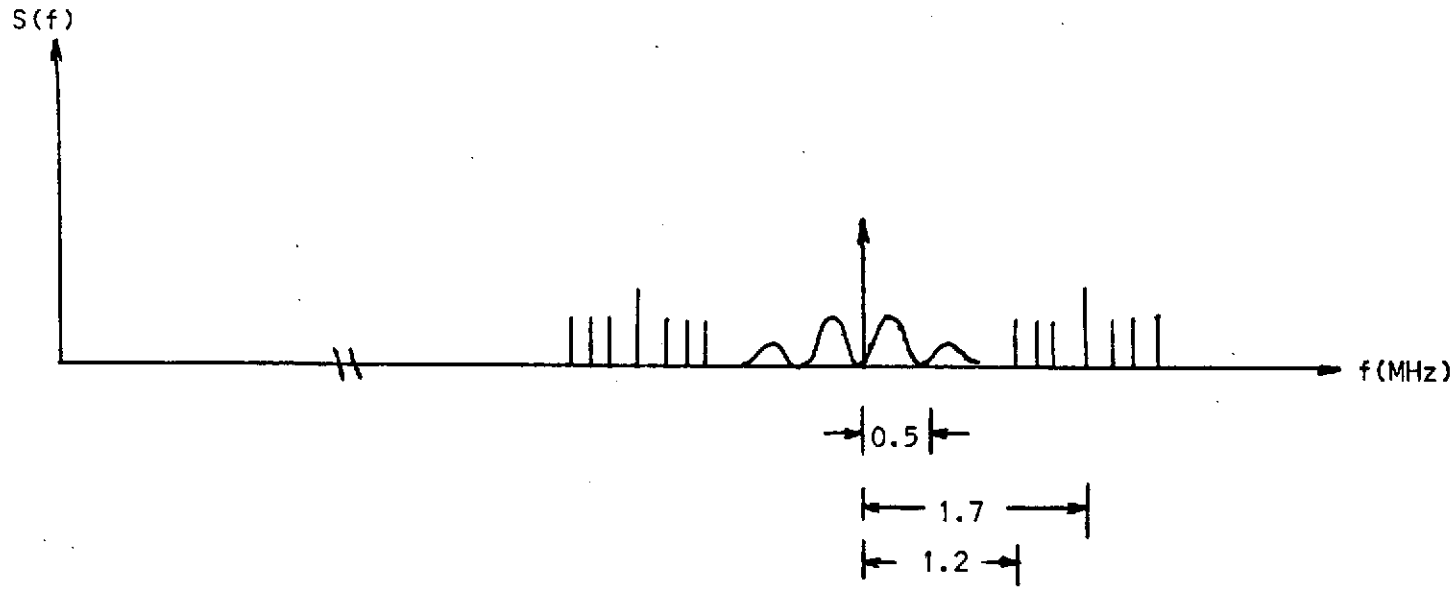

(a) Baseline Direct Link TLM/Ranging Spectrum

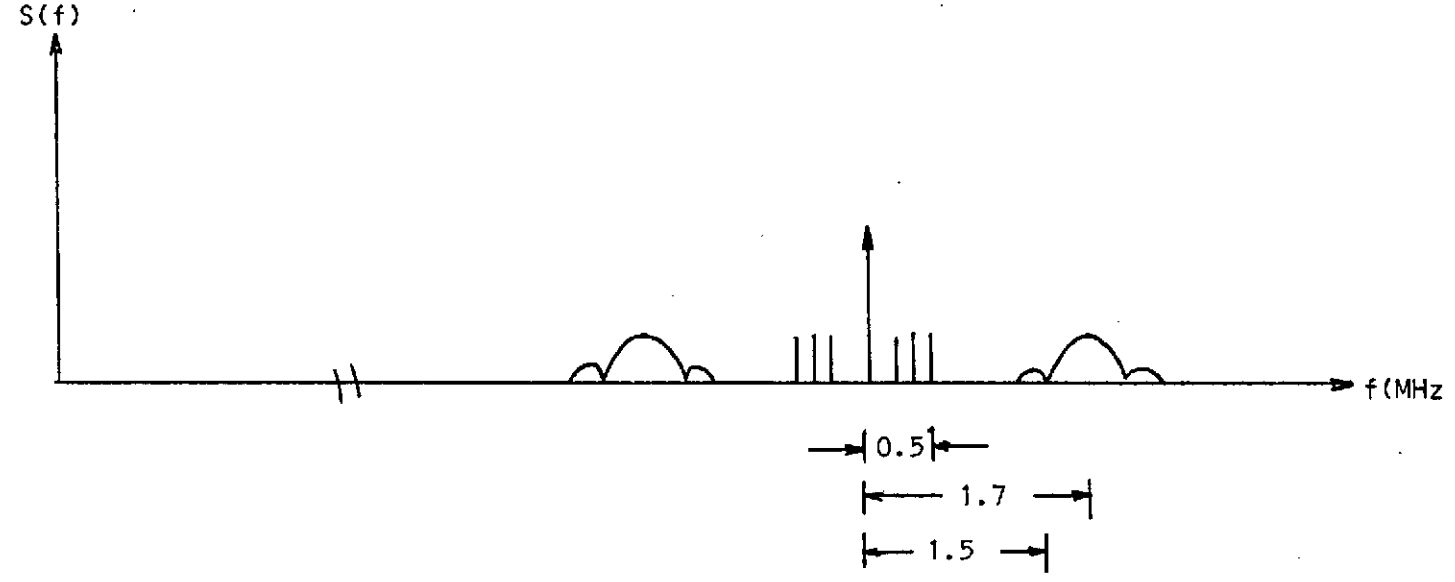

(b) Alternate Direct Link TLM/Ranging Spectrum

FIGURE 2.5 DIRECT LINK TLM/RANGING SPECTRUMS

Consider Figure 2.6. A direct comparison of the two schemes shows that the switch S2 must have an added pole to select TDRS or STDN, and that the subcarrier modulator is now a PSK type (which is simpler than a general phase modulator). The conclusion is that the impact to Shuttle is the same or slightly less.

Consider Figure 2.7. The savings in complexity is obvious. The reason that the baseline system is so much more complex at the STDN is that the ranging system is to be designed to work with the MFR. It thus requires a phase modulated carrier at 110 MHz! It also receives several other signals from the MFR, one of which is a 55 MHz reference. Since the baseline system does not provide a 110 MHz ranging signal at the output of the wideband combiner the necessary processing must be included. Note that two mixers are shown. To up convert from 1.7 MHz to 110 MHz in one step would require very sharp filters and there would be image problems.

The alternate system provides the ranging in the form desired. In addition the wideband phase demodulator in the MFR can be used for the prime carrier with a PSK demodulator placed at the "TLM" output of the MFR.

The interference analysis follows directly from that done in the baseline section with one important change. Since NRZ can now be used instead of split phase the bandwidth of the telemetry spectrum is cut in half with a concomitant decrease in the interference; that is, whatever the interference in the baseline system, the interference in the alternate system is less (greater than 30 dB rejection of the telemetry can be obtained with the MFR filters). The extra margin can be used to leave more prime carrier power and/or more data power.

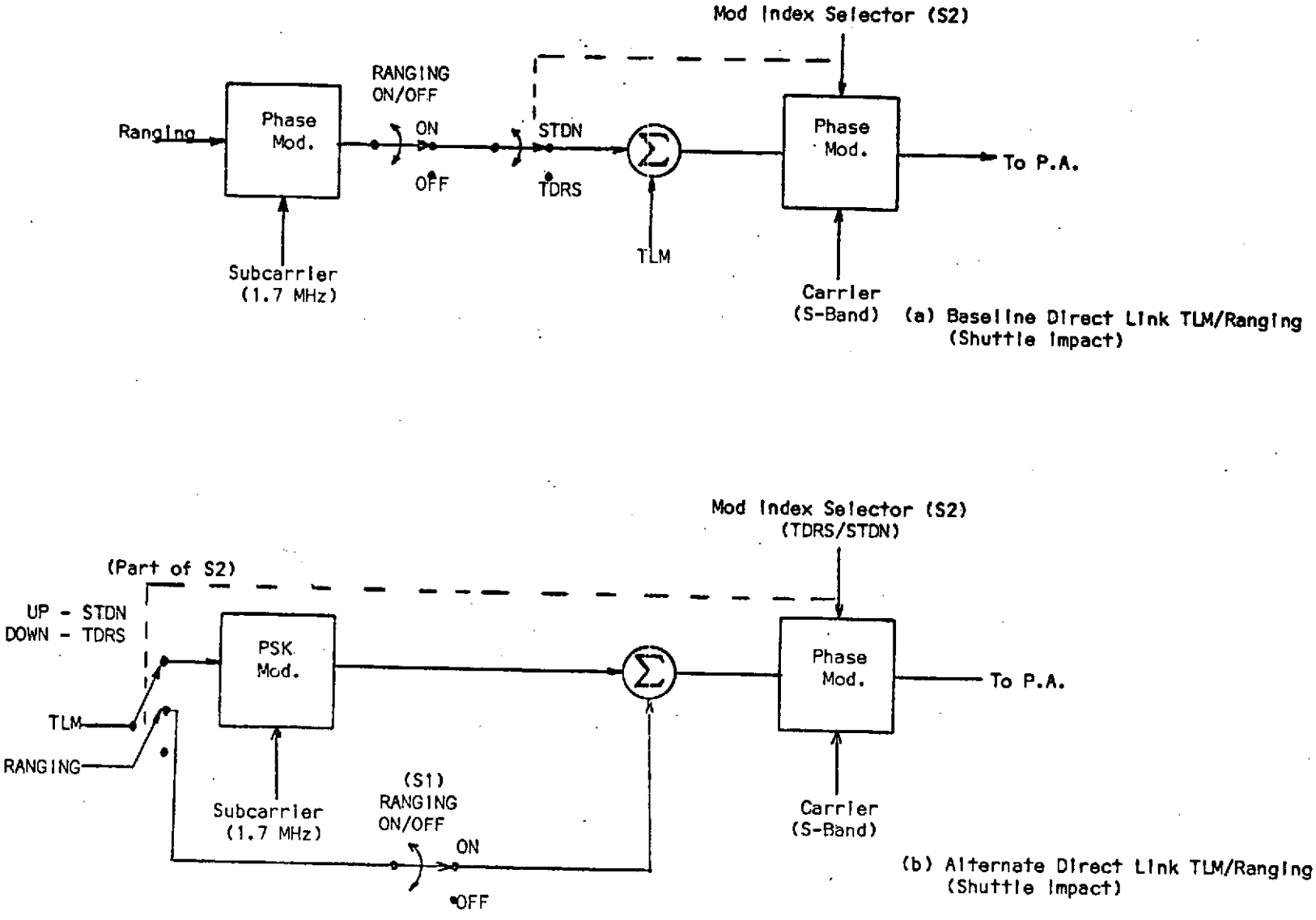

FIGURE 2.6 DIRECT LINK TLM/RANGING SHUTTLE IMPACT

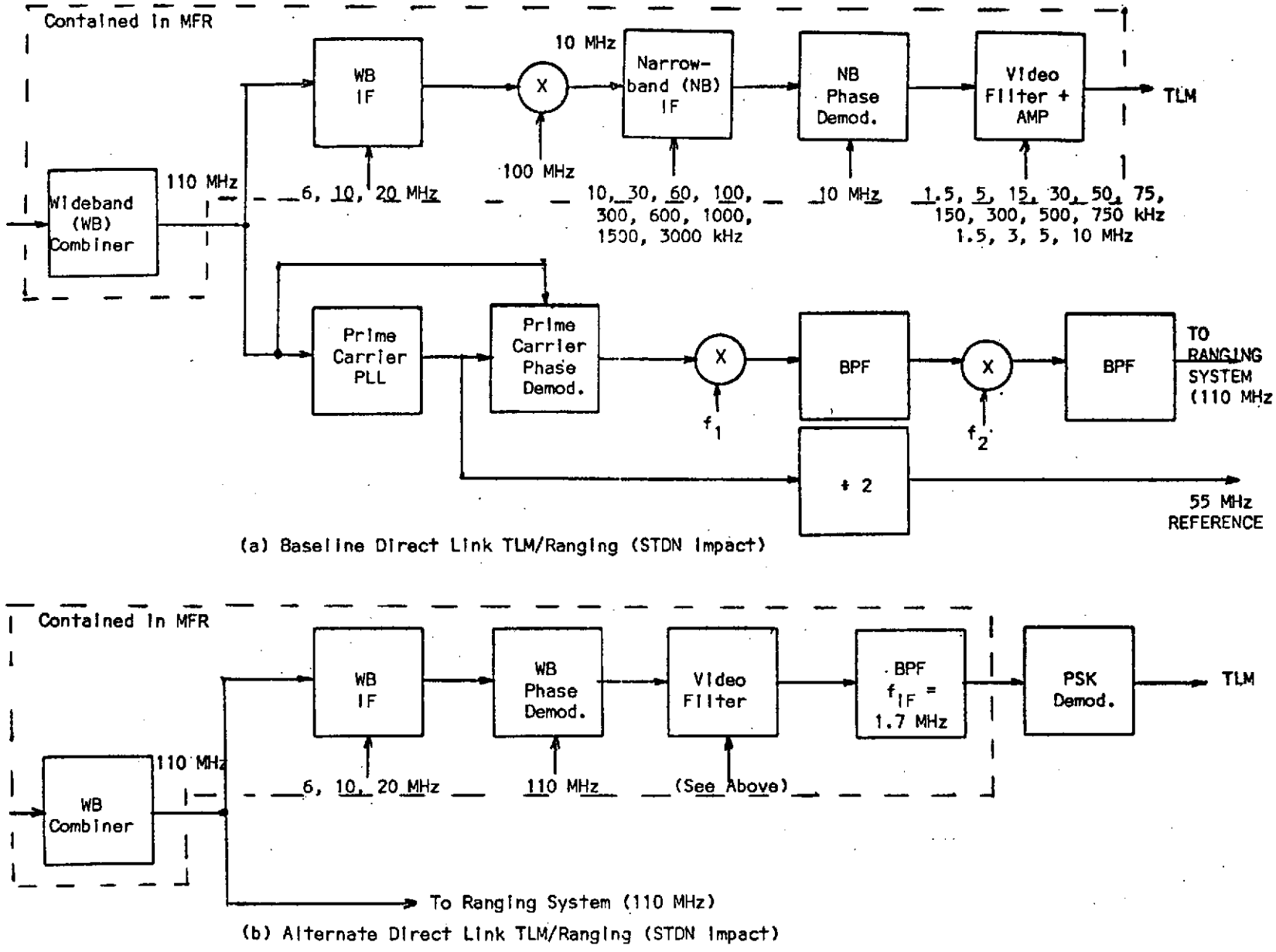

FIGURE 2.7 DIRECT LINK TLM/RANGING STDN IMPACT

2.2.7 Conclusions and Recommendations

Since the impact on Orbiter is negligible (just another pole on an existing switch), the complexity of the required STDN support is so much less, and the interference between the ranging signal and the telemetry signal is less, it is recommended that the telemetry be suppressed carrier modulated onto the 1.7 MHz subcarrier in an NRZ form with Δ-coding to resolve ambiguities, and the ranging be placed on the prime carrier. The other schemes are deemed to be either inefficient in STDN use or impact too heavily on Orbiter. The baseline system could be used; however, the impact on STDN is considerable and an adjustment in modulation parameters from the baseline is needed to minimize interference problems with the ranging recovery.

2.2.8 References

(1) D. E. Cartier, "Shuttle Communications Design Study," First Monthly Report, NASA Contract No. NAS9-13791, April 30, 1974.

(2) D. E. Cartier, "Direct Link Telemetry and Ranging for Shuttle," letter to S. W. Novosad, May 9, 1974.

(3) Shuttle Orbiter/GSFC Communications and Tracking Interface Control Document, ICD-0D044, NASA Lyndon B. Johnson Space Center, LEC-1161, January 1974, p. 5-14.

(4) D. E. Cartier, "Baseband Power Spectrums," The Magnavox Company Technical Memorandum, ASAO-TM72-0004, April 1972.

(5) W. C. Lindsey, "Design of Block-Coded Communication Systems," IEEE Transactions on Communication Technology, Vol. COM-15, No. 4, August 1967, pp. 525-534.

(6) Aerospace Data Systems Standards, NASA/GSFC X-Document, X-560-63-2, July 1, 1971.

APPENDIX 2.A

IF FILTER SELECTION

The IF filters used in the MFR are divided into two categories. The wider bandwidth filters, those with bands of interest (Δf) ranging from 3MHz to 20 MHz, are specified with group delay variations ratios

of 1.2/1 over the Δf bandwidth. The narrower bandwidth filters, from 1.5 MHz to 10 kHz are specified with group delay variation ratios of 1.4/1 over the Δf bandwidth. These narrower filters possess steeper skirts than do the wider filters. The pertinent characteristics of the two categories are listed below.

CHARACTERISTIC	CATEGORY I WIDEBAND 3 MHz - 20 MHz	CATEGORY II NARROWBAND 10 kHz - 1.5 MHz
Band of Interest (Δf)	3.0, 6.0, 10, 20 MHz	10, 30, 60, 100, 150 300, 600 kHz 1.0, 1.5 MHz
Minimum 1 dB BW	.9 Δf	.9 Δf
Maximum 3 dB BW	1.5 Δf	1.7 Δf
Maximum 50 dB BW	3.5 Δf	5 Δf
Group Delay Variation Ratio, Max/Min, Over Δf Bandwidth	1.4/1	1.2/1
Minimum Ultimate Attenuation	80 dB	80 dB
Passband Ripple Δf Bandwidth	0.5 dB	0.5 dB

APPENDIX 2.B

INTERFERENCE ANALYSIS DERIVATION

The worst case condition for the baseline in the telemetry or carrier phase lock case is for single tone ranging with the highest tone applied. (GRARR applies the tones sequentially to use power most efficiently.) This puts the most power closest to the prime carrier. This will be assumed in what follows.

Knowing the subcarrier mod index gives the power in each sideband and the subcarrier, viz., for a signal of the form $\sqrt{2P_{TS}}$ $\sin [\omega_{sc} t + m_s \cos \omega_r t]$,

$$\frac{P_{SC}}{P_{TS}} = J_0^2(m_s), \tag{2.B.1}$$

where m_s is the mod index, P_{SC} is the power in the subcarrier, and P_{TS} is the total subcarrier power, and $J_i(x)$ is the ith order Bessel function.

$$\frac{P_{SC}}{P_{TS}} = 2J_1^2(m_s), \tag{2.B.2}$$

where P_{SB} is the power in both of the 1st sidebands. For low m_s this is the only one of concern (note high indices create severe interference problems). For the baseline system $m_s = 0.3$ gives 95.57% of the power in the subcarrier and 4.4% in both 1st sidebands (2.2% per sideband) for a total of 99.967%. The rest is in the other sidebands and is negligible.

Consider[5] now the baseline signal, i.e.,

$$S(t) = \sqrt{2P} \sin [\omega_c t + \tau b(t) + m_p \cos (\omega_{sc} t + m_s \cos \omega_r t)], \tag{2.B.3}$$

where τ is the telemetry index, b(t) is S/P telemetry with values ± 1, and m_p is the subcarrier index. Write S(t) in terms of a complex frequency.

$$S(t) = \sqrt{2P}\ \mathrm{Im}\left[e^{i\omega_c t}\ e^{i\theta(t)}\right]. \tag{2.B.4}$$

$$e^{i\theta(t)} = e^{i\tau b(t)}\ e^{im_p \cos\ (\omega_{sc} t + m_s \cos \omega_r t)} \tag{2.B.5}$$

$$= e^{i\tau b(t)} \sum_{K=-\infty}^{\infty} i^K J_K(m_p)\ e^{iK[\omega_{sc} t + m_s \cos \omega_r t]}$$

$$= \sum_{K=-\infty}^{\infty} i^K J_K(m_p)\ e^{iK[\omega_{sc} t + m_s \cos \omega_r t]} [\cos \tau + i\ b(t) \sin \tau]$$

(2.B.6)

To find the carrier power, P_c, we want only constant terms in the above, i.e., $e^{j(\omega_c t + \lambda)}$ type of terms, therefore set K = 0. Thus

$$\sqrt{2P}\ \mathrm{Im}\left[e^{i\omega_c t}\ J_0(m_p)\ [\cos \tau + i\ b(t) \sin \tau]\right] \tag{2.B.7}$$

Eliminate the b(t) term* to get

$$2P\ \mathrm{Im}\left[e^{i\omega_c t}\ J_0(m_p) \cos \tau\right]. \tag{2.B.8}$$

Hence $\frac{P_c}{P} = J_0^2(m_p) \cos^2\tau$.

To find the power in the subcarrier <u>plus</u> all of its sidebands, P_s, set K = ±1. Thus

$$\sqrt{2P}\ \left[\mathrm{Im}\{J_1(m_p) i e^{i[(\omega_c+\omega_{sc})t+m_s \cos \omega_r t]} [\cos \tau+i\ b(t) \sin \tau]\}\right.$$

$$\left. - \mathrm{Im}\{J_{-1}(m_p) i e^{i[(\omega_c-\omega_{sc})t-m_s \cos \omega_r t]} [\cos \tau+i\ b(t) \sin \tau]\}\right]$$

(2.B.9)

Eliminating the b(t) term as before

$$\frac{P_s}{P} = 2J_1^2(m_p) \cos^2\tau. \tag{2.B.10}$$

---

* $\mathrm{Im}\ e^{i(\omega_c t + \tau b(t))}$ is a PM signal with residual carrier given by $\cos^2\tau$.

Note that P_s is the total available power to the subcarrier and its sidebands, i.e., $P_s = 2P_{TS}$ in equation (2.B.1). The power in the data, P_d, is

$$\frac{P_d}{P} = \sin^2\tau \; J_0^2(m_p). \tag{2.B.11}$$

The power in <u>one</u> interference tone is thus

$$P_{tone} = \frac{P_{SB}}{2} = J_1^2(m_s) \times P_{TS} = J_1^2(m_s) \times P_s/2$$

$$= J_1^2(m_s) \times J_1^2(m_p) \cos^2\tau \times P. \tag{2.B.12}$$

Example: $m_s = m_p = 0.3$, $\tau = 1.1$ implies

$$\frac{P_{SB}}{P} = (.1483188)^4 \times (0.20564) = 9.95 \times 10^{-3}\%. \tag{2.B.13}$$

The power in the data is

$$\frac{P_d}{P} = 75.96\%. \tag{2.B.14}$$

The power in the carrier is

$$\frac{P_c}{P} = 19.65\%. \tag{2.B.15}$$

From the above example a conclusion can be drawn about the baseline case. The ranging presents no interference to the carrier PLL or the telemetry due to the filtering and the small amount of power in the subcarrier and its ranging signal.

The interference from the telemetry when trying to isolate the ranging is another matter. Since there is so much data power and since the split phase spectrum is so close, sharp filters are required. Also phase distortion in the isolation filters is critical in the ranging, therefore sharp filters are hard to realize (equalization may be needed).

The interference can best be pointed up by the following.

$$\frac{P_d}{P_s} = 84 \ (19.2 \text{ dB}) \qquad (2.B.16)$$

The conclusion is therefore to put more power in ranging subcarrier and sidebands. As of now 19.2 dB rejection is needed from the filter to break even, "powerwise" (ranging power = telemetry power).

The above equations applied to the alternate scheme give the following results. There is no problem with the carrier PLL due to the large power differential and filtering. The ranging and data sideband power are equal, therefore 20 dB of filtering gives good results. The only drawback over the baseline is the 4.2% for the data in the alternate versus the 75.96% in the baseline. The overall conclusion is that less interference is present with the alternate, but still some tradeoff is needed in the modulation indices. Parameter adjustments will equalize this however.

3.0 SPACE SHUTTLE COMMUNICATIONS BLACKOUT DUE TO ROCKET EXHAUST FLAMES

3.1 INTRODUCTION

This study is concerned with the communication blackout effect due to the rocket exhaust flames which supposedly produce up to 8 minutes of no communication between Space Shuttle and some ground stations during the Shuttle launch period. Due to the high temperature of the exhaust flames, the flames develop a plume of plasma region. (Here, the plasma is defined to be an ionized gaseous system which has no average space charge.) Since the plasma contains free electronics as well as ionized molecules, it constitutes an electrically conducting zone. Hence,

the microwave propagating through the plume will experience severe attenuation and thus the plume results in a blackout zone. For engineering purposes, the geometry of the blackout zone is approximated by a cone. The task of this study is to estimate the aspect angle of the blackout cone based on the exhaust flame plume shapes of the Space Shuttle, which includes Solid Rocket Motors (SRM) and the Shuttle Orbiter (SO) main engine, considering the effect of microwave attenuation in the plume.

3.2 BACKGROUND AND APPROACH

The generally accepted theory[1] of microwave propagation in a plasma pays heed only to the motion of the free electrons, the effect of the comparatively inert ions being disregarded. The electrons are assumed to be vibrating in an inertial manner under the force of the applied electric field, their motion being damped by a frictional force; this frictional force, averaged over a large number of electrons, is proportional to the velocity of the electrons and is due to the collisions that the electrons make with the molecules of the gas. As a consequence, the effective dielectric constant in the plasma is reduced below that of free space, and the plasma has an effective conductivity which depends upon the electron density and the collision frequency as derived in reference 2 by

$$\varepsilon_\gamma = \left[1 - \frac{Ne^2}{\varepsilon_\nu(\nu^2 + \omega^2)}\right] \tag{3.1}$$

and

$$\sigma = \frac{Ne^2\nu}{m(\nu^2 + \omega^2)} \tag{3.2}$$

where

ε_γ = dielectric constant in the plasma

N = number of electrons per cubic meter

E = electron charge = 1.59×10^{-9} coulomb

ε_ν = dielectric constant in vacua

ν = collision frequency of rad/sec

ω = wave frequency in rad/sec

σ = conductivity in the plasma

m = electron mass = 9×10^{-31} Kg

Since the electrical property of the plasma region is characterized by the effective dielectric constant ε_γ and the effective conductivity σ, it can be easily shown[2] that the attenuation factor in the plasma is given by

$$\alpha = \frac{60\pi Ne^2\nu}{\sqrt{\varepsilon_\gamma}\, m(\nu^2 + \omega^2)} \tag{3.3}$$

The total attenuation of the wave in the plume would then be obtained by integrating along the whole length of the path through the plume.

The path of the wave in the plume is affected by the distribution of the electron density, since the refractive index of the plume is a function of electron density given by

$$n = \sqrt{1 - \frac{81N}{f^2}} \tag{3.4}$$

for $\omega^2 >> \nu^2$. Therefore it is not easy to predict the path of the wave in the plume unless the electrons are distributed uniformly in which case the path will become a straight line. For a specific electron distribution, the ray-optic technique is commonly used to trace the path of the wave in practice. The Three-Dimensional Ray-Tracing Program[3] is an example of a ray tracing technique.

As mentioned above, since both the microwave path and attenuation are functions of the electron density in the plume it is essential to find the electron density distribution in the plume to evaluate the attenuation of the microwave.

As illustrated in Figure 3.1, the main electron source in the plume is considered to be the impurities such as Na^{+}, K^{+}, $A\ell^{+++}$ in the fuel in the rocket motor chamber. The electron density in the chamber is supposedly determined by the chemical equilibrium[4] of chamber temperature and pressure. The electrons thus generated in the chamber are ejected out of the chamber through the nozzle into the plume and are distributed again depending on the pressure and temperature distribution in the plume (since the recombination coefficient of the electrons are functions of pressure and temperature).[4] The pressure and temperature distributions in the plume are determined by the nozzle and plume flowfield properties. The Lockheed-Huntsville Method-of-Characteristics Computer Program[5][6] is typical for calculating the nozzle and plume flowfield properties and NASA-Lewis Chemical Equilibrium Combustion (CEC) Computer Program[7] is typical for calculating the chemical Equilibrium compositions to the author's knowledge. The Boeing Company[3][8][9] developed a computer program to evaluate the microwave attenuation in the Saturn V exhaust flame and also used the program to calculate the flame effect on the unified S-Band performance for Saturn AS-202. Smoot, et al.[10][11] has developed an improved plume model to enhance the accuracy based on the aforementioned MOC and CEC Computer Programs. However, it seems that there is still a large gap between the computer calculated results and the experimental data[11][12] with the present state-of-the-art.

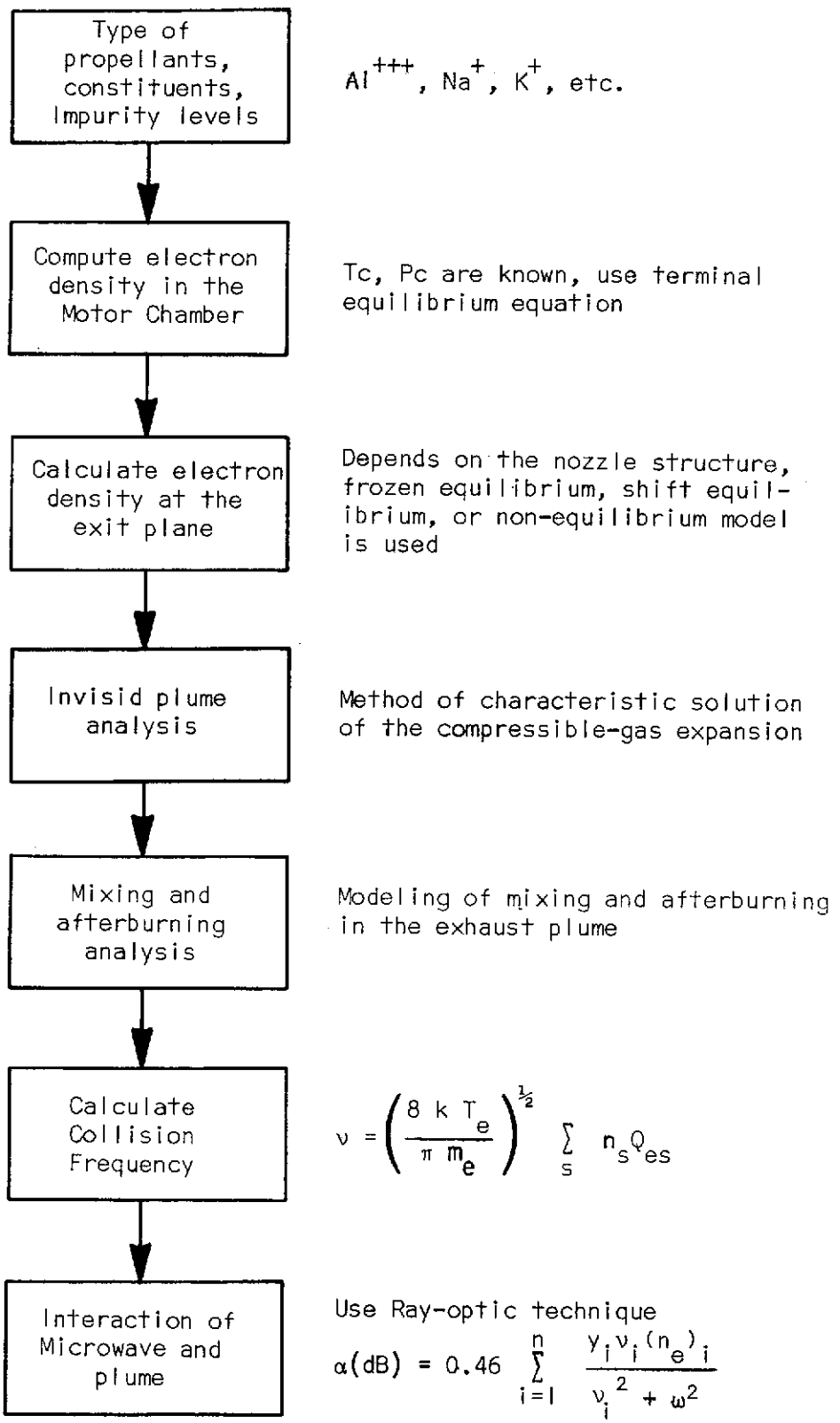

FIGURE 3.1 FLOWCHART OF CALCULATING THE MICROWAVE ATTENUATION IN THE ROCKET EXHAUST PLUME

In all of the above computer programs it was assumed that the plume shapes were symmetric about the plume axis. However, as we will see later, since the exhaust plume of the Space Shuttle will consist of flames from two Solid Rocket Motor nozzles and three Shuttle Orbiter main engine nozzles whose configurations are asymmetric about the Shuttle axis, the resultant flame plumes will obviously not be symmetric at all. Furthermore, to the author's knowledge, no work seems to have been done to date to find the shape and structure of the resultant flame plumes of the Space Shuttle, though the individual plume shapes have been predicted by using the aforementioned MOC and CEC Computer Programs[13] and confirmed partly by experiments.[14]

Since it was our opinion that finding the shape of the plumes in the formal way such as suggested by Smoot, et al.[4] would be beyond the scope of this study, considering the research period and its application, our study has been performed with the following assumptions:

- The resultant plume shapes of the Space Shuttle will be the same as those obtained by simple geometric summation of the individual plumes.
- The microwave propagates on the straight line connected between the transmitter and the receiver locations. This implies that the reflection and refraction effects of the wave are not considered.
- The microwave propagating through the plume will be completely blocked out, since the wavepath of interest in the plume makes a small angle with the plume axes and thus constitutes a relatively long path as compared to the width of the plume. This assumption is based on the experimental results of Poehler[12], Wood and Demore[15], and Baghdady and Ely[16], which show around 20 dB signal attenuation in the plume for the similar problem, and is considered reasonable for our purposes. More justification for this assumption is given in a later section.

With the above assumptions, one can simplify the communication blackout problem as depicted by Figure 3.2, where the signal paths indicated by B and C will be blocked out, while path A will not experience any attenuation due to the exhaust flames except for the free-space loss. Therefore, the problem is now reduced to finding the aspect angle of the path B.

In the following section, we will discuss the individual plume shapes due to the Solid Rocket Motor and Shuttle Orbiter main engine. In Section 3.4, we will draw the resultant flame shapes of the Space Shuttle on the basis of the individual plume shapes, upon which we will ascertain the blackout cone angles for various Shuttle altitudes. The conclusion of this study follows in Section 3.5. As a supplement, we discuss the microwave attenuation in the exhaust flame of the TITAN III C solid rocket motor in Section 3.6. This is to help justify the aforementioned assumption by noting the differences between the empirical data and theoretical calculations.

3.3 EXHAUST PLUME MODELS OF SOLID ROCKET MOTOR AND SHUTTLE ORBITER MAIN ENGINE

In this section, we will discuss the exhaust flame plume shapes of the SRM and SO main engine originally computed using a 0.019-scale model launch configuration of the Space Shuttle (JSC 040 A) and the Lockheed-Huntsville MOC Computer Program[5][6] by the Lockheed Company.[13] In the computation, the thermochemistry properties were computed using the NASA-Lewis CEC Computer Program.[7] The thermochemistry properties of the nozzle-plume flow field were computed assuming the flow to be in chemical equilibrium.

The SO main engine and SRM exhaust plumes were calculated for conditions corresponding to the test points M = 0.765, 1.4, 1.6 and 2.2.

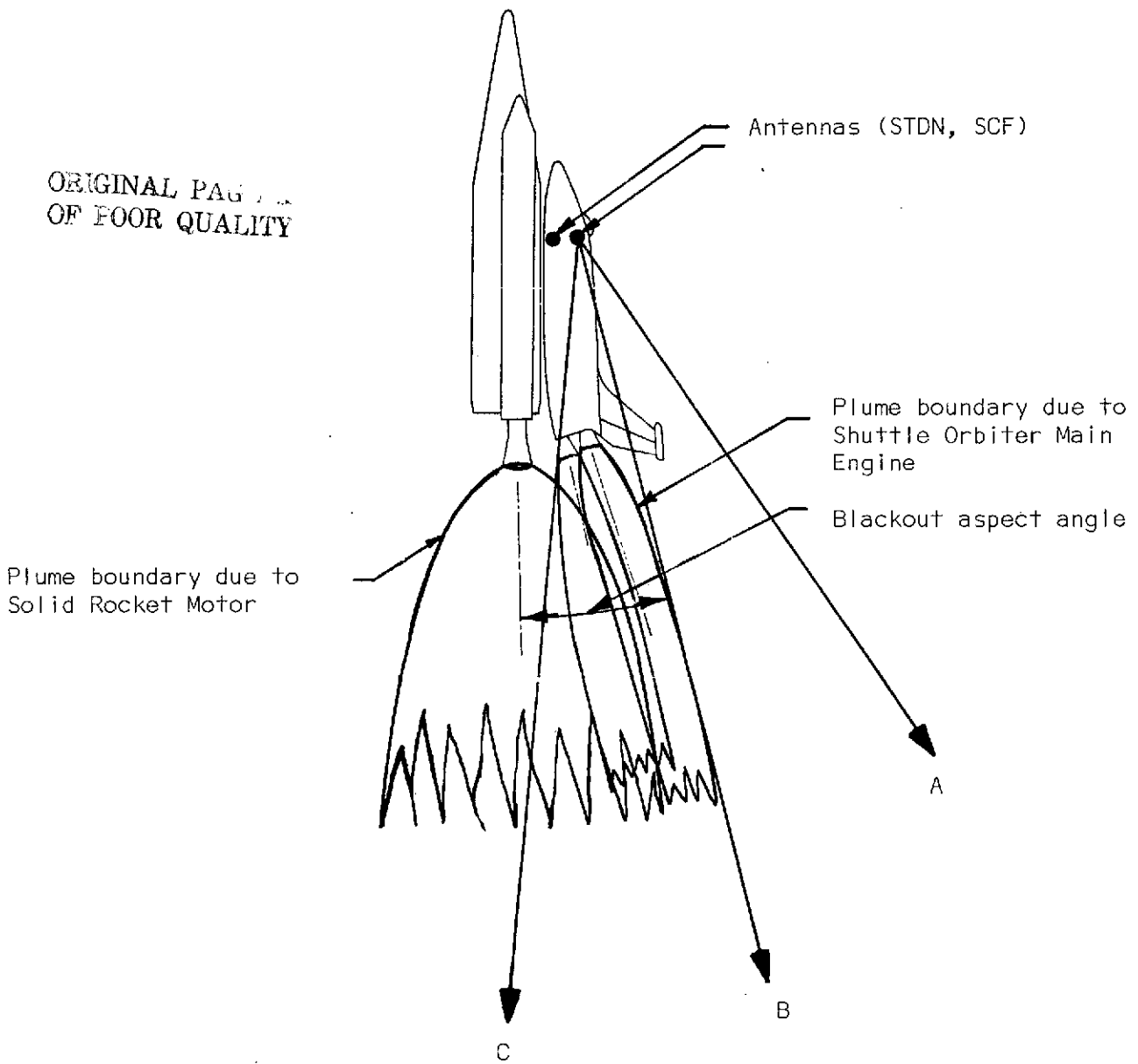

FIGURE 3.2 SPACE SHUTTLE CONFIGURATION AND POSSIBLE SIGNAL PATHS

Figure 3.3 shows the variation of the full-scale Space Shuttle launch vehicle Mach number with time (t = 0 sec at liftoff) for the applicable launch vehicle trajectory in use when this study was conducted. Figures 3.4 and 3.5 show the corresponding variation of altitude and static pressure with time. Utilizing Figures 3.3 through 3.5 the external environment for the various plumes was obtained.

The exhaust plumes were computed assuming the prototype engine exhaust gases expand to quiescent conditions at the trajectory altitude corresponding to the test Mach numbers.

3.3.1 The Solid Rocket Motor Exhaust Plume Shapes

The SRM flow fields were calculated for a nozzle with an area ratio of 8.0 and a nozzle half angle of 17.5 deg as given in Table 3.1. The propellant used in the combustion was an aluminum-filled P BAND propellant typical of propellants used in 3.96m (156-inch) SRMS. The combustion chamber pressure for each test point is given in Figure 3.6. Due to the preliminary state of the SRM nozzle design, a one-dimensional exit plane start line was employed to initiate the SRM plume flowfield analysis. Table 3.2 presents the plume coordinates for a single plume for each respective test point with the graphical representation of the plume shapes shown in Figure 3.7. For the test points corresponding to M_∞ of 0.875, 1.237, and 1.4, the plume shapes were computed to the axial station downstream of the nozzle exit at which the maximum plume radius occurred and then assumed to be cylindrical at this radius until the 0.3m (12-inch) limit was reached. The plumes for the test points of M_∞ equal to 1.6 and 2.2 which did not reach the maximum within the 0.3m (12-inch) limit were also terminated at the 0.3m (12-inch) station.

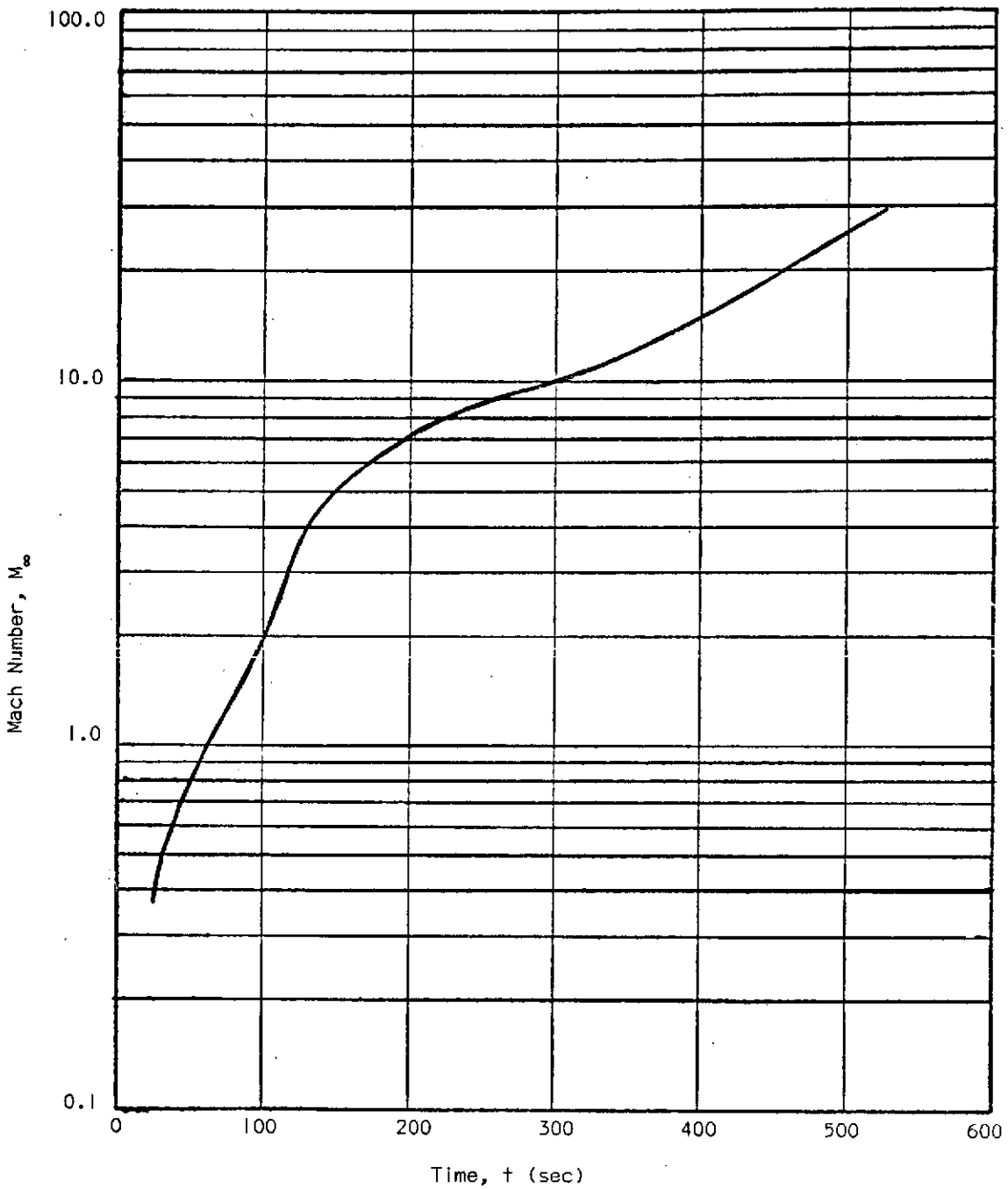

FIGURE 3.3 VARIATION OF THE VEHICLE MACH NUMBER WITH TIME FOR THE SPACE SHUTTLE LAUNCH VEHICLE TRAJECTORY

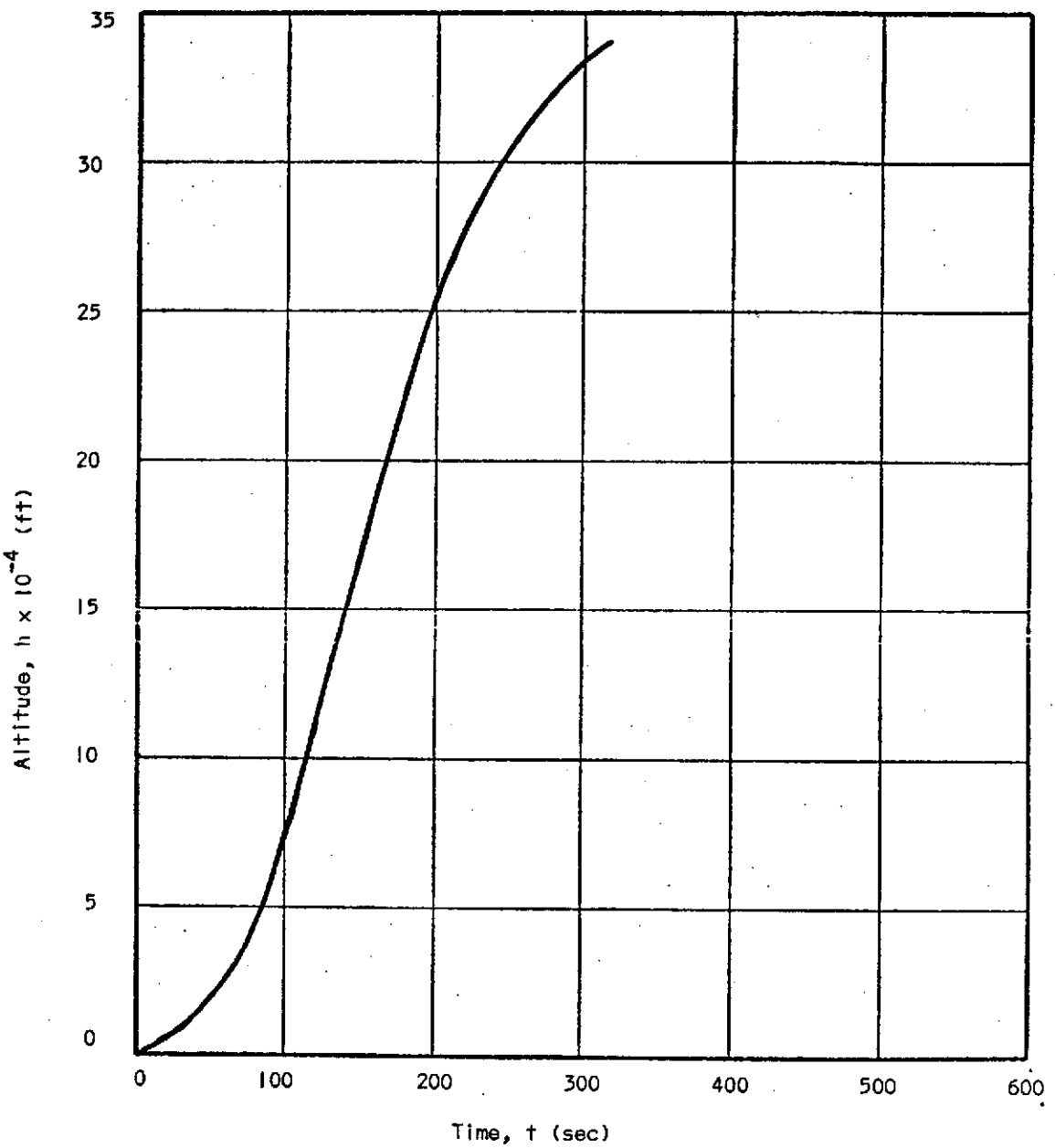

FIGURE 3.4 VARIATION OF ALTITUDE WITH TIME FOR THE SPACE SHUTTLE LAUNCH VEHICLE TRAJECTORY

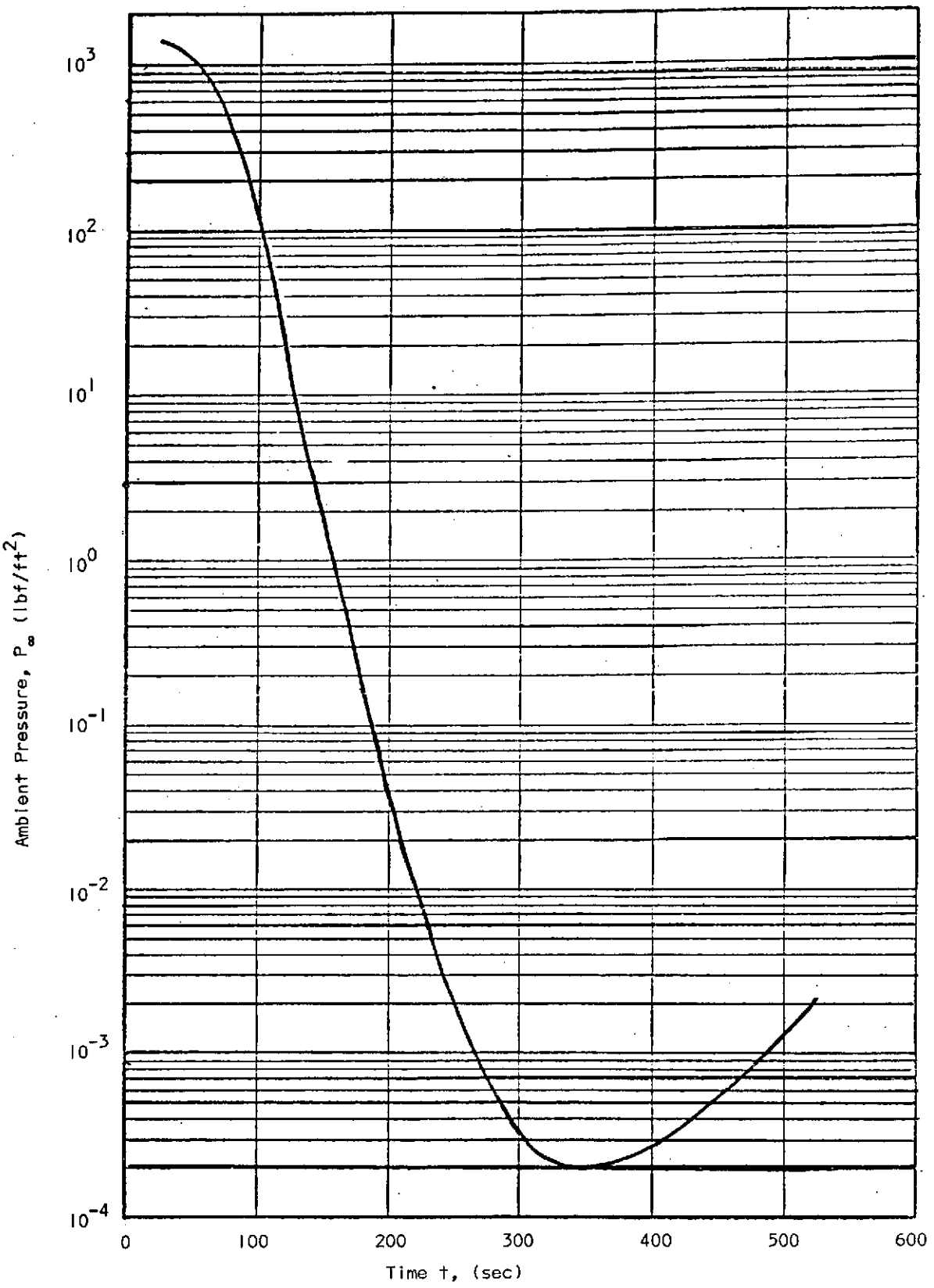

FIGURE 3.5 VARIATION OF THE AMBIENT PRESSURE WITH TIME FOR THE SPACE SHUTTLE LAUNCH VEHICLE TRAJECTORY

TABLE 3.1 PROTOTYPE NOZZLE - MOTOR CHARACTERISTICS

SRM	ORBITER
P_c (see Figure 6)	Area ratio ε = 79.436:1
A/A^* = 8.0	P_c = 200 atm θ_{lip} = 7.87°
θ_{lip} = 17.5°	D_t = 0.2585 m (0.85 ft) D_{ex} = 2.3043 m (7.6 ft)
D_{ex} = 3.5921 m (11.8 ft)	
D_T = 1.27 m (4.2 ft)	
Propellant Composition	Propellant Composition
AP 69.0 Aℓ 15.0 PBAN 9.6 Binder materials 6.4% by weight	O/F = 6.0 Oxidizer $-O_2$(L) Fuel $-H_2$(L)

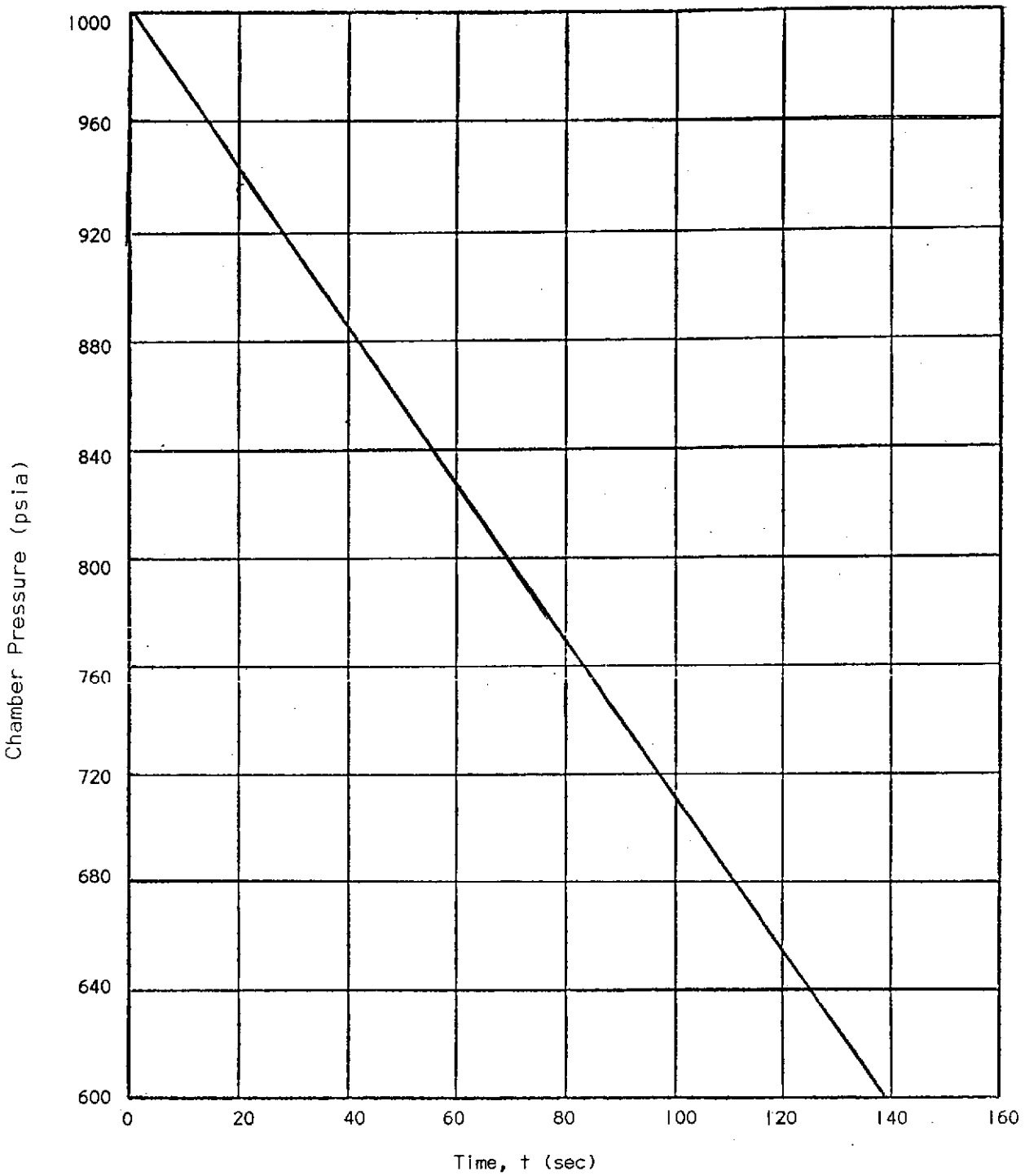

FIGURE 3.6 ASSUMED VARIATION OF THE SOLID ROCKET MOTOR COMBUSTION CHAMBER PRESSURE WITH TIME FOR THE SPACE SHUTTLE LAUNCH VEHICLE TRAJECTORY

TABLE 3.2

TABLE OF THE SPACE SHUTTLE LAUNCH VEHICLE MODEL SOLID ROCKET MOTOR EXHAUST PLUME COORDINATES FOR THE VARIOUS TEST POINTS

TEST POINT
$M_\infty = 0.765$

x (in.)	r (in.)
0	1.3433
0.3266	1.5007
0.8223	1.7032
1.7724	1.9975
2.8872	2.2246
3.9883	2.3516
5.2601	2.3998
r = constant	
12.000	2.3998

TEST POINT
$M_\infty = 1.239$

x (in.)	r (in.)
0.0	1.3433
0.1413	1.4580
0.3225	1.5954
0.8064	1.9209
1.7243	2.4191
2.7984	2.8653
3.5846	3.1217
6.5417	3.6957
9.8214	3.8156
r = constant	
12.000	3.8156

TEST POINT
$M_\infty = 1.4$

x (in.)	r (in.)
0	1.3433
0.2187	1.5420
0.7165	1.9365
1.4082	2.3930
2.3754	2.9104
3.4063	3.3502
4.3827	2.6840
6.0854	4.1124
8.0425	4.4079
9.1033	4.4939
10.2049	4.5337
10.9439	4.5344
r = constant	
12.000	4.5344

TEST POINT
$M_\infty = 1.6$

x (in.)	r (in.)
0.0	1.3433
0.6987	2.0223
1.6596	2.7480
2.8416	3.4513
3.7305	3.8844
4.7577	4.3054
5.9234	4.6977
7.2205	5.0430
10.1406	5.5337
12.2580	5.0811

TEST POINT
$M_\infty = 2.2$

x (in.)	r (in.)
0.	1.3433
1.1970	2.8408
2.9394	4.3688
3.9877	5.1040
5.2360	5.8577
7.7624	7.0788
11.4880	8.3360
12.0000	8.4800

NOTES:

1. Plume axial coordinates referenced to the nozzle exit plane.
2. Model Scale = 1.9%

Sym.	t (sec)	P_c (psia)	P_∞ (psfa)	h (ft)	M (TEST POINT)
A	50	857.0	1057.0	18000	0.765
B	75	784.5	432.0	38000	1.239
C	82	764.0	309.0	43100	1.400
D	89	745.0	201.0	51500	1.600
E	103	694.0	73.7	71000	2.200

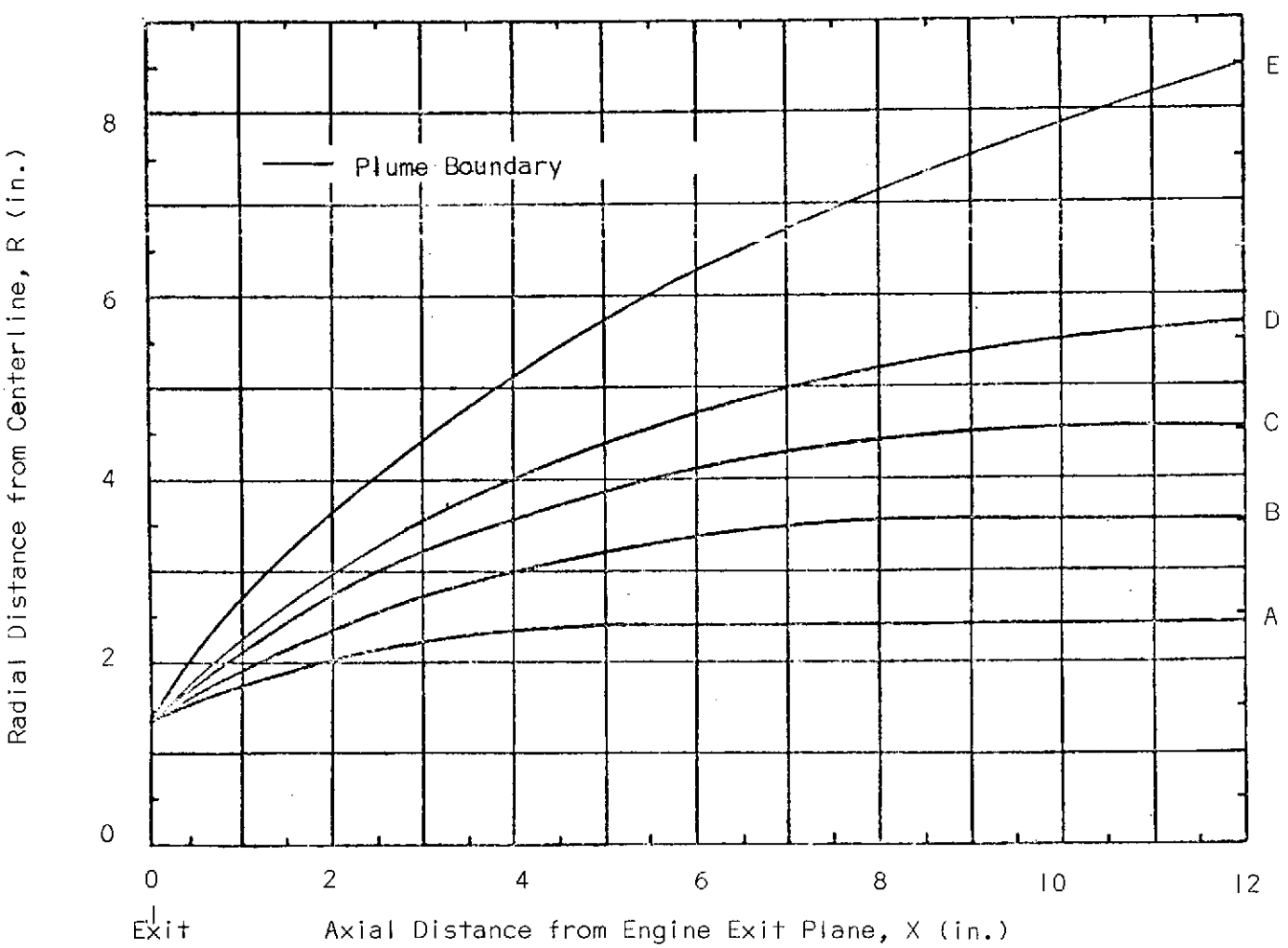

FIGURE 3.7 SPACE SHUTTLE MODEL SOLID ROCKET MOTOR EXHAUST PLUME SHAPES FOR VARIOUS TEST POINTS

3.3.2 The Orbiter Main Engine Exhaust Plume Shapes

The Orbiter main engine nozzle flow fields were computed for a current Orbiter nozzle configuration as given in Table 3.1. The nozzle has a contoured geometry with an area ratio of 79.43. An engine chamber operating pressure of 3000 psia was used in the analysis with the propellant being liquid hydrogen and oxygen at a mixture ratio of 6.0. The nozzle flowfield solution was initiated at the nozzle geometric throat and the subsequent plume calculations performed for the respective conditions for each test point. Table 3.3 presents the exhaust plume shapes for a single plume for each respective test point with graphical representation of each point given in Figure 3.8. The Orbiter plume boundaries were computed based on the same axial plume length limitation (0.3m (12-inches)) that was applied to the SRM calculations. All of the Orbiter plume shapes (except the $M_\infty = 2.2$ test point) reached a radial maximum within the 0.3m (12-inch) limit.

Since we have found the individual plume shapes of the SRM and SO main engine, we are ready to predict the overall plume shapes of the Space Shuttle by placing the individual plumes at the corresponding nozzle exits of the Shuttle model. We will treat this in the next section to find the blackout aspect angle for various points of the Shuttle trajectory.

3.4 DETERMINATION OF COMMUNICATION BLACKOUT ASPECT ANGLE

In this section, we will determine the blackout aspect angle of no communication by drawing the overall exhaust plume shape on the basis of individual plume shapes discussed in the previous section. The basic idea of finding the overall plume shape is to fit the individual plumes into the corresponding nozzles of the 0.019-scale model configuration of the Space Shuttle as mentioned previously.

TABLE 3.3

TABLE OF THE SPACE SHUTTLE LAUNCH VEHICLE MODEL ORBITER MAIN ENGINE EXHAUST PLUME COORDINATES FOR THE VARIOUS TEST POINTS

TEST POINT $M_\infty = 0.765$

x (in.)	r (in.)
0	0.8618
0.1156	0.8649
0.1450	0.8654
0.2194	0.8656
r = constant	
12.0	0.8656

TEST POINT $M_\infty = 1.239$

x (in.)	r (in.)
0	0.8618
0.2097	0.9005
0.5406	0.9479
0.7737	0.9723
1.0159	0.98051
1.4010	1.0061
1.6712	1.0082
r = constant	
12.0	1.0082

TEST POINT $M_\infty = 1.4$

x (in.)	r (in.)
0	0.8618
0.4800	0.9701
1.7929	1.1133
1.9100	1.1200
2.0690	1.1249
2.3920	1.1287
r = constant	
12.0	1.1287

TEST POINT $M_\infty = 1.6$

x (in.)	r (in.)
0	0.8618
0.7265	1.0642
1.3680	1.1887
1.7097	1.2381
2.2517	1.2958
3.2849	1.3477
3.9570	1.3488
r = constant	
12.0	1.3488

TEST POINT $M_\infty = 2.2$

x (in.)	r (in.)
0	0.8618
0.3234	1.0147
0.8284	1.2230
1.2699	1.3807
2.2159	1.6570
2.9800	1.8304
3.7898	1.9732
4.7380	2.0950
5.6920	2.1758
6.6105	2.2194
8.7735	2.2280
9.0829	2.2308
9.4260	2.2408
9.8000	2.2500
12.0000	2.2645

NOTES:

1. Plume axial coordinates referenced to the nozzle exit plane.
2. Model Scale = 1.9%

Sym.	† (sec)	P_c (psia)	P_∞ (psfa)	h (ft)	M (Test Point)
A	50	3000	1057.0	18000	0.765
B	75		432.2	38000	1.239
C	82		309.0	43100	1.400
D	89		201.0	51500	1.600
E	103		73.7	71000	2.200

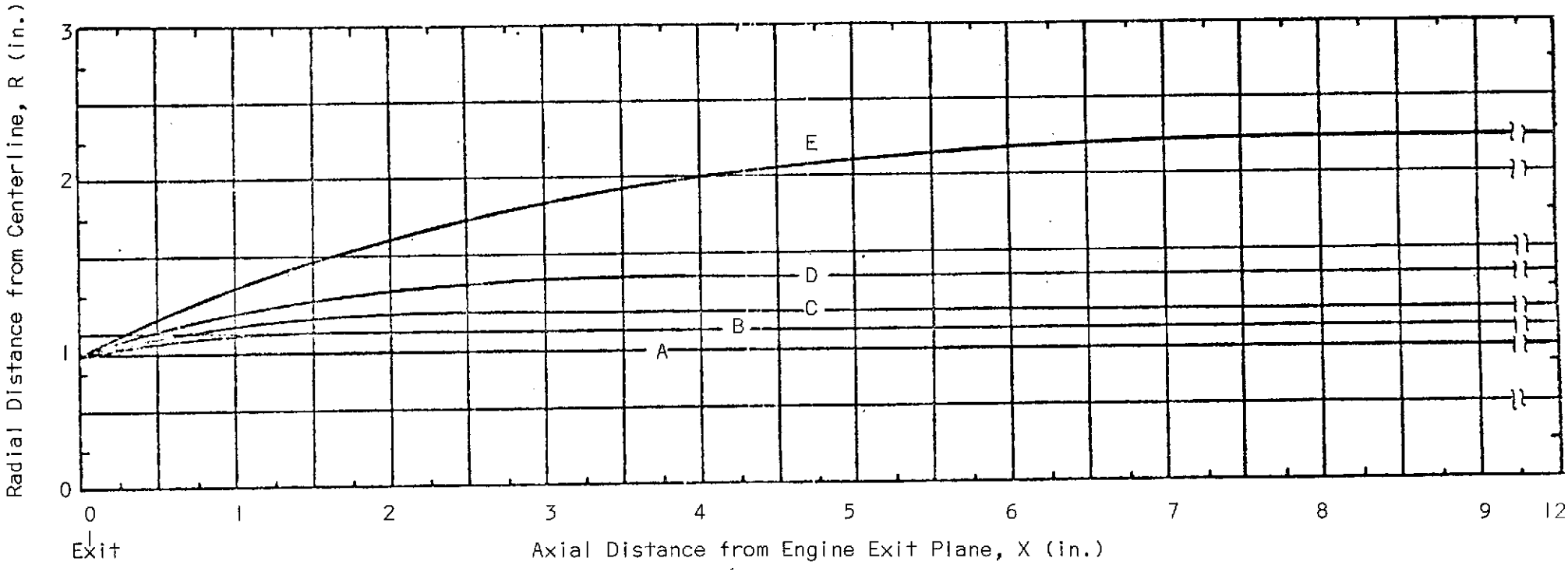

FIGURE 3.8 SPACE SHUTTLE MODEL ORBITER MAIN ENGINE EXHAUST PLUME SHAPES FOR VARIOUS TEST POINTS

The 0.019-scale model (JSC 040 A) geometry and configuration used for this purpose are shown in Table 3.4 and Figure 3.9. Figure 3.10 shows the top view of the overall plume shapes for various test points and Figure 3.11 shows their side views. Both figures are drawn with the aid of Figures 3.7, 3.8, and 3.9. By drawing tangential lines from the prospective antenna locations and the center of gravity to the respective plume boundaries, we are able to obtain the aspect angles as shown in Table 3.5. This table shows that the aspect angle due to the SRM plumes varies from 35.2 degrees to 43.2 degrees and from 17.4 and 28.4 degrees depending on the test points with respect to the center of gravity and antenna location respectively with increasing values as the altitude of the point increases. The angle due to the SO plume varies from 21.8 degrees to 25.5 degrees and from 10.0 to 12.5 degrees with the same tendency respectively. Figures 3.12 and 3.13 show the variations of the aspect angle with time which are obtained by interpolation from the results of Table 3.5.

Considering the Space Shuttle mission profile shown in Figure 3.14, if the ground station is located in such a way that the signal path is formed on the Orbiter side, the aspect angle can be minimized to a value between 10.0 degrees and 12.5 degrees which depends on the SO plume only.

3.5 SUMMARY AND CONCLUSION

The purpose of this study has been to find the communication blackout aspect angle due to the exhaust flame during the Space Shuttle launch period, which supposedly produces up to 8 minutes of no communication between the Space Shuttle and some ground stations.

TABLE 3.4 MODEL GEOMETRY (JSC 040A)

Orbiter Body (BI)		
	Full Scale	Model Scale
Length, m	33.401	0.6346
Maximum width, m	5.1816	.09845
Maximum depth, m	6.0452	.1149
Maximum cross-sectional area, m^2	28.4429	.01027
Projected base area, m^2	27.4863	.009923
Wing (WI)		
Total Data		
Area		
Planform, m^2	293.1368	.1058
Span (equivalent), m	22.4028	.4257
Aspect Ratio	1.71212	1.71212
Taper Ratio	.14860	.14860
Dihedral angle, deg	7	7
Incidence angle, deg	1.5	1.5
Aerodynamic twist, deg	0	0
Sweep back angles		
Leading edge, deg	60	60
Trailing edge, deg	0	0
0.25 element line, deg	52.42	52.42
0.5 element line, deg	40.9	40.9
Chords		
Root (wing station 0.0), m	22.7838	.4329
Tip (equivalent), m	3.3858	.06433
MAC, m	15.4813	.2941
FS of 0.25 MAC, m	26.8714	.5106
BL of 0.25 MAC, m	4.2164	.0801
Airfoil section		
Root	NACA 0008-64	0008-64
Tip	NACA 0008-64	0008-64
Exposed Data		
Area, m^2	186.7356	0.06741
Span (equivalent), m	17.2212	.3272
Aspect Ratio	1.58818	1.58818
Taper Ratio	.18501	.18501
Chords		
Root, m	18.3007	.3477
Tip, m	3.3858	.06435
MAC, m	12.5527	.2385
FS of 0.25 MAC, m	29.0661	.5523
BL of 0.25 MAC, m	5.9090	.1123

TABLE 3.4 MODEL GEOMETRY (JSC 040A) - Continued

	Full Scale	Model Scale
Elevon (WI) (each)		
Area, m^2	21.1509	.007635
Span (equivalent), m	7.0612	.1342
Inboard equivalent chord, m	2.9972	.05695
Outboard equivalent chord, m	2.9972	.05695
Chord/total surface chord		
At inboard equivalent chord	.166	.166
At outboard equivalent chord	.516	.516
Sweep back angles		
Trailing edge, deg	0	0
Hingeline, deg	0	0
Vertical Tail (V2)		
Leading-edge sweepback, deg	45	45
Airfoil section		
Root	NACA 0012-64	0012-64
Tip	NACA 0012-64	0012-64
Exposed Data		
Area, m^2	45.0562	.01626
Span (equivalent), m	9.3769	.1782
Aspect Ratio	1.95	1.95
Taper Ratio	.3137	.3137
Chords		
Root, m	7.3152	.1390
Tip, m	2.2949	.04361
MAC, m	5.2421	.09959
FS of 0.25 MAC, m	37.3136	.7090
WP of 0.25 MAC, m	16.5720	.3149
BL of 0.25 MAC, m	0	0
Rudder (V2)		
Area, m^2	18.4585	.006663
Span (equivalent), m	8.7630	.1665
Inboard equivalent chord, m (WL=12.700)	2.921	.0555
Outboard equivalent chord, m (WL=21.463)	1.016	.01930
Ratio movable surface chord/total surface chord		
At inboard equivalent chord	.4	.4
At outboard equivalent chord	.4	.4

TABLE 3.4 MODEL GEOMETRY (JSC 040A) - Concluded

	Full Scale	Model Scale
Sweep back angles		
Trailing edge, deg	25	25
Hingeline, deg	35	35
Body of Revolution (EHOT)		
Length, m	48.4566	.9207
Maximum width (diam), m	8.2885	.1575
Fineness ratio	5.846	5.846
Maximum cross-sectional area, m^2	53.9558	.01948
Body of Revolution (SRM)(each)		
Length, m	39.3835	.7483
Maximum width (diam), m	3.9624	.07529
Fineness ratio	9.939	9.939
Maximum cross-sectional area, m^2	12.3313	.004452

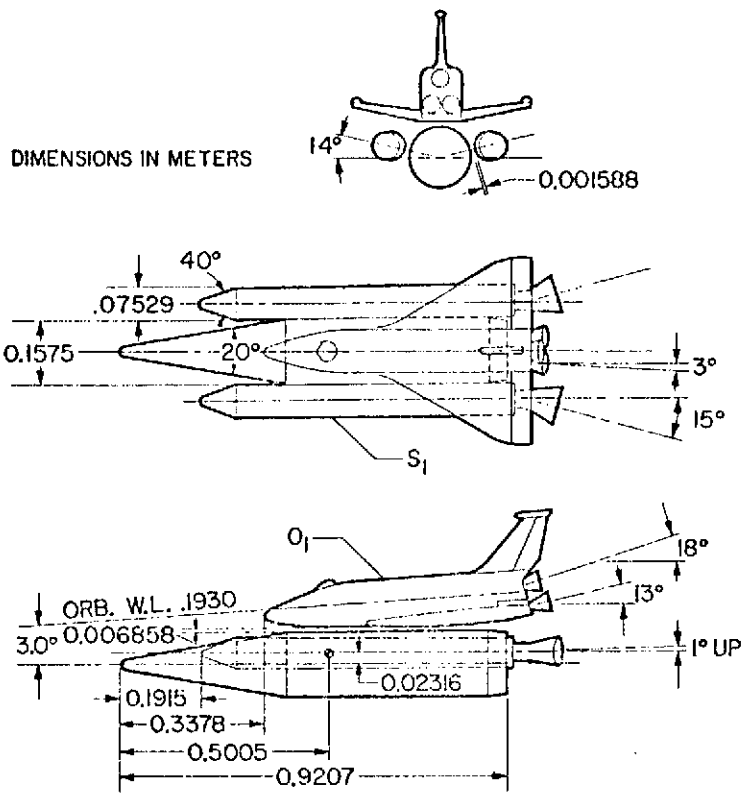

(a) 040A integrated vehicle

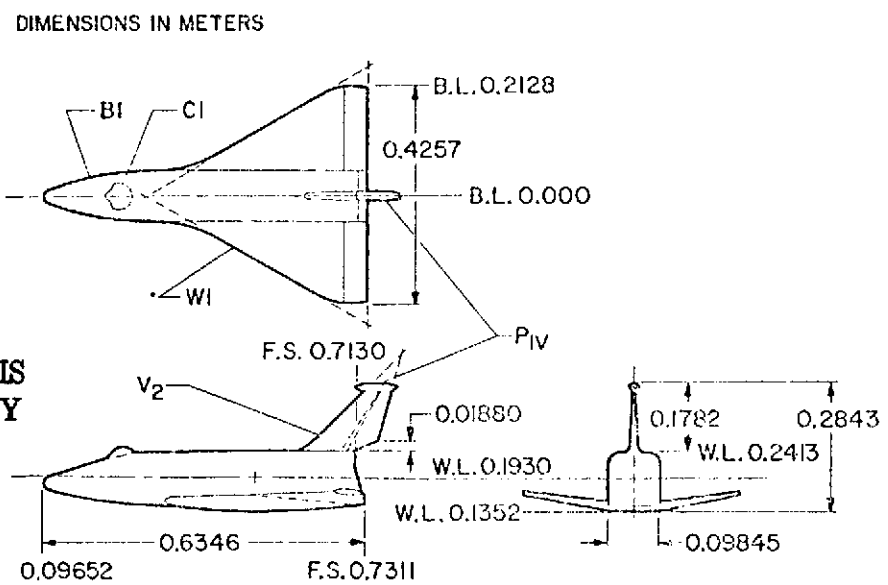

ORIGINAL PAGE IS
OF POOR QUALITY

(b) Shuttle Orbiter

FIGURE 3.9 MODEL OF SPACE SHUTTLE (JSC 040 A)

Sym	t	P_c	P_∞	h	M
	(sec)	(psia)	(psfa)	(ft)	(Test Point)
A	50	857.0	1057.0	18000	0.765
B	75	784.5	432.0	38000	1.239
C	82	764.0	309.0	43100	1.400
D	89	745.0	201.0	51500	1.600
E	103	694.0	73.7	71000	2.200

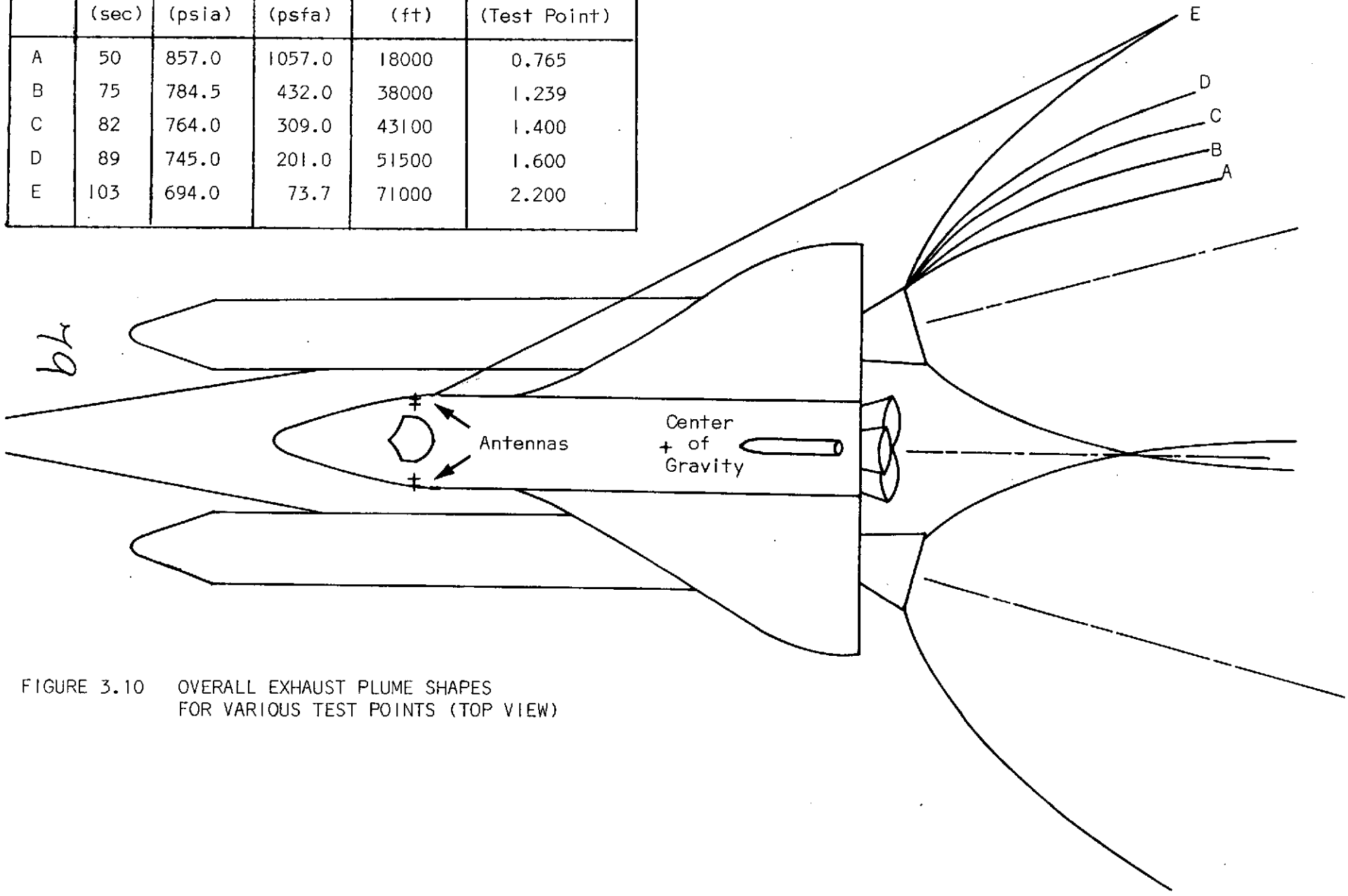

FIGURE 3.10 OVERALL EXHAUST PLUME SHAPES
FOR VARIOUS TEST POINTS (TOP VIEW)

Sym	t	P_c	P_∞	h	M
	(sec)	(psia)	(psfa)	(ft)	(Test Point)
A	50	857.0	1057.0	18000	0.765
B	75	784.5	432.0	38000	1.239
C	82	764.0	309.0	43100	1.400
D	89	745.0	201.0	51500	1.600
E	103	694.0	73.7	71000	2.200

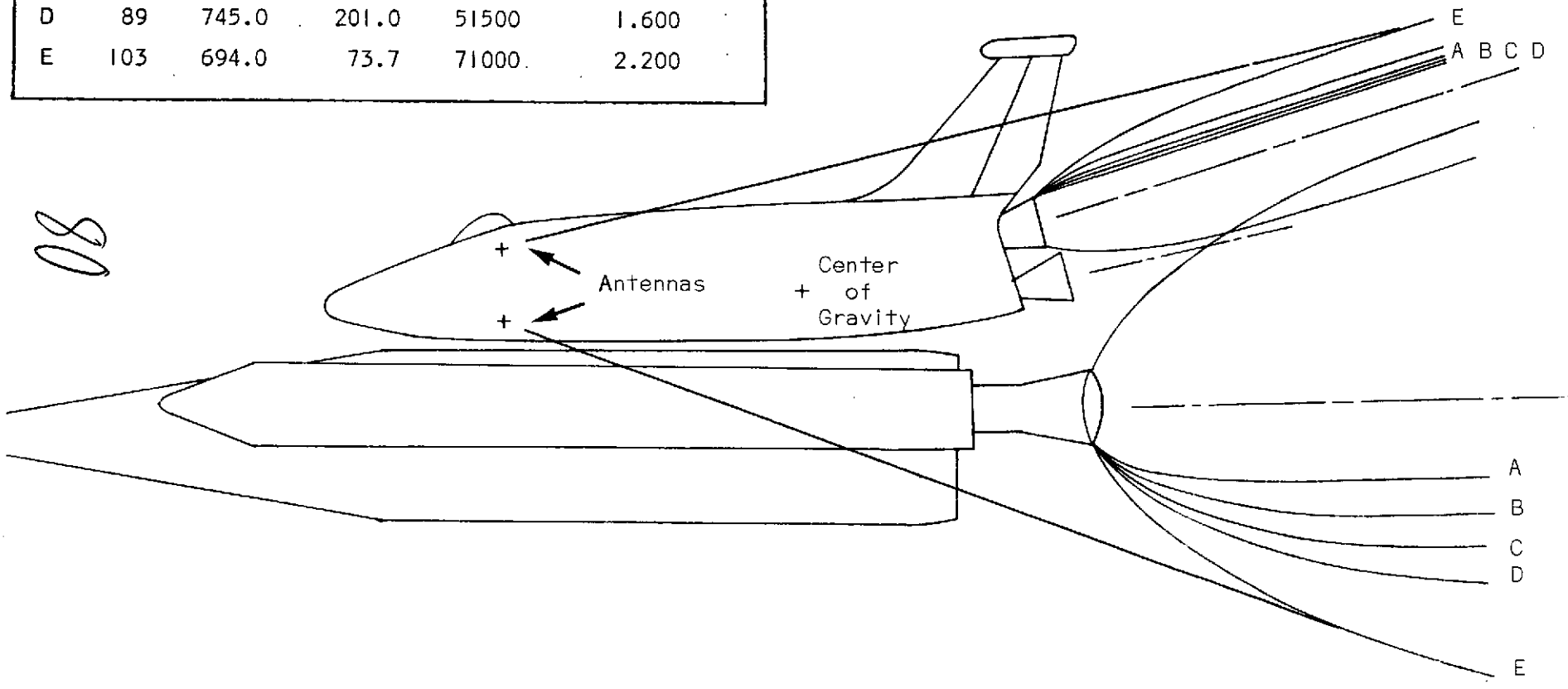

FIGURE 3.11 OVERALL EXHAUST PLUME SHAPES FOR VARIOUS TEST POINTS (SIDE VIEW)

TABLE 3.5 BLACKOUT ASPECT ANGLES

UNIT: DEGREE

Sym	t(sec)	h(ft)	@ CENTER OF GRAVITY			@ ANTENNA		
			TOP VIEW	SIDE VIEW		TOP VIEW	SIDE VIEW	
			SRM PLUME	SO PLUME	SRM PLUME	SRM PLUME	SO PLUME	SRM PLUME
A	50	18,000	35.2	21.8	29.0	17.4	10.0	14.0
B	75	38,000	36.0	21.8	29.6	19.5	10.2	15.0
C	82	43,100	38.0	22.3	30.7	21.4	10.5	16.5
D	89	51,500	39.0	23.2	31.5	23.5	11.0	17.5
E	103	71,000	43.2	25.5	34.5	28.4	12.5	21.0

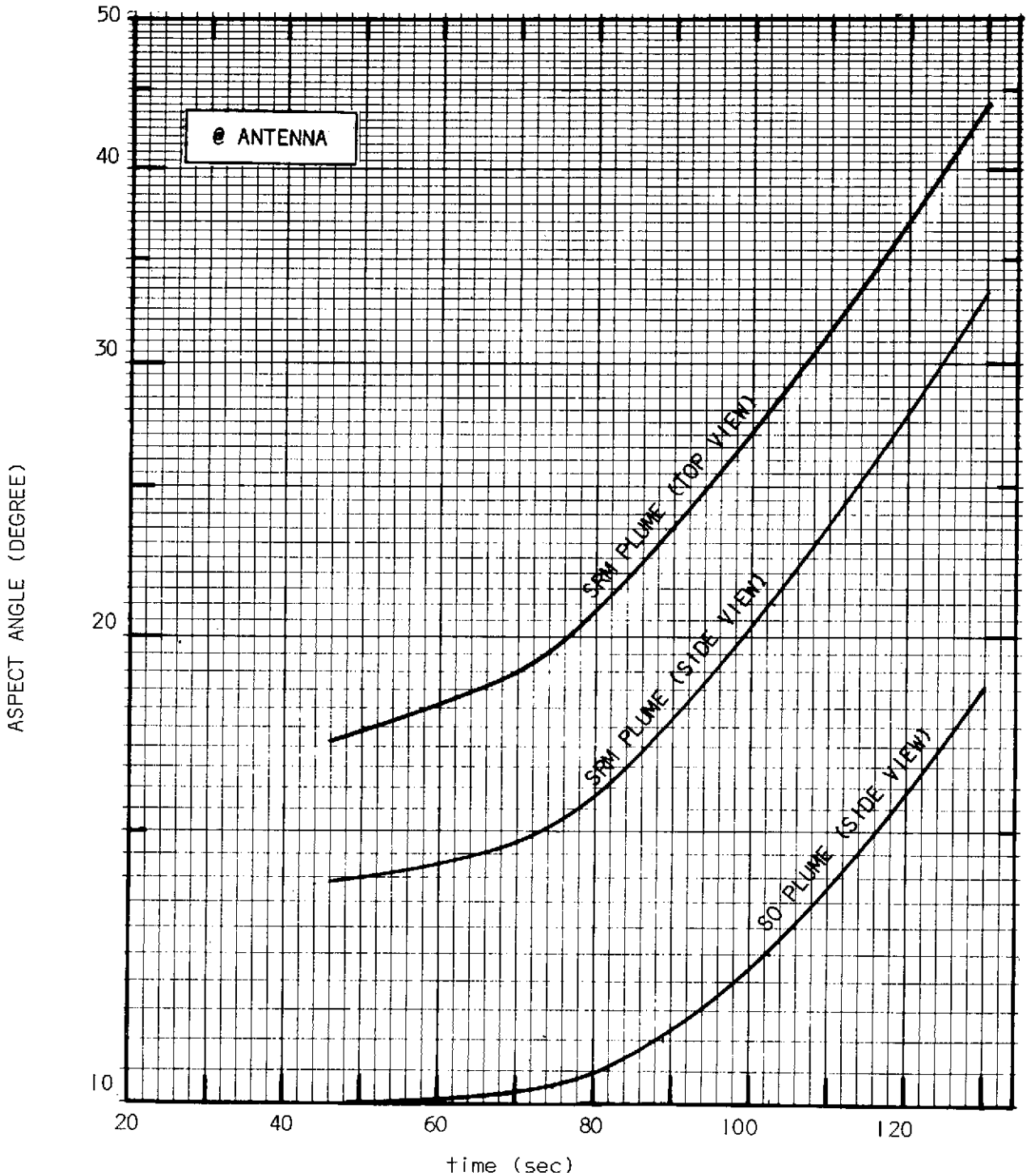

ORIGINAL PAGE IS
OF POOR QUALITY

FIGURE 3.12 VARIATION OF ASPECT ANGLE WITH RESPECT TO THE ANTENNA LOCATION VS. TIME

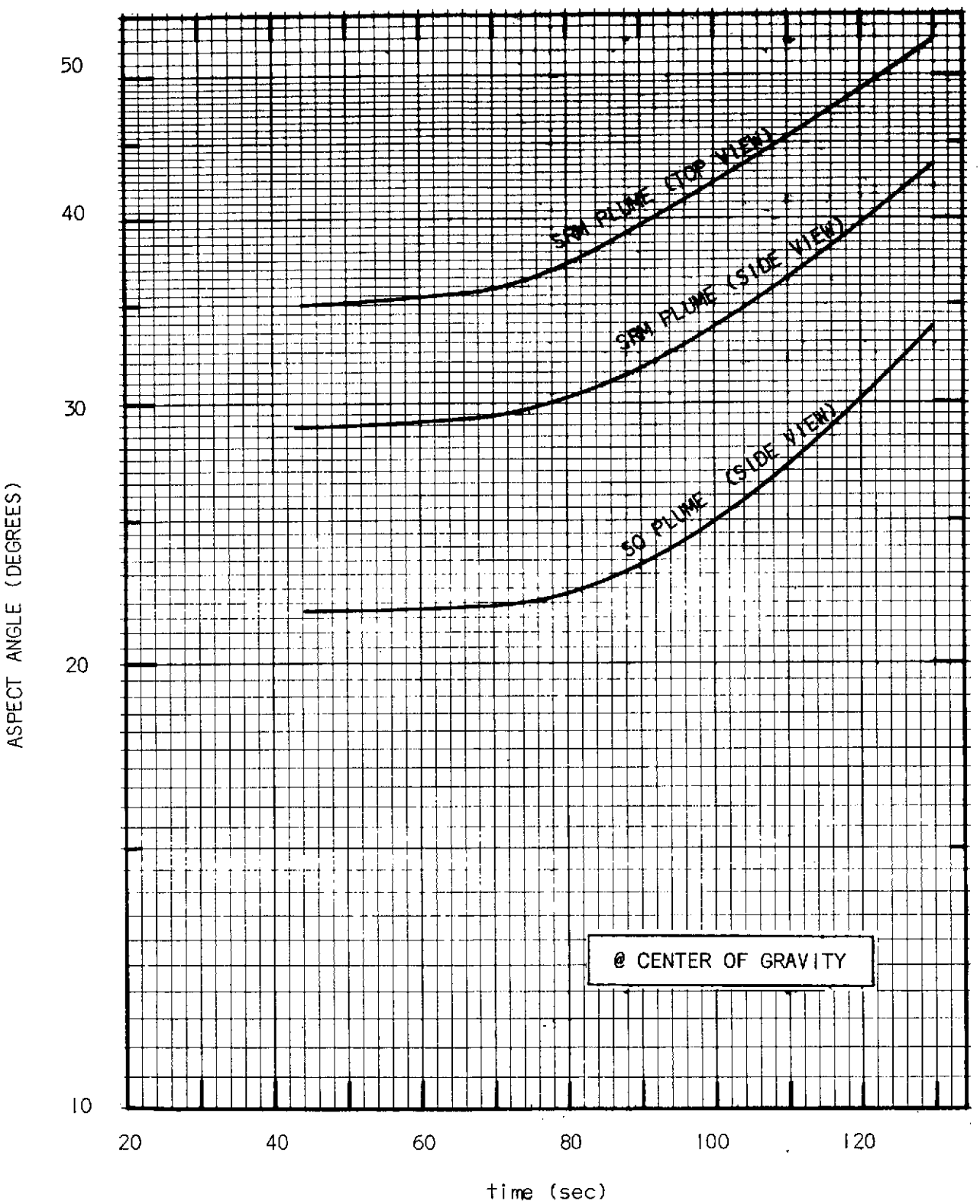

FIGURE 3.13 VARIATION OF ASPECT ANGLE WITH RESPECT TO CENTER OF GRAVITY vs. TIME

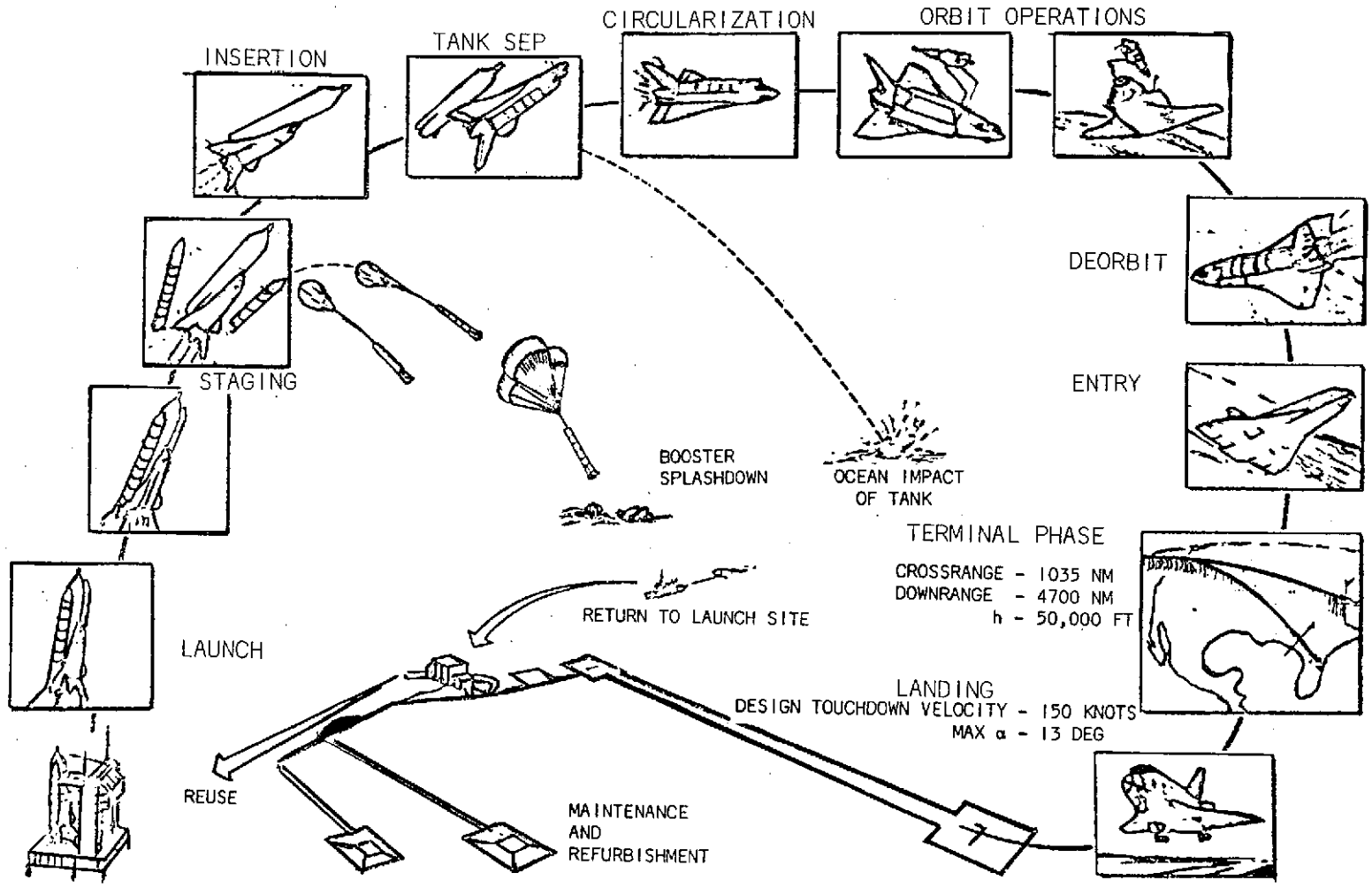

FIGURE 3.14 SPACE SHUTTLE MISSION PROFILE

To attack this problem, this study has been performed with the following assumptions:

- o The overall plume shapes of the Space Shuttle will be the same as those obtained by simple geometric summation of the individual plumes of SRM and SO main engines.
- o The microwave propagates on the straight line connecting the transmitter and receiver locations.
- o The microwave propagating through the plume will be completely blocked out, since the wave path of interest in the plume makes a small angle with the plume axes and thus constitutes a relatively long path as compared to the width of the plume.

With the above assumptions, we used the individual plume shapes of the SRM and SO main engine which were originally computed using 0.019-scale launch configurations of the Space Shuttle (JSC 040 A) and the Lockheed-Huntsville MOC Computer Program by The Lockheed Company to find the overall plume shape.

Based on the overall plume shape thus drawn, the blackout aspect angles for various test points have been found as shown in Table 3.5. This table shows that the aspect angle due to the SRM plumes varies from 35.2 degrees to 43.2 degrees and from 17.4 to 28.4 degrees depending on the test points with respect to the center of gravity and antenna locations respectively with increasing values as the altitude of the point increases while that due to the SO plume varies from 21.8 degrees to 25.5 degrees and from 10.0 to 12.5 degrees with the same tendency respectively. Considering the Space Shuttle mission profile, if the ground station is located in such a way that the signal path is formed on the Orbiter side, the aspect angle can be minimized to a value between 10.0 and 12.5 degrees which depends on the SO plume only.

3.6 DISCUSSION

As described in this study, we approximated the blackout zone by a cone inside which no microwave propagation was assumed. This section is to help justify this assumption by reviewing results of previous work done by Poehler[12] with flight data for the Titan III C Solid Rocket Motor.

Poehler presented an exhaust plume ionization model based on the gas dynamic model of Vicente[17] for the seven-segment 120 inch Titan III C SRM. The model for the Titan III C vehicle is unclassified and is shown in Figure 3.15. He tested the Vicente model against flight test data to see how well predicted attenuation compares with X-, C-, S-, and P-Band data collected on Test 8275/2250 (Tables 3.6 through 3.9). The measured data showed that predicted attenuation is orders of magnitude too low. Thus he felt it useful to fashion a model that would more closely fit the experimental data. Essentially maintaining the basic flow field contours developed by Vicente, he tried various levels of electron density and collision frequency. In this manner an empirical model of the Titan III C plume was arrived at that was in good agreement with the measured data. This model is shown in Figure 3.16. He took the afterburning effect into account as Smoot[4] did, while the Vicente model did not.

A close look at the Poehler model of Figure 3.14 shows that the electron density is very high along and near the plume boundary. Therefore, for a first-cut analysis, we can consider the plume boundary as the blackout zone boundary.

Finally, it is noteworthy that the average attenuation in the plume of the Titan III C SRM is about 20 dB for the frequency bands of interest.

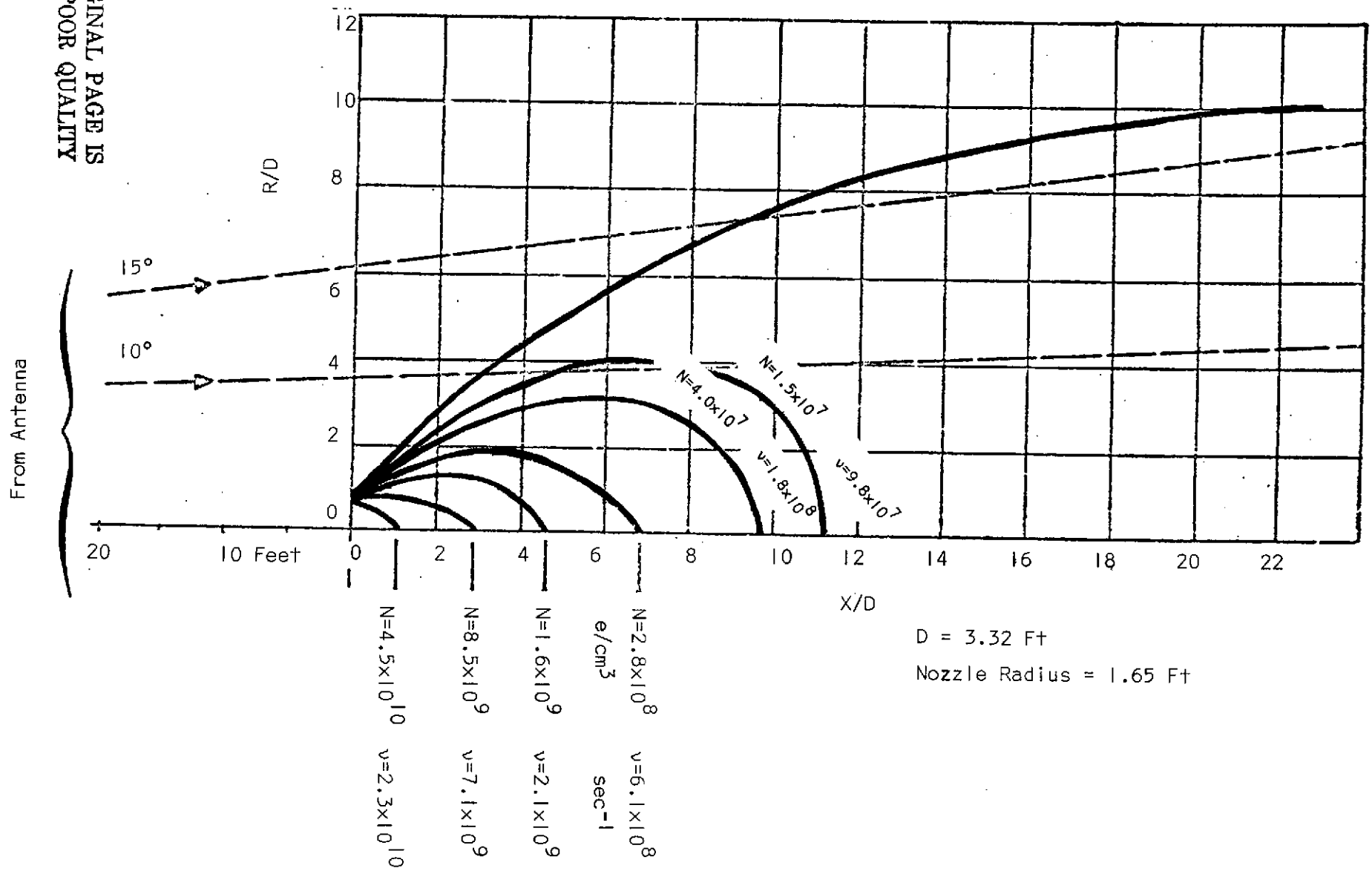

FIGURE 3.15 ZERO STAGE, TITAN III C, 120-INCH, 7-SEGMENT SRM PLUME AT 136,000 FEET (VICENTE MODEL)

TABLE 3.6

X-BAND SIGNAL LOSS**, ZERO STAGE

Aspect Angles*		Signal Loss	Test Time	Site
$\alpha = 180 - 0$	$\emptyset$			
> 16	70-150	0 dB	0-110 sec	UC-2
16	339	>10	+65	19.1
10-8	245-223	<30	95-110	UC-11
9	186	30	108-110	19.1
4-5	199-188	40	100-110	UC-13

TABLE 3.7

C-BAND ATTENUATION, ZERO STAGE

		Attenuation	Test Time	Site
> 15^{o}	50-150	0 dB	0-110 sec	CIF
11	346	>10	+74	UC-13
6	188	>20	+110	UC-13

TABLE 3.8

S-BAND ATTENUATION, ZERO STAGE

> 25^{o}	100-137	0 dB	0-110 sec	STS
> 16	70-150	0	0-110	UC-2
> 15	50-150	0	0-110	CIF
15	306	> 8	+75	UC-11
10	346	>12	+74	UC-13
8	223	>10	+110	UC-11
5	188	>20	+110	UC-13

TABLE 3.9

P-BAND FLAME ATTENUATION, ZERO STAGE

> 15^{o}	329-306	0 dB	0-75 sec	UC-11 (and UC-13)
8	223	15	+110	UC-11
5	191	15	+105	UC-13
2	281	20	+90	UC-13

P-BAND ATTENUATION, STAGE 1

6^{o}	188	20 dB	+285	UC-13

* 0 and $\emptyset$ are the standard antenna angles as defined in IRIG Document 111-65 "IRIG Standard Coordinate System and Data Format for Antenna Patterns."

** Note the distinction between "signal loss" and "attenuation".

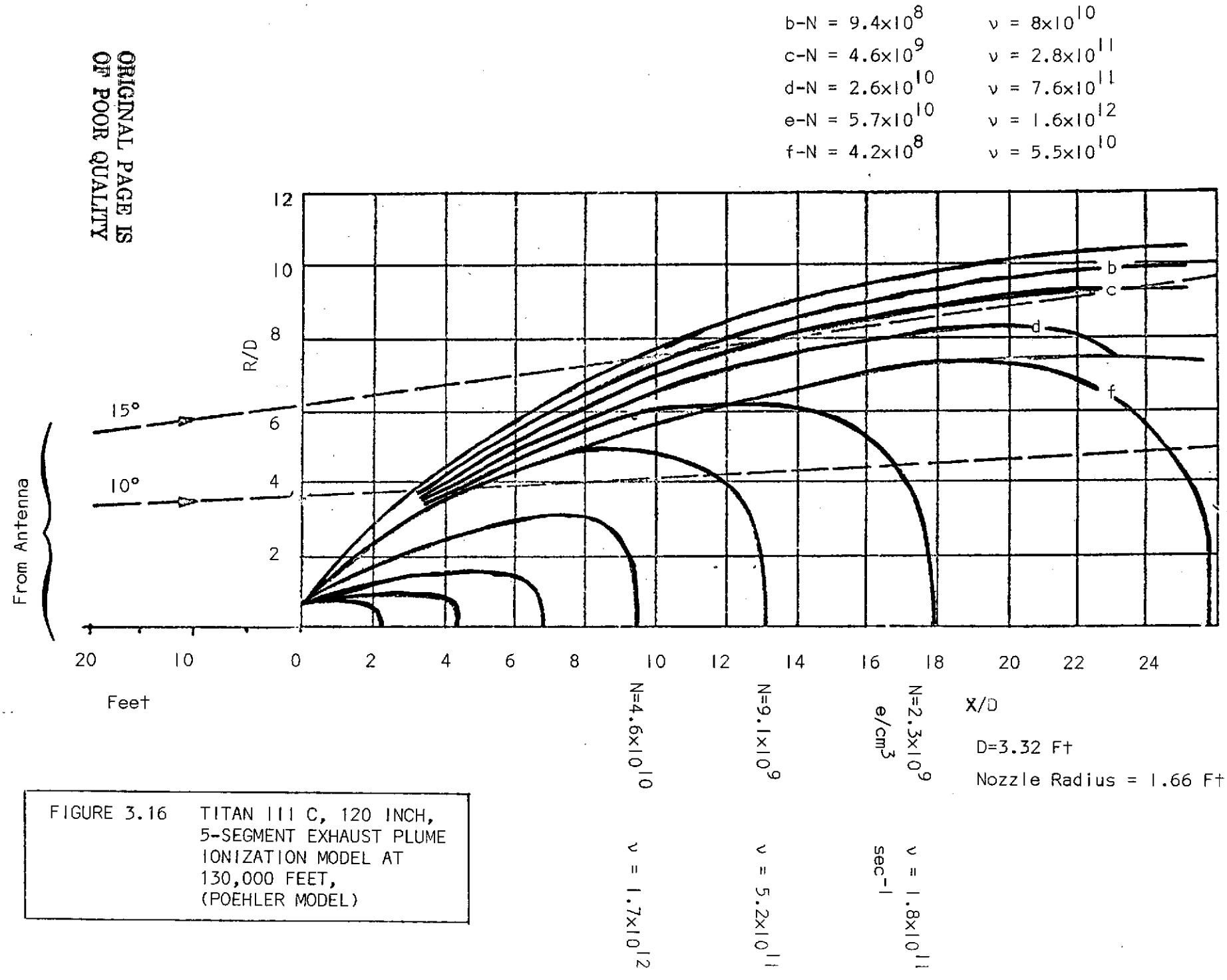

FIGURE 3.16 TITAN III C, 120 INCH, 5-SEGMENT EXHAUST PLUME IONIZATION MODEL AT 130,000 FEET, (POEHLER MODEL)

3.7 REFERENCES

(1) R. Stevens, "The Effect of Jet Flame on Electromagnetic Wave Propagation," Jet Propulsion Lab, CIT, Memorandum No. 4-55, March 14, 1950.

(2) E. C. Jordan, Electromagnetic Waves and Radiation Systems, Prentice-Hall, N. J. 1950.

(3) Boeing Document D5-15606, "Saturn V Exhaust Effects on Radio System Performance," August 15, 1966.

(4) L. D. Smoot, D. L. Underwood, and R. G. Schroeder, "Prediction of Microwave Attenuation Characteristics of Rocket Exhausts," AIAA Papers No. 65-181.

(5) R. J. Prozan, "Solution of Non-Isoenergetic Supersonic Flow by Method-of-Characteristics, Vol. III, Final Report," LMSC-HREC D162220-111, Lockheed Missiles & Space Company, Huntsville, Ala., June 1971.

(6) S. D. Smith and A. W. Ratliff, "Rocket Exhaust Plume Computer Program Improvement, Vol. I-Final Report," LMSC-HREC D162220-1, Lockheed Missiles & Space Company, Huntsville, Ala., June 1971.

(7) S. Gordon and B. J. McBride, "Computer Program for Calculation of Complex Chemical Equilibrium Compositions, Rocket Performance, Incident and Reflected Shocks and Chapman-Jouguet Detonations," NASA SP-273, NASA-Lewis Research Center, Cleveland, Ohio.

(8) D. B. Jacobs, "Rocket Exhaust Effects on Unified S-Band Performance, Saturn AS-202," The Boeing Company, Document No. T5-6628, NASA Contract No. NAS8-5608, November 18, 1966.

(9) D. B. Jacobs, "Apollo Unified S-Band Radio Flame Effects Study, Final Report," The Boeing Company, Document No. T5-6631, NASA Contract No. NAS8-5608, January 10, 1967.

(10) L. D. Smoot, J. M. Simonsen and P. O. Hedman, "Development and Evaluation of a Flight Attenuation Model, Final Report," NWC TP5048, Naval Weapon Center, China Lake, California, November 1971.

(11) L. D. Smoot, J. M. Simonsen, and G. A. Williams, "Development and Evaluation of an Improved Aft-Plume Model," NWC TP5521, Naval Weapon Center, China Lake, California, November 1973.

(12) Horst A. Poehler, "Project See-Through Flame Interference Measurements, TITAN III C Launch Test 8275/2250," Pan American World Airways, ASD, Patrick AFB, Fla. 32925.

(13) M. M. Penny, L. R. Baker, Jr., and R. W. McCanna,"Prediction of the Space Shuttle Launch Vehicle Exhaust Plumes Shapes for Several Trajectory Points," CR-115 728, 1972.

(14) J. B. Dods, Jr., etal., "Effect of Gaseous and Solid Simulated Jet Plumes on an 040A Space Shuttle Launch Configuration at M = 1.6 to 2.2," NASA TM X-3032, April 1974.

(15) W. A. Wood and J. E. Demore, "Microwave Attenuation Characteristics of Solid Propellant Rocket Exhaust Products," AIAA Paper No. 65-183.

(16) E. J. Baghdady and O. P. Ely, "Effects of Exhaust Plasma Upon Signal Transmission To and From Rocket-Powered Vehicles," Proc. IEEE Vol. 54, pp. 1134-1146, September 1966.

(17) F. A. Vicente, "Preliminary Flame Attenuation Analysis for Standard Launch Vehicles," Report No. TOR-699 (6107-25)-2, 1 Oct. 1965, Aerospace Corp., El Segundo, California, Contract No. AF04(695)-699.

4.0 ORBITER POST BLACKOUT DIRECT LINK ACQUISITION ANALYSIS

4.1 INTRODUCTION

The purpose of this report is to document the analysis performed as a result of the task to be described below. The analysis draws from many references which are directly related to the Shuttle program. Care was taken to make all assumptions realistic and based on previously established parameters.

The task itself was to ascertain how long it would take the Shuttle/Ground system to establish a coherent two way link immediately after coming out of blackout. The problem statement, while simple, implies many facets of the Shuttle system and interfaces with other systems which are quite complex. As an example consider an Orbiter landing at the Eastern Test Range (ETR). Orbiter is moving at a high velocity thereby inducing doppler frequency shifts; it is decelerating thereby causing the doppler itself to vary; the Orbiter phase lock loop (PLL) is sweeping its VCO to acquire; and finally the ground receiver loop is being swept to acquire. The questions arise: "Are the combination of the doppler sweep, Orbiter sweep, and ground sweep too much for

the loops to handle?" "Does the doppler force the frequency out of the loop VCO pull range?" These and other questions will be answered in the report that follows.

The plan of attack is to assume that the doppler and the various rates are within acceptable bounds, then to derive the system lockup times as the maximum of the Orbiter acquisition time and the appropriate ground receiver acquisition time (depending on where Orbiter is landing). Having established the above the maximum velocity and deceleration that Orbiter can attain and still keep the frequency shifts and rates in bounds is calculated. This last approach is "sort of" backwards from what would normally be done, however, as of this writing the landing profiles, decelerations, etc., are not firmly determined. The establishment of maximum limits provides the most flexibility and the most useful results at this stage of the Orbiter design.

Finally a set of conclusions and recommendations are made which ASAO feels will preclude design problems in the future and which give parameter values which are useful now.

4.2 ANALYSIS

Figure 4.1a is a block diagram of a 2-way tracking system with Figure 4.1b depicting the actual Shuttle situation. A very stable master oscillator (controlled by a frequency reference) generates the ground transmitter frequency, ω_{GT}. The spacecraft receives the (one-way) Doppler shifted frequency[1]

$$\omega_{SR} = \sqrt{\frac{c-\dot{r}}{c+\dot{r}}}\ (\omega_{GT} + \dot{\phi}_{UD}) \doteq (1 - \frac{\dot{r}}{c})(\omega_{GT} + \dot{\phi}_{UD}), \qquad (4.1)$$

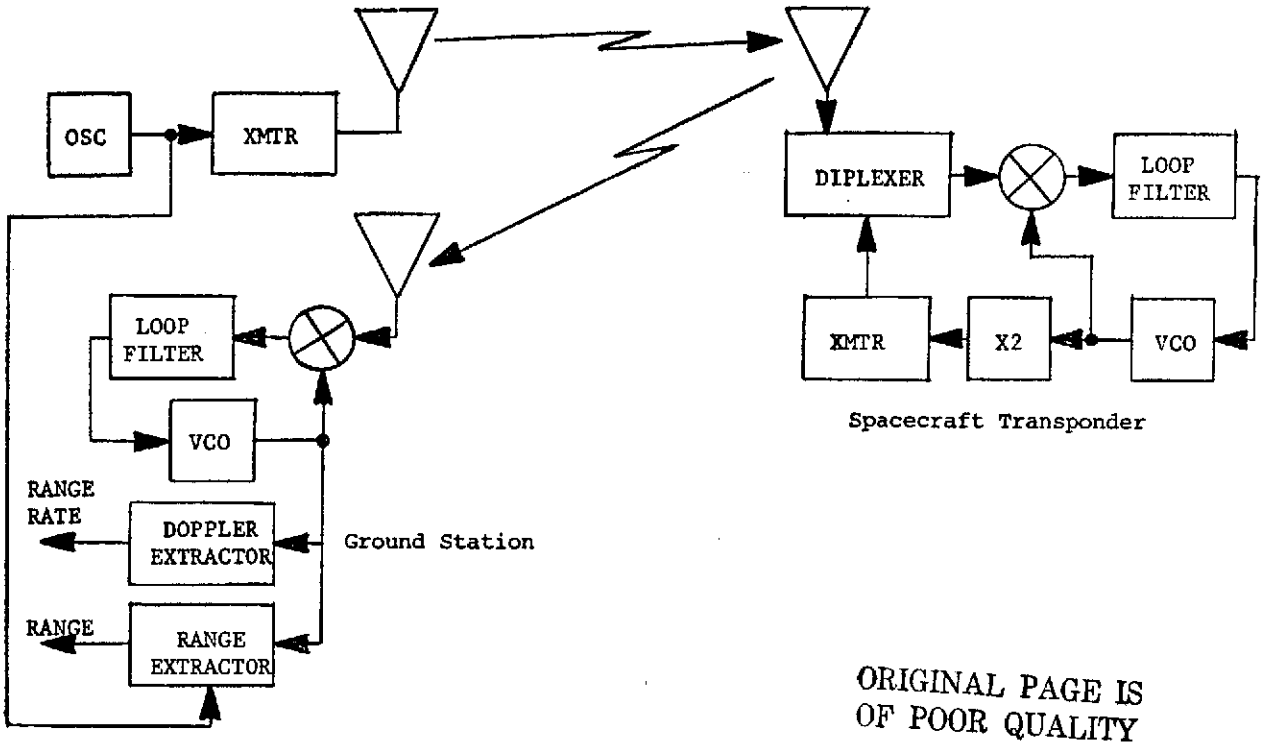

FIGURE 4.1a A 2-WAY TRACKING SYSTEM

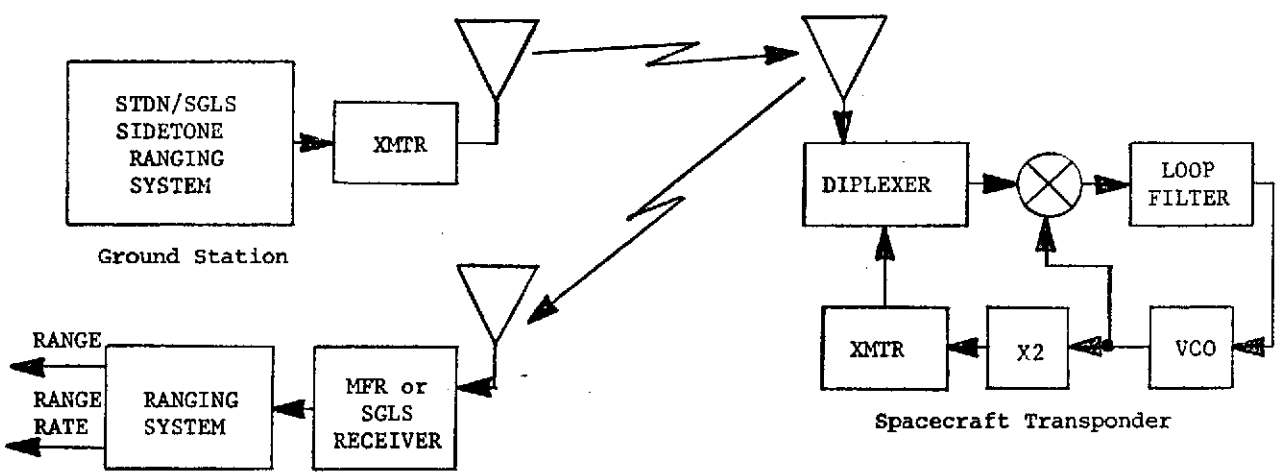

FIGURE 4.1b SHUTTLE DIRECT LINK TRACKING SYSTEM

where $c >> \dot{R}$ was used for the approximation

c = velocity of light

$\dot{r}$ = spacecraft range rate relative to the ground transmitter

$\dot{\phi}_{UD}$ = rate of change of uplink delays other than that due to relative spacecraft/ground velocity.

The Orbiter receiver must attempt to lock to ω_{SR}. It does so by sweeping its VCO by R_s Hz/Sec. First frequency lock is obtained, then phase lock. Since the time for phase lock T_ϕ is on the order of the reciprocal of a single tuned circuit response time and is roughly (for 4 time constants)

$$T_\phi \leq B_n^{-1} \text{ seconds},^{(2)} \tag{4.2}$$

where B_n is the one sided loop noise bandwidth (BW) defined for a filter transfer function H(f) by

$$B_n = \int_0^\infty |H(f)|^2 df, \tag{4.3}$$

it is a negligible part of the overall acquisition time. For example, a B_n of 100 Hz implies a T_ϕ of roughly 10 ms. It will be seen later that the acquisition of frequency is on the order of several seconds, hence 10 ms can be ignored.

Turning now to the time to acquire frequency, T_f, some backup material will be helpful. Frequency lock is defined to be the event where the loop stops skipping cycles or in terms of the phase plane plots of Viterbi,[3] et. al., the point in time where the phase trajectory remains on one modulo 2π-reduced plot. After that phase lock takes place. Since unaided lockup times are so long in practical cases, being of the form[4][5]

$$T_f \sim 4.2\ \Delta f^2 / B_n^3, \text{*} \tag{4.4}$$

* This equation is limited in its usage (see the reference).

where Δf is the initial offset frequency, acquisition aids are nearly always employed. Important exceptions to this are the Multifunctional Receiver (MFR) secondary loops which are unaided. This is done to keep them from going into a sweep mode when one or the other polarization channel fades thereby forcing the primary loop to drop lock. Since the primary loop tracks errors common to both polarization channels, the secondary loops are always within their acquisition range and thus lock instantaneously (for all practical purposes).

The crucial question is, then, what is the frequency acquisition time when a receiver VCO is swept. The answer is not known, however, since all analyses show that a loop will phase lock almost instantaneously when the frequency difference between the incoming signal and the loop VCO is zero (or very small, see (4)), the maximum acquisition time is taken to be the time to sweep over a given frequency uncertainty range at a predetermined sweep rate. For example, in the MFR the sweep times, which change with tracking BW settings, run from 1 second for the 3 kHz BW to 15 seconds for the 10 Hz BW. To see that this is an improvement over unaided acquisition times, equation (4.4) applied to these extremes yields 1 second for the 3 kHz BW and 263 seconds for the 10 Hz BW. Table 4.1 gives the MFR sweep parameters.

TABLE 4.1[6]

MFR Sweep Parameters

TRK BW* (Hz)	Sweep Time (One Ramp) (sec)	Total Sweep Range (Hz) ±300 kHz VCO	±15 kHz VCO
10	15	500	500
30	15	1,500	1,500
100	3	5,000	5,000
300	1	15,000	15,000
1000	1	50,000	30,000
3000	1	150,000	30,000

* 1 sided loop noise BW.

The problem has narrowed down to finding the sweep rate and maximum VCO deviation (double sided) that is needed. While the above examples were for the MFR the exact same reasoning applies to the Orbiter and SGLS ground station during its acquisition. Frazier and Page[7] have developed the most used criterion for a better than 90% probability of acquisition for an effective frequency rate R_e* and a loop signal-to-noise ratio of SNR_L, viz.,

$$\frac{90\ R_e}{B_n^{\ 2}} + \frac{40.5}{\sqrt{SNR_L}} \leq 60^\circ \quad (SNR_L > 6.5\ \text{dB}). \tag{4.5}$$

This equation merely adds the criterion for keeping the noiseless phase error due to a frequency ramp in the linearized loop small and the rms error due to noise small. The equation effectively ignores any frequency offset of the input signal with the stipulation that the incoming frequency be within the limits of the loop VCO sweep.

The procedure then for finding the acquisition time of a swept second order phase lock loop is as follows.

- Determine the limits of the frequency offset of the input frequency.
- Check that it is within the VCO sweep range Δf (answer must be yes).
- Determine B_n and SNR_L for the acquisition mode by picking B_n as large as is consistant with a $SNR_L \geq 10$ dB.
- Calculate R_e from equation (4.5).
- Check that the VCO sweep rate R_s is less than R_e minus the maximum doppler rate.
- Divide Δf by R_s; i.e., $T_f = \Delta f/R_s$.

Then T_f is the maximum time to acquire with a 90% probability. The average acquisition time is $T_f/2$ if the sweep is uniform.

---

* This includes the input frequency rate and the VCO sweep rate.

The loop will have to track the frequency from its most negative pull from rest frequency to its most positive. Thus the loop design must make sure that this range is within a reasonably linear portion of the VCO characteristic. This is really an independent problem from that considered here, however, it is essential to the overall design. Assuming that the VCO range is sufficient the next question is how wide the acquisition bandwidth can be. For good tracking the loop should have at least a 10 dB SNR. This is a universal rule of thumb and will be assumed here. Of course, a very small BW can give just about any SNR_L desired, but the loop will drop lock more often with small BW's. It is therefore a good design criterion to widen the loop BW as far as possible without dropping the loop SNR too far.

Up to this point we have dealt exclusively with residual carrier tracking loops and second order ones in particular. Orbiter will employ suppressed carrier tracking loops and as of this writing will not make use of any bandpass limiters ahead of it. It is then assumed that sufficiently sophisticated AGC circuits are used to restrict the dynamic range that the loops see. The reason is that loops designed to work at very low SNR's will overload easily and hence drop lock or false lock. In general this must be avoided at all costs.

As a point worth noting this system will be very unusual in that no limiter is used either in Orbiter or on the ground when landing at ETR.

Now a tracking loop designed to work with PSK can be implemented in several ways, e.g., Costas, squaring, I-Q, data aided, etc. For purposes of analysis the squaring loop will be used. It has been actually used in NASA systems and can be shown to be mathematically

equivalent to the Costas loop. By way of comment the 10 dB rule of thumb for carrier tracking loops mentioned earlier is increased to 12 dB for suppressed carrier tracking loops. Figure 4.2 shows a typical squaring loop. The squaring of a signal of the form

$$S(t) = \sqrt{2P} \cos\left(\omega_0 t + \frac{\pi}{2} m(t)\right) \tag{4.6}$$

where $m(t)$ is a sequence of ± 1's yields

$$\hat{S}(t) = P + P \cos\left[2\,\omega_0 t + \pi m(t)\right] = P + P \cos 2\,\omega_0 t. \tag{4.7}$$

The loop then tracks the $2\omega_0$. Two problems occur. The first is that the noise is also squared and hence non Gaussian, and second an ambiguity arises when reducing $2\omega_0$ to ω_0. Of concern here is the noise problem, in fact, the term "squaring loss" is used to take this into account. This is the reason for the 12 dB rule of thumb.

It is appropriate at this time to investigate how much SNR is available to the loops after blackout. Per ICD-2-0D044[8] there will be in excess of 30 dB for both the uplink and downlink loops. The value of 30 is conservative since the range involved immediately after blackout is only 520 KM (322 miles) as opposed to the maximum of 2300 KM (1440 miles) or roughly 13 dB gain used in the ICD link calculation. In short there is "infinite" SNR in the loop for analysis purposes, i.e., the noise-free loop can be used.

The problem becomes simpler now since the tracking bandwidths on Orbiter and the landing site can be opened up as far as is compatible with the data rates and thus can be swept rapidly.

As a note of caution, care must be taken to avoid overloading the circuits as mentioned above in connection with the AGC, and this is assumed to be the case hereafter. Extremely high SNR's can be a hindrance if they become too large!

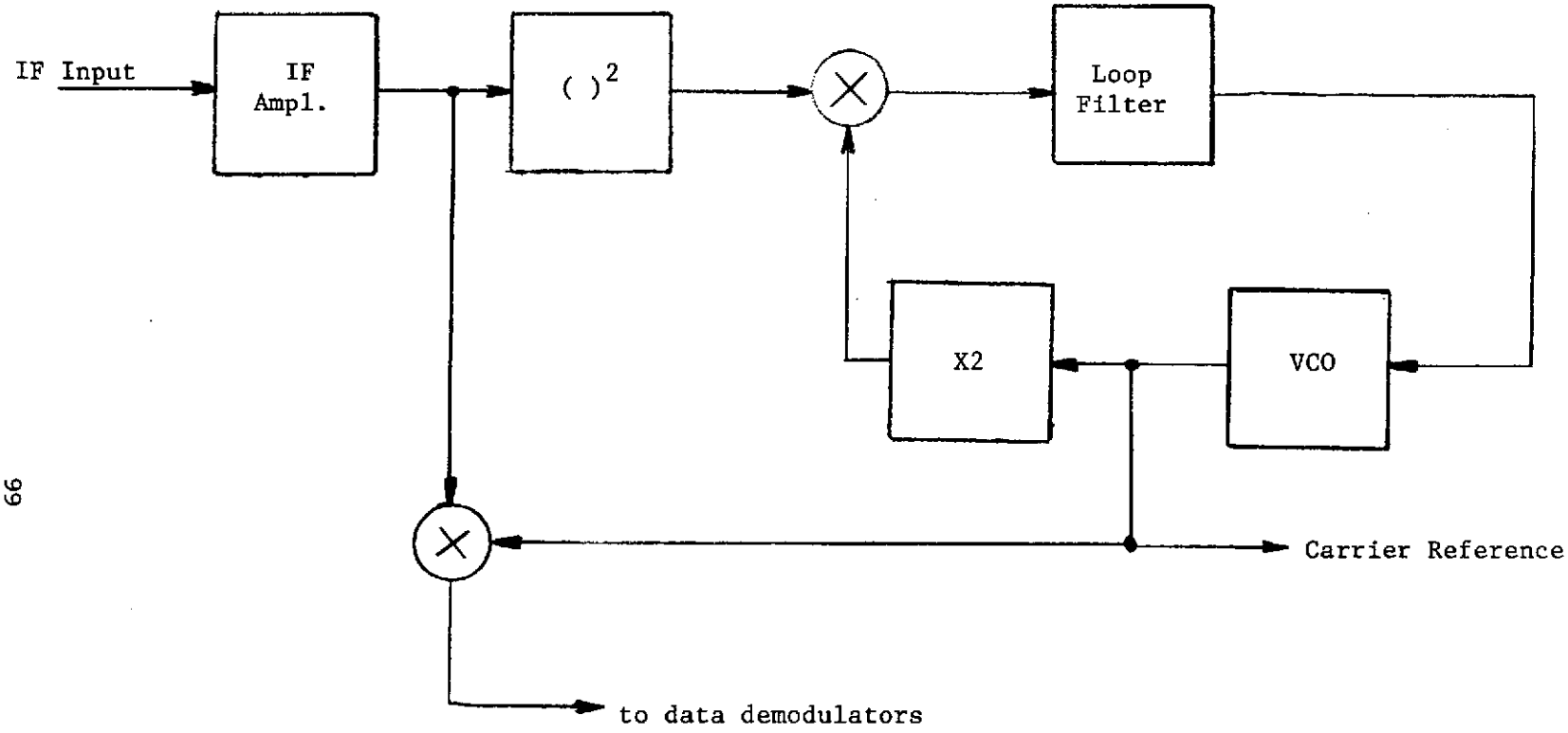

FIGURE 4.2 A SUPPRESSED CARRIER TRACKING SYSTEM (SQUARING LOOP)

For Orbiter then we are working with a second order PLL with no squaring loss (high SNR's) and the only effect of the squarer is to change the center frequency at which we work. Since SGLS and STDN also use second order loops (in the acquisition mode for STDN) the problem reduces further to analyzing the acquisition time of a second order loop when being swept linearly at a rate R_s.

The time to lock immediately after reentry blackout is, per the above rationale, the maximum of the acquisition times of the Orbiter and the landing facility. Each of these will be found below.

The MFR which will be used by STDN will employ a tracking BW of 3 kHz since the bit rate is 192 kbps in a split phase format. This is the widest BW possible and thus the maximum sweep rate can be used. Per Table 4.1 the sweep time is

$$T_1 = 1 \text{ sec.} \tag{4.8}$$

When Orbiter lands at the Western Test Range (WTR) the AFSCF/SGLS system will be used. Per reference (9) the block diagram of the receiver counterpart of the STDN MFR is as shown in Figure 4.3. As can be deduced from the implementation of the sweep, namely, a pulse applied to the loop filter, the loop is second order. It is also a high gain loop preceded by a limiter. This is of interest but of little consequence here due to the high SNR available. The high SNR again allows the use of the maximum loop BW and sweep. Table 4.2 lists the pertinent parameters, and as can be seen the maximum time is

$$T_2 = \frac{400 \text{ kHz}}{500 \text{ kHz/sec}} = 1 \text{ sec.} \tag{4.9}$$

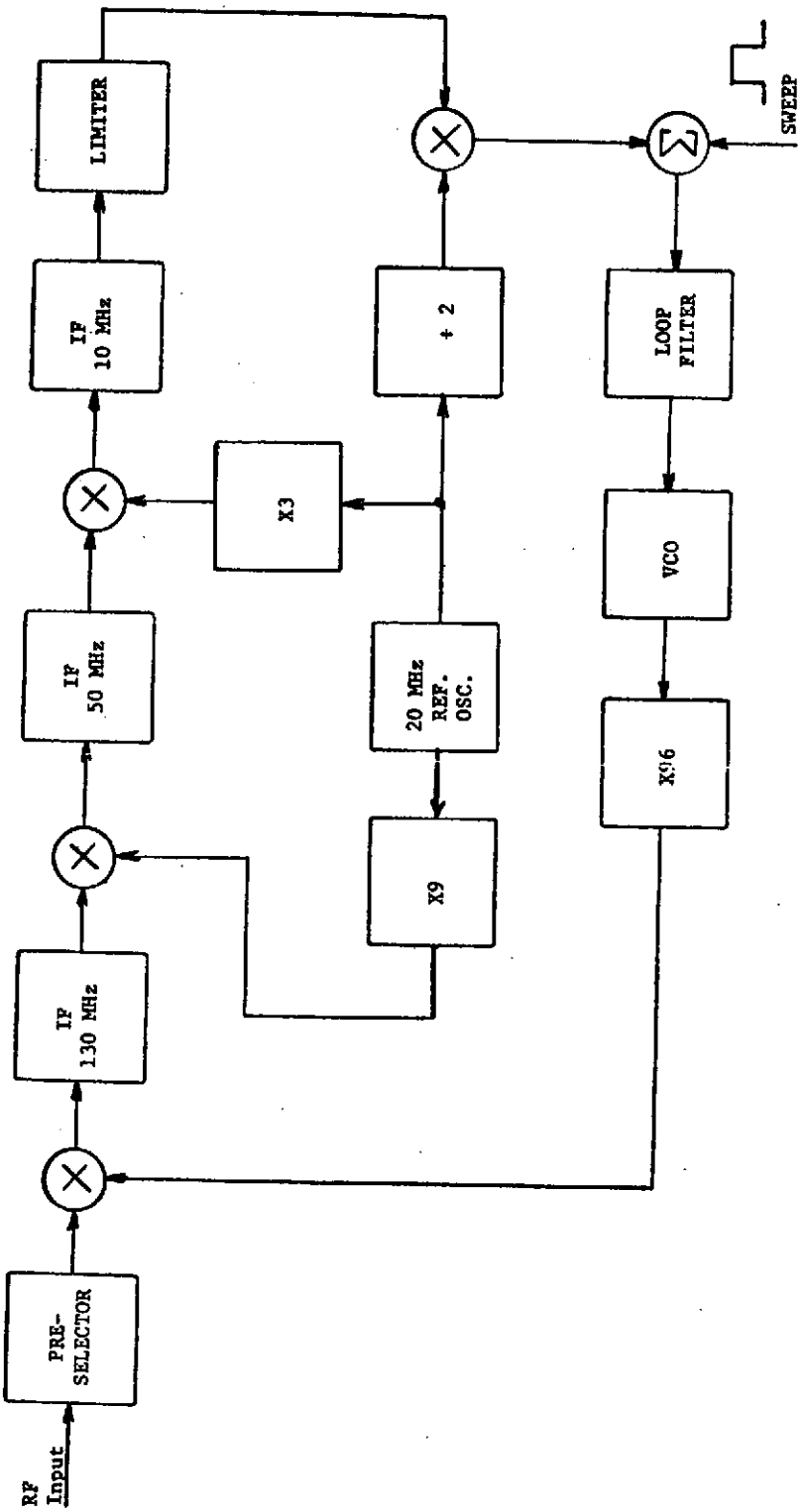

FIGURE 4.3 SGLS GROUND TRACKING RECEIVER

TABLE 4.2

SGLS GROUND STATION PARAMETERS

$2B_L$ (Hz)	Sweep Rate (kHz/sec)	Deviation (kHz)
200	1	±10
1000	25	±100
5000	500	±200

The last receiver which needs to be considered is that utilized by the Orbiter. Unfortunately the design is in the preliminary stages at this point in time. In order to solve this task some assumptions will have to be made. To this end the USB[10] and SGLS transponders are shown in Figures 4.4 and 4.5, and Table 4.3 lists the pertinent parameters. Per reference (11) the maximum deviation is expected to be ±90 kHz on the Orbiter. From Table 4.3 this coincides with the SGLS and USB deviations. Since the sweep rates are 16.8 kHz/sec and 35 kHz/sec respectively for SGLS and USB the parameters shown in Table 4.3 will be assumed for Orbiter. Thus the last acquisition time can be calculated.

$$T_3 = \frac{180 \text{ kHz}}{35 \text{ kHz/sec}} \doteq 5 \text{ secs.} \qquad (4.10)$$

TABLE 4.3

TRANSPONDER PARAMETERS

	Sweep Rate (kHz/sec)	Deviation (kHz)
USBE	35	±90
SGLS	16.8	±84
Orbiter	35	±90

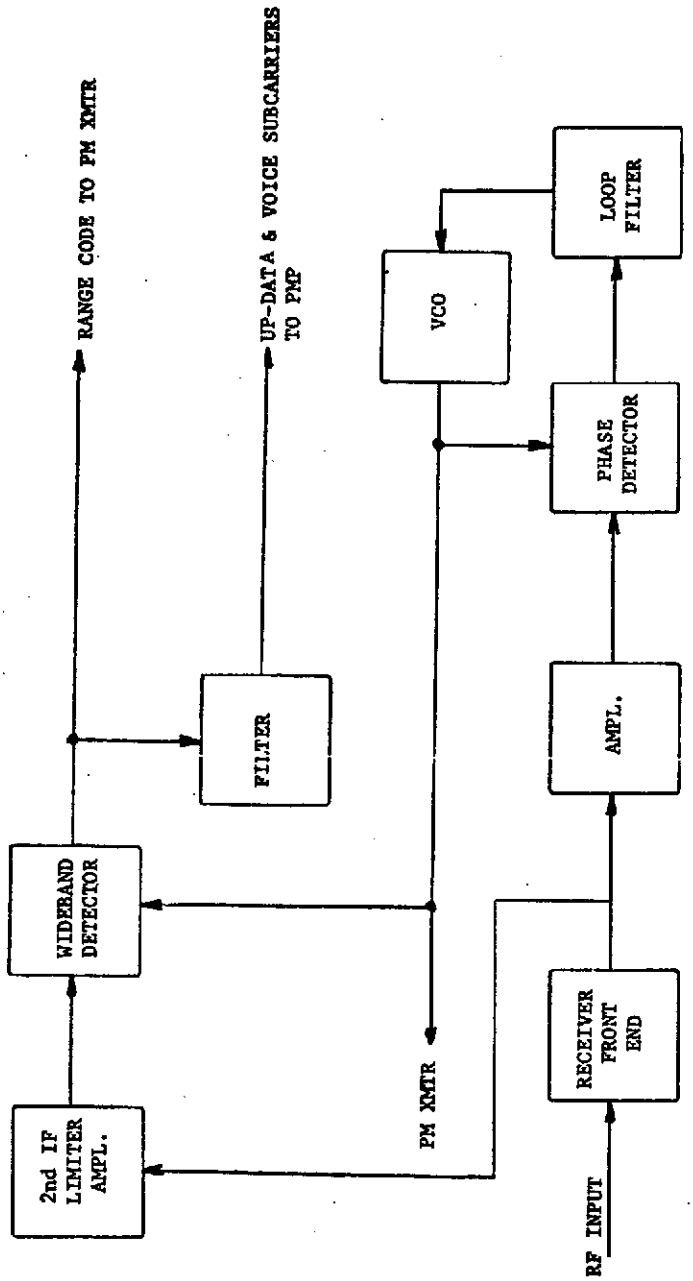

FIGURE 4.4 USB TRANSPONDER

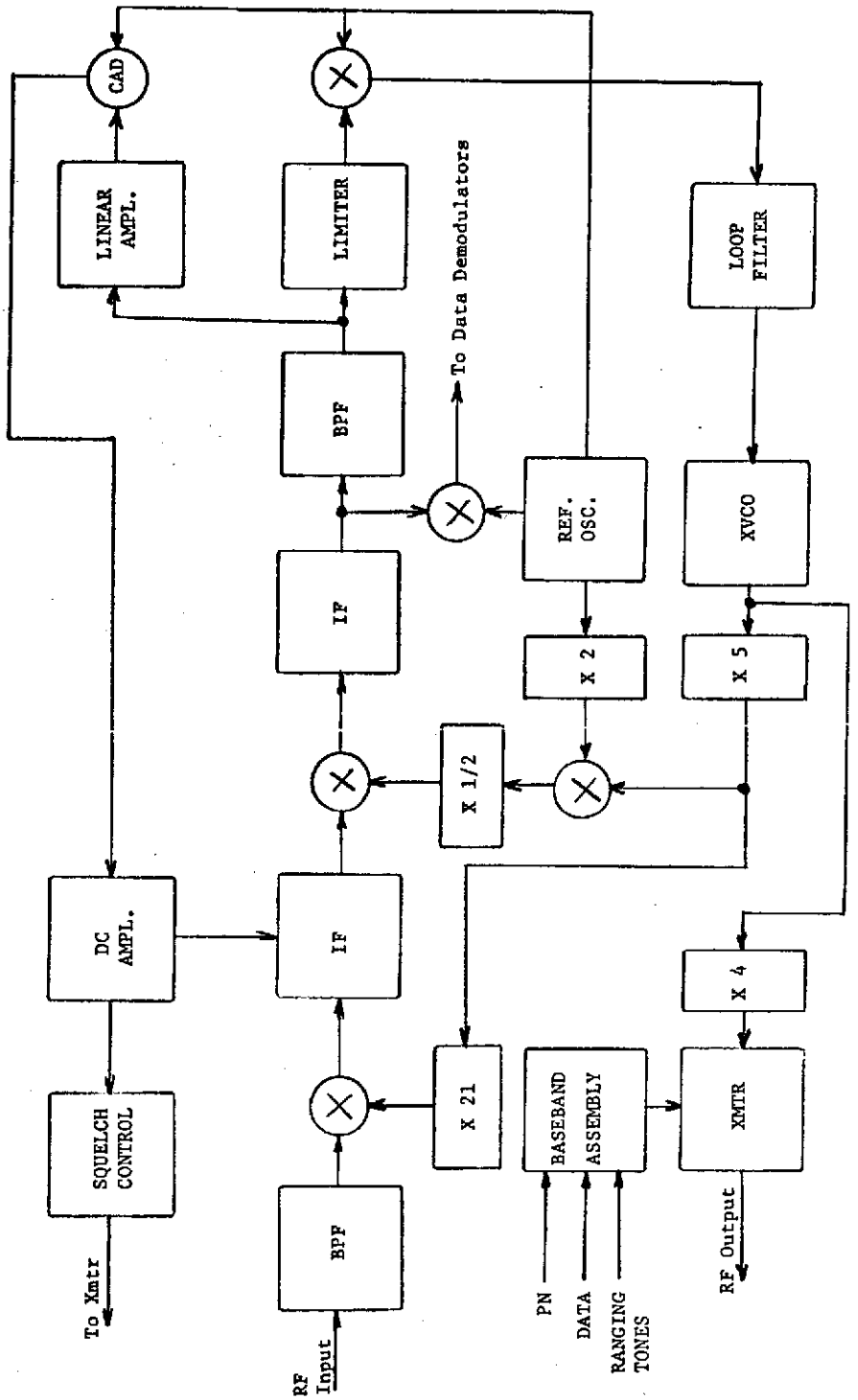

FIGURE 4.5 SGLS TRANSPONDER

ORIGINAL PAGE IS
OF POOR QUALITY

Table 4.4 consolidates the acquisition times and leaves the conclusion that the total system acquisition time (Orbiter and Ground) is as shown in the right hand column of Table 4.4. It is seen then that the Orbiter is the pacing item.

TABLE 4.4

MAXIMUM ACQUISITION TIMES

	Individual Acq. Time (secs)	System Acq. Time (secs)
ETR	1	5
WTR	1	5
Orbiter	5	

The only other major aspect of the problem is to make sure that the doppler and doppler rate are not so large that the loop cannot pull in due to the former and will not drop lock immediately after acquisition due to the latter. In other words the loop sweeps, but the instantaneous frequency at the input is outside of the maximum loop frequency offset due to excessive doppler, and/or the doppler rate is so high that even when locked initially the loop cannot follow fast enough (maintain a sufficiently small phase error) and therefore drops lock.

In the case of the Orbiter loop this is a problem as a result of the high velocity and deceleration involved in reentry. In the case of the ground it is compounded by the fact that Orbiter is sweeping at the same time that the ground is and also experiences the high deceleration. Since the landing pattern and other factors are not known

at this time this part of the analysis will "work the problem backwards" resulting in a specified maximum deceleration and velocity in order to acquire successfully.

For the Orbiter Table 4.3 shows a maximum deviation of ±90 kHz (multiplication of the VCO is assumed) hence using equation (4.1), ignoring $\dot{\phi}_{UD}$, and assuming $\dot{r} << c$,* the Orbiter received frequency is

$$f_{OR} = f_{GT} \mp \Delta f = \left[1 - \frac{\dot{r}}{c}\right] f_{GT}. \tag{4.11}$$

Solving for $\dot{r}$ gives

$$|\dot{r}| = \Delta f \left(\frac{c}{f_{GT}}\right). \tag{4.12}$$

For Orbiter (using 2 GHz for f_{GT})

$$|\dot{r}|_{max} = 9 \times 10^4 \left(\frac{3 \times 10^8 \text{ m/s}}{2 \times 10^9 \text{ Hz}}\right) = 1.35 \times 10^4 \text{ m/s.} \quad (30{,}000 \text{ mph}) \tag{4.13}$$

Note that 1.35×10^4 m/s$<<3 \times 10^8$ m/s, and so the approximation on r is very accurate. Thus 13.5 KM/s (30000 mph) is the maximum radial velocity that is allowed if the Orbiter loop is to have the ability to offset the rest frequency enough to capture the doppler shifted ground transmitted frequency. In reality the velocity will have to be less than this for margin purposes. Table 4.5 shows equation (4.12) results for the actual frequencies used.

TABLE 4.5

MAXIMUM ORBITER POST BLACKOUT RADIAL VELOCITIES (UPLINK)

Ground Transmit Frequency (GHz)		Maximum Velocity (KM/s) MPH
STDN PM-1 :	2.0419	13.2 [29,751]
STDN PM-2 :	2.1064	12.8 [28,840]
AFSCF PM-1 :	1.775733	15.2 [34,211]
AFSCF PM-2 :	1.831787	14.7 [33,164]

* Both assumptions are good due to the link being direct and the velocity limits of the Shuttle.

In the ground station cases the frequency is higher and the doppler is double, i.e., the ground receive frequency is

$$f_{GR} = \frac{240}{221} f_{GT} \pm \Delta f_e = (1- \frac{\dot{r}}{c}) f_{0T} = (1- \frac{\dot{r}}{c}) \frac{240}{221} (1- \frac{\dot{r}}{c}) f_{GT}$$

$$\doteq \frac{240}{221} (1- 2 \frac{\dot{r}}{c}) f_{GT}, \qquad (4.14)$$

where $\frac{240}{221}$ is the turnaround ratio, Δf_e is the overall effective doppler offset, f_{0T} is the Orbiter transmit frequency, and $(\frac{\dot{r}}{c})^2 << 1$ was assumed. Solving (4.14) for $|\dot{r}|_{max}$ gives

$$|\dot{r}|_{max} = \frac{1}{2} (\frac{221}{240}) (\frac{c}{f_{GT}}) \Delta f_c \qquad (4.15)$$

Table 4.6 tabulates $|\dot{r}|_{max}$ for STDN and SGLS maximum offsets of 75 kHz and 200 kHz respectively.

TABLE 4.6

MAXIMUM ORBITER POST BLACKOUT RADIAL VELOCITIES (DOWNLINK)

Ground Transmit Frequency (GHz)		Maximum Velocity (KM/s)	MPH
STDN PM-1	2.0419	5.07	11,423
STDN PM-2	2.1064	4.92	11,088
AFSCF PM-1	1.775733	15.56	35,069
AFSCF PM-2	1.831787	15.08	33,987

The conclusion to the above analysis is that the STDN velocity after blackout must be roughly three times less than the SGLS velocity. Since the two landing patterns will be different this could well be the case.

The problem of deceleration will be analyzed next. Differentiating (4.1) with respect to time gives

$$\dot{f}_{OR} = \frac{1}{2}\left[\frac{c-\dot{r}}{c+\dot{r}}\right]^{-1/2}\left[\frac{(c+\dot{r})(-\ddot{r})-(c-\dot{r})(\ddot{r})}{(c+\dot{r})^2}\right] f_{GT}$$

$$= \frac{1}{2}\left[1 - 2\frac{\dot{r}}{c+\dot{r}}\right]^{-1/2}\left[\frac{-2c\ddot{r}}{(c+\dot{r})^2}\right] f_{GT}$$

$$\doteq \frac{1}{2}\left[1 + \frac{\dot{r}/c}{1+\dot{r}/c}\right]\left[\frac{-2\ddot{r}/c}{(1+\dot{r}/c)^2}\right] f_{GT}. \qquad (4.16)$$

Solving for $|\ddot{r}|_{max}$ and dropping higher order powers of $(\dot{r}/c)$ gives

$$|\ddot{r}|_{max} \doteq \left(\frac{c}{f_{GT}}\right)\left(1+\frac{2\dot{r}}{c}\right)\dot{f}_{OR} \doteq \left(\frac{c}{f_{GT}}\right)\dot{f}_{OR} \qquad (4.17)$$

Now $\dot{f}_{OR}$ is limited by the effective sweep rate of the VCO due to internal (acquisition) sweep and external doppler rate, hence using (4.5) and recalling that $SNR_L >> 1$

$$|\ddot{r}|_{max} \doteq \left(\frac{c}{f_{GT}}\right)\left(1+\frac{2\dot{r}}{c}\right)\left(\frac{60}{90}B_{n0}^2 - R_{SO}\right), \qquad (4.18)$$

where R_{SO} is the acquisition sweep rate for Orbiter and B_{n0} is its noise BW. In other words at high SNR_L's the loop can be swept very rapidly, but the circuits only use a portion R_S of the available. The rest is to handle any doppler rate that might be present.

In the case of the ground stations equation (4.1) is used twice and a turnaround ratio is involved, viz.,

$$f_{GR} = \left[\frac{c-\dot{r}}{c+\dot{r}}\right]^{1/2} f_{OT} = \left[\frac{c-\dot{r}}{c+\dot{r}}\right]^{1/2} \alpha\left[\frac{c-\dot{r}}{c+\dot{r}}\right]^{1/2} f_{GT}, \qquad (4.19)$$

where f_{OT} is the Orbiter transmit frequency and α is the turnaround ratio.

Taking derivatives as before

$$\dot{f}_{GR} = - \frac{2c\ddot{r}\alpha}{(c+\dot{r})^2} f_{GT}. \tag{4.20}$$

Solving for $|\ddot{r}|_{max}$ and dropping $(\dot{r}/c)$ powers greater than one gives

$$|\ddot{r}|_{max} = (\frac{c}{f_{GT}})(1+2\frac{\dot{r}}{c})\frac{\dot{f}_{GR}}{2\alpha}. \tag{4.21}$$

The same reasoning as before applies with the added ground sweep rate R_{SG} taken into account.

$$|\ddot{r}|_{max} = (\frac{c}{f_{GT}})(1+2\frac{\dot{r}}{c})\frac{1}{2\alpha}(\frac{60}{90} B_{nG}^2 - R_{SO} - R_{SG}), \tag{4.22}$$

where B_{nG} is the ground receiver noise BW. Table 4.7 lists $|\ddot{r}|_{max}$ for all the pertinent cases.

TABLE 4.7

MAXIMUM DECELERATION LIMIT

	$\underline{\lvert\ddot{r}\rvert_{max}}$
Orbiter	390 KM/sec^2*
STDN	395 KM/sec^2
SGLS	284 KM/sec^2

Note that due to the relative values involved equations (4.18) and (4.22) respectively simplify to

$$|\ddot{r}|_{max} \doteq (\frac{c}{f_{GT}})\frac{60}{90} B_{n0}^2 \tag{4.23}$$

$$|\ddot{r}|_{max} \doteq (\frac{c}{f_{GT}})\frac{60}{90}\frac{B_{n0}^2}{2\alpha}. \tag{4.24}$$

* A B_{n0} = 2 kHz was used for Orbiter.

The above values are actually worst case since the probability of the sweep rates adding directly is not 1. On the contrary it is most likely that they will add sometimes and cancel at other times, e.g., the doppler rate may tend to bring the frequency at the input closer to the VCO rather than away. Such a case is where the sweep on the VCO is negative while the doppler rate is positive. The worst case condition is relevant however, because the rates and periods of sweep are different and so at some point they will add thus stressing the loop to its maximum and making it tend to drop lock.

4.3 RESULTS AND CONCLUSIONS

In the preceding analysis certain assumptions and actual parameter values for the Orbiter/ground communications system have led to the following results.

- The SNR's after blackout are so high that essentially noise-free circuits are involved.
- The total system acquisition is paced by the Orbiter loop.
- The acquisition time is less than 5 seconds which is that of Orbiter.
- The maximum radial velocity allowable for Orbiter after blackout is about 30,000 mph (Table 4.5).
- The maximum radial deceleration for Orbiter is dependent on the loop BW employed and given in Table 4.6.

Two points of interest arose during the analysis and should be considered in the design. They are:

- High SNR's can cause circuit overloading with attendant spurious signals which can cause false lock. These should be minimized through AGC since no limiting is now foreseen on Orbiter.
- The reentry velocity and deceleration can very likely be high enough to prevent acquisition.

If the above recommendations are incorporated into the design of the transponder, there should be no acquisition problem immediately after reentry blackout.

4.4 REFERENCES

(1) R. E. Edelson, et. al., Telecommunications Systems Design Techniques Handbook, Jet Propulsion Laboratory, Pasadena, Calif., Technical Memorandum 33-571, NASA-GR-129108, July 15, 1972, p. 116.

(2) S. L. Goldman, "Second-Order Phase-Lock-Loop Acquisition Time in the Presence of Narrow-Band Gaussian Noise," IEEE Transactions on Communications Vol. Com-21, No. 4, April 1973, pp. 297-300.

(3) A. J. Viterbi, Principles of Coherent Communication, McGraw-Hill Book Co., 1966, Chapter 1 through 4.

(4) A. F. Ghais, et. al., Phase-Locked Loops for the Apollo Vehicle Re-Entry Tracking System, GSFC Contract NAS5-9742 Radio Communications Study on Noise Threshold Reduction, ADCOM Incorporated, June 30, 1966, p. 17.

(5) D. R. Hummels, "Some Simulation Results for the Time to Indicate Phase Lock," IEEE Transactions on Communications, Vol. Com-20, No. 1, Feb. 1972, pp. 37-43.

(6) Operation and Maintenance Manual for Multifunctional Receiver, RF Communications Inc., prepared for NASA/GSFC, March 1974.

(7) J. P. Frazier and J. Page, "PLL Frequency Acquisition Study," IRE Transactions SET-8, Sept. 1962, pp. 210-227.

(8) Shuttle Orbiter/GSFC Communications and Tracking Interface Control Document, ICD-0D044, NASA LBJ Space Center, LEC-1161, Jan. 1974, pp. 5-14.

(9) B. Mosher and H. Wagner, Airborne SGLS, Originally written for Motorola Engineering Bulletin, TMCWT-156, Oct. 15, 1968.

(10) Proceedings of the Apollo Unified S-Band Technical Conference, NASA SP-87, Held at Goddard Space Flight Center, July 14-15, 1965.

(11) Private Communication, B. H. Batson to D. E. Cartier, June 6, 1974.

5.0 RENDEZVOUS RADAR/WIDEBAND COMMUNICATIONS SYSTEM STUDY

5.1 INTRODUCTION

The purpose of this task is to study the baseline Orbiter rendezvous Ku-Band radar with the intention of identifying the subsystem blocks which can also be used in a wideband communications link. At present the baseline design is a pulse radar of the noncoherent (post-detection) integration type with the transmit power supplied by a 40 KW peak/40 watt average magnetron or other suitable device. The main thrust of the analysis is aimed at reducing the peak power to a value closer to the average power of 40 watts. If, for example, the peak power could be reduced to 160 watts then a dual mode traveling wave tube (TWT) amplifier could be used. The pulse mode would be used for radar and the continuous mode for wideband (WB) communications. This would provide a common power amplifier for both operational modes which, in turn, would allow the employment of a common driver. Only the low level electronics would then need to be separate. Of course the receiver front end and intermediate frequency (IF) section could be common in any event.

Several means of bringing down the peak power will be investigated; they are:

- Optimization of system parameters
- Relaxation of specification
- Combinations of the above
- Multiple range modes
- Pulse expansion/compression techniques

Before delving into the peak power reduction analysis it is appropriate to discuss the general design philosophy of the type of radar being considered in the baseline configuration. Table 5.1[1] lists the specifications of the radar as required for the Orbiter mission. Whether or not these specifications can be met by the type of radar chosen as baseline remains to be seen. As a preview of the results of the analysis to follow, some parameters will have to be adjusted.

A noncoherent radar simply sends out pulses of width τ at a rate of f_r with power P_{peak}. A pulse propagates to the target, is reflected (with a certain loss) and is received by the radar receiver. The range of the target relative to the radar position is "ct/2", where c is the propagation velocity and t is the time difference between the transmitted pulse and the received pulse. The factor of ½ accounts for the two way travel.

If the energy in the received pulse is too low, several pulses can be "looked at" before the measurement is made. Advantage is taken of the randomness of the noise versus the nonrandomness of the signal. If the phase of the received carrier is ignored on a pulse to pulse basis then the summing up process of the pulses is termed "noncoherent." This is what the baseline design uses.

The number of pulses which can be summed is a function of how long the target stays in the antenna beamwidth and how much delay in the range measurement can be tolerated. If the antenna scans rapidly during acquisition, for example, there will be only a limited number of pulses available.

TABLE 5.1

BASELINE RADAR SPECIFICATIONS

o	Frequency	15.3 GHz (Ku-Band, λ = 2 cm)
o	Radar Classification	Pulse (Noncoherent)
o	Antenna	0.51 m (20") Parabolic Cassegrain - 4 horn monopulse 35.4 dB Gain (55% efficient) 2.7° - 3 dB beamwidth
o	Polarization	Linear
o	Scan	90° x 90° raster
o	Scan Rate	120°/sec
o	Maximum Range	22.2 KM (12 NMI) 18.5 KM (10 NMI) at detection
o	Pulse Repetition Rate	2500 pps
o	Minimum Range	61 m (200 ft)
o	Pulse Width	0.4 μsec
o	RF Power	40 W (average) (16 dBW) 40 KW (peak) (46 dBW)
o	Receiver Noise Figure	8 dB
o	Probability of Detection	0.99
o	False Alarm Rate	1 per hour
o	Acquisition Time	60 seconds (10 sec. reacquisition)
o	Target Radar Cross-section	1 m^2 (11 ft^2) (average σ)
o	Fluctuation Model	Swerling Case I
o	Target Range Rate	30 m/sec (+100 ft/sec) -15 m/sec (-50 ft/sec)

The width of the pulse must be less than the two way range at the minimum distance to a target, otherwise the receiver will receive part of the high energy transmitted pulse thereby possibly damaging some components. Too short a pulse decreases the available return energy, thus the pulse width is made as large as possible within the constraints of the system.

The repetition rate, on the other hand, must be high enough to have at least one pulse returned at the maximum range. If this were not the case an ambiguity would be present, namely, two or more transmitted pulses before one received pulse. Figure 5.1 illustrates the above concepts.

The previous points are straightforward applications of radar theory. Another point which needs to be addressed before the detailed analysis begins is the "Fluctuation Model." Swerling Case I takes into account the fact that the scan rate is so rapid that the return pulse amplitudes are essentially constant on any one scan, but are independent, distribution-wise, from scan to scan. This means that the scan rate is much faster than the target spin rate. The spinning, however, does cause less energy to be returned on the average, and so the radar must transmit more energy at the outset.

Finally, radars use linear polarization to avoid the loss when the reflected wave returns. For example, if circular polarization were employed then the received wave would be reversed in its polarization sense, and so the loss would be devastating. The reason this is mentioned is that the wideband communication mode will require circular

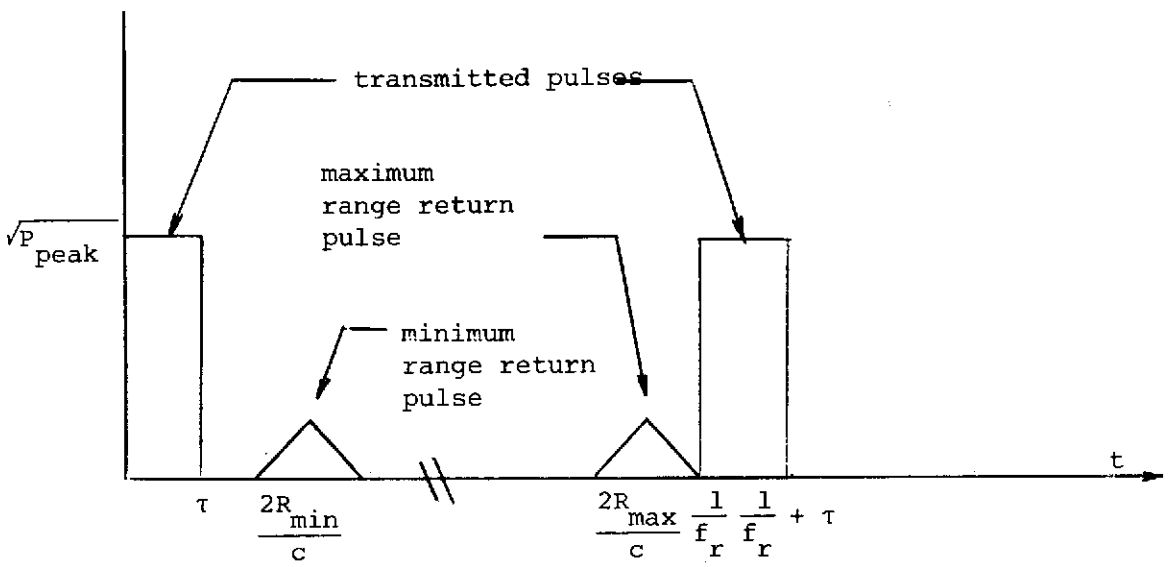

Figure 5.1 Pulse Radar Waveforms

polarization to be compatible with TDRS. A possible solution is to use a fifth horn for communication over and above the four horn monopulse with the appropriate polarization for each mode.

5.2 ANALYSIS

5.2.1 Baseline Analysis

This analysis will draw heavily from well established radar theory and results as expounded in references (2) and (3). Table 5.2 lists the pertinent relations which will be used throughout the analysis to follow; they will be designated as eqn. A, eqn. B, etc. As the analysis progresses certain specifications will be "taken as Gospel" and results will be derived. Later when it is seen that some results are unacceptable parameters will be adjusted and the problem will be reworked.

Since $R_{max} = 22.2$ KM (12 NMi) is one of the more sacred specifications, being 18.5 KM (10 NMi) with 3.7 KM (2 NMi) allocated for acquisition, relation F gives an upper bound on the repetition rate.

$$f_r \leq 161{,}440 \frac{\text{NMi}}{\text{sec}} \times \frac{1}{2\text{x}12 \text{ NMi}} = 6726 \text{ pps} \tag{5.1}$$

with

$$\frac{1}{f_r} \geq 148.7 \text{ μsec.} \tag{5.2}$$

The pulse width is upper bounded by relation G.

$$\tau \leq 2 \times 200 \text{ ft} \times \frac{1}{9.8 \times 10^8 \text{ ft/sec}} = 0.41 \text{ μsec} \tag{5.3}$$

Since as much energy as possible is desired τ will be set to its upper bound, i.e.,

$$\tau \triangleq 0.4 \text{ μsec.} \tag{5.4}$$

TABLE 5.2

PULSE RADAR EQUATIONS

A. $$R_{max}^4 = \frac{P_{avg} G^2 \lambda^2 \sigma G_{nc}}{(4\pi)^3 K T_0 F (B\tau) f_r (SNR_1) L_s L_A L_p}$$: Radar Eqn.

B. $$G = \left(\frac{\pi D}{\lambda}\right)^2 \epsilon$$: Parabolic Antenna Gain Eqn.

C. $$P_{fa} = \frac{n\tau}{T_{fa}}$$: False Alarm Eqn.

D. $$n_B = \frac{\theta_B f_r}{\dot{\theta}_s}$$: No. of pulses in 3 dB beamwidth

E. $$G_{nc}(dB) = \begin{cases} 3 + 6 \log n & : \quad n \geq 10 \\ 9 \log n & : \quad 1 \leq n \leq 10 \end{cases}$$ Swerling Case I; Postdet. Integ. Gain

F. $$\frac{2R_{max}}{C} \leq \frac{1}{f_r}$$: Max. Range Ambiguity Inequality

G. $$\frac{2R_{min}}{C} \geq \tau$$: Min. Range Ambiguity Inequality

H. $$\dot{\theta}_s = \frac{A_s}{(1 - \frac{P}{100}) \theta_B T_s}$$: Scan Rate Eqn.

I. $$P_{avg} = P_{peak} \tau f_r$$: Peak to Average Power Relation

TABLE 5.2 (continued)

- P_{avg} is the average transmitted power
- G is the antenna gain
- λ is the wavelength
- σ is the radar cross-section
- G_{nc} is the postdetection integration gain
- K is Boltzman's constant
- T_0 is 290^{o} Kelvin
- F is the receiver noise figure
- B is the matched filter noise bandwidth
- τ is the transmitted pulse width
- f_r is the pulse repetition rate
- SNR_1 is the single pulse signal-to-noise ratio for a given probability of detection P_d and false alarm P_{fa}
- L_s is the miscellaneous system loss
- L_A is the off axis antenna loss
- L_p is the polarization loss
- D is the parabolic dish diameter
- ϵ is the antenna efficiency
- n is the number of pulses integrated
- T_{fa} is the false alarm time
- n_B is the number of pulses in the 3 dB beamwidth
- θ_B is the 3 dB antenna beamwidth
- $\dot{\theta}_s$ is the antenna scan rate
- R_{max} is the maximum radar range

TABLE 5.2 (continued)

- R_{min} is the minimum radar range
- C is the speed of light (propagation velocity)
- A_s is the scan area
- P is the percentage of antenna beam overlap on consecutive scans
- T_s is the allocated scan time (acquisition time)
- P_{avg} is the average power
- P_{peak} is the peak power

Let the peak to average ratio of the power be 1000 as given in Table 5.1 for this first analysis, then per eqn. I

$$f_r = \frac{40 \text{ watts}}{40 \text{ kw}} \times \frac{1}{0.4 \text{ } \mu\text{sec}} = 2500 \text{ pps.} \tag{5.5}$$

Note that this repetition rate is far below the upper bound set by eqn. (5.1), thus it can be seen that the peak power could be lowered. Per eqn. A this would also lower the maximum range. This tradeoff will be investigated later.

The next item of interest is the amount of integration gain that can be achieved. This will depend on the number of pulses used. Eqn. D gives

$$n_B = \frac{2.7^\circ \times 2500 \text{ pps}}{120^\circ/\text{sec}} = 56. \tag{5.6}$$

Using all the pulses possible gives the most gain, thus eqn. E results in

$$G_{nc}(\text{dB}) = 3 + 6 \log 56 = 13.5 \text{ dB.} \tag{5.7}$$

Eqn. C gives the false alarm probability

$$P_{fa} = \frac{56 \times 0.4 \text{ } \mu\text{sec}}{1 \text{ hr} \times 3600 \times 10^6 \text{ } \mu\text{sec/hr}} = 6.2 \times 10^{-9} \tag{5.8}$$

References (2) and (3) state that the resulting loss of an antenna beam passing through a target will be 1.6 dB. This is because the target does not see the maximum gain for the whole time that it is scanned. If the target is off the maximum gain scan path then there is another loss. This depends upon the amount of overlap.

The rationale behind the calculation of scan rate is illustrated in Figure 5.2 for a 50% overlap. In this case the scan area is in degrees squared and the number of lines needed is

$$N = \frac{\sqrt{A_s}}{\theta_B/2} + 1. \tag{5.9}$$

The rest of the relationships needed are

$$(N-1)\Delta = \sqrt{A_s}/\dot{\theta}_s^{*} \tag{5.10}$$

$$\dot{\theta}_s t_r = \sqrt{A_s} \tag{5.11}$$

$$\dot{\theta}_s t_s = \sqrt{A_s} \tag{5.12}$$

The overall scan time, T_s, is

$$T_s = Nt_s + (N-1)\Delta + t_r = \left(\frac{\sqrt{A_s}}{\theta_B/2} + 1\right)\left(\frac{\sqrt{A_s}}{\dot{\theta}_s}\right) + \left(\frac{\sqrt{A_s}}{\dot{\theta}_s}\right) + \left(\frac{\sqrt{A_s}}{\dot{\theta}_s}\right)$$

$$= \left(\frac{\sqrt{A_s}}{\theta_B/2} + 3\right)\left(\frac{\sqrt{A_s}}{\dot{\theta}_s}\right) \tag{5.13}$$

Solving for $\dot{\theta}_s$ gives

$$\dot{\theta}_s = \frac{2A_s}{\theta_B T_s}\left[1 + \frac{3\theta_B}{2\sqrt{A_s}}\right]. \tag{5.14}$$

In general then it can be seen that a good approximation for $\dot{\theta}_s$ with a given percentage, P, of overlap is

$$\dot{\theta}_s = \frac{A_s}{(1 - \frac{P}{100})\theta_B T_s}. \tag{5.15}$$

---

* The beam center is scanned to avoid the loss at the edges.

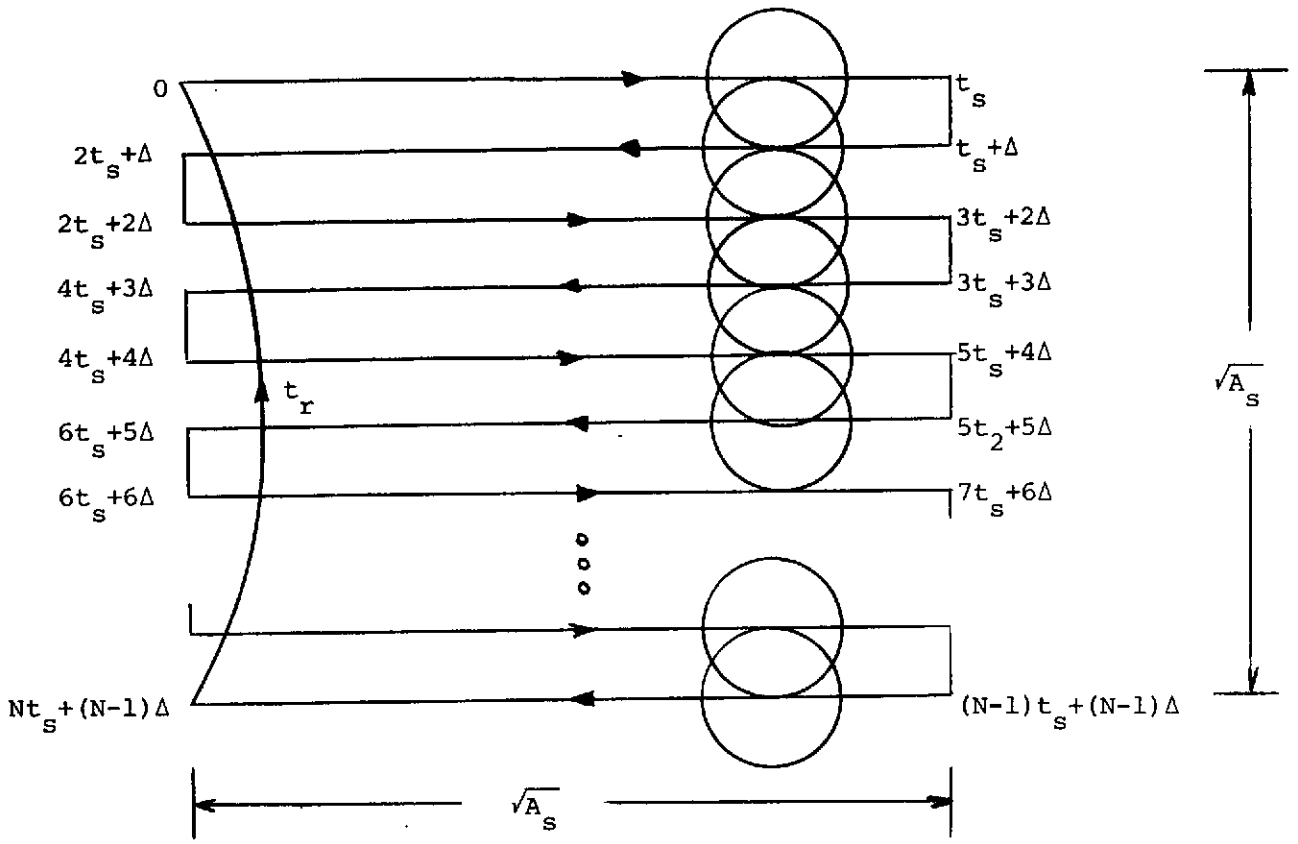

N = no. of scans

t_s = scan time for one scan

Δ = line to line transfer time

A_s = scan area in degrees squared

T_s = overall scan time

t_r = retrace time

Figure 5.2 Raster Scan Sweep Rate and Timing

As examples of the use of eqn. (5.15), $\sqrt{A_s} = 90^\circ$ and $\sqrt{A_s} = 40^\circ$, $\theta_B = 2.7^\circ$, $T_s = 60$ secs, P = 50% give

$$\dot{\theta}_s = \frac{8100}{\frac{1}{2} \times 2.7 \times 60} = 100^\circ/\text{sec} \tag{5.16}$$

$$\dot{\theta}_s = \frac{1600}{\frac{1}{2} \times 2.7 \times 60} = 20^\circ/\text{sec} \tag{5.17}$$

As can be seen from the examples the specification of 120°/sec is conservative, and if the $90^\circ \times 90^\circ$ scan area can be reduced to $40^\circ \times 40^\circ$ then the number of pulses integrable is 5 to 6 times as many. This translates into roughly 4 dB more integration gain. These results will be alluded to later when tradeoffs are made.

For a 50% overlap of beamwidth on consecutive scans the off axis loss is roughly $L_A = 0.9$ dB. Assuming negligible polarization loss, the only other parameter needed before applying eqn. A is SNR_1. Consider Figures 5.3 and 5.4 which were reproduced from reference (2). Rather than solving for SNR_1 for $P_d = 0.99$ as specified, eqn. A will be used to arrive at the SNR_1 needed for $R_{max} = 12$ NMi. The achievable P_d will then result. Using decibel quantities

$$\begin{aligned} SNR_1 &= 16 \text{ dBW} + 2(35.4) + 2(-17) + 0 + 13.5 \\ &\quad -[33 - 204 \text{ dBW/Hz} + 8 + 0 + 34 + 1.6 + 0.5 + 174] \\ &= 18.8 \text{ dB} \end{aligned} \tag{5.18}$$

Table 5.3 lists the P_d achievable for a given SNR_1 taking into account Figures 5.3 and 5.4 for a P_{fa} of 6×10^{-9}.

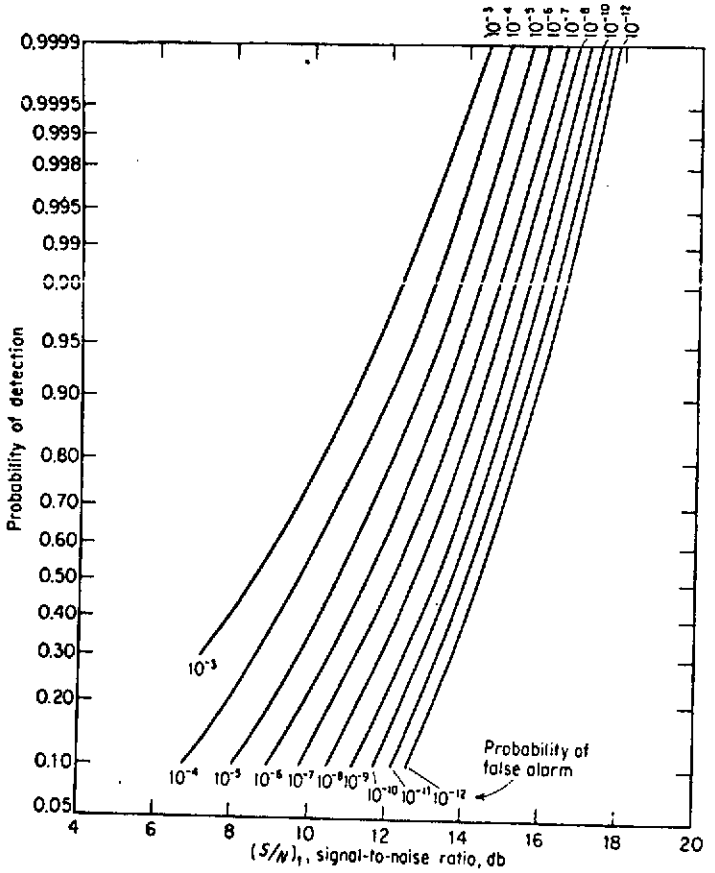

FIGURE 5.3 SINGLE PULSE NONFLUCTUATING P_d, P_{fa}, SNR

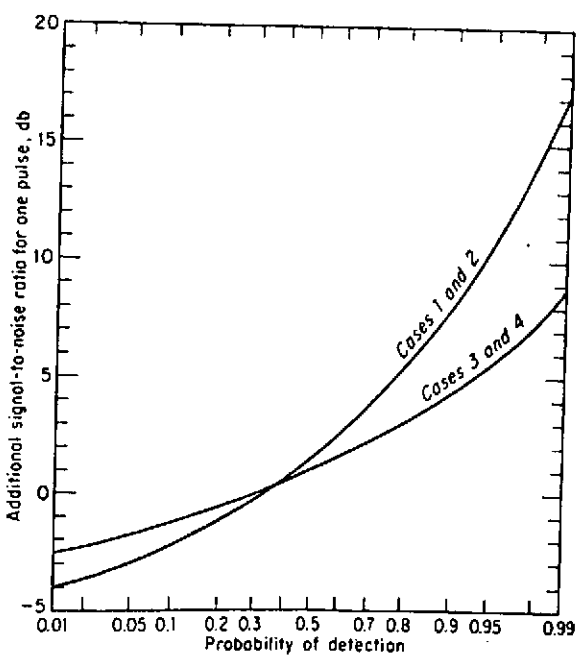

FIGURE 5.4 SWERLING CASES FLUCTUATION ADJUSTMENT FACTOR

TABLE 5.3

P_d for Various SNR_1 at $P_{fa} = 6 \times 10^{-9}$

P_d	SNR(dB)	Fluctuation Factor (dB)	Total SNR_1 (dB)
0.99	15.4	17	32.4
0.95	14.7	10.5	25.2
0.9	14.4	8	22.4
0.85	14.0	6.5	20.5
0.8	13.8	5.5	19.3
0.7	13.5	3.8	17.3

As is readily apparent from Table 5.3 the 18.8 dB available will give a P_d of less than 80% rather than the 99% specified. If 99% is needed then R_{max} could be sacrificed. Further tradeoffs will be looked at later.

From the above analysis it can be said that the specifications of Table 5.1 cannot be met with the baseline radar. It is also obvious that the high scan rate is the major culprit. In short the fluctuating target requires more energy from the radar, but the high scan rate does not allow enough pulses to get the energy.

Since the gain G is squared in eqn. A and since the reflector diameter, D, is squared in eqn. B the easiest way to pick up the needed "dB's" is to increase D. Before looking at this it should be said that a P_d of 99% is unrealistic at R_{max}. At closer ranges P_d will rise to this value or greater as a natural result of R_{max} decreasing by the fourth power. It is therefore advisable to decrease P_d to 95% at 12 NMi. This buys back roughly 7 dB leaving 6.4 dB more to be gained. (Note when the range is 11 KM (6 NMi) the SNR_1 will improve by 12 dB which is enough to give P_d's near 99%.)

Increasing the dish to 0.76m (30") will give 7 dB more gain, hence this alone would do it.

If the dish size is "sacred" then decreasing the scan area to 30° x 30° will give the extra 6.4 dB by allowing more pulses to be integrated and increasing P_{fa} via eqn. C.

As another alternative the 8 dB noise figure could be lowered to about 4 dB by use of an uncooled parametric amplifier. The other 2.4 dB could come from the scan size or dish diameter or both.

In connection with the scan rate, it might be tempting to decrease the overlap, but this is futile since post-detection "dB's" gained will never make up for predetection "dB's" lost where a one to one tradeoff is involved, i.e., the off axis loss would rise too rapidly.

Of course more average power could be used, but 6.4 dB is prohibitive.

The minimum range of 61m (200 ft.) is critical for safety reasons, however, the maximum range could be compromised to 14.8 KM (8 NMi) to pick up the needed gain.

Finally the acquisition time could be extended, but this is inefficient since it ultimately affects n_B and G_{nc} through a (6 log n) law, i.e., doubling T_s only gives 1.8 dB gain.

Table 5.4 summarizes the tradeoffs described above. In actuality several of these techniques would most likely be employed rather than any single one.

For the baseline design it is recommended that the antenna reflector diameter be increased to 0.61m from 0.51m (24" from 20") (this gives 3 dB), the P_d should be decreased to 0.95 from 0.99 at 22 KM (12 NMi) while remaining at 0.99 for 14.8 KM (8 NMi), and finally the noise figure should be improved to 4.6 dB (this gives 3.4 dB). The total gain is 6.4 dB which when added to the 18.8 dB available gives 25.2 dB. Thus these compromised specifications can be met at the maximum range of 22 KM (12 NMi) while the more stringent specifications can be met at 14.8 KM (8 NMi).

TABLE 5.4

RADAR TRADEOFF TECHNIQUES

	Technique	Added Gain Achievable (dB)*
a.	Decrease P_d to 0.95 at 22 KM (12 NMi)	7.2
b.	Increase reflector diameter to 0.76 m (30")	7.0
c.	Decrease scan area to 30° x 30°	6.4
d.	Improve Noise Figure	4.0
e.	Increase average power to 160 watts	6.0
f.	Decrease maximum range to 14.8 KM (8 NMi)	7.0
g.	Increase acquisition time to 120 secs	1.8

* The added gain desired is 13.6 dB.

5.2.2 Multiple Range Mode Analysis

The purpose of the previous section was to introduce the problem, gain familiarity, and provide a system that would satisfy the radar part of the radar/wideband communications problem. No mention was made of wideband communications (WBC). Clearly the baseline design requires high peak powers and therefore the only commonality possible with WBC is after the power amplifier. In this section the single range mode will be discarded and multiple range modes will be investigated. This approach could, in theory, provide a P_d of 0.99 at the maximum range of 22 KM (12 NMi) while not compromising the minimum range requirements and/or lower the peak power required.

Refer to eqn. A. Since $B\tau \doteq 1$ is the case and all factors other than f_r have been considered or are fixed, consider varying f_r. At first glance it looks as though (10 log f_r) dB could be gained, but such is not the case because

$$G_{nc}(dB) = 3 + 6 \log n = 3 + 6 \log \left(\frac{\theta_B}{\dot{\theta}_s} \right) f_r$$

$$= \text{constant} + 6 \log f_r. \qquad (5.19)$$

But then the G_{nc}/f_r term in eqn. A results in only

$$|6 \log f_r - 10 \log f_r| = +4 \log f_r. \qquad (5.20)$$

What is actually happening here is a trade between predetection (coherent integration) gain and postdetection (noncoherent integration) gain. The net result follows eqn. (5.20) rather than 10 log f_r.

As an example let SNR_1 = 32.4 dB rather than the 18.8 dB found in the previous section, and let τ increase by 23 (32.4 dB-18.8 dB expressed as a ratio). So as not to change either P_{avg} or P_{peak} let $f_r\tau$ remain constant. Then eqns. C and D give

$$P_{fa} = \frac{\theta_B}{\dot{\theta}_s T_{fa}} (f_r \tau), \tag{5.21}$$

i.e., the false alarm probability remains the same, so SNR_1 = 32.4 dB still represents P_d = 0.99. However increasing τ and keeping τf_r constant decreases f_r so that G_{nc} decreases by 8.2 dB. The end result therefore is not 32.4-18.8 dB = 13.6 dB, but only 5.4 dB, and so R_{max} would change. (Note that 4 log 23 = 5.4.)

To keep R_{max} at 22 KM (12 NMi) and still increase P_d to 0.99 will require τ to increase by 2512, i.e.,

$$13.6 = 4 \log 2512. \tag{5.22}$$

Thus a τ of about 1 ms is required.

If the pulse gets too long the high scan rate may cause the target to disappear before the whole pulse illuminates it, thus the following calculation is pertinent. The time that a 1 meter (11 ft^2) target stays in the 3 dB beamwidth at 120°/sec is

$$t_{3dB} = \frac{2.7^\circ}{120^\circ/\text{sec}} = 22.5 \text{ ms}. \tag{5.23}$$

Thus a 1 ms pulse is acceptable.

A τ = 1 ms implies f_r = 1 pps to maintain to peak to average power of 1000, therefore

$$n_B = 22.5 \text{ ms} \times 1 \text{ pps} = 22.5 \text{ pulses}, \tag{5.24}$$

i.e., all the pulses are still used.

The tradeoff, however, is

$$R_{min} \geq \frac{1.61 \times 10^5 \text{ NMi/sec} \times 1 \text{ ms}}{2} = 150 \text{ KM (81 NMi)} \tag{5.25}$$

As can be seen from eqn. 25 it is not possible to totally tradeoff f_r for P_d.

The conclusion to this section is that multiple range modes, while theoretically attractive, do not tradeoff R_{min} for P_d efficiently enough.

While the peak to average ratio of the power was held constant in the above analysis it should be apparent that the same f_r versus P_{peak} tradeoff technique could be attempted. It should also be apparent that it is again futile.

5.2.3 Pulse Expansion/Compression Techniques

When radars became peak power limited ways were sought to achieve better range resolution without incurring larger peak powers. Basically the radar waveform was coded in one way or another so as to enhance its autocorrelation properties. An application of this method will be investigated below.

One technique of "compansion" is to expand the pulse width while simultaneously changing the frequency of the r.f. wave. In the case at hand there is an isolation problem between the transmitter and receiver at the minimum range if the pulse is any longer than 0.4 sec. Thus a modification to the compansion technique is needed.

Consider a linear frequency modulation of the basic radar frequency with a pulse width expansion, however, prior to transmitting the pulse let it be amplified and then passed through a waveguide compression filter. Since the pulse when applied to the power amplifier is wide the peak power output is low. The compression operation effectively raises the peak power while narrowing the pulse. As long as the pulse width into the transmit/receiver (TR) box is narrow there is no isolation problem. The receiver, by the way, is a standard pulse receiver with only the matched filter changed to accommodate a "sinc(x)" pulse rather than a rectangular pulse.

Now if the peak power can be lowered sufficiently so that the power amplifier is, say, a TWT, then coherent integration is possible. The G_{nc} in eqn. A becomes 10 log n rather than 3 + 6 log n which gains an additional

$$(10 \log 56) - 3 - (6 \log 56) = 4 \text{ dB}. \qquad (5.26)$$

The 18.8 dB calculated before plus 4 dB leaves 9.6 dB yet to be acquired somehow for a $P_d = 0.99$.

Since the output of the transmitter is still a narrow pulse all of the tradeoffs and analysis done in the foregoing sections apply. For example, decreasing P_d to 0.95 at 22 KM (12 NMi) and taking into account the 4 dB above means that only 2.4 dB needs to be gained now rather than the 6.4 dB worked with earlier.

The theory above is sound, but implementation is not possible since the waveguide filter must be operated near cutoff and so suffers insertion losses on the order of 60 dB. It should be noted that time-bandwidth products of 30 dB[4] can be achieved with the foregoing technique so if the insertion loss could be lowered enough the method would be very attractive. To reiterate, however, this method will not work in the present case.

5.3 CONCLUSION

The previous two sections of this report looked at the adequacy of the proposed Orbiter baseline radar in providing rendezvous information. Furthermore, techniques were investigated which could possibly reduce the peak power requirements enough so as to employ a common power amplifier between the radar and a wideband communications system. It was found that due to the high maximum to minimum range requirements and the large scan area, thus forcing a high scan rate, the baseline system could not meet all of the proposed specifications. Several areas of compromise were recommended.

Since the baseline could not meet the requirements there was not much hope in lowering the peak power. The multiple range approach was helpful, however, too many "range bands" would be needed to do the job. A pulse compression technique seemed promising, however, upon investigation into the hardware aspects it too was seen to be deficient because more was lost than was gained.

The conclusion therefore, if the baseline radar is to be used, is to

a) accept a P_d of 0.95 at 22 KM (12 NMi),

b) increase the antenna reflector diameter to 0.61m (24 inches),

c) decrease the receiver noise figure by 3.4 dB.

The only commonality with a wideband communications system would then be the antenna and possibly some transmission line. It is further recognized that a 3 dB polarization loss would be incurred unless steps are taken to accommodate the circular polarization in the wideband communications mode and the linear polarization in the radar mode.

5.4 REFERENCES

(1) G. K. Huth and C. L. Weber, "Integrated Source and Channel Encoded Digital Communication System Design Study," Axiomatix, NASA Contract NAS9-13467.

(2) M. I. Skolnik, Introduction to Radar Systems, McGraw-Hill Book Co., 1962.

(3) R. S. Berkowitz, et. al., Modern Radar, John Wiley & Sons Inc., 1965.

(4) M. I. Skolnik, Radar Handbook, McGraw-Hill Book Co., 1970.

6.0 ORBITER KU-BAND RELAY SYSTEM STUDY

6.1 INTRODUCTION

The minimum antenna gains required to support a relay link for both command and telemetry at Ku-Band between the TDRS and the Shuttle Orbiter are calculated in this report. To do this, link budgets are developed, the required Orbiter EIRP and G/T are found, and the losses between the transmitter and antenna, and the receive system noise temperature are determined. This information is used to calculate the minimum antenna gains required for specific data rates. Next the factors affecting the implementation of the system are discussed. Two appendices are included. One lists the available hardware at Ku-Band (waveguide, diplexer, rotary joints, TWT's), and the other discusses high vacuum voltage breakdown.

6.2 CALCULATION OF MINIMUM ANTENNA GAIN REQUIRED ON THE TELEMETRY LINK

A block diagram of a candidate Ku-Band Shuttle Orbiter relay system is shown in Figure 6.1. The antenna, diplexer and pre-amp are located in the forward area of the Orbiter. The receiver, power amp and modem are located in the payload area. A 12M (40 foot) waveguide run links the two areas.

The link budget[1] for the telemetry (Orbiter to TDRS) link is given in Table 6.1. ΔPSK modulation is used with a bit error probability of 10^{-5}. The TDRS system noise temperature is assumed to be 710^{o}K. The relationship between achievable data rate and Orbiter EIRP is presented in Figure 6.3. It is seen that EIRP's of 19.3 dBW and 21.0 dBW are required for data rates of 128 Kbps and 192 Kbps respectively with rate 1/3 convolutional coding included.

Now that the required EIRP is known, the RF losses between the transmitter and antenna must be found. From Figure 6.1, it is seen that the

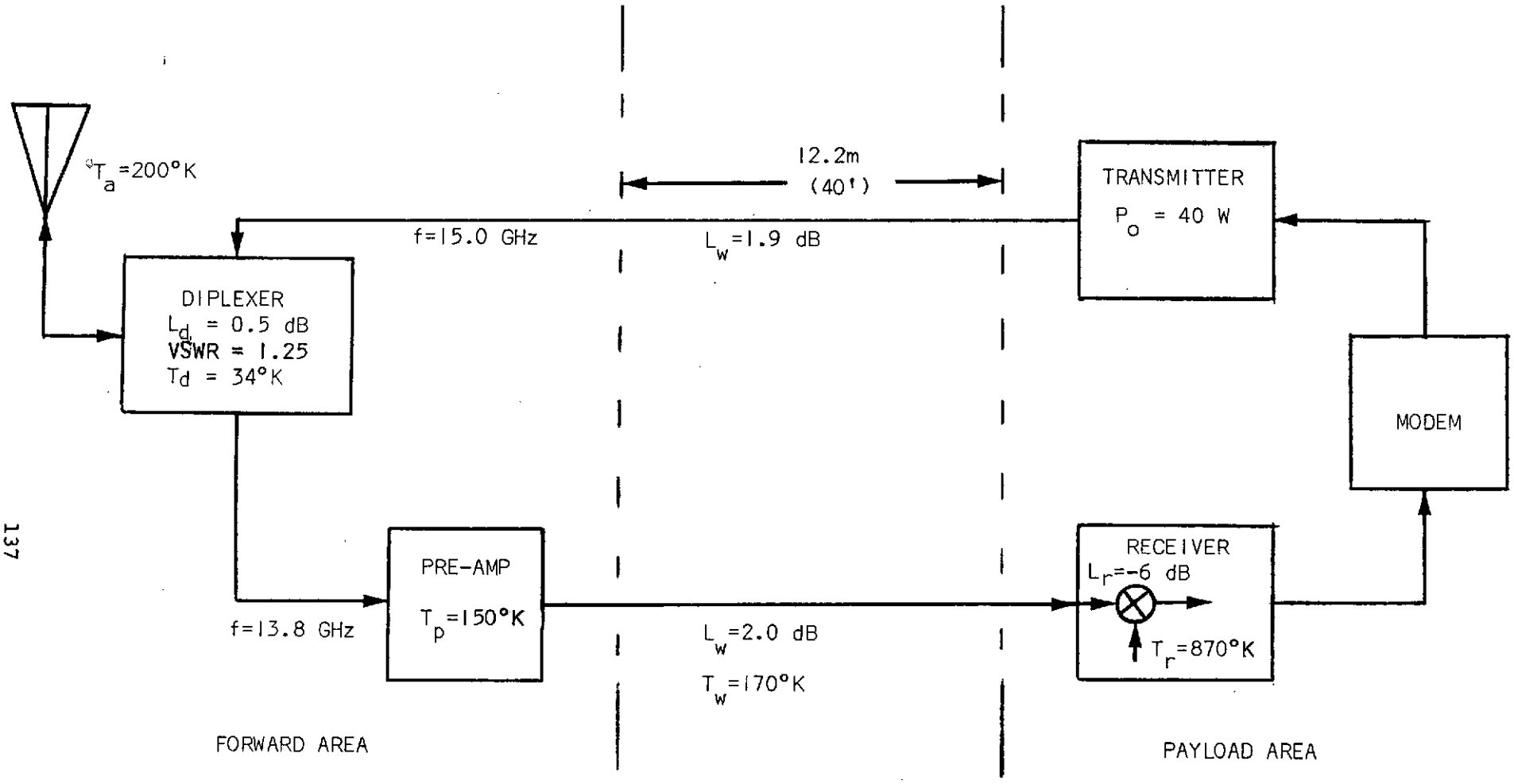

FIGURE 6.1 BLOCK DIAGRAM OF SHUTTLE ORBITER KU-BAND RELAY SYSTEM

TABLE 6.1

SINGLE-ACCESS KU-BAND TELEMETRY LINK BUDGET

PARAMETER	VALUE
Binary Error Probability	10^{-5}
Orbiter EIRP (dBW)	EIRP
Space Loss (dB)	-209.2
Pointing Loss (dB)	-0.5
Polarization Loss (dB)	-0.5
TDRS Antenna Gain (dB)	52.6 (55% efficiency)*
P_s at Output of Antenna (dBW)	-157.6 + EIRP
T_s (Antenna Output Terminals) (^{O}K)	710
kT_s at Output of Antenna (N_o) (dBW/Hz)	-200.1
Carrier-to-Noise Density, P_s/N_o, (dB-Hz)	42.5 + EIRP
Transponder Loss (dB)	-2.0
Demodulation Loss (dB)	-1.5
System Margin (dB)	-3.0
Required E_b/N_o, ΔPSK (dB)	-9.9
Achievable Data Rate (dB)	26.1 + EIRP
FEC Gain, R = 1/3, K = 7 (dB)	5.7
Achievable Data Rate (dB)	31.8 + EIRP

*On Axis

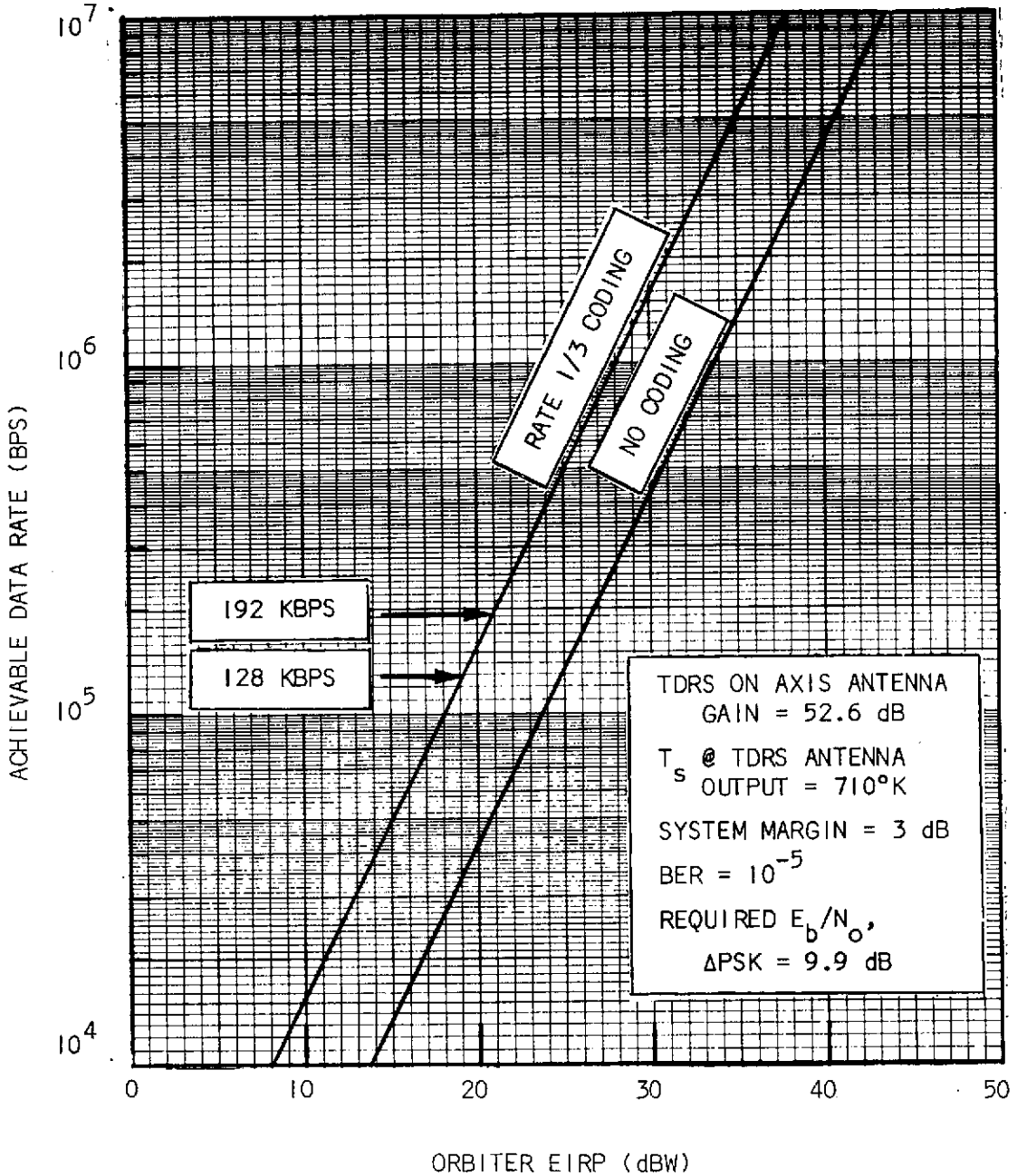

FIGURE 6.2 ORBITER EIRP vs. ACHIEVABLE DATA RATE

loss will be the sum of the waveguide and diplexer losses and any losses due to mismatches.

Various manufacturers were contacted to determine the waveguide type with the least loss and the approximate loss due to a diplexer. Table 6.2 presents the types of waveguides considered and their losses at 15 and 13.8 GHz. Rigid circular waveguide was also considered but is not included in the table because it is not available above 13.2 GHz. Andrew's Heliax elliptical flexible waveguide has the least loss at 15 GHz. Rigid rectangular waveguide has the least loss at 13.8 GHz. Flexible rectangular waveguide has the greatest loss at all frequencies. Heliax elliptical waveguide was chosen for these calculations because it had the lowest loss at 15 GHz. Actually it makes little difference whether rigid rectangular or flexible elliptical waveguide is used because a 12M (40') length of rigid rectangular waveguide has a 2.2 dB of loss compared to 1.9 dB for flexible elliptical waveguide. Table 6.2 also shows the losses and VSWR's for a diplexer and for waveguide connectors.

In addition to resistive losses there are also losses due to mismatches between the various components of the system. However, since this system has low resistive losses and VSWR's below 1.5, the mismatch losses are on the order of a tenth of a dB and are ignored.

The EIRP and system losses are known and the transmitter power is given, therefore the required antenna gain in decibels is determined by the following equation:

$$G_{min} = EIRP + L - P_o \qquad (6.1)$$

TABLE 6.2 WAVEGUIDE ATTENUATION DATA

WAVEGUIDE TYPE	FREQUENCY RANGE (GHz)	ATTENUATION (dB/30m) (dB/100')		VSWR (max)
		@13.8 GHz	@15 GHz	
Rigid Rectangular WR62	12.4 - 18.0	6.0	5.5	1.05
Rigid Rectangular WR75	10.0 - 15.0	4.0	---	1.05
Flexible Rectangular WR62	12.4 - 18.0	≈25	≈25	1.10
Flexible Rectangular WR75	10.0 - 15.0	≈15	---	1.10
Heliax® Flexible Elliptical EW132	11.0 - 16.0	5.0	4.7	1.15

WAVEGUIDE CONNECTORS	L ≈ 0 dB	VSWR = 1.15	
DIPLEXER	L ≈ 0.5 dB	VSWR = 1.25	ISOLATION = 70 dB

where:

G_{min} = Minimum Orbiter antenna gain required for a particular data rate

EIRP = Orbiter EIRP required for a particular data rate (obtained from Figure 6.2)

L = Losses due to waveguide and diplexer = 2.4 dB @ 15 GHz (shown in Figure 6.1)

P_o = Orbiter transmitter output power = 40 watts.

We find that G_{min} = 5.7 dB for a 128 Kbps data rate and 7.4 dB for a 192 Kbps data rate.

If the transmitter is moved to the forward area of the Orbiter then the waveguide loss is eliminated and G_{min} = 3.8 dB for 128 Kbps data rate and 5.5 dB for 192 Kbps data rate.

It should be pointed out here that a problem which may be encountered with a high transmitter power is the high vacuum voltage breakdown inside the components of the system. Even though the nominal power rating of the waveguide and other components is in excess of the 40 watts available at the transmitter output it is not applicable in space. This breakdown phenomenon is discussed further in Appendix 6.B.

6.3 CALCULATION OF MINIMUM ANTENNA GAIN REQUIRED ON THE COMMAND LINK

To calculate the minimum antenna gain needed on the command (TDRS to Orbiter) link both the required G/T and the receive system noise temperature must be known.. The G/T is related to data rate in the link budget of Table 6.3. Notice that two different TDRS EIRP's are listed. The low power EIRP of 47.0 dBW will be used here. The high power EIRP is only for back-up and has a 25% duty cycle. Furthermore, ΔPSK modulation with a BER of 10^{-5} is assumed.

TABLE 6.3

SINGLE-ACCESS KU-BAND COMMAND LINK BUDGET

PARAMETER	LOW POWER LINK	HIGH POWER LINK**
Binary Error Probability	10^{-5}	10^{-5}
TDRS EIRP* (dBW)	47.0	50.5
Space Loss (dB)	-208.6	-208.6
Orbiter Antenna Gain (dBi)	G_u	G_u
Polarization Loss (dB)	-0.5	-0.5
P_s Out of Orbiter Antenna (dBW)	$-162.1 + G_u$	$-159.6 + G_u$
System Noise Temperature, (^oK)	T_s	T_s
Boltzmann's Constant, k, (dBW/^oK-Hz)	-228.6	-228.6
Carrier-to-Noise Density, P_s/N_o, (dB-Hz)	$66.5 + G_u/T_s$ dB	$69.0 + G_u/T_s$ dB
Demodulation Loss (dB)	-1.5	-1.5
PN Loss (dB)	-1.0	-1.0
System Margin (dB)	-3.0	-3.0
Required E_b/N_o, ΔPSK (dB)	-9.9	-9.9
Achievable Data Rate (dB)	$51.1 + G_u/T_s$ dB	$54.6 + G_u/T_s$ dB
FEC Gain, R = 1/3, K = 7 (dB)	5.7	5.7
Achievable Data Rate (dB)	$56.8 + G_u/T_s$ dB	$60.3 + G_u/T_s$ dB

* On Axis

** For contingency only - 25% duty cycle

Figure 6.3 shows the relationship between G/T and achievable data rate. It is seen that G/T's of -10.8 dB/^{o}K and -8.2 dB/^{o}K are required for data rates of 40 Kbps and 72 Kbps respectively if rate 1/3 convolutional coding is used.

Now that the G/T is known, the system temperature must be found before the antenna gain can be calculated. The system noise temperature is given by:

$$T_s = T_a + T_e \tag{6.2}$$

where

T_s = Total system noise temperature referred to the antenna

T_a = Antenna temperature = 200^{o}K

T_e = Effective temperature of the rest of the system

T_e is calculated from this equation (referring to Figure 6.1):

$$T_e = T_d + T_p \cdot L_d + \frac{T_w \cdot L_d}{G_p} + \frac{T_r \cdot L_d \cdot L_w}{G_p} \tag{6.3}$$

where

T_d = Effective noise temperature of diplexer = 34^{o}K

T_p = Effective noise temperature of pre-amp = 150^{o}K

L_d = Loss due to diplexer = .5 dB

T_w = Effective noise temperature of waveguide = 170^{o}K

G_p = Gain of pre-amp

T_r = Effective noise temperature of receiver = 870^{o}K

L_w = Loss due to waveguide = 2.0 dB @ 13.8 GHz

The antenna temperature and pre-amp noise temperature were assumed to be 200^{o}K and 150^{o}K respectively. The other temperatures were calculated

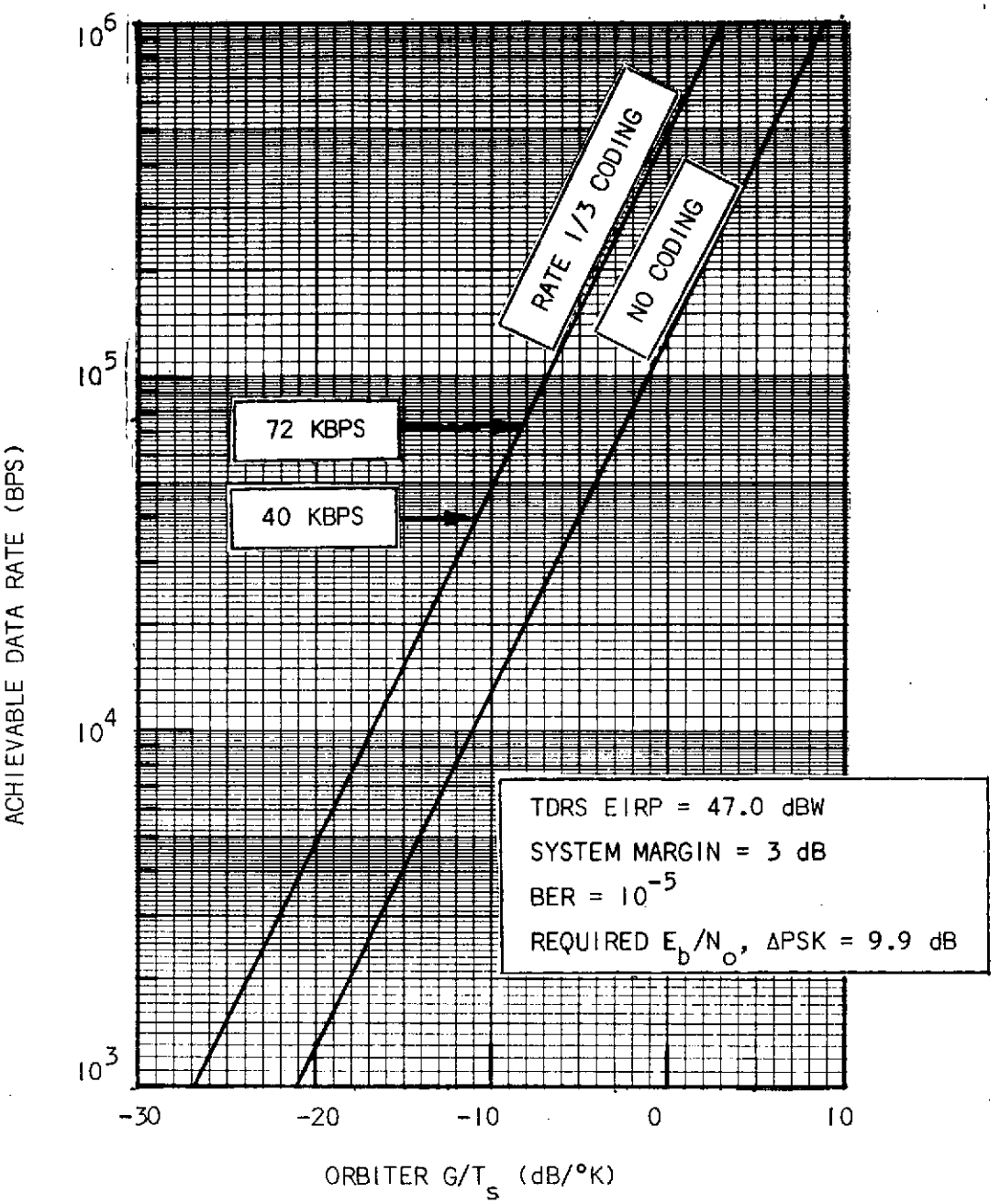

FIGURE 6.3 ORBITER G/T_s vs. ACHIEVABLE DATA RATE

from the equation $T = (L-1) \cdot 290^{\circ}K$ where L is the loss of a component and $290^{\circ}K$ is room temperature. The waveguide and diplexer losses have previously been given in Table 6.2. The receiver was assumed to have a mixer with 6 dB of loss as shown in Figure 6.1.

From equation (6.1) and Equation (6.2) the system noise temperature is: $T_s = 402^{\circ}K + 1640^{\circ}K/G_p$. If the pre-amp gain is $\sim$20 dB then $T_s \simeq 420^{\circ}K$.

The minimum antenna gain can now be found from the following equation:

$$G_{min} = G/T_s + T_s \qquad (6.4)$$

where values are in log ratios and

G_{min} = The minimum antenna gain required for a specific data rate

G/T_s = Orbiter gain to noise temperature ratio required for a specific data rate (obtained from Figure 6.3)

T_s = System noise temperature = $420^{\circ}K$ = 26.2 dB-$^{\circ}K$

The minimum antenna gain required for a 40 Kbps data rate is 15.4 dB and for 72 Kbps is 18.0 dB.

6.4 SUMMARY AND CONCLUSIONS

Table 6.4 summarizes the results of the previous calculations. It is seen that the command link requires 15 to 18 dB antenna gain depending on the data rate. This is much greater than the telemetry link requires; it is the command link therefore which places severe constraints on the system.

Directional antennas must be used to obtain the required gain on the command link. This implies a narrow beamwidth and so a number of fixed antennas must be placed around the spacecraft if omnidirectional coverage is desired (for safety and operational reasons it is our opinion that such coverage is mandatory).

TABLE 6.4

SUMMARY OF REQUIRED ANTENNA GAIN

LINK	DATA RATE (KBPS)	REQUIRED GAIN (dB)	3 dB BEAMWIDTH * (DEGREES)	# OF ANTENNAS REQUIRED FOR 360° COVERAGE
COMMAND	40	15.4	20	18
	72	18.0	15	24
TELEMETRY W/TRANSMITTER IN PAYLOAD	128	5.7	60	6
	192	7.4	50	8
TELEMETRY W/TRANSMITTER IN FORWARD AREA	128	3.8	75	5
	192	5.5	62	6

*This is the beamwidth of an antenna whose gain at the 3 dB point equals the required gain.

Table 6.4 also shows the half power beamwidth of helix antennas which have the desired gain. This is the beamwidth of an antenna which has 3 dB more gain that the link requires. This allows the TDRS to be off beam center without degrading system performance below its designed value.

The number of antennas required for 360° coverage is also shown in Table 6.4. For example, the command link requires an antenna gain of 18 dB at 72 Kbps. An antenna with 21 dB gain has a 3 dB beamwidth of 15°. 24 of these antennas are required for 360° coverage. However, the coverage provided is only in one plane because of the symmetrical beam pattern. For spherical coverage additional antennas would have to be employed.

If parabolic dishes are used rather than helices the beamwidth and hence the required number of antennas is about the same as before. The dish diameter for 18 dB gain at 15 GHz would be less than 15 cm (6"). If steerable antennas* were employed only two or three would be required; however, additional hardware would be required for pointing. A rotary joint would also have to be added, introducing loss in the system. Typical rotary joint specs are presented in Table 6.5. An insertion loss of 0.3 dB would increase Orbiter system temperature by 2 dB, thus necessitating a 2 dB increase in antenna gain. The dish diameter would still be less than 15 cm (6"), however.

On the telemetry link, the required antenna gain is relatively small compared to the command link. The loss due to a 12m (40') waveguide run does not affect the system much. It might be difficult to implement in practice however, because it would be subject to severe mechanical and vibrational stress.

---

*The underlying assumption for this link is that flush mounted antennas will be used. Comments pertaining to steerable antennas are for information purposes only.

TABLE 6.5

TYPICAL ROTARY JOINT SPECIFICATIONS

CHANNEL	VSWR	INSERTION LOSS (dB)	ISOLATION (dB)
TRANSMIT	1.05	0.1	95
RECEIVE	1.15	0.3	95

A problem which may be encountered in the system is the high vacuum voltage breakdown within the components due to the low dielectric strength of a vacuum. The system may have to be pressurized to overcome this difficulty. Additional information is given in Appendix 6.B.

6.5 REFERENCES

(1) Tracking and Data Relay Satellite System (TDRSS) User's Guide Report No. X-805-74-126, prepared by NASA/Goddard Space Flight Center, June 10, 1974.

(2) Andrew's Catalog #28 - Antennas/Transmission Lines

(3) Private Correspondence with Microwave Development Laboratories, Inc.

(4) TWT's - Traveling wave tube Amplifiers, Short Form Catalog, Hughes Aircraft Co.

(5) Private communication with Fairchild Space and Electronics Company.

(6) T. D. Breeden, "Microwave Breakdown in Space Communication," RCA Engineer, Vol. 10 #4, December 1974.

(7) Private communication with DELTA μWave Company.

APPENDIX 6.A

KU-BAND HARDWARE AVAILABILITY

A summary of waveguide, rotary joints, diplexers, and TWT's available at Ku-Band is presented below.

WAVEGUIDE

Andrews manufacturers rigid rectangular and flexible elliptical waveguide. Figure 6.A.1 is a curve of attentuation vs. frequency for the various types of waveguide. This was taken from Reference 2. In the figure solid lines represent elliptical waveguide and dotted lines

represent rectangular waveguide. Flexible rectangular waveguide is also available at Ku-Band but not from Andrews. Circular waveguide is not available above 13.2 GHz. Table 6.A.1 summarizes the waveguide data. The data for flexible rectangular guide was obtained from the Airtron Co. of Morris Plains, N. J.

ROTARY JOINTS

Rotary joints come in single channel or multi-channel configurations. Microwave Development Labs (MDL) manufacturers both types. Table 6.A.2 lists their off-the-shelf single channel rotary joints.[3]

TABLE 6.A.1 - WAVEGUIDE ATTENUATION DATA

WAVEGUIDE TYPE	FREQUENCY RANGE (GHz)	ATTENUATION (dB/30m) (dB/100')		VSWR (max)
		@13.8 GHz	@15 GHz	
Rigid Rectangular WR62	12.4 - 18.0	6.0	5.0	1.05
Rigid Rectangular WR75	10.0 - 15.0	4.0	---	1.05
Flexible Rectangular WR62	12.4 - 18.0	≈25	≈25	1.10
Flexible Rectangular WR75 10.0 - 15.0	10.0 - 15.0	≈15	---	1.10
Heliax® Flexible Elliptical EW132	11.0 - 16.0	5.0	4.7	1.15

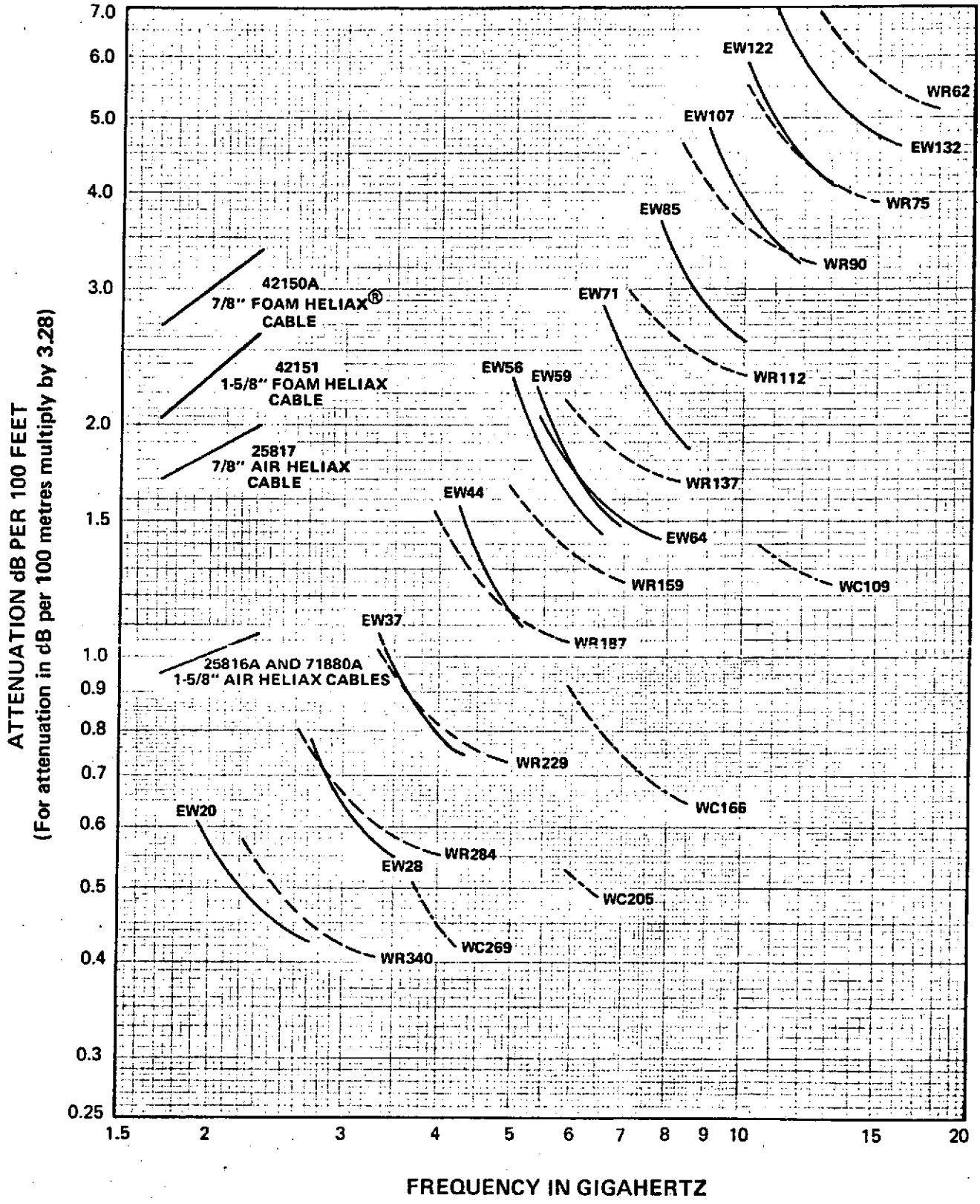

Attenuation curves based on:
VSWR 1.0
Ambient Temperature 24° C (75° F)

Attenuation curves are guaranteed within ± 5%, except Types 42150A and 42151 within ± 10%.

FIGURE 6.A.1 MICROWAVE WAVEGUIDE AND CABLE ATTENUATION

TABLE 6.A.2 - SINGLE CHANNEL ROTARY JOINTS

FREQUENCY (GHz)	VSWR	INSERTION LOSS (dB)	PEAK POWER (w)
15.0 - 17.5	1.15	0.10	100 K
14.0 - 18.0	1.25	0.15	75 K

MDL has built a dual-channel rotary joint for GE as part of the Skylab program. The specs for this are listed in Table 6.A.3.

TABLE 6.A.3 - SKYLAB ROTARY JOINT SPECIFICATIONS

CHANNEL	FREQUENCY (GHz)	VSWR	INSERTION LOSS (dB)	ISOLATION (dB)
1 - Transmit	13.7 - 14.0	1.05	0.1	95
1 - Receive	13.7 - 14.0	1.15	0.3	95

This rotary joint was part of a Microwave Altimeter/Radiometer/Scattermeter System used to study the earth. It was unpressurized. The transmit channel handled 2 kw peak power and 2 w average power when used with the altimeter. It handled 20 w peak power and 12 w average power when used with the scattermeter.

MDL has also developed a pressurized dual-channel rotary joint. This was not a space application. Its specs are given in Table 6.A.4.

TABLE 6.A.4 - DUAL CHANNEL ROTARY JOINT SPECIFICATION

CHANNEL	FREQUENCY (GHz)	VSWR	INSERTION LOSS (dB)	ISOLATION (dB)	POWER (w) PEAK	POWER (w) AVE.
1	15.1 - 17.3	1.35	0.2	60	10K	2K
2	15.1 - 17.3	1.5	0.5	60	100K	20K

DIPLEXERS

After a phone conversation with Wavecom. The following specs can be considered typical of diplexers at Ku-Band:

Insertion Loss = 0.5 dB

Isolation = 70 dB

VSWR = 1.25

These values are not exact and can easily be changed to fit the needs of a particular application.

TRAVELING WAVE TUBES (TWT's)

Hughes has manufactured space qualified TWT's at Ku-Band for specific applications[4]. These are listed in Table 6.A.5.

TABLE 6.A.5 - SPACE QUALIFIED TWT's

SPACECRAFT	CENTER FREQUENCY (GHz)	OUTPUT POWER (watts)	GAIN (dB)	EFFICIENCY (%)
Skylab/GEOS	14.0	1.5	46	15
Skylab	14.0	20	40	25 (66% duty cycle)
Skylab/GEOS	14.0	2.5 K	50	16 (1% duty cycle)
Comsat	20.0	4.0	50	20
ATS-F	20.0	2.0	42	15

Hughes also has off-the-shelf space qualified TWT's. These are listed in Table 6.A.6.

TABLE 6.A.6 - KU-BAND SPACE QUALIFIED TWT's

FREQUENCY (GHz)	OUTPUT POWER (watts)	GAIN (dB)
13.5 - 14.5	20.0	53
*17.0 - 22.0	3.0	50
18.0 - 22.0	2.0	42

*under development

Hughes also has non-space qualified TWT's available off-the-shelf. These are shown in Table 6.A.7.

TABLE 6.A.7 - CW TWT's

FREQUENCY (GHz)	OUTPUT POWER (watts)	GAIN (dB)
12.0 - 14.0	20	30
12.4 - 18.0	10	30
*15.3 - 15.8	8K	40
*15.5 - 17.5	1K	30

*under development

Although Hughes has no 40 watt space qualified TWT at Ku-Band, Hughes personnel have said that it would be no problem to develop one.

APPENDIX 6.B

VOLTAGE BREAKDOWN AT MICROWAVE FREQUENCIES

This appendix describes the problem of voltage breakdown at microwave frequencies. The types of breakdown are explained and methods of overcoming the problem and various factors which must be considered are discussed.

A problem frequently encountered at microwave frequencies is the limitation of power handling due to voltage breakdown within a component such as a waveguide, diplexer, coaxial cable, or connector. There are two types of RF voltage breakdown in a space environment: an ionization partial vacuum breakdown and a multipactor or hard vacuum breakdown. Ionization breakdown occurs at pressures of several torr, the multipactor effect occurs at lower pressures - typically 10^{-4} to 10^{-6} torr[5].

In both types of breakdown, free charge carriers are formed in the breakdown gap. Ionization breakdown uses the ionized intervening gaseous medium as its source of free charges. Multipactor breakdown requires the right combination of electric field intensity, frequency, pressure and boundary conditions to produce free charges. These charges are generated by secondary emission at the breakdown gap boundaries. The effect of both mechanisms is identical. A power dropout is experienced and the region around the breakdown gap is blackened considerably[6].

Determining the breakdown voltage is not a trivial exercise. Much of the published work is for well terminated transmission lines. However, in actual spacecraft, higher VSWR's and high Q elements can significantly lower the potential breakdown threshold[5].

The general philosphy behind the elimination of the breakdown problem is to raise the breakdown threshold by raising the dielectic strength

of the material in the breakdown gap. In the case of a vacuum this implies oil filling or pressurization of waveguide components and the redesign of coaxial connectors to eliminate interface voids between the connectors and cables. Pressurization is the most common method used.

In general, the breakdown threshold is proportional to the pressure in a component. The exact amount of pressure required to achieve a certain threshold depends upon such factors as geometry, required power handling ability and the pressurizing gas used.

Pressurization requires additional hardware such as gauges, pressure tanks, gaskets and pressure windows. Extremely tight seals are required in space. In most spacecraft once a leak occurs there is no way to repair it. For this reason designers tend to shy away from pressurization in space. However, since the Shuttle Orbiter will return to earth periodically, it might be possible to hold the pressure for the duration of a flight and then repressurize or repair on the ground.

Another consideration is the selection of a suitable gas. Dry nitrogen is used in most terrestrial systems where the primary purpose is to keep out moisture. Electronegative gases have been used in radar systems where pulsed megawatt powers are required. These gases tend to suppress breakdown by capturing free charges that are generated in the breakdown region[5].

A diplexer is usually most susceptible to voltage breakdown because of its high Q factor. Therefore, its removal from a system might alleviate the breakdown problems. Whether or not it can be removed depends upon the amount of isolation required between the transmit and receive

channels. A circulator and a transmit reject filter in the receive leg could replace a diplexer but the isolation provided might not be adequate.

In summary, the following points are emphasized:

- There is a high vacuum voltage breakdown problem at microwave frequencies.
- The actual breakdown threshold of a specific system is difficult to predict without actually testing the system.
- Pressurization of waveguide components will raise the breakdown threshold - exactly how much pressure is needed depends upon the gas used, the geometry involved and other factors.
- Keeping the pressure in a space environment requires tight seals and careful design.
- High Q components are most susceptible to breakdown. Replacing them with the lower Q parts should be considered if the system requirements allow it.

7.0 ORBITER AEROFLIGHT CAPABILITIES STUDY

7.1 INTRODUCTION

This report documents the analyses and results of a task to review the communications and tracking factors for the Space Shuttle Orbiter's Atmospheric Flight (Aeroflight) profile.

The aeroflight phase of the Shuttle mission encompasses the period immediately after re-entry blackout through approach, landing and rollout. The aeroflight communications and tracking subsystem configurations assumed for this analysis are those outlined in Reference 1. Systems of interest for this review include the Tactical Aerial Navigation (TACAN) subsystem, the Microwave Scanning Beam Landing System (MSBLS), the Radar Altimeter (RA) and the UHF transceivers for Air Traffic Control (UHF/ATC).

The aeroflight profile depicted in Reference 2 was used to determine range-rate and deceleration factors for this task. Antenna considerations are based upon the locations shown in Reference 2.

The analytical approach used for this task was to investigate the engineering parameters of the communications and tracking subsystems of interest, and then to analyze their functional capabilities in relation to the aeroflight flight profile and the orbiter antenna locations.

7.2 ANALYSIS

The Aeroflight phase of the Shuttle mission encompasses the period immediately after re-entry blackout through approach, landing and rollout. Systems of interest for this review task include the Tactical Aerial Navigation (TACAN), the Microwave Scanning Beam Landing System (MSBLS), the Radar Altimeter (RA), and the UHF Transceiver. The following short discussion of each of these equipments provides a reference as to their use.

TACAN (L-Band Transmitter/Receiver) (3 Systems)

Provides position reference (range and bearing) to various TACAN ground station sites immediately after re-entry blackout and until the start of the terminal area landing phase. This starts at about 46 kilometers (150,000 feet) altitude and 520 kilometers (280 nautical miles) from the landing site, extending to around 3,600 meters (12,000 feet) altitude and 15 kilometers (8 nautical miles) from touchdown.

Microwave Scanning Beam Landing System (MSBLS)(Ku-band) Receiver/ Interrogator) (3 Systems)

The airborne MSBLS equipment uses an angle decoder, distance measuring equipment (DME), and an interrogator unit to provide precision azimuth, elevation and slant range to guide the Orbiter during the final stages of approach and touchdown. MSBLS intercept occurs about 3,600 meters (12,000 feet) altitude and 15 kilometers (8 nautical miles) from touchdown.

Radar Altimeter (C-Band Transmitter/Receiver) (2 Systems)

A leading edge pulse-type RF altimeter used to refine MSBLS altitude information during the last 750 meters (2,500 feet) of descent to touchdown.

UHF Transceiver (2 Systems)

An off-the-shelf unit with minimum mission modifications which provides an Air Traffic Control (ATC) two-way voice link in the simplex mode.

A graphic presentation of the Shuttle Orbiter's aeroflight profile is shown in Figure 7.1 for purposes of general orientation. Table 7.1 contains the same parameters in an analytically more useful matrix format.

The values for time, range, altitude, range-rate and deceleration were obtained from the set of curves included in Reference 2. Worst-case values are shown for range-rate and deceleration inasmuch as they reflect values related to an on-the-nose reference at the touchdown point, i.e., measurements to a position which accounts for maximum range-rate and deceleration. Any reference point which is away from the "nose position" will show a reduced value and thus have less impact on the communications and tracking systems.

7.2.1 Aeroflight Profile Analysis

None of the communications and tracking equipments of interest utilize tracking loops. Therefore, the problem of degraded lock acquisition, and the problems of maintaining, dropping and re-acquiring lock normally caused by doppler frequency shifts and doppler rates are not of concern. This narrows the investigation to analyses of equipment bandwidth problems, specular multipath interference, and placement of antennas on the Orbiter.

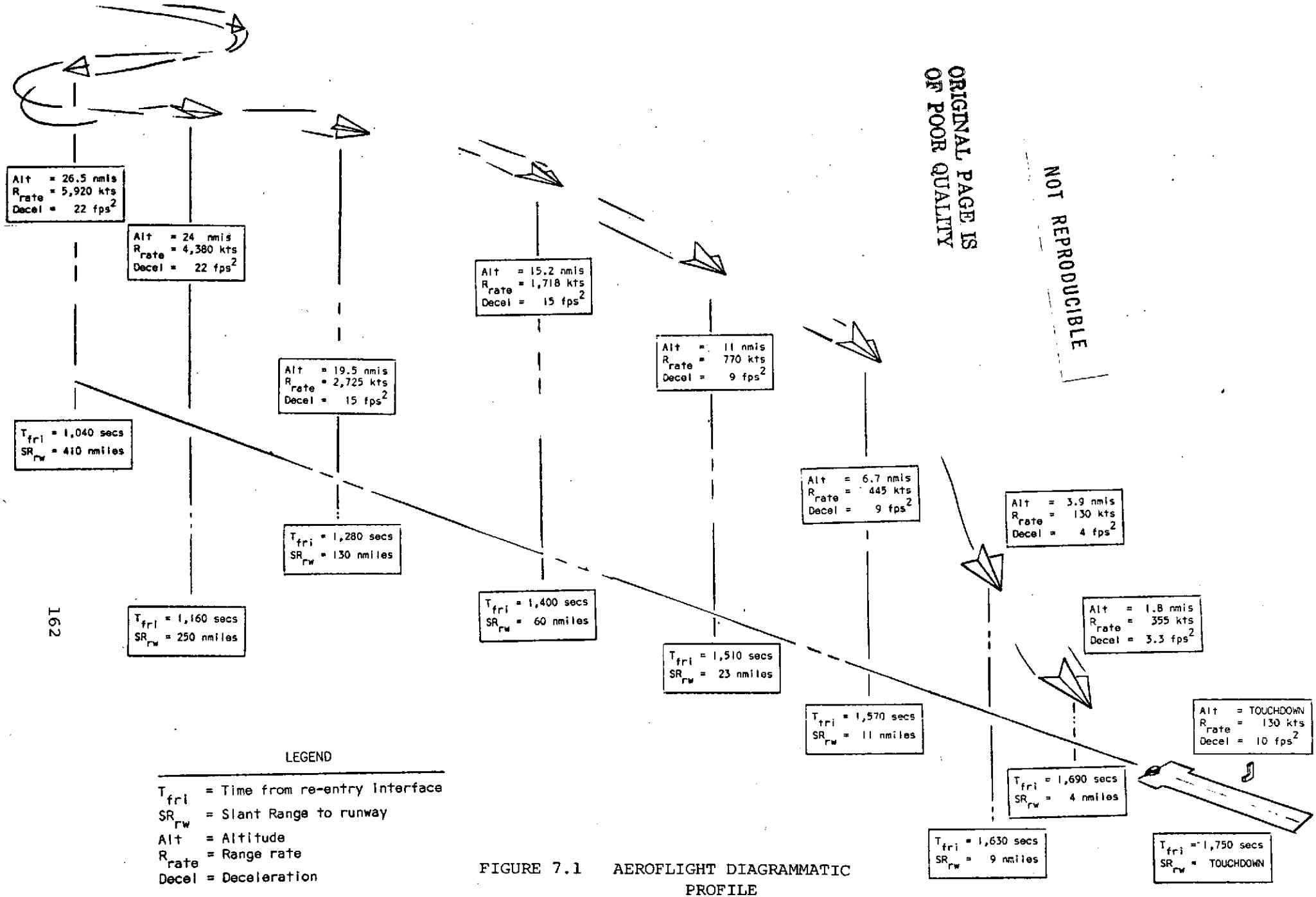

FIGURE 7.1 AEROFLIGHT DIAGRAMMATIC PROFILE

TABLE 7.1 MATRIX OF SELECTED AEROFLIGHT PARAMETERS

Time from Re-entry Interface (Seconds)	Slant Range to Runway KM (n miles)	Altitude KM (n miles)	Range-rate Referenced to Runway KM/hr (Knots)	Deceleration Referenced to Runway m/s^2 (fps^2)	Time to Touchdown (Seconds)
1,040	760 (410)	49 (26.5)	11,000 (5,920)	6.6 (22)	710
1,160	463 (250)	44 (24)	8,100 (4,380)	6.6 (22)	590
1,280	241 (130)	36 (19.5)	5,041 (2,725)	4.5 (15)	470
1,400	111 (60)	28 (15.2)	3,178 (1,718)	4.5 (15)	350
1,510	43 (23)	20 (11)	1,424 (770)	2.7 (9)	240
1,570	20 (11)	12 (6.7)	823 (445)	2.7 (9)	180
1,630	17 (9)	7 (3.9)	240 (130)	1.2 (4)	120
1,690	7 (4)	3 (1.8)	620 (335)	1.0 (3.3)	60
1,750	0	0	-	-	0

7.2.1.1 Bandwidth Problems

In determining whether or not there is a problem with equipment bandwidths for those portions of the aeroflight profile where each equipment is to be used, the maximum range-rate for each of these segments is converted to equivalent frequencies, using the expression:

$$\Delta f \approx f \frac{v}{c}$$

where:

Δf = amount of frequency shift

f = operating frequency

v = Shuttle range-rate

and c = velocity of light

Table 7.2 lists the pertinent results. In each of the cases shown in Table 7.2, the maximum doppler shift due to range-rate is less than 1/1000 of 1% of the carrier frequency.

The performance of the UHF/ATC and the TACAN equipments should not be degraded due to range-rate doppler during the earlier part of the aeroflight sequence when highest range-rates are experienced. For the UHF/ATC equipment, a maximum 3.8 kHz doppler shift within a nominal 15 kHz detection bandwidth will have little effect on performance. In the case of TACAN, the minimum required detection bandwidth based on the specified pulse duration is 286 kHz. This minimum figure is more than sufficient to absorb the 9.3 kHz maximum doppler shift due to range-rate.

No doppler/bandwidth problems are foreseen for the MSBLS system. However, high range rates with the associated extreme variations in signal strength at close ranges could impact the AGC capability of the MSBLS receiver. In discussions with engineers at AIL who

TABLE 7.2 DOPPLER FREQUENCY SHIFT FACTORS

	PRIME PERIOD OF INTEREST		MAXIMUM RANGE-RATE FOR PERIOD OF INTEREST			
EQUIPMENT	TIME AFTER RE-ENTRY	KM (N MILES) FROM TOUCHDOWN	Knots	Meters/Sec	EQUIPMENT FREQUENCY RANGE	MAXIMUM DOPPLER Δf
TACAN	1150-1590 secs	518-18.5 (280-10)	4,440	2,285.9	960-1215 MHz	7.3-9.3 kHz
UHF/ATC	ENIRE PROFILE	758-0 (410-0)	5,920	3,047.6	225-400 MHz	2.2-3.8 kHz
MSBLS	1540-1750 secs	22.2-0 (12-0)	600	308.9	15.4-15.7 GHz	15.8-16.1 kHz
RADAR ALT	1700-1750 secs	7.4-0 (4-0)	119*	6.17*	4.3 GHz	0.89 kHz*

* Vertical range-rate (altitude change) calculations

are responsible for the MSBLS system, it was learned that AGC circuitry is designed to a specification which will permit the AGC system to operate satisfactorily above range rates of 1,665 KM/Hr (900 knots).

Inasmuch as the Radar Altimeter (RA) is designed to measure altitude and altitude-rate, parameters shown in Table 7.2 for the Radar Altimeter uses vertical range as a reference rather than slant range. Maximum vertical doppler for the RA period of interest is 0.89 kHz. Based on the specified pulse duration of the RA equipment, a minimum bandwidth of 1428 kHz is required. This minimum bandwidth can readily absorb the calculated maximum doppler frequency shift of less than one kHz.

7.2.1.2 Specular Multipath

Based upon the results of previous analyses reported in References 3 and 4, degradation of the UHF/ATC and the TACAN links in the early aeroflight phases of interest due to specular multipath signals is effectively zero. For the worst-case condition when the Orbiter is above an altitude of 44.4 KM (24 nautical miles) and at a range of 463 KM (250 nautical miles), differential doppler due to multipath is less than 0.03 Hz. This result can be readily obtained from the graph shown as Figure 2 of Reference 3.

7.2.1.3 Orbiter Antenna Locations

Analysis of antenna locations has been limited to a perfunctory review, inasmuch as antenna contours are not available. The antenna configuration shown in Reference 2 generally corresponds to those used on operational high-performance aircraft, with the exception of the MSBLS antenna.

Location of the MSBLS antenna on the upper nose section forward of the cockpit might cause some blanking of signals. However, it appears that the attitude of the Orbiter is "nose-down" for most of the approach phase. Landing flare manuevers with possible signal blanking would occur only during the last few seconds of the approach, when the Radar Altimeter would be used as the primary landing aid.

Signal attenuation due to heat shield coating of antenna surfaces might degrade the capabilities of the aeroflight communications and RF-NavAid systems. However, insufficient information is currently available to properly evaluate this factor.

7.3 SUMMARY AND CONCLUSIONS

A review of the communications and tracking factors for the Space Shuttle Orbiter's Aeroflight profile encompassed analyses of functional capabilities related to doppler and doppler-rate frequency shifts, differential doppler due to signal multipath, and location of subsystem antennae on the Orbiter. The analyses included the UHF/ATC, TACAN, Microwave Landing System and the Radar Altimeter.

Based upon the equipment specifications currently available, it would appear that none of the four systems will be adversely affected by range-rate or deceleration factors associated with the aeroflight profile. Spectral differential doppler due to signal multipath will not degrade UHF/ATC or TACAN performance.

The adequacy of antenna locations on the Orbiter cannot be sufficiently determined due to unknown factors related to heat shield coatings. It is recommended that additional analyses and tests of this aspect of the aeroflight RF-equipment functions be undertaken.

7.4 REFERENCES

(1) "Space Shuttle Orbiter Communications and Tracking Subsystem Configuration Description," LBJ Space Center, EE7-73-431 of November 1973.

(2) "Data for Tracking and Communications Systems Design Analysis," LBJ Space Center, FM4/Flight Performance Branch Memorandum FM42 (74-37) dated May 1, 1974.

(3) R. H. French, "Analysis of Differential Doppler Encountered in Radio Communications to an Aircraft or Re-Entering Spacecraft," IEEE Transactions submittal.

(4) J. N. Birch and R. H. French, "Definition of Multipath/RFI Experiments for Orbital Testing with a Small Applications Technology Satellite," NASA Contractor Report NASA-CR-128717, Magnavox Company Report ASAO-PR20441-8, of 1 December 1972.

8.0 SHUTTLE PN ACQUISITION DESIGN ANALYSIS

8.1 INTRODUCTION

This report presents the results of a study made by The Magnavox Company's Advanced Systems Analysis Office concerning the Shuttle Orbiter relay forward link. The link incorporates the Tracking and Data Relay Satellite System (TDRSS) to transmit uplink command and digital voice to Orbiter from the earth. In conformance with the guidelines set by the CCIR of the ITU on the maximum flux density at the earth's surface by emissions from space, the TDRSS-to-Orbiter link will be required to employ spread spectrum techniques. This study addresses the problem of acquiring and tracking a direct sequence pseudonoise (PN) code which has been phase shift keyed (PSK) onto a carrier along with the uplink data.

Several factors affect the analysis of the PN receiver. They are:

- Up to ±60 kHz of doppler shift on the carrier
- The use of Manchester coding on the uplink
- The low energy per symbol
- The length of the PN code required
- The chip rate of the PN code required
- The multiple bit rates to be accommodated.

The most damaging of these are the restrictions on the code. It will be seen in Section 8.2 that these restrictions do not allow us to take full advantage of the code properties. To be a bit more specific, the flux density requirements dictate a chip rate of at least 10 Megachips per second and a code length of at least 2047, whereas the bandwidth limitations of the system limit the chip rate to roughly 20 Megachips per second. This bounds the sync time.

Due to the desirability of having Orbiter be as autonomous as possible it was deemed necessary to be independent of any doppler correction on the ground, and so the full doppler range must be taken into account. Also Orbiter would like to receive data or not without affecting the PN acquisition scheme.

All of the above considerations severaly limited the receiver design. The one chosen is thought to be the best compromise among all parameters.

The major results of the study are summarized as follows:

- Partial code processing is mandatory due to data and doppler.
- An adaptive threshold for coarse PN sync is required.
- 1 to 7 seconds are required on the average for coarse sync.
- Total sync time is about 10 seconds.

8.2 PN EPOCH SYNCHRONIZATION

8.2.1 System Description

In the analysis found below we will present the performance of circuits that can be used to align a PN code which is modulated by binary data and which has associated with it a doppler shifted carrier. We will begin by giving a short tutorial on the general method of synchronizing a PN code and then proceed to bring into play the practical factors which dictate modifications to the general method.

A PN code is an easily generated (n stage shift register with appropriate feedback) string of symbols, called chips, which have properties very similar to a random set of symbols. When multiplied by lower rate data the resulting spectrum is essentially that of the code, hence it is spread relative to the data spectrum. The receiver removes the code by re-multiplying the product above by a locally generated replica of the code. When aligned correctly the code is squared, giving all ones, and thus removed. The main problem is to align the two codes.

A PN synchronizer seeks to "recognize" the code alignment by making use of its autocorrelation function. It is well known that the peak to null ratio of this function is N, i.e., the length of the code ($N = 2^n-1$). Since N is large the output of the correlator rises enough when close to perfect sync to trigger threshold circuits. A fine tuning is then done to get closer to the peak.

Basically, then, one needs to slip the local code by some amount, correlate, check the threshold, and if it is not triggered, repeat the process. Somewhere along the line the code will align sufficiently to stop the process. Data detection can then take place.

A common circuit to implement the above process is shown in Figure 8.1a. The correlator consists of the multiplier and the bandpass filter. The circuit captures power in the incoming signal. This power is proportional to the code alignment (see reference 1 and Appendix 8.A) and so after accumulating enough signal in the low pass filter to "beat" the noise, the threshold detector can be "fired".

Now if the bandpass filter in Figure 8.1a is implemented by an integrate and dump bandpass filter so that the low pass filter is replaced by a sample accumulator, one has an easily implementable PN synchronizer with all timing derived at the receiver (Figure 8.1b). Note that Figure 8.1b merely weights the samples by the impulse response of the bandpass filter. In general uniform weighting (I&D) is optimum, however, the analysis in Section 8.2.2 is still applicable with the weighting taken into account. Hereafter when referring to Figure 8.1 we will assume uniform weighting.

8.2.2 Analysis

Figure 8.1 is a serial correlator to obtain a PN epoch synchronization to within a 1/4 chip of the PN sequence. The received signal is a constant amplitude carrier which is bi-phase modulated by a PN sequence and Manchester coded data, and its frequency can be offset from the carrier frequency f_o by as much as $f_d = \pm 60$ kHz.

The synchronization scheme discussed above is capable of operation either "with" or "without" data modulation on the PN sequence.

The synchronizer tests the first cell of the time uncertainty to verify the presence of correct code alignment. If a positive indication (threshold detection) occurs that a code alignment is achieved, a

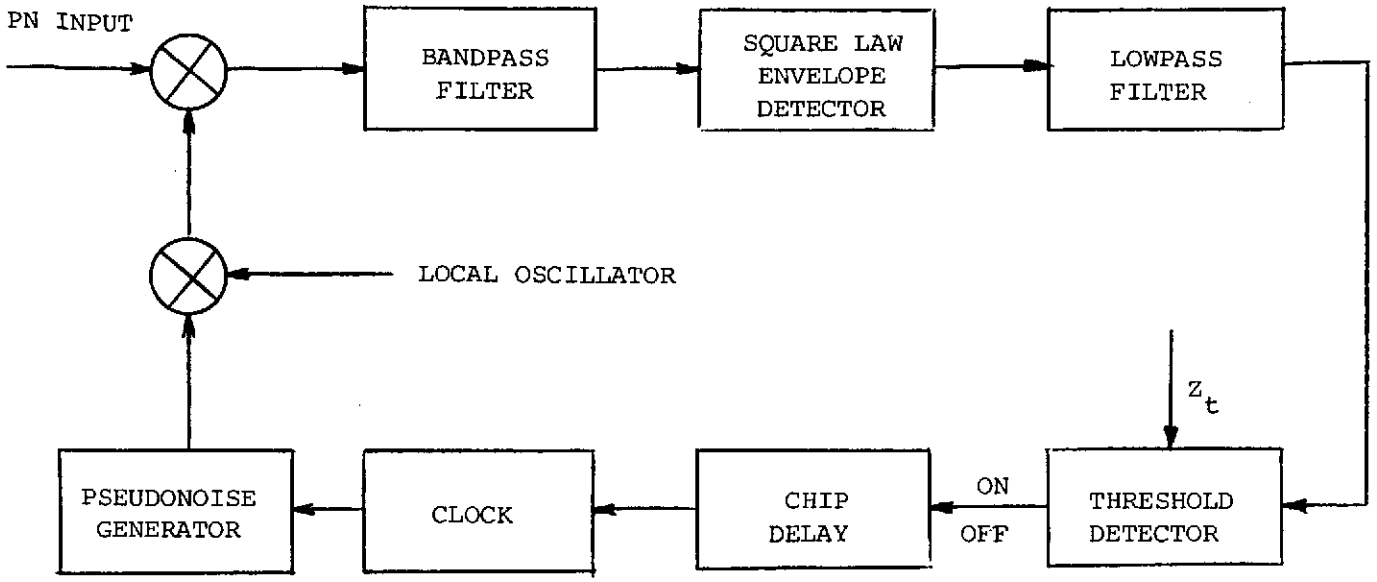

FIGURE 8.1a GENERIC PN SYNCHRONIZER

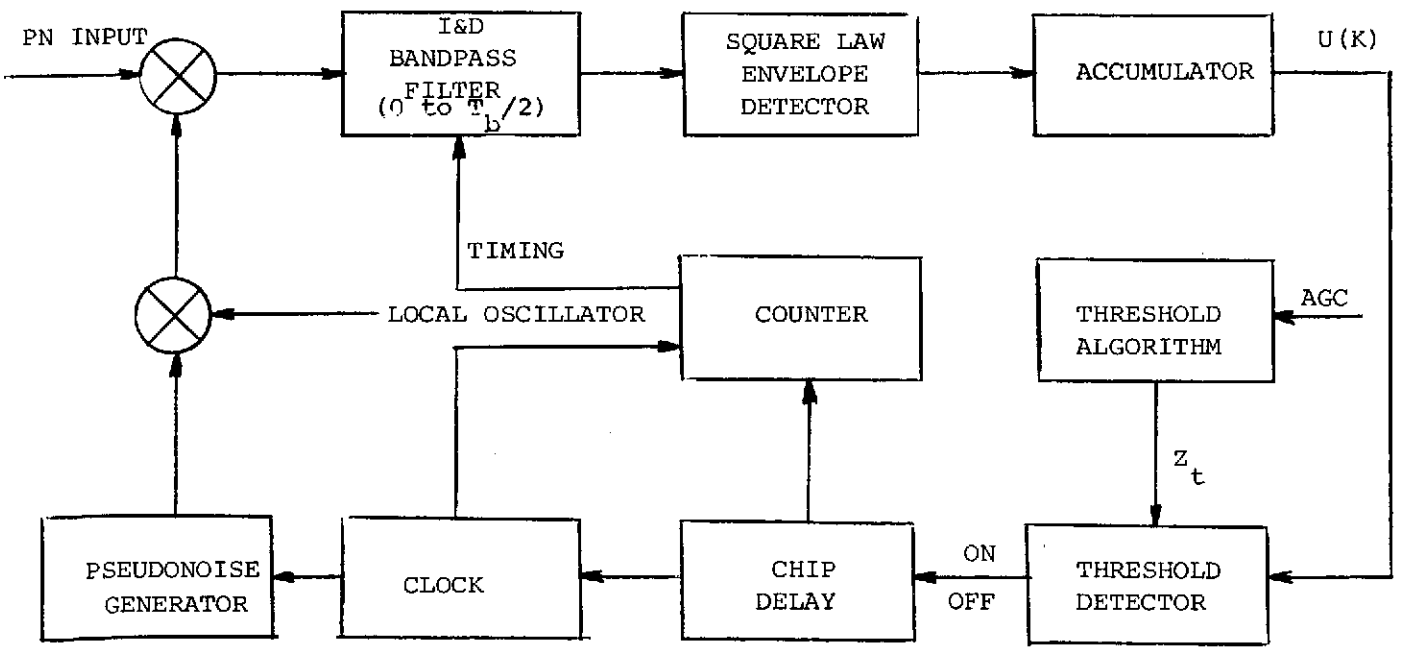

FIGURE 8.1b I&D PN SYNCHRONIZER

tracking circuit is triggered and the time cell is continuously tested. If, however, the test result does not indicate a code alignment the next cell is tested.

We assume that the Pseudonoise Generator (PNG) is a linear feedback shift register (FSR) of n stages, so that the length or period of the sequence is $2^n - 1 \triangleq N$. The rate of this sequence is assumed to be greater than $R_N \triangleq 10$ Mchips/sec. A "bit" in this report will be a received symbol and can be 216, 96, 72, and 32 kilobits per second.

Note from Figure 8.1 that the time required to test one cell is given by $\frac{KT_b}{2}$, where T_b is the time duration identical to "a bit time duration". The choice of $T_b/2$ as the integration time is based on the results of Appendix 8.A and maximizes the signal-to-noise ratio out of the integrator. This choice is not only optimum, but also it will further simplify the problem of re-establishing the "lost synchronization". That is, the sync circuit of Figure 8.1 can be used for sync recovery purposes without resorting to a separate system.

Since K is the number of integrations performed for testing a time cell, the determination of this constant can be obtained when the probability of sync detection and false alarm probability of testing a cell is specified. A false sync probability will also have to be considered.

The "uncertainty time" is the PN sequence period. Normally, the uncertainty time divided by the PN sequence chip duration constitutes the number of cells to be tested. In our situation, however, we have decided to test a 1/2 cell size (i.e., 1/4 chip misalignment) to prevent a large degradation when the received code and the local code are more than a quarter chip out of phase. Now consider the detailed analysis.

The incoming frequency is reduced to IF, integrated over a bit duration, and dumped. Each integrated and dumped result is square law envelope detected, accumulated K times, and the result is compared with a threshold set by the false alarm probability specification. Note that all timing requirements are provided from the PN clock. The integrator reset timing as well as the sampling clock pulse for the "accumulator" output are easily derived from the PN clock, and is independent of bit synchronization.

Let the incoming waveform be represented by

$$r(t) = AS(t)D(t) \cos\left[(\omega_o - \omega_{IF} - \omega_d)t - \phi\right] + n_W(t) \qquad (8.1)$$

where

A = received signal amplitude

$S(t)$ = incoming PN sequence waveform, $(1,-1,1,\ldots,)$

$D(t)$ = bi-polar data sequence (this data may or may not be present during the sync acquisition time)

ω_o = S-band carrier frequency in radians

ω_{IF} = the intermediate frequency in radians

ω_d = Doppler frequency offset in radians

ϕ = random phase associated with the carrier

$n_W(t)$ = zero-mean white Gaussian noise with power density $N_0/2$ Watts/Hz (two-sided)

The PN'ed local oscillator is given by $2S(t+\tau) \cos(\omega_o t - \theta)$ where θ is a random phase associated with the local oscillator, hence ignoring double frequency terms gives

$$AS(t)S(t+\tau)D(t) \cos\left[(\omega_{IF}+\omega_d)t - \psi\right] + 2n_W(t)S(t+\tau) \cos(\omega_o t - \theta)$$

$$= y_c(t) \cos \omega_{IF} t - y_s(t) \sin \omega_{IF} t, \qquad (8.2)$$

where

$$y_c(t) = A\, S(t)S(t+\tau)D(t)\cos(\omega_d t-\psi) + 2n_c(t)\, S(t+\tau)\cos(\omega_o t-\theta) \tag{8.3}$$

and

$$y_s(t) = A\, S(t)\, S(t+\tau)D(t)\sin(\omega_d t-\psi) + 2n_s(t)\, S(t+\tau)\sin(\omega_o t-\theta) \tag{8.4}$$

where

$$n_w(t) = n_c(t)\cos\omega_{IF}t - n_s(t)\sin\omega_{IF}t$$

$$\psi \triangleq \theta-\phi$$

The quadrature outputs $y_c(t)$ and $y_s(t)$ are then bandpass integrated and dumped. Carrying out the integrations indicated, we have

$$\begin{aligned} u_{ci} &\triangleq \int_0^{T_b/2} y_c(t)dt \\ &= A\int_0^{T_b/2} S(t)S(t+\tau)D(t)\cos(\omega_d t-\psi)dt \\ &\quad + 2\int_0^{T_b/2} S(t+\tau)n_c(t)\cos(\omega_o t-\theta)dt \\ &= M_{ci} + n_{ci} \end{aligned} \tag{8.5}$$

where

$$M_{ci} \triangleq A\int_0^{T_b/2} S(t)S(t+\tau)D(t)\cos(\omega_d t-\psi)dt \tag{8.6}$$

The noise term in (8.5) is given by

$$n_{ci} \triangleq 2\int_0^{T_b/2} S(t+\tau)n_c(t)\cos(\omega_o t-\theta)dt \tag{8.7}$$

which is a zero-mean Gaussian random variable with variance $\sigma^2 = N_o T_b/2$.

We will denote a Gaussian random variable by the following notation:

$$G(\text{mean, variance}) \tag{8.8}$$

so that

$$n_{ci} = G(0, N_o T_b/2) \tag{8.9}$$

Similarly,

$$u_{si} = \int_0^{T_b/2} y_s(t)dt$$

$$= M_{si} + n_{si} \tag{8.10}$$

where

$$M_{si} \triangleq A \int_0^{T_b/2} S(t)S(t+\tau)D(t) \sin(\omega_d t - \psi)dt \tag{8.11}$$

and

$$n_{si} \triangleq G(0, N_o T_b/2) \tag{8.12}$$

It is therefore seen that

$$u_{ci} = G(M_{ci}, \sigma_b^2) \tag{8.13a}$$

$$u_{si} = G(M_{si}, \sigma_b^2) \tag{8.13b}$$

where

$$\sigma_b^2 \triangleq N_o T_b/2 \tag{8.13c}$$

The decision variable U(K) is given by the envelope squared, summed K times, i.e.,

$$U(K) = \sum_{i=1}^{K} (u_{ci}^2 + u_{si}^2) \tag{8.14}$$

Since u_{ci} and u_{si} are statistically independent, and, further, knowing that the sum of two statistically independent noncentral Chi-square variables is also a noncentral Chi-square variable, the "decision" random variable U(K) is a noncentral Chi-square variable with 2K degrees of freedom.

The probability density function (pdf) of (K) is therefore given[2] by

$$p_{sn}(U) = \frac{1}{2\sigma_b^2}\left(\frac{U}{\lambda_b^2}\right)^{(K-1)/2} \exp - \left[\frac{\lambda_b^2+U}{2\sigma_b^2}\right] I_{K-1}\left(\frac{U\lambda_b}{\sigma_b^2}\right) \tag{8.15}$$

where λ_b^2 is the "noncentrality parameter" given by

$$\lambda_b^2 = \sum_{i=1}^{K} (M_{ci}^2 + M_{si}^2) \tag{8.16}$$

Let

$$Z = U/\sigma_b^2 \tag{8.17}$$

Then the pdf of this normalized random variable is given by

$$p_{sn}(Z) = \frac{1}{2}\left(\frac{Z}{\nu}\right)^{(K-1)/2} \exp\left(-\frac{Z}{2} - \frac{\nu}{2}\right) I_K(\sqrt{\nu Z}) \tag{8.18}$$

where

$$\nu \triangleq \lambda_b^2/\sigma_b^2 = \frac{KA^2nT_c}{N_o}\ \overline{\rho_n^2(\tau)} \tag{8.19}$$

$$= 2K\left(\frac{E}{N_o}\right)\overline{\rho_n^2(\tau)} \tag{8.20}$$

$$= K\,(SNR) \tag{8.21}$$

where K is the number of integrations performed, T_c is the chip width, $E = A^2nT_c/2$ is the energy per integration, $\rho_n^2(\tau)$ is the equivalent PN autocorrelation function as a result of partial code processing of n chips per integration (see Appendix 8.A) and $\overline{\rho_n^2(\tau)}$ is its mean. Note that ν is also the noncentrality parameter of the normalized noncentral Chi-square variable Z with 2K degrees of freedom.

When the signal is assumed absent, Z has a central Chi-square distribution with 2K degrees of freedom, and the pdf is then given by

$$p_n(Z) = \frac{1}{2^K \Gamma(K)} Z^{K-1} \exp(-Z/2). \tag{8.22}$$

Let Z_T be the normalized threshold. Then the false alarm probability P_{fa} is given by

$$P_{fa} = \int_{Z_T}^{\infty} p_n(Z)dZ = 1 - \int_0^{Z_T} p_n(Z)dZ$$

$$= 1 - \int_0^{Z_T} \frac{1}{2^K \Gamma(K)} Z^{K-1} \exp(-Z/2)dZ$$

$$= 1 - I\left(\frac{Z_T}{2\sqrt{K}}, K-1\right) \tag{8.23}$$

where I(u,v) is Pearson's form of the incomplete Gamma function.[3]

The above P_{fa} assumes no signal. There is, however, another "no signal" case, namely, when the relative code alignment is more than a chip but less than a full code length. Some caution must be used here. Consider a PN code of length N = 2047. From the results of Appendix 8.A if we look at the whole code, i.e., integrate from zero to NT_c, where T_c is the chip duration, then when the code misalignment is more than a chip we have $\rho^2 = 2047^{-2}$. However when we process the code as in this analysis we do not have as low a number. In fact the data in Appendix 8.A shows that $\overline{\rho^2}=4.8^{-2}$ is actually the case. The vast discrepancy in the ρ's is of concern when we are calculating false alarm probability since <u>there is still signal present</u>.

Now the question is whether or not this signal can be neglected. The answer is that if it is negligible relative to the noise then it can be ignored, i.e., equation (8.23) holds. If not then the "clutter noise" must be considered.

The above facts are brought out to caution a potential designer to the pitfalls of partial correlation. One can easily visualize the case where problems can occur, e.g., since 4.8^2 represents only 14 dB power variation, as opposed to the 64 dB for the whole code, there is a very real possibility that a 14 dB variation elsewhere could cause the signal to trigger the threshold and thus not be negligible relative to the noise. Some factors which could do this are

- o correlation worst case design
- o antenna gain variation of the S-Band omni's (null depths)
- o TDRS antenna gain variation
- o variation is slant range from TDRS to Shuttle
- o TDRS power amplifier output variation (hot transmitter)
- o doppler loss variation
- o system loss variations (polarization, coupling, etc.)
- o minimum EIRP system design.

Based on the above analysis the procedure we will follow will be to calculate the probability of detection when within a quarter of a chip, the false alarm assuming no signal, and lastly we will consider the effect on these specifications when signal is present, but the code is not within the quarter chip alignment. This will be called the probability of false sync case.

Now turning to the computation of the probability of detection P_D, it can be shown[2] that

$$P_D = \int_{Z_T}^{\infty} \frac{1}{2} (Z/\nu)^{(K-1)/2} \exp\left(-\frac{Z}{2} - \frac{\nu}{2}\right) I_{K-1}(\sqrt{\nu Z})\, dZ \qquad (8.24)$$

This integral will result in the following:

$$P_D = Q_K(\sqrt{\nu}, \sqrt{Z_T}) \qquad (8.25)$$

where

$$Q_K(\alpha,\beta) \triangleq \int_{\beta}^{\infty} t\left(\frac{t}{\alpha}\right)^{K-1} \exp -\left(\frac{t^2+\alpha^2}{2}\right) I_{K-1}(\alpha t)\, dt \qquad (8.26)$$

is the generalized Marcum Q-function. (We shall see later that it is very well approximated by an error function expression.)

We immediately recognize then that we have a standard non-coherent radar problem, and so draw heavily from previously published result. Using references 4 or 5 we obtain Figure 8.2.

8.2.3 Determination of K, The Number of Integrations for a Given (P_D, P_{fa})

From the JSC document[6] we can calculate the SNR in the integration period as follows:

$$\frac{2E}{N_o} = \frac{2P_r nT_c}{N_o} = \frac{2P_r}{2N_o R_b} = \frac{P_r}{N_o R_b} \qquad \text{(split phase assumed)} \qquad (8.27)$$

where

P_r = EIRP - 192.5 dB

N_o = -204.3 dBW/Hz

$R_b = 10 \log_{10} (216 \times 10^3)$ = 53.4 dB-Hz (worst case symbol rate)

Thus the available (pre-detection) SNR per interval is given by

$$\text{SNR} = \text{EIRP(dBW)} - 41.6 + 10 \log \overline{\rho_n^{\,2}(\tau)} \qquad (8.28)$$

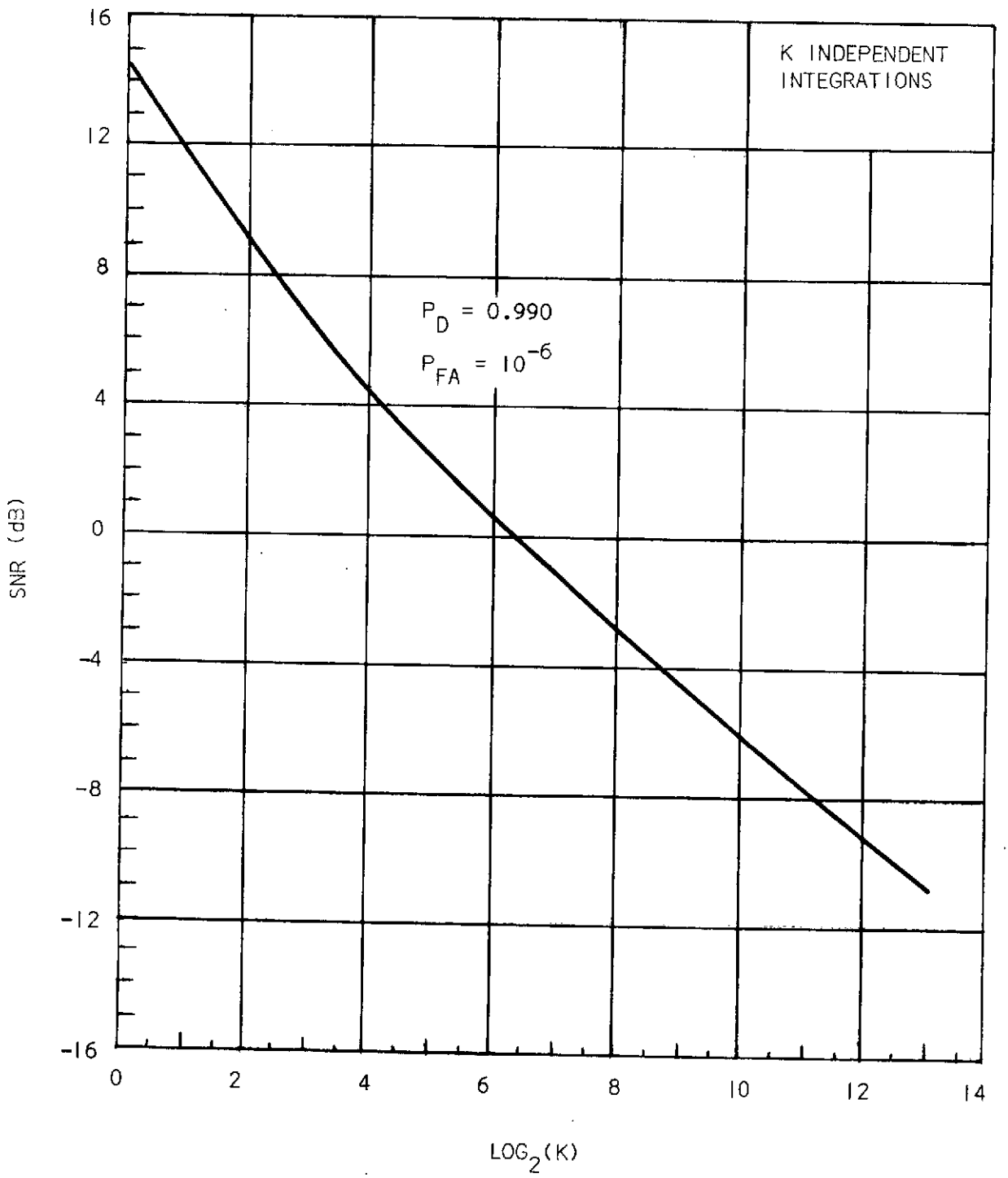

FIGURE 8.2 SENSITIVITY RELATED TO NUMBER OF INTEGRATIONS FOR $P_D = 0.99$ AND $P_{FA} = 10^{-6}$

Once EIRP is given and $\overline{\rho_n^2(\tau)}$ is calculated, SNR is obtained and then the corresponding value of K is determined from the curve in Figure 8.2.

From (8.25) we may write for K = 1

$$P_D = Q_1(\sqrt{SNR}, \sqrt{Z_T}) \tag{8.29}$$

Now for $|\tau| \leq T_c/4$ per Appendix 8.A

$$\overline{\rho_n^2(\tau)} = \left(1 - \frac{\tau}{T_c}\right)^2 \left[\left(\frac{\sqrt{6}}{\omega_d n T_c}\right)\left(1 - Sa(\omega_d n T_c)\right) - \frac{1}{2} Sa^2\left(\frac{\omega_d n T_c}{2}\right)\right] \tag{8.30}$$

where $Sa(x) = \frac{\sin x}{x}$. (8.31)

Assuming the worst case, namely, that the two PN sequences are 1/4 chip out of phase, $f_d = \pm 60$ kHz, and noting that $nT_c = T_b/2$, where T_b is the bit interval

$$\overline{\rho_n^2(T_c/4)} = 0.28 \tag{8.32}$$

Thus

$$10 \log \overline{\rho_n^2(T_c/4)} = -5.6 \text{ dB} \tag{8.33}$$

Therefore the SNR due to worst case doppler and code misalignment is

$$\gamma = (SNR)_{\text{worst case}} = EIRP - 47.2 \tag{8.34}$$

We are now ready to specify K as a function of EIRP corresponding to $P_D = 0.99$ and $P_{fa} = 10^{-6}$. The result is summarized in the following table.

TABLE 8.1

ACCUMULATION NUMBER

EIRP (dBW) (Assumed)	γ (db)	$\log_2 K$ (from Fig. 3)	[K] (computed)
44.4	-2.8	8	256
43.4	-3.8	8.6	386
42.4	-4.8	9.2	590
41.4	-5.8	9.8	905
40.4	-6.8	10.45	1400

This Table corresponds to $P_D = 99\%$, $P_{fa} = 10^{-6}$

8.2.4 Computation of Sync Acquisition Time

During the sync acquisition time period we assume that a PN sequence of period $N = 2^n-1$ (n is the number of stages in the FSR) is either modulated or unmodulated by the data sequence. The acquisition scheme proposed in this study works in either case.

The time required for a test of one cell to decide upon the presence or absence of an aligned PN code sequence is KT, where $T \triangleq nT_c$.

Let T_u be the uncertainty time. Then $L = T_u/T_c$ is the number of cells to be tested, where T_c is the chip duration. In our situation we have decided to test 1/2 cell size to prevent a large degradation when the received code and the local code are 1/2 chip out of phase; thus, L = 2N.

Let T_d be the average time required to test and reject a cell not containing the proper code phasing. Although two adjacent cells would conceivably contain the signal (due to 1/2 chip delay increments of the code phasing during search), we will assume that only one contains signal. The probability $P(\ell)$ that exactly ℓ tests ($\ell = 0,1,2,\ldots, L-1$) will be required before a positive decision will be made is uniform, so that $P(\ell) = 1/L$. This assumption is tantamount to saying that each time cell is equally likely to contain "signal". Thus, the average time to arrive at the cell containing the proper code alignment for the first time is given by

$$E\{t_a\} = \sum_{\ell=0}^{L-1} \ell T_d P(\ell) = (L-1)T_d/2 = LT_d/2 \text{ for } L>>1 \qquad (8.36)$$

We now need to consider the time "lost" due to false dismissals. We will assume a search process that requires a scan of the entire uncertainty region and returns to the origin of the initial search if all cells tested are dismissed. The average time lost due to false dismissals is given by

$$E\{t_{fd}\} = T_d L(1-P_{fd}) \sum_{i=1}^{\infty} i[P_{fd}]^i$$

$$= T_d L \left(\frac{P_{fd}}{1-P_{fd}}\right) \tag{8.37}$$

where

P_{fd} = probability of false dismissal

$1-P_{fd}$ = probability of detection

Therefore, the average time to synchronize the code sequence is given by

$$E\{T_{sync}\} = E\{t_a\} + E\{t_{fd}\}$$

$$= \frac{LT_d}{2} + T_d L \left(\frac{P_{fd}}{1+P_{fd}}\right)$$

$$= \frac{LT_d}{2} \left(\frac{1+P_{fd}}{1-P_{fd}}\right) \tag{8.38}$$

Let us now relate the "cell test time" KT to the time required for dismissal, T_d. Since each test takes KT time duration, T_d is the average number of "testing" times, T, until a false or correct decision is made. Thus,

$$T_d = KT \quad (1-P_{fa})[1+2P_{fa}+3P_{fa}^2+\ldots+jP_{fa}^{j-1}+\ldots]$$

$$= KT\ (1-P_{fa}) \sum_{j=1}^{\infty} j\ (P_{fa})^{j-1}$$

$$= KT\ (1-P_{fa}) \sum_{j=1}^{\infty} \frac{d}{dP_{fa}} (P_{fa})^j$$

$$= KT\ (1-P_{fa}) \frac{d}{dP_{fa}} \sum_{j=1}^{\infty} (P_{fa})^j$$

$$= KT\ (1-P_{fa}) \frac{d}{dP_{fa}} \left(\frac{P_{fa}}{1-P_{fa}}\right)$$

$$= KT\ (1-P_{fa}) \left(\frac{1}{1-P_{fa}}\right)^2$$

$$= \frac{KT}{1-P_{fa}} \tag{8.39}$$

where P_{fa} is the false alarm probability.

We thus obtain the expected time to synchronize as follows:

$$E\{T_{sync}\} = \frac{LT_d}{2} \left(\frac{1+P_{fd}}{1-P_{fd}}\right)$$

$$= \frac{L}{2} \frac{KT}{1-P_{fa}} \left(\frac{1+P_{fd}}{1-P_{fd}}\right)$$

$$= \frac{NKT}{1-P_{fa}} \left(\frac{1+P_{fd}}{1-P_{fd}}\right) \tag{8.40}$$

In terms of data rate R_b, we have since $T = 1/2R_b$

$$E\{T_{sync}\} \quad \frac{NK}{R_b(1-P_{fa})} \left(\frac{1+P_{fd}}{1-P_{fd}}\right) \doteq N[KT_b/2] \tag{8.41}$$

for P_{fd} and P_{fa} small relative to 1.

Since we require

$$P_{fa} = 10^{-6},\ P_D = 1 - P_{fd} = 0.99$$

and

$$T_b = (216 \times 10^3)^{-1} \text{ sec.}$$

(8.41) may be written as

$$E\{T_{sync}\} = NK\ (2.3 \times 10^{-6}) \text{ sec.} \tag{8.42}$$

$$= 1.023 \times 2.3 \times 10^{-3} K \text{ sec. for n = 10 stages} \tag{8.43a}$$

$$= 2.047 \times 2.3 \times 10^{-3} K \text{ sec. for n = 11 stages} \tag{8.43b}$$

Using the K values from Table 8.1, we compute the average sync time as a function of EIRP. The result is given in Table 8.2 below.

TABLE 8.2

AVERAGE COARSE SYNC TIME

$N = 2^n - 1$	EIRP (dBW)	K	$E\{T_{sync}\}$ in Sec
1023 (n=10)	44.4	256	0.6
2047 (n=11)			1.2
1023 (n=10)	43.4	386	0.9
2047 (n=11)			1.8
1023 (n=10)	42.4	590	1.4
2047 (n=11)			2.8
1023 (n=10)	41.4	905	2.1
2047 (n=11)			4.2
1023 (n=10)	40.4	1400	3.3
2047 (n=11)			6.6

The average sync time shown in Table 8.2 is plotted in Figure 8.3 as a function of EIRP for N = 1023 (N = 10 stages) and N = 2047 (n = 11 stages).

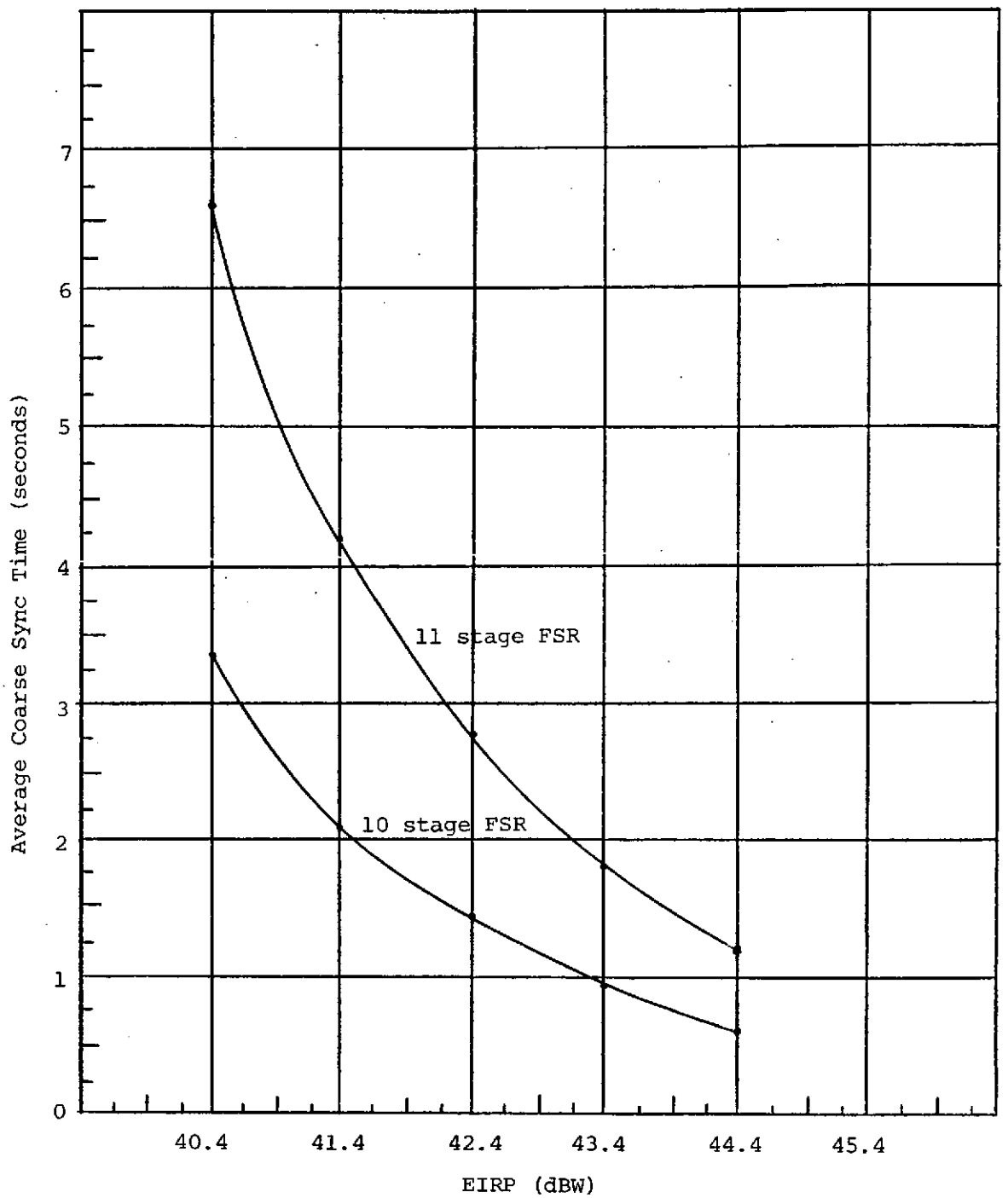

Figure 8.3 AVERAGE COARSE SYNC TIME VS. EIRP

It is seen that the determination of K, the number of integrations, should be made after considering a degradation margin of EIRP to insure a reliable operation of the sync system. An example may illustrate this point. Assume that the available EIRP is 44.4 dBW. If no degradation is assumed, K = 256 (from Tables 8.1 or 8.2), that is, a cell decision variable is obtained as a result of summing 256 integrations. In this system, the average sync time is 1.2 sec for an 11-stage FSR.

If, however, an EIRP degradation of 3 dB is a probable occurrence, the accumulator design should be based on K = 905 and we should expect the average sync time to be 4.2 sec. Caution is again warranted here, however, since raising K to 905 increases the signal level when the codes are uncorrelated by 5 dB, i.e., our 14 dB margin has now shifted to 9 dB. This new margin is getting too low to reliably adapt to system fluctuations, i.e., designing for worst case is jeopardizing the best case! We shall soon see a way of alleviating this difficulty.

As a final note to this section the maximum sync time will be roughly twice the average due to the essentially uniform density.

8.2.5 The Probability of False Synchronization

There is one more subject which must be addressed before leaving the subject of coarse sync, namely, the probability of locking to an off correlation peak of the PN code. As was mentioned earlier, due to the partial code processing (coherently over n chips and then noncoherently over K integrations) the level of $\overline{\rho_n^2(\tau)}$ is only 2/n (the factor of 2 is the degradation in the peak due to data) down from the full correlation peak with doppler being assumed to effect $\overline{\rho_n^2(\tau)}$ equally over τ, a good assumption per Appendix 8.A.

The threshold Z_T was fixed based on the no signal case giving the false alarm probability, and then K was chosen to produce the specified probability of detection. Consder the case of $\tau \geq T_c$. Here we have a maximum level of 1/n at integer multiple slips. This will be assumed as worst case along with $f_d = 0$. The probability of false sync then is given by equation (8.24).

$$\overline{\rho_n^2(T_c)} = \frac{1}{n} = \frac{T_c}{nT_c} = \frac{T_c}{T_b/2} = \frac{1}{23} \text{ (-14 dB)} \tag{8.44}$$

Thus the single pulse SNR for this case,

$$\gamma = \text{EIRP} - 41.6 - 14 = \text{EIRP} - 55.6. \tag{8.45}$$

Since for K's in the hundreds the distribution out of the detector becomes very Gaussian via the Central Limit Theorem. Equation (8.24) is well approximated by

$$P_{fs} = \frac{1}{2} \operatorname{erfc} \left(\frac{(Z_t - b)\sqrt{K}}{\sqrt{2[4(1+\text{SNR})/\pi - b^2]}} \right) \tag{8.46}$$

(7)

where

$$b = e^{-\text{SNR}/2} \left[(1+\text{SNR}) I_0\left(\frac{\text{SNR}}{2}\right) + \text{SNR}\ I_1\left(\frac{\text{SNR}}{2}\right) \right] \tag{8.47}$$

and I_i is the modified bessel function of the first kind and of order i. Now Z_t and K being fixed leaves only SNR as a variable. Table 8.3 gives P_{fs} as a function of EIRP and K. Several K's were used to let the reader see the effect of overspecifying K for good P_d without regard to P_{fs}; P_{fa} was held at 10^{-6}.

TABLE 8.3

FALSE ALARM PROBABILITY

EIRP (dBW)	γ	P_{fs}				
		K = 256	K = 386	K = 590	K = 905	K = 1400
50.4	-10.8	4×10^{-4}	1×10^{-3}	3.2×10^{-3}	1.1×10^{-2}	4.1×10^{-2}
47.4	-13.8	2.8×10^{-5}	5×10^{-5}	1.2×10^{-4}	2.6×10^{-4}	6.8×10^{-4}
44.4	-16.8	6.2×10^{-6}	7.8×10^{-6}	1.2×10^{-5}	1.8×10^{-5}	4×10^{-5}
43.4	-17.8	3.8×10^{-6}	5×10^{-6}	7.8×10^{-6}	1.2×10^{-5}	1.8×10^{-5}
42.4	-18.8	3×10^{-6}	3.9×10^{-6}	5×10^{-6}	7×10^{-6}	1×10^{-5}
41.4	-19.8	2.4×10^{-6}	3×10^{-6}	3.9×10^{-6}	5×10^{-6}	7.8×10^{-6}
40.4	-20.8	2×10^{-6}	2.4×10^{-6}	3×10^{-6}	3.9×10^{-6}	5×10^{-6}

The conclusion to all of the above is that type of processing done here introduces a probability that sync will be declared when the codes are not aligned which cannot be ignored. As an example of the calculation, suppose we wished to design for the 41.4 dBW case so that K = 905 was necessary. If the signal level were actually 6 dB higher and we were off correlation then there would be a probability of false sync of roughly 2.4×10^{-4}. If the signal level rises even more then the P_{fs} would completely negate the sync operation because false syncs would dominate, i.e., the code cannot be recognized!

It is because of the above considerations that it is recommended that the threshold be made a function of the total input power via a noncoherent AGC as shown in Figure 8.1.

As a final note the sync times can be decreased if a multi-level threshold criterion is used or even a continuous one such as described in Reference 8. The decision to employ the more complex circuitry is dependent upon the value of sync time desired.

Also note that lower bit rates increase n and therefore lower P_{fs} with a concommitant increase in doppler loss. The 216 kbps is worst case.

8.3 FINE SYNC

Having covered all aspects of the coarse sync process we now turn to the fine sync process, that is, the procedure of bringing the code alignment to within a tenth of a chip or less. Since we are now within a quarter of a chip there are several possibilities for fine sync. All methods rely upon a continuous epoch tracker, for example, a delay lock loop[9] or a dither loop.[10] Noncoherent methods which do not make use of carrier phase lock can be used, however since there is very little degradation due to the code now, the suppressed carrier recovery loop may be used. It will lock provided the SNR is high enough and then this carrier reference and even bit estimation can be employed to coherently fine tune the PN alignment.

The following is considered to be the best approach to fine sync. Since the phase lock loop is very narrow compared to the data, it integrates over the whole code, thus we are now dealing with $\rho(\tau)$ and not $\rho_n(\tau)$ as in Section 8.2. Figure 8.4[1] shows the power spectrum seen by the loop if $\tau = T_c/4$. The loop will react to the main lobe since the others are at the code rate away from the carrier. The power in the main lobe is, per reference 1, $\rho^2(\tau)$ times the total. Since $\rho^2(\tau) \geq \rho^2(T_c/4)$

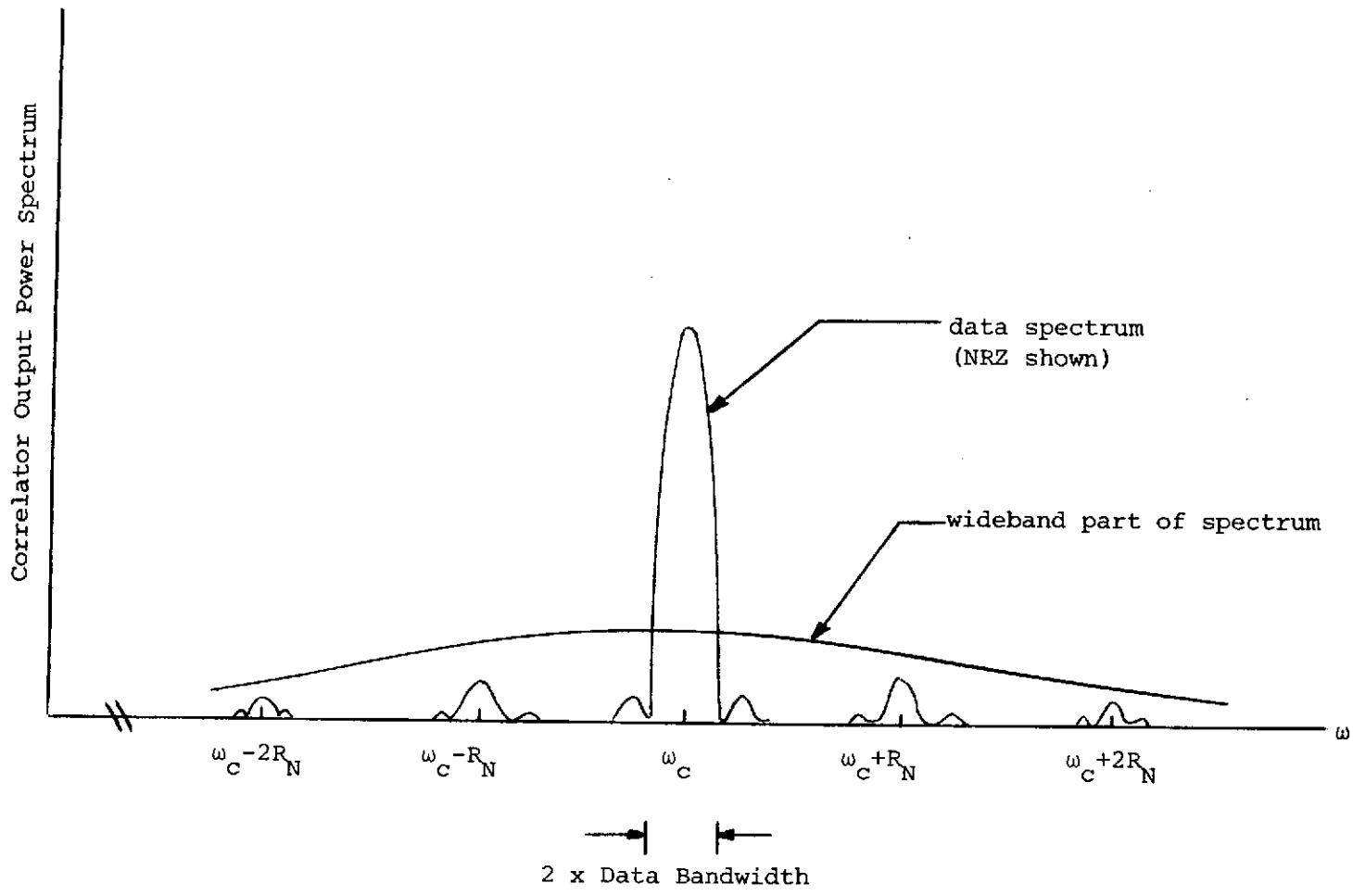

FIGURE 8.4 POWER SPECTRUM OF THE CORRELATOR OUTPUT FOR $\tau = T_c/4$

in this case there is less than 2.5 dB loss over $\rho^2(0)$. The rest of the spectrum appears as negligible white Gaussian noise. Also for $\tau < T_c/4$ the situation improves.

The result of the above insight is that within a few seconds after coarse sync, phase lock and bit sync occur (probably sooner since $\rho^2(T_c/2)$ represents a 6 dB loss and the loop will attempt to lock). We will then assume that the doppler is tracked out and that bit estimation is sufficient to remove the data from the fine tracker input. Actually a small loss will occur due to bit errors, but the tracker is not very sensitive to these since it has an extremely narrow bandwidth and so averages over many many bits.

The analysis below is for a delay lock loop as representative of what can be done.

Figure 8.5 shows a phase-coherent Delay Lock Tracking Loop system. The "coherent" carrier necessary for demodulation is assumed to be obtained by a squaring loop as indicated in the figure after course sync in Section 8.2 has been obtained.

As shown in Figure 8.5, the input waveform is represented by

$$r(t) = A\, S(t)D(t) \cos(\omega_c t - \phi) + n(t) \qquad (8.48)$$

where

$A^2/2$ = average signal power

$S(t)$ = bi-polar PN sequence, $1,-1,\ldots,$

ω_c = the "center" frequency which includes any residual Doppler shift

ϕ = uniform phase random variable $\varepsilon[0,2\pi]$

$n(t)$ = sample function of a white Gaussian noise process of power spectrum density $N_0/2$.

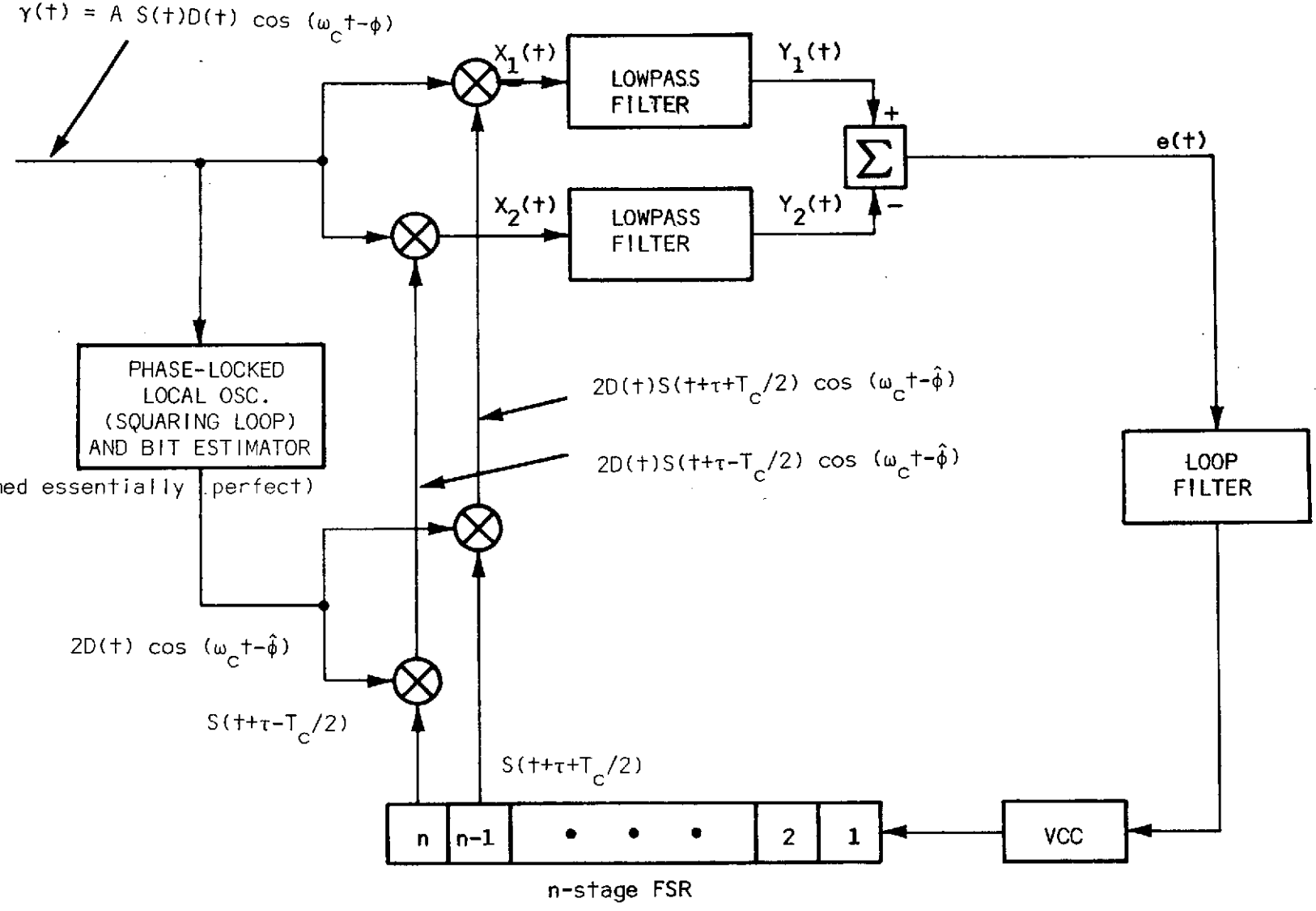

FIGURE 8.5 DELAY-LOCK TRACKING LOOP CONFIGURATION

From the figure,

$$x_i(t) = S(t)\, S(t-\tau \pm T_c/2) \cos(\phi-\hat{\phi}) + n_i(t) + \text{double frequency terms} \qquad (8.49)$$

$$i = 1,2$$

where

$2P_s \triangleq A^2$

τ = delay estimate of the local sequence

T_c = PN chip interval

$\hat{\phi}$ = phase estimate by the phase locked loop

$n_i(t)$ = noise terms

The double frequency terms are rejected by the lowpass filters. Due to the smoothing effect of the lowpass filters, we obtain

$$y_1(t) = \sqrt{P_s}\, \rho(\tau+T_c/2) \cos(\phi-\hat{\phi}) + n_1(t) \qquad (8.50)$$

and

$$y_2(t) = \sqrt{P_s}\, \rho(\tau-T_c/2) \cos(\phi-\hat{\phi}) + n_2(t) \qquad (8.51)$$

where

$\rho(\tau) = E\{S(t)S(t+\tau)\}$

= autocorrelation function of the PN sequence

The error signal e(t), which is the input to the "Loop Filter", is given by

$$e(t) = E(\tau) + n_o(t) \qquad (8.52)$$

where

$$E(\tau) \triangleq \sqrt{P_s}\, [\rho(\tau+T_c/2) - \rho(\tau-T_c/2)] \cos(\phi-\hat{\phi}) \qquad (8.53)$$

and

$$n_o(t) \triangleq n_1(t) - n_2(t) \qquad (8.54)$$

If we assume that carrier phase lock is achieved we may put

$$\phi = \hat{\phi}$$

and then we have

$$E(\tau) = \sqrt{P_s}[\rho(\tau+T_c/2) - \rho(\tau-T_c/2)] \tag{8.55}$$

which is plotted in Figure 8.6.

Thus we have

$$e(t) = E(\tau) + n_o(t) \tag{8.56}$$

$$= 2\sqrt{P_s}\left(\frac{\tau}{T_c}\right) + n_o(t) \tag{8.57}$$

Following the analysis method of Gill,[9] we will arrive at a tracking error expression given by

$$\sigma_\tau = T_c\sqrt{\frac{B_n N_o}{2P_s}}$$

$$= \frac{1}{R_N}\sqrt{\frac{B_n N_o}{2P_s}}\ ; \quad \frac{P_s}{N_o} \geq \left(\frac{P_s}{N_o}\right)_{\text{threshold}} \tag{8.58}$$

where

$\sigma_\tau^2 = E\{\tau^2\}$

$B_n \triangleq$ equivalent noise bandwidth of the loop

$R_N \triangleq$ PN chip rate

$\left(\frac{P_s}{N_o}\right)_{\text{threshold}} = 4.75\ p_\phi$

p_ϕ = loop frequency constant in rad/sec

$\simeq 2B_n$

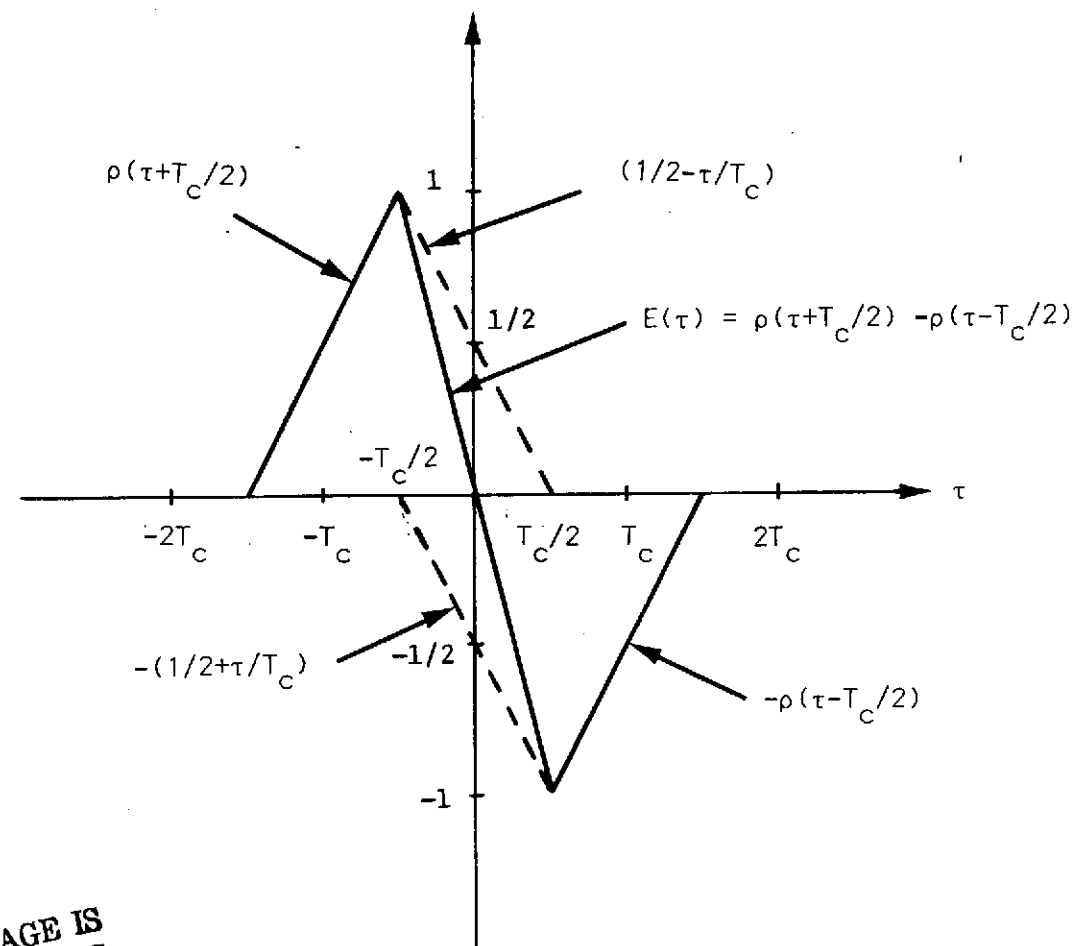

FIGURE 8.6 TRACKING ERROR SIGNAL VOLTAGE WAVEFORM OF THE DLTL

Example:

Let us express (8.58) as follows:

$$\sigma_\tau(\text{dB}) = -R_N(\text{dB}) + \frac{1}{2}\left[B_n(\text{dB}) - \frac{P_s}{N_o}(\text{dB}) - 3\right] \qquad (8.59)$$

Then, for the following assumptions:

$R_N = 10^7$ chips/sec = 70 dB

$B_n = 100$ (20 dB)

$\frac{P_s}{N_o} = 56.2$ dB (for EIRP = 44.4 dBW)

we obtain

$$\sigma_\tau = -87.6 \text{ dB} = 1.738 \times 10^{-9} \text{ sec}$$
$$= 1.738 \times 10^{-2}\ T_c;\ (T_c = 10^{-7})$$

This example indicates that the tracking error is less than a two-hundreth of one chip.

8.4 RE-ACQUISITION OF A LOST SYNC

When a loss of synchronization is detected, the task of re-establishing the synchronization in the shortest possible time is of paramount importance. Presumably the loss of synchronization occurs during the "data mode". Thus, a loss of sync is an event that occurs amid the normal tracking process. It is therefore reasonable to assume that the receiver clock is still within a few chips of the transmitted PN sequence.

The synchronization scheme discussed in Section 8.2 (Coarse Sync Scheme) can still be used for sync recovery purpose. In the sync recovery situation, the time uncertainty is not as great as that of initial synchronization. In fact, the time uncertainty would most likely be no more than a few cells (chips). The analysis pertaining to the sync recovery system is identical to that for the initial sync system treated in Section 8.2. The number K remains the same since (P_D, P_{fa}) remains the same. However, the average sync time is much smaller in the present case. Let us repeat the average sync time expression given in (8.40):

$$E\{T_{sync}\} = \frac{NKT}{1-P_{fa}} \left(\frac{1+P_{fd}}{1-P_{fd}}\right) \tag{8.60}$$

In this equation, N is the PN sequence period. Thus it is the "number of uncertainty cells". With this view we can write the average re-sync time as

$$E\{T_{resync}\} = \frac{N'KT}{1P_{fa}} \left(\frac{1+P_{fa}}{1-P_{fd}}\right) \tag{8.61}$$

where N' is the number of uncertainty cells which is expected to be a very small number compared to N.

Thus

$$N' << N \tag{8.62}$$

In real situations, whenever sync is lost, the PN clock may be retarded a few chips and then search. This would be a workable scheme, and the re-sync time estimation may be obtained by fixing N' which could be reasonably estimated through a simulation or actual experimentation. Of course if resync has not occurred within the total code uncertainty then the initial acquisition process would be employed.

8.5 CONCLUSION

In this report we have proposed and analyzed a synchronization scheme for acquiring PN sequence clock on the TDRSS-to-Orbiter link. The sync scheme is based on the worst case of a PN rate of 10 Mchips/sec modulating a 216 Kbps channel data rate, and the maximum doppler frequency range of ±60 kHz.

The synchronization circuit we have proposed is of the envelope detector type, and due to the high doppler frequency, integration is performed over one half of a channel bit time interval. This integration is then incoherently combined K times to "level up to" a SNR enough to insure the requirement of $P_D = 0.99$, $P_{fa} = 10^{-6}$, and $P_{fs} < 10^{-5}$.

The sync scheme is capable of initial acquisition as well as re-establishing a lost sync.

The average coarse sync times as a function of different EIRP's are given in a table. Analysis was provided for two different PN codes (10 and 11 stage FSR's).

As a result of the study it was noted that problems could exist when system power levels fluctuated over a wide range, roughly 10 dB, thus requiring an adaptive threshold.

For completeness, a brief discussion on the essential features of a code tracking loop was also given in this report, and it should be noted that the overall sync time will be the sum of the coarse PN sync and the carrier tracking lock times, i.e., the fine PN lock is instantaneous using the recommended scheme.

8.6 REFERENCES

(1) D. E. Cartier, "A Frequency Domain Approach to Shuttle PN Acquisition," NTC 1974 Conference Record, pp. 713-717.

(2) A. D. Whalen, Detection of Signals in Noise, Academic Press, New York (1971), Chapter 4.

(3) K. Pearson, Tables of the Incomplete -Function, Cambridge Univ. Press, London and New York, 1965.

(4) M. I. Skolnik, Introduction to Radar Systems, McGraw-Hill, 1962.

(5) R. S. Berkowitz, et. al., Modern Radar, John Wiley and Sons, 1965.

(6) Shuttle Orbiter/GSFC Communications and Tracking Interface Control Document, ICD-0D044, NASA Lyndon B. Johnson Space Center, LEC-1161, January 1974, p. 530.

(7) L. V. Blake, "A Guide to Basic Pulse Radar Maximum Range Calculation," Part 2, Naval Research Laboratory Document, 31 December 1970, AD-703 211.

(8) C. R. Cahn, "Spread Spectrum Applications and State-of-the-Art Equipments," Paper No. 5, AGARD-NATO Lecture Series No. 58 on "Spread Spectrum Communications," 28 May - 6 June 1973.

(9) W. J. Gill, "A Comparison of Binary Delay-Lock Tracking-Loop Implementations," IEEE Transactions on Aerospace and Electronic Systems, Vol. AES-2, No. 4, July 1966, pp. 415-424.

(10) H. P. Hartman, "Analysis of a Dithering Loop for PN Code Tracking," IEEE Transactions on Aerospace and Electronic Systems, Vol. AES-10, No. 1, January 1974, pp 2-9.

(11) B. H. Batson, "An Analysis of the Relative Merits of Various PCM Code Formats," Internal Note No. MSC-EB-R-68-S, NASA Manned Spaceflight Center, Houston, Texas, NTIS No. N70-35709, Nov. 1, 1968.

(12) D. E. Cartier, "Partial Correlation Properties of PN Codes and Their Use in PN Acquisition," to be published.

APPENDIX 8.A

In this Appendix we investigate the statistical properties of the quantity ν which was developed in Section 8.2 of the report. Recall that ν was defined by

$$\nu = \frac{\lambda_b^2}{\sigma_b^2} = \frac{1}{N_0 T} \sum_{i=1}^{K} (M_{ci}^2 + M_{si}^2) \tag{8.A.1}$$

The random variable ν is the signal-to-noise ratio at the input to the threshold detector, therefore we are interested in its expected value. Note that in (8.A.1) we have used T rather than $T_b/2$. The first item of business then is to determine the optimum value of T. Reference 1 would seem to indicate that $T_b/2$ is indeed the optimum value since it implies a filter at twice the bit rate of a Manchester coded signal and thus passes most of the power. However, since we are only integrating over part of the bit stream and then dumping, there is a question as to whether or not the power spectrum is still that wide. It turns out that it is, but the analysis below proves it also in the time domain.

Consider the case of perfect PN correlation and $\omega_d = 0$

$$I(T) = \frac{2\,\overline{M_{ci}^2}}{A^2 T} = \frac{2\,\cos^2\psi}{T} \int_0^T \int_0^T \overline{D(\alpha)D(\beta)}\, d\alpha d\beta$$

$$= \frac{1}{T} \int_0^T \int_0^T R(\alpha-\beta)\, d\alpha d\beta \tag{8.A.2}$$

where the expectation is over data values, $\overline{\cos^2\psi} = 1/2$ was used, and $R(\alpha-\beta)$ is the autocorrelation function of the split phase data stream. Recognizing that the double integral depends only on $(\alpha-\beta)$ we have

$$I(T) = 2 \int_0^T \left(1 - \frac{\tau}{T}\right) R(\tau)\, d\tau \tag{8.A.3}$$

The question now is what value of T maximizes I(T)? We simply plug into $R(\tau)$ and differentiate. Per Reference 11

$$R(\tau) = \begin{cases} 1 - \dfrac{3|\tau|}{T_b} : & |\tau| \leq T_b/2 \\ \dfrac{|\tau|}{T_b} - 1 : & \dfrac{T_b}{2} < |\tau| \leq T_b \\ 0 : & \text{elsewhere} \end{cases}$$

$$\frac{dI(T)}{dT} = \frac{2}{T^2} \int_0^T \tau R(\tau)\, d\tau$$

$$\begin{cases} 0 : T = 0 \\ 1 - \dfrac{2T}{T_b} : 0 < T \leq T_b/2 \\ \dfrac{2T}{3T_b} - 1 + \dfrac{T_b^2}{6T^2} : T_b/2 < T \leq T_b \end{cases} \qquad (8.A.4)$$

Clearly T = 0 is a minimum, thus we look for some other value. $T = T_b/2$ gives a maximum.

Having established that $T_b/2$ is the best value for T with no doppler and perfect correlation, we ask if T would be different under other circumstances. The answer is yes, however, practicality requires that T be independent of ω_d, the doppler frequency, (otherwise a doppler tracker would be needed); also a $T = NT_c$, i.e., the code period, would make the doppler effect on correlation devastating due to multiple doppler cycles.

The fact that we are integrating over small "chunks" of the code, squaring, and then accumulating severely degrades the code auto-correlation properties, that is, if we had no doppler or data then $T = NT_c$ would be the best integration time so that

$$M_{ci} = A \cos \psi \int_0^{NT_c} S(t)S(t+\tau)\, dt = ANT_c \cos \psi\, \rho(\tau) \qquad (8.A.5)$$

Thus

$$\frac{\lambda_b^2}{\sigma_b^2} = \frac{KA^2N^2T_c^2\, \rho^2(\tau)}{N_o\, NT_c} = \left(\frac{KA^2NT_c}{N_o}\right)\rho^2(\tau) \qquad (8.A.6)$$

where $\rho(\tau)$ is the PN code autocorrelation function and K is the number of integrations performed. Since $\rho^2(\tau)$ varies from 1 to $1/N^2$ there is a very large dynamic range and recognizing the code is straightforward. Figure 8.A.1 plots $\rho^2(\tau)$.

Consider the present case, however.

$$M_{ci} = A \cos \psi \int_0^{nT_c} S(t)S(t+\tau)dt, \qquad (8.A.7)$$

where n<<N is the case. For $n \geq 20$ or so and ψ constant M_{ci} is very Gaussian looking due to the smoothing effect of the integrator. Treating the PN code as a random bit stream gives M_{ci}^2 to be a central Chi-squared random variable denoted X^2 (mean, variance). Since

$$\overline{M_{ci}} = A\, \overline{\cos \psi}\, nT_c\, \rho(\tau) = 0 \qquad (8.A.8)$$

where $\rho(\tau)$ is the autocorrelation function of the "random noise" code which is very well approximated by the PN autocorrelation function and here considered equal, T_c is the chip width, and

$$\overline{M_{ci}^2} = A^2\overline{\cos^2\psi} \int_0^{nT_c}\int_0^{nT_c} \overline{S(\alpha)S(\alpha+\tau)S[\alpha+(\beta-\alpha)]S[\alpha+(\beta-\alpha)+\tau)]}\, d\alpha d\beta$$

$$= \left(\frac{A^2}{2}\right) 2 \int_0^{nT_c} (nT_c-\lambda)C(\lambda,\tau)d\lambda = A^2C_n(\tau) \qquad (8.A.9)$$

where

$$C(\lambda,\tau) \triangleq \overline{S(t)S(t+\tau)S(t+\lambda)S(t+\lambda+\tau)}, \qquad (8.A.10)$$

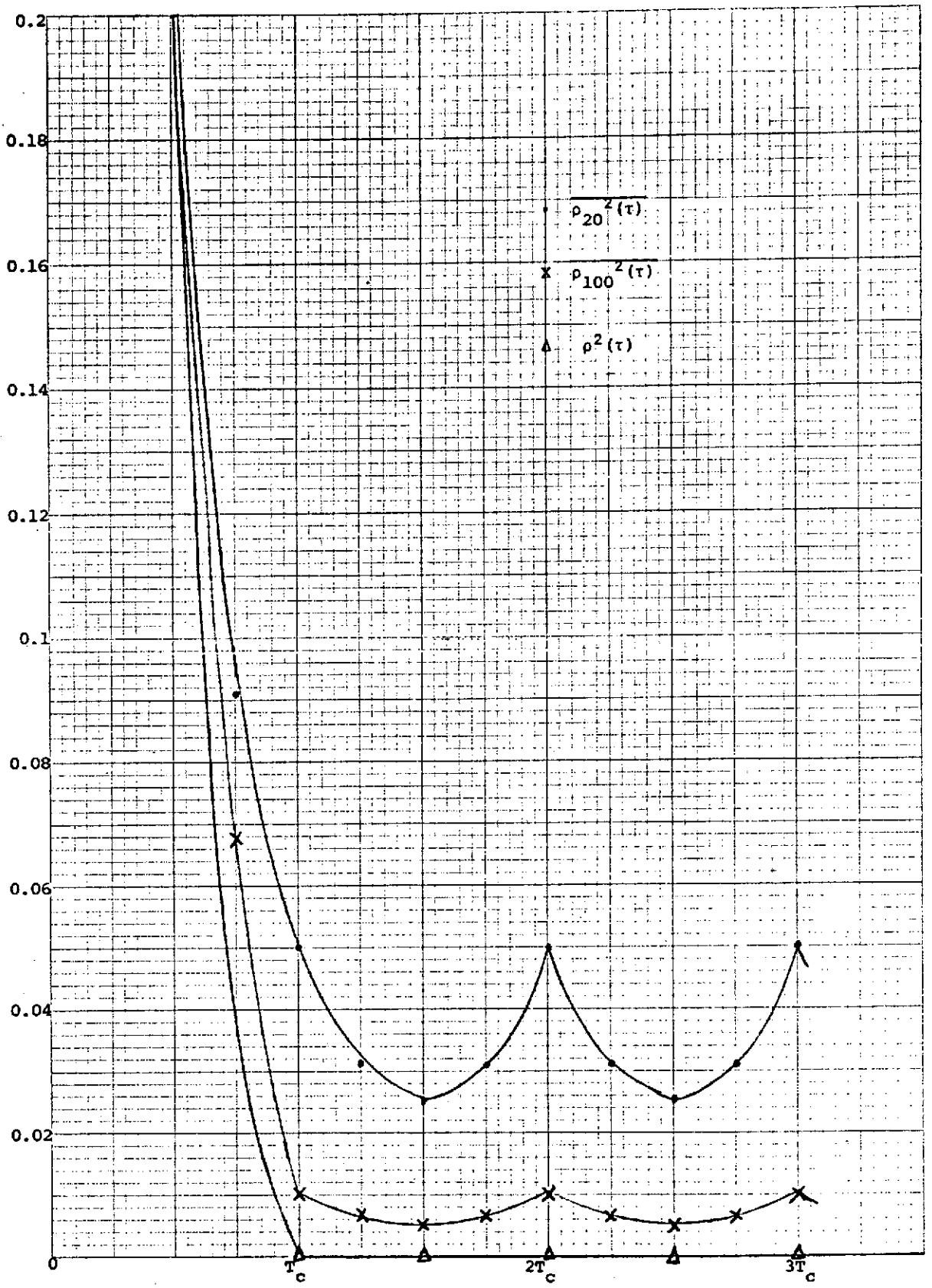

FIGURE 8.A.1 PN CODE CORRELATION FUNCTIONS

we have M_{ci}^2 is $\chi^2(m_c,\sigma_c^2)$, where

$$m_c = \overline{M_{ci}^2}$$

$$\sigma_c^2 = 2\overline{M_{ci}^2} = 2m_c$$

Note that m_c and σ_c^2 are actually independent of i!

A similar result holds for M_{si}^2 and since $M_{ci}^2 + M_{si}^2$ is again Chi-square we have

$$\frac{\lambda_b^2}{\sigma_b^2} = \frac{KA^2nT_c}{N_o}\rho_n^2(\tau) \tag{8.A.11}$$

where $\rho_n^2(\tau)$ is a Chi-squared random variable given by $\chi^2(\overline{\rho_n^2(\tau)},\sigma_n^2(\tau))$ i.e.,

$$\rho_n^2(\tau) = \frac{1}{n^2T_c^2}\int_0^{nT_c}\int_0^{nT_c} S(\alpha)S(\alpha+\tau)S(\beta)S(\beta+\tau)d\alpha d\beta, \tag{8.A.12}$$

$$\overline{\rho_n^2(\tau)} = \frac{2C_n(\tau)}{n^2T_c^2} \tag{8.A.13}$$

$$\sigma_n^2(\tau) = 2\left[\left(\overline{\rho n^2(\tau)}\right)^2 - \rho^4(\tau)\right] \tag{8.A.14}$$

If $C_n(\tau)$ can be found[12] then we can compare $\rho^2(\tau)$ with $\overline{\rho_n^2(\tau)}$ and thus find the degradation due to partial code processing. The quantity $\overline{\rho_n^2(\tau)}$, with n = 20 and 100 is plotted in Figure 8.A.1 for ease of comparison with $\rho^2(\tau)$. Note that due to the partial code correlation the PN code looks highly random and so produces values on each integration which vary considerably except near $\tau = 0$. Thus a mean is the crucial parameter. What is even more important the above analysis gives the distribution.

With split phase data applied the $\tau \geq T_c$ part of the $\overline{\rho_n^2(\tau)}$ does not change as should be expected, however, $\overline{\rho_n^2(0)}$ drops from 1 to 1/2 (3 dB). As a matter of interest if NRZ data were present then the degradation would be from 1 to 2/3 (1.8 dB).

Finally applying doppler shifts gives

$$\overline{\rho_n^2(\tau)} = \frac{2}{nT_c} \int_0^{nT_c} C(\lambda,\tau)R(\lambda) \cos \omega_d\lambda \ (1- \frac{\lambda}{nT_c})d\lambda. \qquad (8.A.15)$$

For split phase data

$$\overline{\rho_n^2(0)} = \frac{6}{(\omega_d nT_c)^2}\left[1 - Sa(\omega_d nT_c)\right] - \frac{1}{2} Sa^2(\frac{\omega_d nT_c}{2}) \qquad (8.A.16)$$

and for $\tau \geq T_c$

$$\overline{\rho_n^2(\tau)} = \frac{1}{n} (\frac{2}{\omega_d nT_c})^2 \left[\sin^2\left[\frac{\omega_d}{2} (2T_c-\tau)\right] + \sin^2\left[\frac{\omega_d}{2} (\tau-T_c)\right]\right] \qquad (8.A.17)$$

where the mirror image and repetitive property of $\overline{\rho_n^2(\tau)}$ still apply. As can be seen by (8.A.16) and (8.A.17) the doppler causes the usual inverse square dropp off as a function of the integration time, nT_c. Table 8.A.1 lists the values of $\overline{\rho_n^2(0)}$ for $\omega_d nT_c$ from 0.1 to 3.0 and the percentage error if it is approximated by $1/2\ Sa^2(\omega_d nT_c/4)$. As expected due to the short integration time, i.e., large equivalent bandwidth, there is negligible doppler degradation.

To sum up this appendix, with data and doppler the dynamic range of the PN operator function, $\overline{\rho_n^2(\tau)}$ is n/2. This is quite a different value than N^2 and affects the acquisition results as analyzed in Section 8.2 of this report.

TABLE 8.A.1

DOPPLER DEGRADATION VERSUS $\omega_d nT_c$

$\omega_d nT_c$	$\rho_n^2(0)$	$[\rho_n^2(0) - \frac{1}{2} Sa^2(\frac{\omega_d nT_c}{4})]X100$
0.1	0.4999166468	0.004161657827
0.2	0.4996663497	0.01658657577
0.3	0.4992483989	0.03709496787
0.4	0.4986616211	0.06538845167
0.5	0.4979043946	0.10105191 59
0.6	0.4969746693	0.143556088
0.7	0.4958699932	0.1922607561
0.8	0.4945875431	0.2464185888
0.9	0.4931241614	0.3051794865
1	0.491476397	0.3675953908
1.1	0.4896405509	0.4326254707
1.2	0.4876127254	0.4991416025
1.3	0.4853888779	0.5659340547
1.4	0.4829648761	0.6317172925
1.5	0.4803365579	0.6951358143
1.6	0.4774997915	0.754769937
1.7	0.4744505388	0.8091414528
1.8	0.4711849184	0.8567190824
1.9	0.4676992706	0.8959236603
2	0.4639902207	0.9251329921
2.1	0.4600547436	0.9426863355
2.2	0.4558902253	0.9468884624
2.3	0.4514945244	0.9360132712
2.4	0.44686603	0.9083069263
2.5	0.4420037182	0.8619905111
2.6	0.4369072036	0.7952621925
2.7	0.4315767889	0.706298899
2.8	0.4260135088	0.5932575299
2.9	0.4202191704	0.454275716
3	0.4141963875	0.2874721663

9.0 QUADRATURE-MULTIPLEX MODULATION SYSTEM WITH APPLICATION TO THE ORBITER'S KU-BAND LINK

9.1 INTRODUCTION

The Orbiter's return Ku-Band link requires simultaneous transmission of at least two independent data channels, one having a rate of up to 50 Mbps and the other having a rate of up to 2 Mbps. In addition to these data streams, it is also desirable, if feasible, to transmit a third stream of the operational data having a rate of 192 Kbps. Since the above three channels have different clocks, time division multiplexing will not be possible without reclocking which would be overly complex. Consequently, other techniques must be considered as an alternative approach.

Phase modulation of three data channels after being subcarrier modulated (i.e., PSK/PM) is a conventional scheme and PSK/PM for multichannel data is well documented.[1][2] The disadvantage of PSK/PM is that it incurs intermodulation loss which is not desirable especially in deep-space communications where the maximum available power is limited.

As far as the intermodulation is concerned, so-called interplex modulation[3] proved to be more efficient with a minor system modification than conventional PSK/PM. Udalov[4] has shown a possibility of using the interplex modulation system for the Orbiter Ku-Band link.

This paper describes a new modulation scheme (which we call Quadrature-Multiplex (QM) Modulation) that generates the interplexed signals with a simpler system structure and even smaller intermodulation loss than the interplex modulation system for the Orbiter Ku-Band link

when the same conditions which make interplex efficient over the conventional scheme apply. The QM modulator has a similar structure to the quadri-phase modulator as shown in Figure 9.1. In QM, the highest rate data (i.e., 50 Mbps) is multiplied by the inphase component of the carrier, while the other two lower rate data are multipled by the quadrature component after being subcarrier modulated so that they are separable in the frequency domain. The resultant inphase and quadrature components are summed up, power-amplified and transmitted. Here we assumed that the power amplifier is a hard limiter amplifier, which is a reasonable assumption in practice. This QM modulator eliminates the "true" phase modulator required in interplex and is simpler to implement.

In this report, the QM modulation has been restricted to the three channel data transmission case in order to convey its basic features more clearly even though one can generalize it to multichannel transmission. The QM signal is analyzed, compared to the interplex signal, and shown to be essentially identical to it. The receiver performance is studied in terms of the loop loss. Finally, a signal is designed using the QM for the Orbiter's Ku-Band return link.

9.2 THREE-CHANNEL QUADRATURE-MULTIPLEX MODULATION

In this section, we analyze the QM signal and compare it to the interplex signal. It seems to be in order to discuss the interplex signal first, since the two signals will turn out to be essentially identical.

9.2.1 Three-Channel Interplex Modulation

The block diagram of the three-channel interplex modulator is shown in Figure 9.2, and the transmitter output signal s(t) can be represented by[3].

$$s(t) = \sqrt{2P} \sin [\omega_c t + \theta(t)] \qquad (9.1)$$

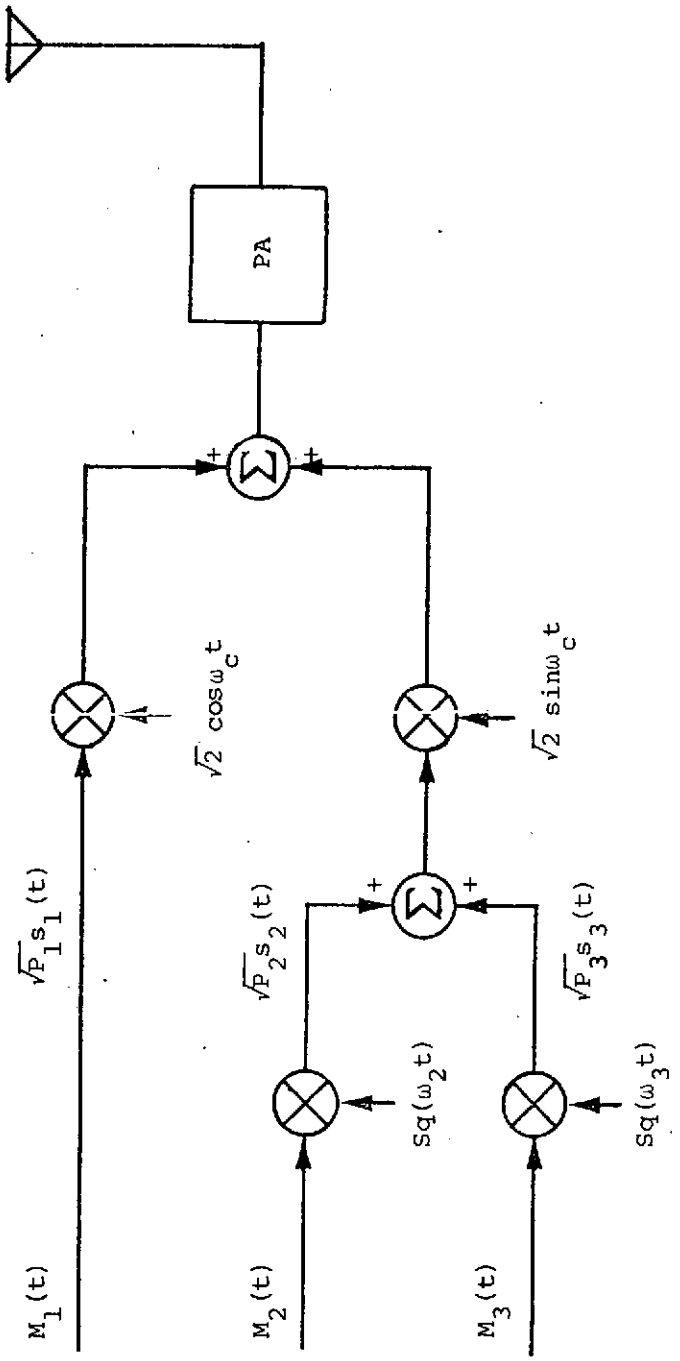

FIGURE 9.1 THREE-CHANNEL QUADRATURE-MULTIPLEX MODULATOR BLOCK DIAGRAM

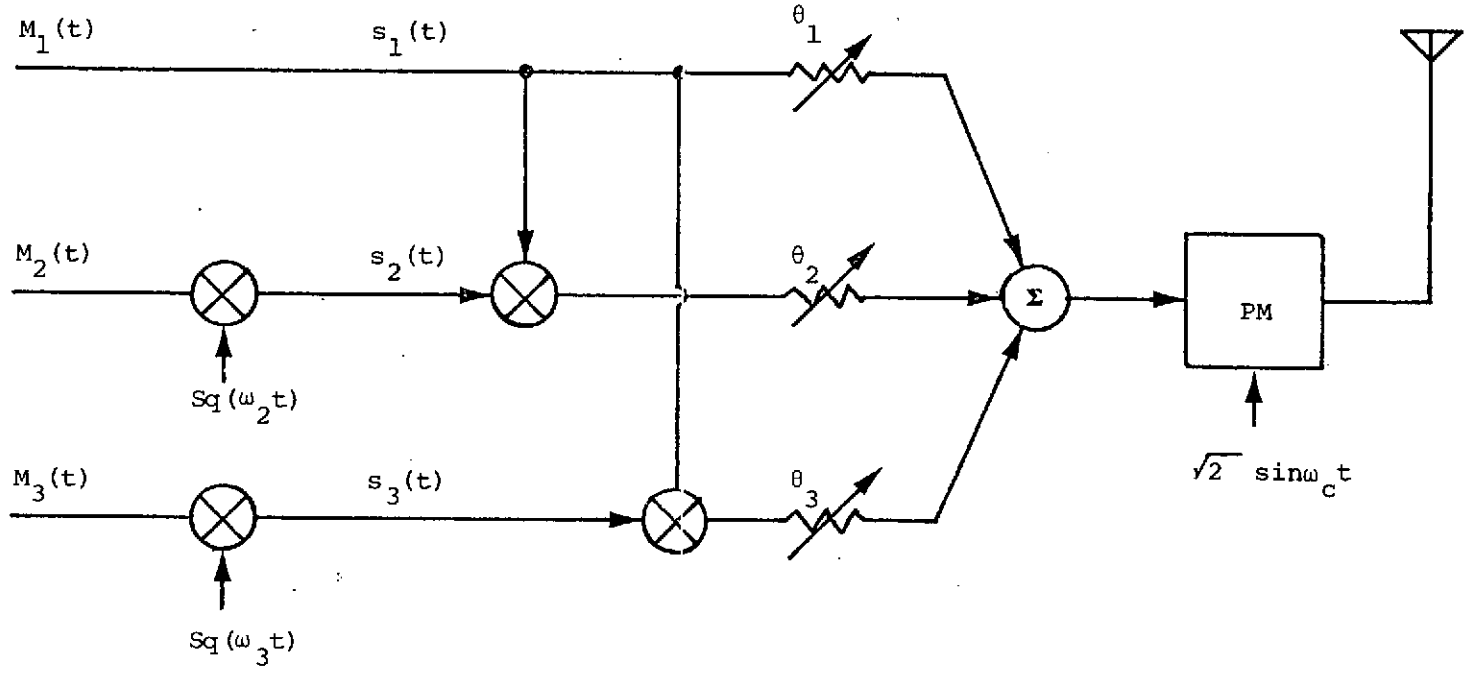

FIGURE 9.2 THREE-CHANNEL INTERPLEX MODULATOR BLOCK DIAGRAM

where

$$\theta(t) = \theta_1 s_1(t) + \theta_2 s_1(t)s_2(t) + \theta_3 s_1(t)s_3(t) \tag{9.2}$$

$$s_1(t) = \pm 1;\ s_2(t) = \pm 1;\ s_3(t) = \pm 1 \tag{9.3}$$

Using trigonometric identities for $\theta(t)$ after plugging Equation (9.2) into Equation (9.1) we get

$$\begin{aligned} s(t) = \sqrt{2}\,\{&\sqrt{P_1}s_1(t) + \sqrt{P_{12}}s_1(t)s_2(t) + \sqrt{P_{13}}s_1(t)s_3(t) \\ &- \sqrt{P_{123}}s_1(t)s_2(t)s_3(t)\}\cos\omega_c t + \sqrt{2}\,\{\sqrt{P_c} \\ &- \sqrt{P_2}s_2(t) - \sqrt{P_3}s_3(t) - \sqrt{P_{23}}s_2(t)s_3(t)\} \\ &\cdot \sin\omega_c t \end{aligned} \tag{9.4}$$

where

$$\begin{aligned} P_c &\triangleq P\cos^2\theta_1\cos^2\theta_2\cos^2\theta_3 \\ P_1 &\triangleq P\sin^2\theta_1\cos^2\theta_2\cos^2\theta_3 \\ P_2 &\triangleq P\sin^2\theta_1\sin^2\theta_2\cos^2\theta_3 \\ P_3 &\triangleq P\sin^2\theta_1\cos^2\theta_2\sin^2\theta_3 \\ P_{12} &\triangleq P\cos^2\theta_1\sin^2\theta_2\cos^2\theta_3 \\ P_{13} &\triangleq P\cos^2\theta_1\cos^2\theta_2\sin^2\theta_3 \\ P_{23} &\triangleq P\cos^2\theta_1\sin^2\theta_2\sin^2\theta_3 \\ P_{123} &\triangleq P\sin^2\theta_1\sin^2\theta_2\sin^2\theta_3 \end{aligned} \tag{9.5}$$

Defining

$$\begin{aligned} x(t) &= \sqrt{P_1}s_1(t) + \sqrt{P_{12}}s_1(t)s_2(t) + \sqrt{P_{13}}s_1(t)s_3(t) \\ &\quad - \sqrt{P_{123}}s_1(t)s_2(t)s_3(t) \\ y(t) &= \sqrt{P_c} - \sqrt{P_2}s_2(t) - \sqrt{P_3}s_3(t) - \sqrt{P_{23}}s_2(t)s_3(t) \end{aligned} \tag{9.6}$$

Equation (9.4) is rewritten as

$$s(t) = \sqrt{2}x(t)\cos\omega_c t + \sqrt{2}y(t)\sin\omega_c t \tag{9.7}$$

Equations (9.6) and (9.7) show that the interplex signal has the first channel signal $s_1(t)$ with power P_1 in the inphase component of the signal, and the carrier, the second and third channel signals with the power P_c, P_2, P_3 respectively in the quadrature component. The intermodulation loss in this case is

$$P_d = P_{12} + P_{13} + P_{23} + P_{123}. \tag{9.8}$$

It is desired that P_1, P_2, and P_3 be as large as possible, and P_c and P_d be as small as possible for an efficient use of the available total power. This can be achieved by making

$$\theta_1 = \pi/2 \tag{9.9}$$

In this case

$$\begin{aligned} P_c &= 0 \\ P_1 &= P \cos^2\theta_2 \cos^2\theta_3 \\ P_2 &= P \sin^2\theta_2 \cos^2\theta_3 \\ P_3 &= P \cos^2\theta_2 \sin^2\theta_3 \\ P_d &= P \sin^2\theta_2 \sin^2\theta_3 \end{aligned} \tag{9.10}$$

and Equation (9.6) becomes

$$\begin{aligned} x(t) &= \sqrt{P_1}s_1(t) - \sqrt{P_d}s_1(t)s_2(t)s_3(t) \\ y(t) &= -\sqrt{P_2}s_2(t) - \sqrt{P_3}s_3(t) \end{aligned} \tag{9.11}$$

Therefore, when $\theta_1 = \pi/2$, the interplex signal is carrier suppressed and its intermodulation is caused by the product of the three signals only.

9.2.2 Three-Channel QM Modulation

A scrutiny of Equation (9.7) and (9.11) sheds light on generating an interplex signal in a manner other than using the true phase modulator, i.e., if P_1 is relatively large compared to P_2 and P_3,

Equation (9.7) looks like a quadriphase signal. If

$$P_1 >> P_2; \quad P_1 >> P_3, \tag{9.12}$$

then θ_2 and θ_3 have to be small angles and consequently P_d of Equation (9.10) will become negligible. With this assumption, the interplex signal given by Equations (9.7) and (9.11) may be implemented as shown by Figure 9.1. This is the motivation which led us to consider the QM modulator in lieu of the interplex modulator of Figure 9.2. However, we can start to consider the QM modulator independently with the assumption given by Equation (9.12).

Consider the QM modulator shown by Figure 9.1. The signal generated by the QM modulator can be expressed by

$$s(t) = \sqrt{2}(A(t) \cos \omega_c t + B(t) \sin \omega_c t) \tag{9.13}$$

where

$$A(t) = \sqrt{P_1} s_1(t) \tag{9.14}$$

$$B(t) = \sqrt{P_2} s_2(t) + \sqrt{P_3} s_3(t)$$

Therefore, from Equations (9.13) and (9.14), we get

$$s(t) = \sqrt{2} E(t) \sin (\omega_c t + \zeta(t)) \tag{9.15}$$

where

$$E(t) \triangleq [A^2(t) + B^2(t)]^{1/2} \tag{9.16}$$

$$\zeta(t) \triangleq \tan^{-1} \left(\frac{A(t)}{B(t)}\right) \tag{9.17}$$

Since s(t) passes through the hard-limiter power amplifier as mentioned earlier, the transmitted signal will be

$$s(t) = \sqrt{2P} \sin [\omega_c t + \zeta(t)] \tag{9.18}$$

which can be rewritten as

$$s(t) = \sqrt{2P} \left(\frac{A(t)}{E(t)} \cos \omega_c t + \frac{B(t)}{E(t)} \sin \omega_c t\right) \tag{9.19}$$

Let us now evaluate $E^{-1}(t)$. From Equation (9.14)

$$A^2(t) \triangleq [\sqrt{P_1}s_1(t)] = P_1 \tag{9.20}$$

$$B^2(t) \triangleq \{\sqrt{P_2}s_2(t) + \sqrt{P_3}s_3(t)\}^2$$

$$= P_2 + P_3 + 2\sqrt{P_2P_3}s_2(t)s_3(t)$$

From Equation (9.20)

$$A^2(t) + B^2(t) = P_T + 2\sqrt{P_2P_3}s_2(t)s_3(t)$$

$$= P_T\,(1 + 2\sqrt{P_2/P_T}\sqrt{P_3/P_T}\,s_2(t)s_3(t)) \tag{9.21}$$

where

$$P_T \triangleq P_1 + P_2 + P_3 \tag{9.22}$$

Recalling the fact that $\sqrt{P_2/P_T} \ll 1$; $\sqrt{P_3/P_T} \ll 1$, because of Equation (9.12),

$$E^{-1}(t) = [A^2(t) + B^2(t)]^{-1/2} \simeq \frac{1}{\sqrt{P_T}}[\alpha - \beta\, s_2(t)s_3(t)] \tag{9.23}$$

where three terms in the binomial expansion were used, and

$$\alpha \triangleq 1 + \frac{3}{2}\,\frac{P_2}{P_T}\cdot\frac{P_3}{P_T} \tag{9.24}$$

$$\beta \triangleq \sqrt{P_2/P_T}\;\sqrt{P_3/P_T} \tag{9.25}$$

From Equations (9.14), (9.19), and (9.23), we get

$$s(t)\sqrt{2\,\frac{P}{P_T}}\Big\{[\alpha\sqrt{P_1}s_1(t) - \beta\sqrt{P_1}s_1(t)s_2(t)s_3(t)]\cos\omega_c t$$

$$+ [(\alpha\sqrt{P_2} - \beta\sqrt{P_3})\,s_2(t) + (\alpha\sqrt{P_3} - \beta\sqrt{P_2})s_3(t)]\sin\omega_c t\Big\} \tag{9.26}$$

Defining

$$\sqrt{P_1'} \triangleq \alpha\sqrt{P_1}$$

$$\sqrt{P_2'} \triangleq \alpha\sqrt{P_2} - \beta\sqrt{P_3}$$

$$\sqrt{P_3'} \triangleq \alpha\sqrt{P_3} - \beta\sqrt{P_2}$$

$$\sqrt{P_d'} \triangleq \beta\sqrt{P_1} \tag{9.27}$$

and adjusting so that

$$P = P_T \tag{9.28}$$

Equation (9.26) can be rewritten as

$$s(t) = \sqrt{2}\left\{\left[\sqrt{P_1'}s_1(t) - \sqrt{P_d'}s_1(t)s_2(t)s_3(t)\right]\cos\omega_c t + \left[\sqrt{P_2'}s_2(t) + \sqrt{P_3'}s_3(t)\right]\sin\omega_c t\right\} \tag{9.29}$$

Equation (9.29) is exactly the same as the interplex signal generated by the interplex modulator except for the power reapportionment given by Equation (9.27). It is immediately clear from Equation (9.27) that the intermodulation loss of the QM modulator is

$$P_d' = \beta^2 P_1 \tag{9.30}$$

Now let us investigate the power reapportionment in more detail.

Defining

$$\gamma^2 \triangleq P_3/P_2 \tag{9.31}$$

$$\lambda^2 \triangleq P_3'/P_2' \tag{9.32}$$

We can express α and β of Equations (9.24) and (9.25) in terms of γ and P_1/P_T as

$$\alpha = 1 + \frac{3}{2}\gamma^2\left[\frac{(1-P_1/P_T)}{1+\gamma^2}\right]^2 \tag{9.33}$$

$$\beta = \gamma\,\frac{1-P_1/P_T}{1+\gamma^2} \tag{9.34}$$

It can be shown that $\alpha \simeq 1$ for all practical purposes. From Equations (9.27), (9.31), (9.32), and (9.34) then, it can be shown that

$$\lambda^2 = \frac{\gamma^2\left[(\gamma^2 + P_1/P_T)\right]^2}{\left[1+\gamma^2(P_1/P_T)\right]^2} \tag{9.35}$$

The λ^2 versus γ^2 relationship of Equation (9.35) is illustrated in Figure 9.3. As is clear in Figure 9.3, the power reapportionment between channels 2 and 3 due to going through the limiter becomes

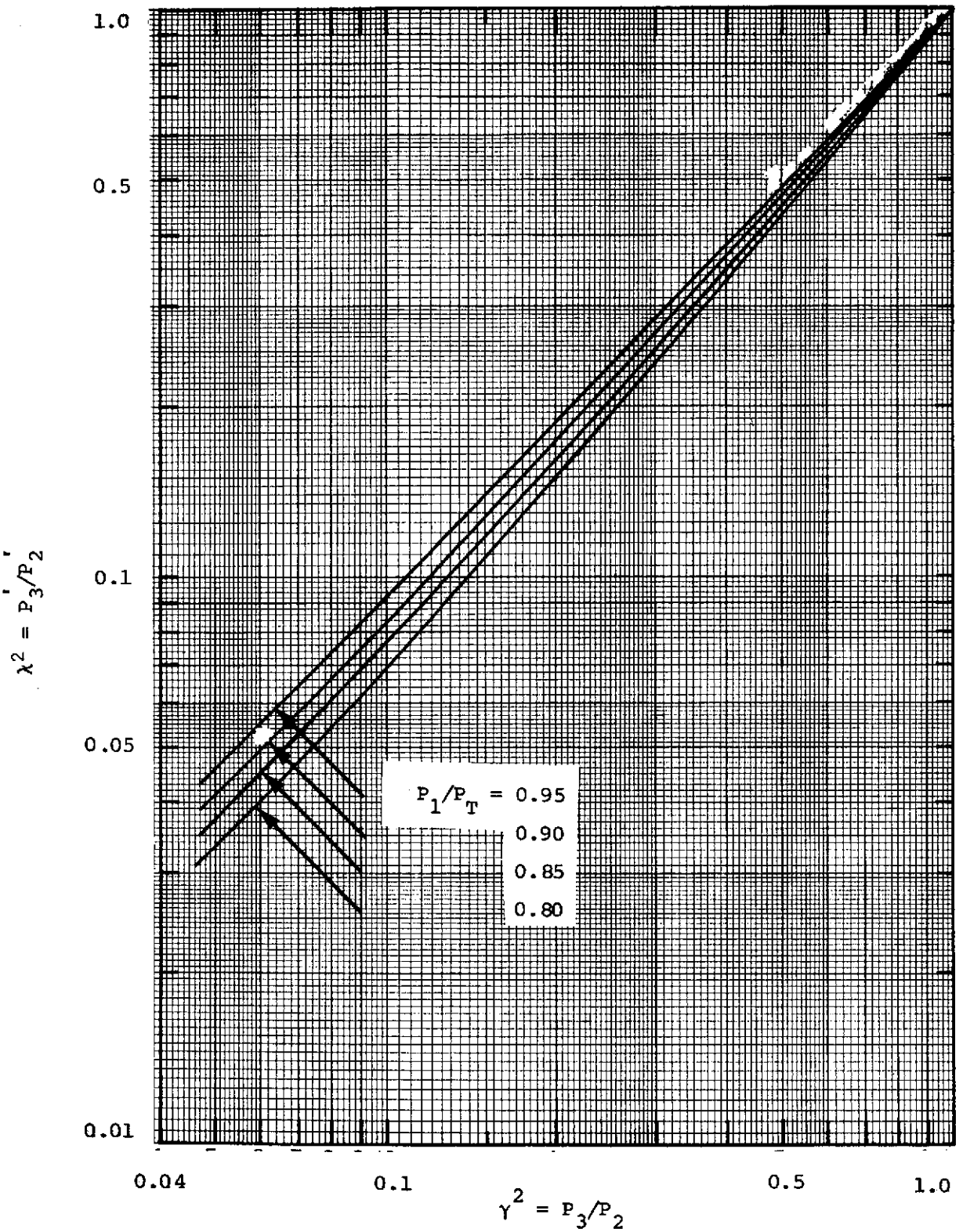

FIGURE 9.3 POWER REAPPORTIONMENT DUE TO THE HARD-LIMITER IN THREE CHANNEL QUADRATURE MODULATION

large as γ^2 and/or P_1/P_T decrease. This is a "capturing" of the limiter effect. When $\gamma^2 = 1$ as an extreme case, there is no power reapportionment.

Equation (9.27) shows that the power reapportionment occurs only between the lower two channels, and the amount of the power transfer is determined by the factor β which we call the power spill-over factor. This factor is shown in Figure 9.4. Since β is a small number, the power reapportionment in the second channel is very small. However, the reapportionment in the third channel will still be considerable when γ^2 is small.

The relative intermodulation loss P_d/P is shown also in Figure 9.5, which turned out to be a very small portion of the total power.

This completes the description of the QM signal and Figures 9.3, 9.4, and 9.5 will prove to be useful for designing the QM modulator. In the next section, we will discuss a receiver system that is pertinent to the QM signal as well as the interplex signal.

9.2.3 Receiver Performance

The demodulator for the QM signal is shown in Figure 9.6, which is a Costas Loop type of demodulator. Considering additive white Gaussian noise in the channel, the received signal is given by (referring to Equation (9.29))

$$r(t) = \sqrt{2}x(t) \cos(\omega_c t + \phi_i) + \sqrt{2}y(t) \sin(\omega_c t + \phi_i) + n(t) \tag{9.36}$$

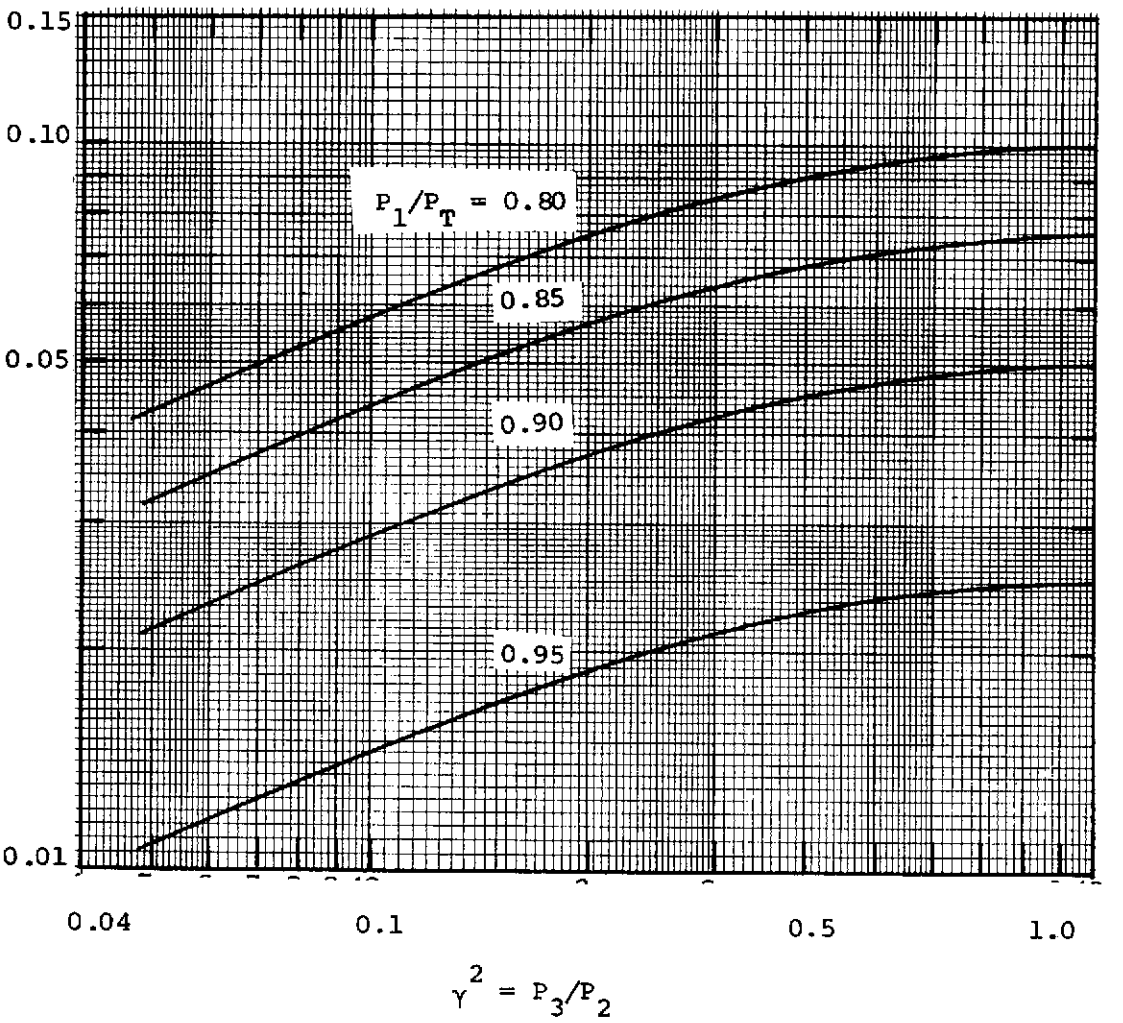

FIGURE 9.4 POWER SPILL-OVER FACTOR (β vs. γ^2) CURVES

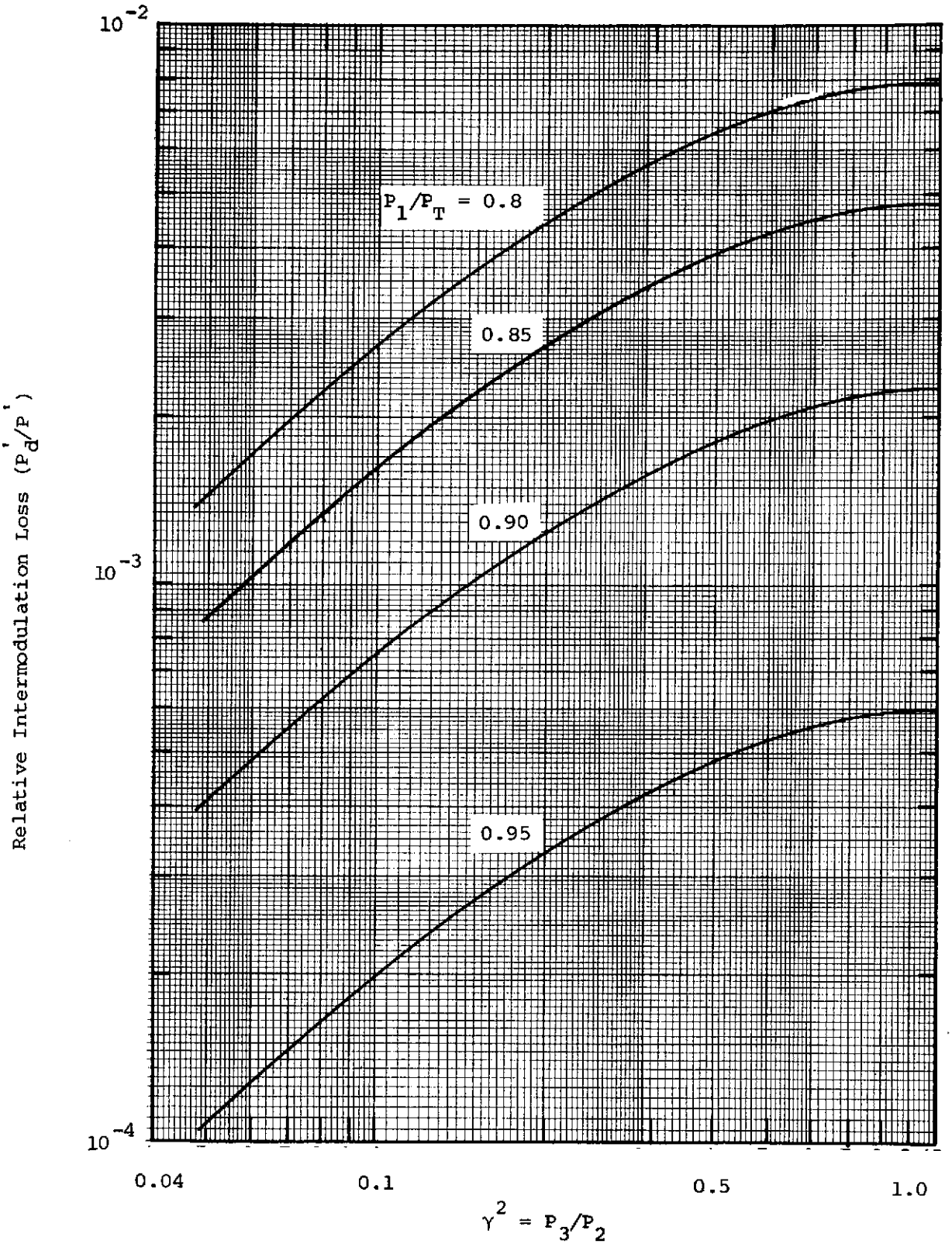

FIGURE 9.5 RELATIVE INTERMODULATION LOSS IN THE THREE CHANNEL QUADRATURE MODULATION

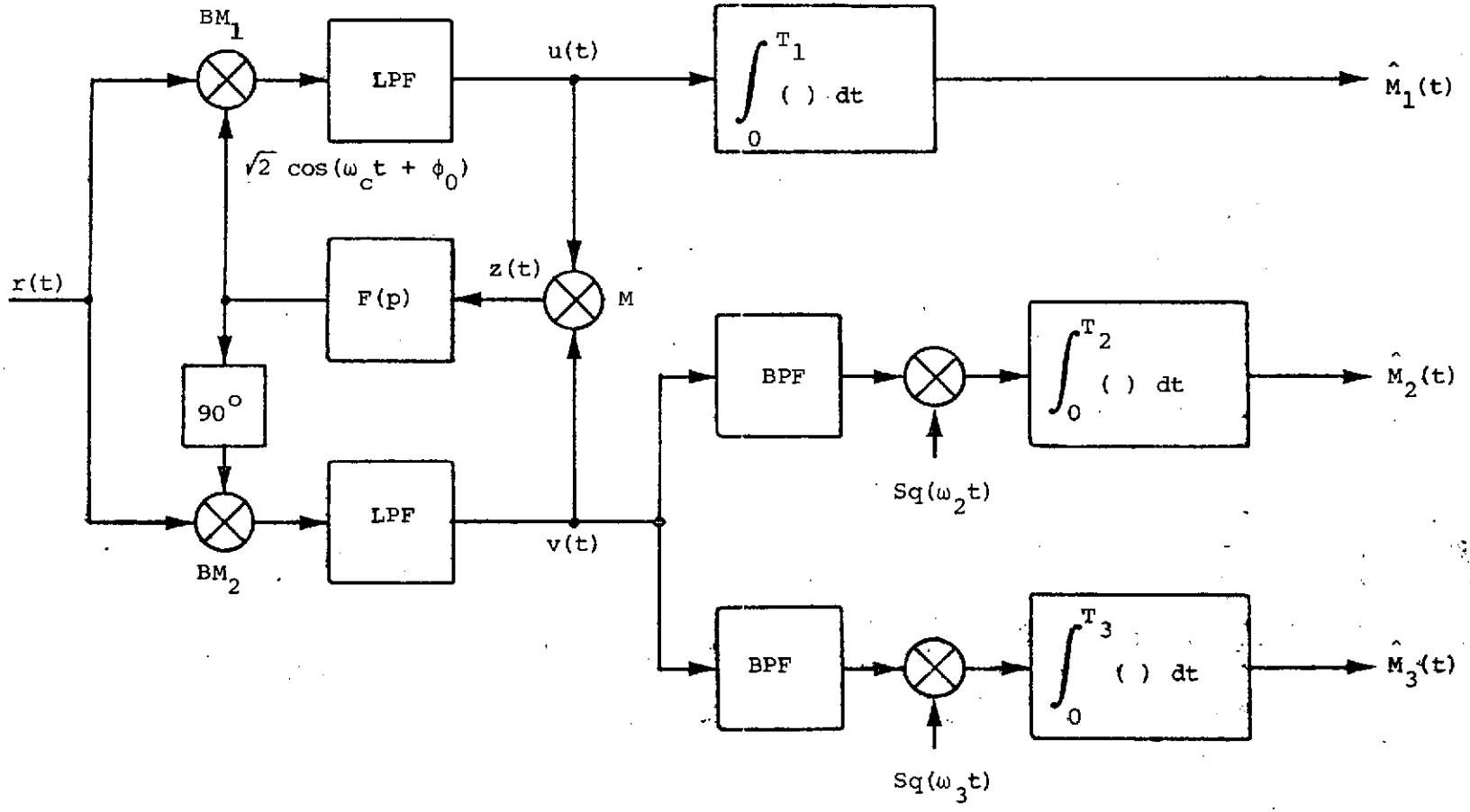

FIGURE 9.6 THREE-CHANNEL QM DEMODULATOR BLOCK DIAGRAM

where

$$x(t) \triangleq \sqrt{P_1}s_1(t) - \sqrt{P_d}s_1(t)s_2(t)s_3(t)^* \tag{9.37}$$

$$y(t) \triangleq \sqrt{P_2}s_2(t) + \sqrt{P_3}s_3(t) \tag{9.38}$$

$$n(t) \triangleq \sqrt{2}N_c(t) \cos \omega_c t - \sqrt{2}N_s(t) \sin \omega_c t \tag{9.39}$$

The low pass filter output of the inphase channel is

$$\begin{aligned} u(t) &= r(t)\sqrt{2} \cos (\omega_c t + \phi_0)\big| \text{ LPF} \\ &= [x(t) + N_c(t)] \cos \phi + [y(t) - N_s(t)] \sin \phi \end{aligned} \tag{9.40}$$

where

$$\phi \triangleq \phi_i - \phi_0 \tag{9.41}$$

The low pass filter output of the quadrature channel is

$$\begin{aligned} v(t) &= r(t)\sqrt{2} \sin (\omega_c t + \phi_0)\big| \text{ LPF} \\ &= -[x(t) + N_c(t)] \sin \phi + [y(t) - N_s(t)] \cos \phi \end{aligned} \tag{9.42}$$

Equations (9.40) and (9.42) show that there is energy leakage between the two channels in the presence of the phase tracking error ϕ. Since $P_1 >> P_2$ and $P_1 >> P_3$, v(t) has the more deleterious effect on the demodulated output than u(t). However, this can be avoided by judiciously choosing the subcarrier frequencies $Sq(\omega_2 t)$ and $Sq(\omega_3 t)$ so that $s_2(t)$ and $s_3(t)$ locate on/near the null point of the $s_1(t)$ power spectrum.

The error control signal, then, is

$$\begin{aligned} z(t) &= u(t)v(t) \\ &= -1/2[x^2(t) - y^2(t)] \sin 2\phi + 1/2\, v_2(t,2\phi) \end{aligned} \tag{9.43}$$

where

$$\begin{aligned} v_2(t,2\phi) \triangleq\ & [N_s^2(t) - N_c^2(t) - 2x(t)N_c(t) - 2y(t)N_s(t)] \sin 2\phi \\ & + [2x(t)y(t) + 2y(t)N_c(t) - 2x(t)N_s(t) \\ & \quad - 2N_c(t)N_s(t)] \cos 2\phi \end{aligned} \tag{9.44}$$

---

* For notational convenience, primes are dropped in the power expressions. To be exact, P_1 has to be P_1' and so on.

We assume that the bandwidth of F(p) is narrow enough to exclude the term $2x(t)y(t)$* in Equation (9.44). Using Equations (9.37), (9.37), $x^2(t)-y^2(t)$ in Equation (9.43) is rewritten as

$$x^2(t) - y^2(t) = P\left[\frac{(P_1+P_d) - (P_2+P_3)}{P} - 2\left(\sqrt{\frac{P_1}{P}}\sqrt{\frac{P_d}{P}} - \sqrt{\frac{P_2}{P}}\sqrt{\frac{P_3}{P}}\right)s_2(t)s_3(t)\right]$$

$$\approx (P_1 + P_d) - (P_2 + P_3) \qquad (9.45)$$

Therefore, the stochastic integrodifferential equation is given by

$$2\frac{d\phi_0}{dt} = -KF(P)\left[\{P_1+P_d - (P_2+P_3)\}\sin 2\phi - v_2(t,2\phi)\right] \qquad (9.46)$$

This equation is similar to that of the Costas Loop except for the phase detector gain $P_1+P_d-(P_2+P_3)$ [5].

Now, we want to evaluate the loop noise level and the loop loss. The autocorrelation function of the loop noise $v_2(t,2\phi)$ can be found to be (using $R_{nc}(\tau) = R_{ns}(\tau)$ as the noise autocorrelation functions and $R_x(\tau)$, $R_y(\tau)$ as the signal autocorrelation functions)

$$R_N(\tau) = 4R_{nc}^2(\tau) + 4R_{nc}(\tau)[R_x(\tau) + R_y(\tau)] \qquad (9.47a)$$

Since $R_{nc}(\tau)$ is very narrow relative to $R_x(\tau)$ or $R_y(\tau)$ we have

$$R_N(\tau) = 4R_{nc}^2(\tau) + 4R_{nc}(\tau)[R_x(0) + R_y(0)]$$

$$= 4R_{nc}(\tau) + 4R_{nc}(\tau)P \qquad (9.47b)$$

The equivalent one sided noise density N_{eq} in the region about $\omega = 0$ is then given by

$$N_{eq} = 2\int_{-\infty}^{\infty} R_N(\tau)d\tau \qquad (9.47c)$$

* Recall that y(t) is baseband on square wave subcarriers hence bandpass.

For an ideal band pass filter with the bandwidth W_i,

$$N_{eq} = 2N_0^2 W_i + 4N_0 P \tag{9.48}$$

The loop loss, then, is given by

$$S_L = \frac{4[P_1 + P_d - (P_2 + P_3)]^2 N_o}{PN_{eq}} \tag{9.49}$$

From Equations (9.48) and (9.49), it can be shown that

$$S_L^{-1} = \left(\frac{P}{P_1 + P_d - (P_2 + P_3)}\right)^2 \left[1 + \left(\frac{N}{S}\right)_i\right] \tag{9.50}$$

Equation (9.50) illustrates that, for large input signal-to-noise ratio $(S/N)_i$, the loop loss is determined by the power distribution in each channel. For $P_1 >> P_2$ and $P_1 >> P_3$, and for large $(S/N)_i$, which is the case here, the loop loss turns out to be practically 0 dB.

In summary, we proposed a QM signal demodulator which is a Costas Loop type. In this section, we discussed power leakage between the inphase and quadrature channels. This power leakage can be reduced by a judicious selection of the subcarrier frequencies of the lower rate channels. We evaluated the loop loss of the demodulator. It turned out that the loop loss is negligible for the case of interest here.

9.2.4 Orbiter's Return Ku-Band Link

In this section, we are concerned with the Orbiter's return Ku-Band link design using the QM modulator and demodulator discussed in the previous sections.

(1) The information to be transmitted by the Orbiter is:

$$M_1(t) = \text{up to 50 Mbps (NRZ)}$$

$$M_2(t) = \text{up to 2 Mbps (NRZ)}$$

$$M_3(t) = 192 \text{ Kbps} \simeq 0.2 \text{ Mbps (NRZ)} \tag{9.51}$$

(2) The TDRS Ku-Band receiver frequency plan and the achievable data rate vs. user EIRP are given in Figures 9.7 and 9.8 respectively according to the TDRSS User Guide.[6]

(3) It is required that the Orbiter provide

$$P_t + L_t + G_t + L_{polarization} = 48.6 \text{ dBW} \tag{9.52}$$

according to a NASA (JSC) memorandum.[7]

With the above three constaints, a communication system has to be designed. We will only consider the worst case of the highest bit rates.

Figure 9.8 shows that the forward error control (FEC) coding has to be employed to accommodate such a high rate data as 50 Mbps. In the present design approach, we maintained the coding scheme only in 50 Mbps channel. The reasons are that the Orbiter EIRP is enough so that there is no need to use the FEC scheme in the lower second and third channels, and that the power leakages in inphase and quadrature channels to be reduced as much as possible. The proposed Shuttle transmitter block diagram is shown in Figure 9.9. The design procedure is as follows:

(1) To maintain equal performance in each channel, the power apportionment has to be:

$$\frac{P_1' \times 3.31}{50} = \frac{P_2'}{2} = \frac{P_3}{0.2} \tag{9.53}$$

where the factor 3.31 corresponds to the FEC gain of 5.2 dB.

(2) From Equation (9.53)

$$\lambda^2 = \frac{P_3'}{P_2'} = 0.1 \tag{9.54}$$

From Figure 9.3, we find P_3'/P_2' given P_3/P_2 as above,

$$\therefore \gamma^2 = \frac{P_3}{P_2} = 0.125 \tag{9.55}$$

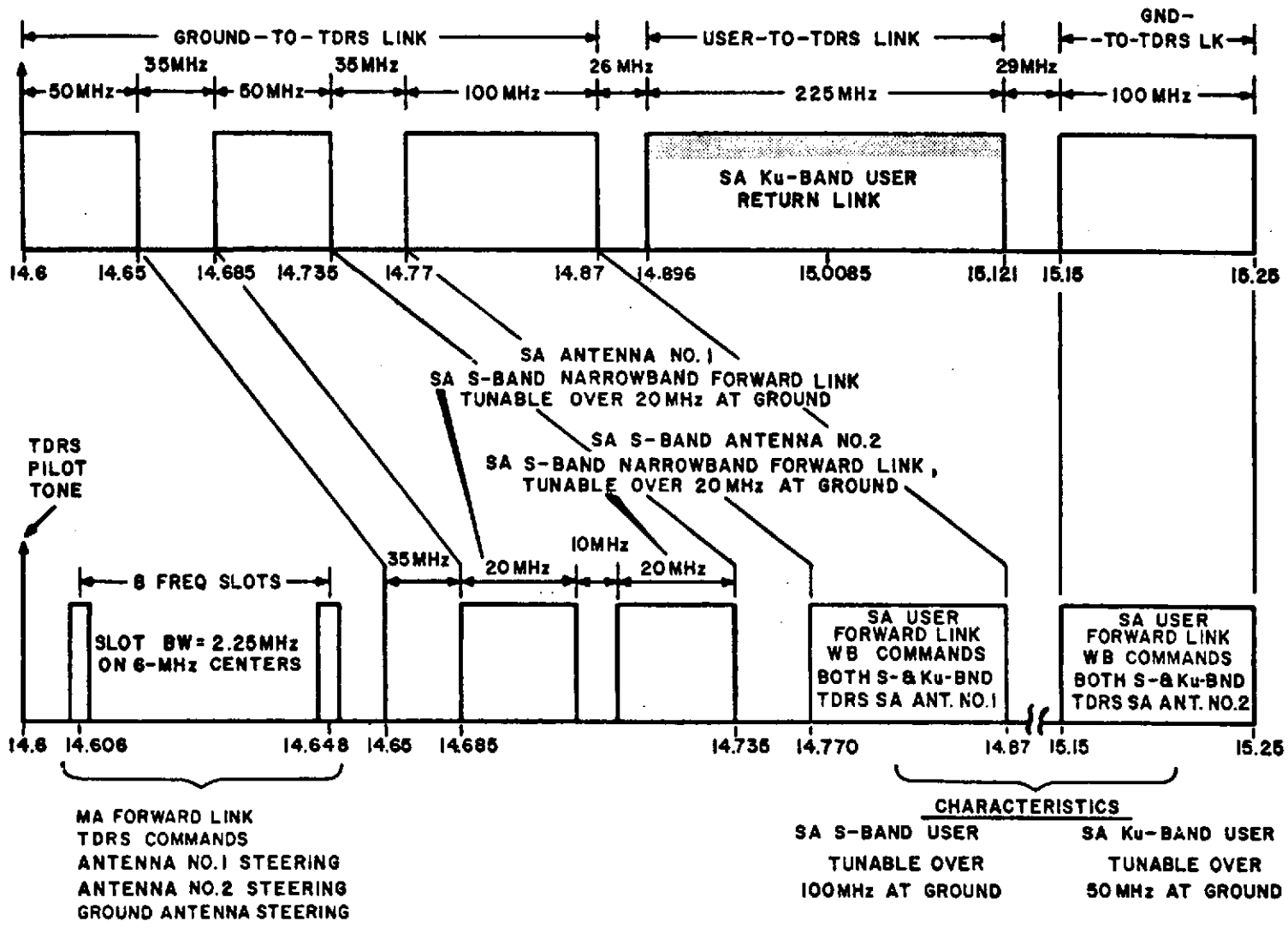

FIGURE 9.7 TDRS KU-BAND RECEIVE FREQUENCY PLAN

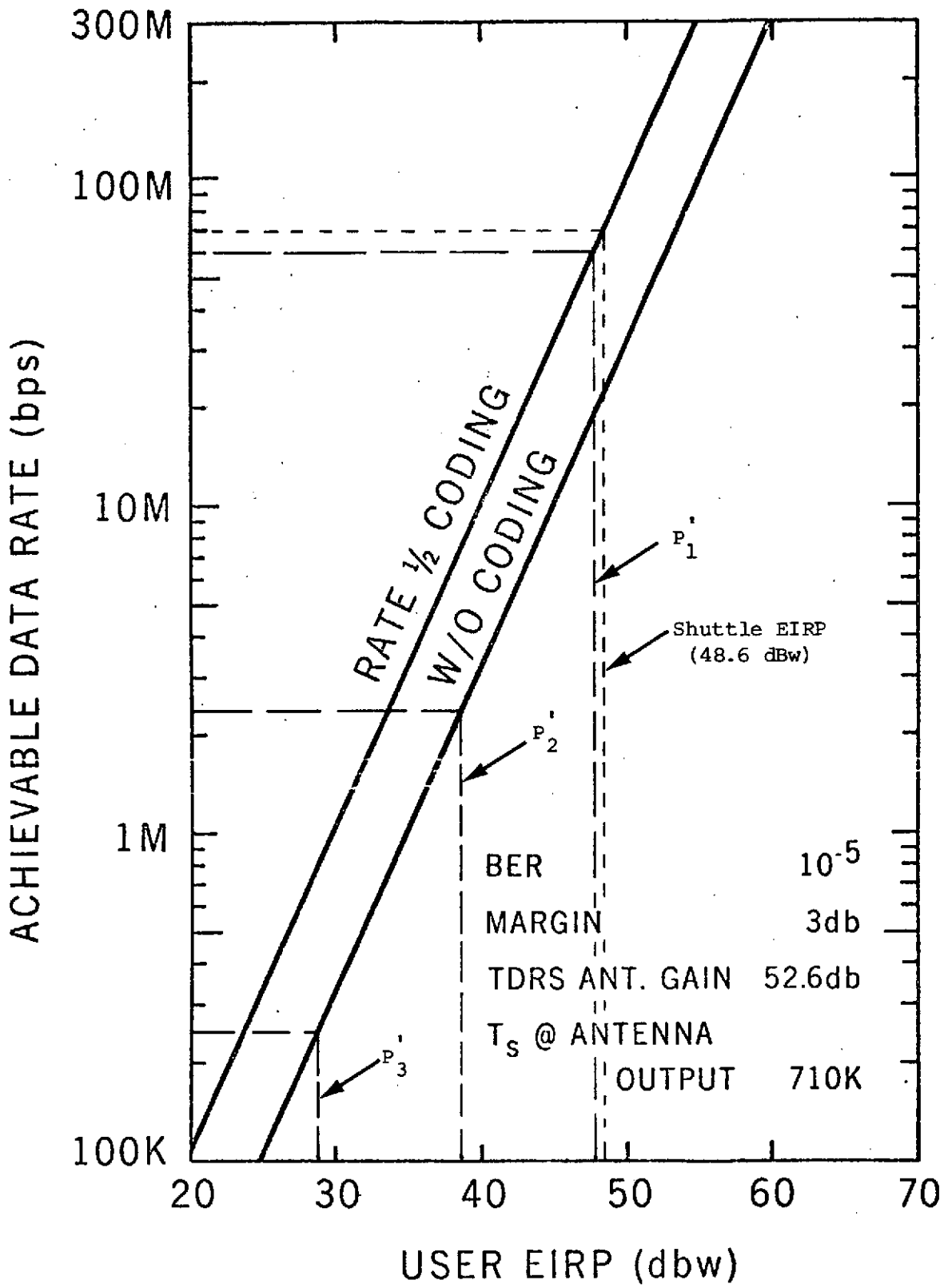

FIGURE 9.8 SINGLE-ACCESS (KU-BAND) RETURN LINK, ACHIEVABLE DATA RATE vs. USER EIRP

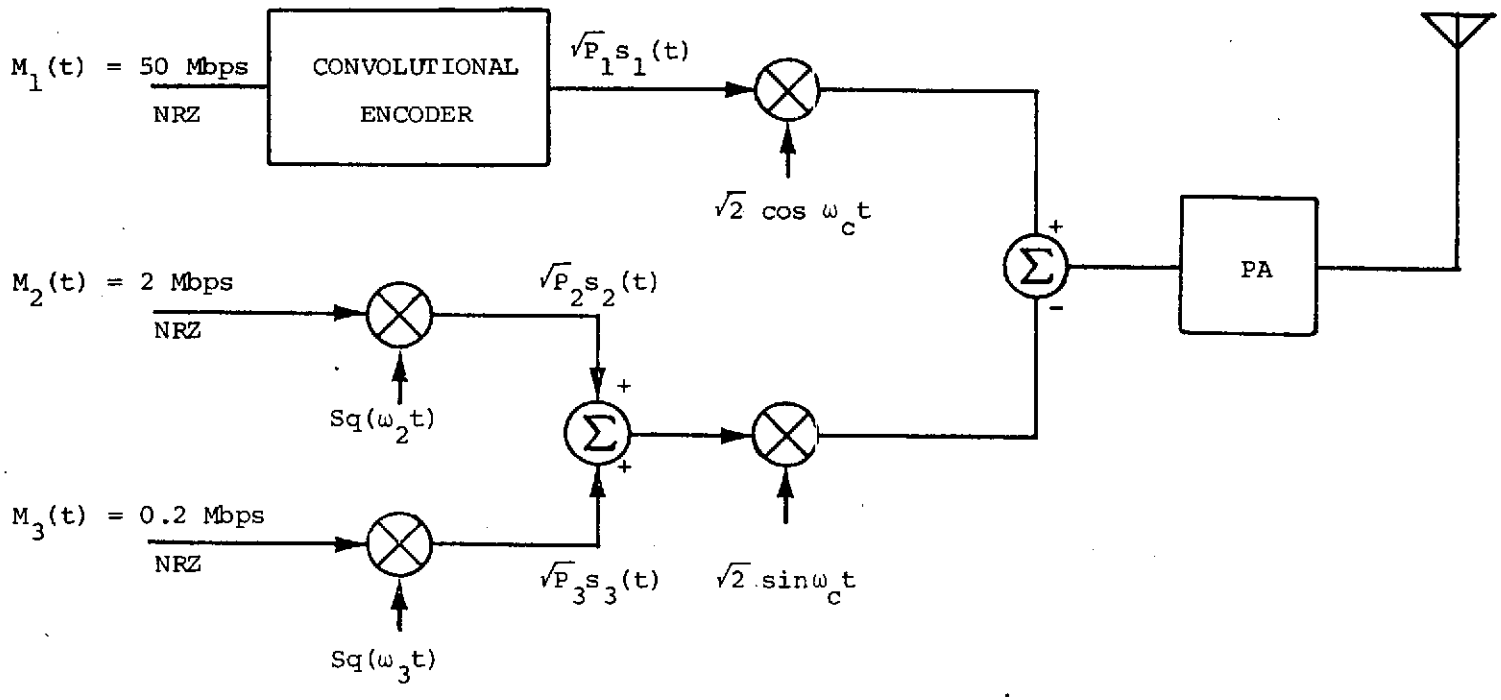

FIGURE 9.9 A PROPOSED SHUTTLE TRANSMITTER BLOCK DIAGRAM USING QUADRATURE-MULTIPLEX WITH CONVOLUTIONAL ENCODER

(3) From Equations (9.27) and (9.53), we can approximate as

$$\frac{P_1 \times 3.31}{50} = \frac{P_2}{2} \tag{9.56}$$

thus,

$$\frac{P_1}{P_T} = 0.87036 \simeq \frac{P'_1}{P} \tag{9.57}$$

From Equation (9.22),

$$P_1/P_T + P_2/P_T\ (1 + \gamma^2) = 1$$

$$P_2/P_T = 0.12964/1.125 = .115236 \tag{9.58}$$

$$P_3/P_T = 0.014404 \tag{9.59}$$

(4) The intermodulation loss in this case is, from Figure 9.5, 1.5×10^{-3} (-28.24 dB). If we had used the interplex system of Figure 9.2, the intermodulation loss would have been 1.529×10^{-3} (-28.16 dB) which is about the same as the previous value.

(5) In Figure 9.8, the corresponding EIRP in each channel has been shown. The figure shows that the power apportionment for the required data rates.

(6) The corresponding QM demodulator is shown in Figure 9.10. The loop loss in this case will be 0.59 dB.

(7) It was tacitly assumed in this design that the subcarriers $Sq(\omega_2 t)$ and $Sq(\omega_3 t)$ were determined such that $s_2(t)$ and $s_3(t)$ were located at the first null of the $s_1(t)$ power spectrum.

9.3 CONCLUSION

In this report, a new modulation scheme, called quadrature multiplex has been proposed to transmit three channel data having different rates. An analysis has been performed for the quadrature

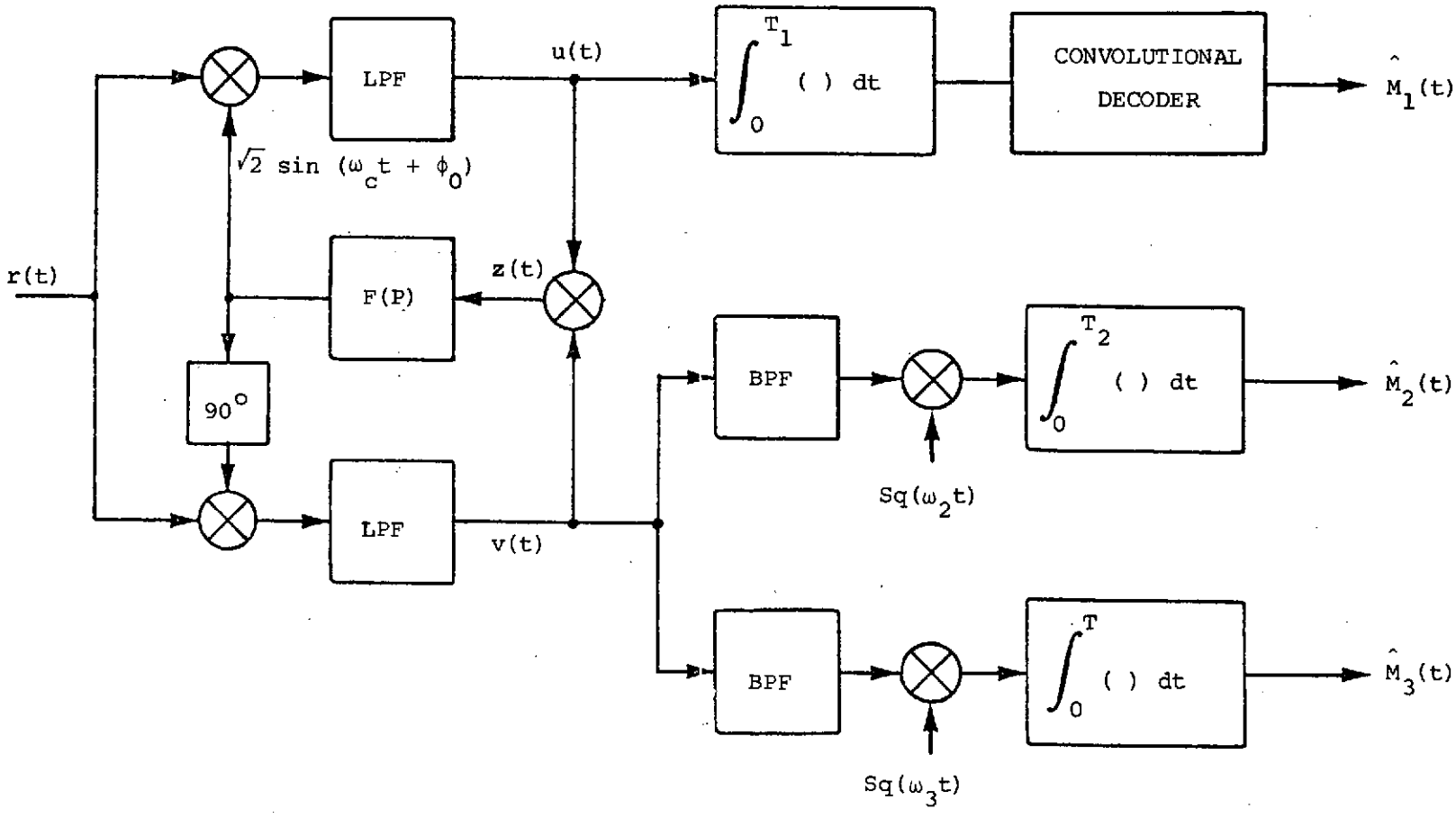

FIGURE 9.10 A PROPOSED RECEIVER BLOCK DIAGRAM FOR THE THREE-CHANNEL QUADRATURE MULTIPLEXED SIGNAL

multiplex modulation and compared to the interplex modulation system. The QM is found to be easier to implement compared to the modulation system with the same performance especially when one data rate is very high relative to the other ones. In implementing the three-channel QM modulator, four balanced modulators and two summing devices are required, while the interplex modulator needs four balanced modulators, a summing device and a (true) phase modulator. Thus, the QM modulator is simpler to implement as compared to the interplex modulator and can be easily modified from, or to the interplex system. Some design curves are provided which are useful to design the QM modulator.

The Orbiter return Ku-Band link has been designed using the QM modulation system as an example. In the link, the 50 Mbps rate channel employs FEC, while the others do not. It turned out that the inter-modulation loss is -28.24 dB which is negligible and each channel has about 5 dB margin.

9.4 REFERENCES

(1) W. C. Lindsey, "Design of Block Coded Communication Systems," IEEE Trans., COM-15, 4, pp. 525-534 (August, 1967).

(2) T. K. Foley and B. J. Gaumond, "Optimum Power Division for Phase Modulated Deep-Space Communications Links," IEEE Trans., AES-3, pp. 400-409 (May, 1967).

(3) S. Butman and Uzi Timor, "Interplex---An Efficient Multichannel PSK/PM Telemetry System," IEEE Trans., COM-20, pp. 415-419 (June, 1972).

(4) Sergei Udalov, "Feasibility Study of An Interplex Modulation System for the Orbiter's Ku-Band Link," Axiomatic Report No. R 7410-5, Axiomatix, Marina del Ray, California 90291 (October 7, 1974).

(5) R. L. Didday and W. C. Lindsey, "Subcarrier Tracking Method and Communication System Design," IEEE Trans., COM-16, pp. 541-550, (August, 1968).

(6) Tracking and Data Relay Satellite System (TDRSS) User's Guide, NASA (GSFC), X-805-74-176, Greenbelt, Maryland (June 10, 1974).

(7) B. H. Batson, "Ku-Band Signal Design," Memorandum (October 7, 1974), NASA, JSC, Houston, Texas.

10.0 STAGGERED QUADRIPHASE SHIFT KEYING (SQPSK)

10.1 INTRODUCTION

Staggered quadriphase shift keying, hereafter denoted as SQPSK, is a relatively new method of phase shift modulations which conserves bandwidth as compared to bi-phase shift keying (BPSK) and overcomes some of the inherent disadvantages of quadriphase shift keying (QPSK). It follows that a good approach to discussing SQPSK is based on comparing it with BPSK and QPSK. In order to accomplish this we must first briefly review BPSK and QPSK. It will then be shown that SQPSK is superior to both BPSK and QPSK with a minimum increase in complexity.

10.2 ANALYSIS

10.2.1 Binary Phase Shift Keying (BPSK)

We first briefly review the modulation format of binary phase shift keying in order to have a basis for later comparison. The general equation describing BSPK is given by

$$s_m(t) = A \cos (\omega_o t + \theta(t)) \tag{10.1}$$

where $\theta(t)$ is derived from a baseband binary signal. For antipodal signaling $\theta(t)$ will take on values of $\pm\pi/2$ corresponding to a random binary digit taking on values of ± 1. We thus have

$$s_m(t) = A \cos (\omega_o t \pm \pi/2) \tag{10.2}$$

or

$$s_m(t) = \pm A \sin \omega_o t \tag{10.3}$$

Thus (10.2) corresponds to modulating $\sin \omega_o t$ with a binary pulse sequence and it follows that the signal space diagram for BPSK is that given in Figure 10.1.

Figure 10.1 SIGNAL SPACE DIAGRAM FOR BPSK

The symbol τ represents one pulse width and A the pulse amplitude. Therefore $A\sqrt{\tau}$ represents the square root of the pulse energy. For white Gaussian noise of spectral density $N_o/2$ watts/Hz, the probability of an error in pulse detection denoted by P_e, is given by[1]

$$P_e = Q\left(\frac{2A\sqrt{\tau}}{\sqrt{2N_o}}\right) \tag{10.4}$$

where

$Q(\alpha)$ is defined as

$$Q(\alpha) \triangleq \frac{1}{\sqrt{2\pi}} \int_{\alpha}^{\infty} e^{-\beta^2/2}\, dB \tag{10.5}$$

One major advantage of BPSK, or PSK in general, as compared with other modulating schemes is its great immunity from noise along with insensitivity to level variations. For example a non-bandlimited BPSK signal can pass through an amplitude limiter without degradation although, in general, a bandlimited BPSK signal will exhibit more frequency spread after amplitude limiting. Since amplitude limiting is either inherent in many systems or purposely applied in order to gain noise immunity and maximum efficiency of the transmitter power amplifier, it follows that the transmitted signal will be more spread in frequency than might be desired causing out of band interference. It will be shown that QPSK also has this disadvantage but that SQPSK is more immune to amplitude limiting.

A major disadvantage of BPSK is wastefulness of available bandwidth. It will be shown in the next section that QPSK uses half the bandwidth of BPSK to transmit the same amount of information.

10.2.2 Quadriphase Shift Keying

In quadriphase shift keying, (QPSK), we transmit information over two orthogonal channels which are chosen so as to not increase the bandwidth requirements over a single channel PSK system. The QPSK modulated signal $s_m(t)$ is represented as

$$s_m(t) = a(t) \sin(\omega_o t + \psi) + b(t) \cos(\omega_o t + \psi) \qquad (10.6)$$

The 'sin' and 'cos' represent orthogonal signals which are modulated by random binary bit streams a(t) and b(t) respectively. Assuming that $s_m(t)$ is narrowband, the two modulating signal components a(t) and b(t) can be separated and recovered at the receiver by using conventional orthogonal demodulation techniques. Therefore we are transmitting two channels of information over one available channel and it will subsequently be shown that the bandwidth requirement is one-half that of one channel PSK. Thus the main advantage of QPSK over BPSK is bandwidth conservation. Of course M'ary PSK also conserves bandwidth but at the price of increased probability of error. For the same overall bit rate, the bit error for QPSK is the same as for BPSK which will be shown later.

Refer to Figure 10.2 and Figure 10.3 which are the simplified block diagrams of a QPSK and SQPSK systems. For QPSK, switch S in Figure 10.2 is closed. In operation, a binary bit stream, s(t), as shown in Figure 10.4 is the input of a signal splitter. The purpose of the signal splitter is to yield two output random bit streams a(t) and b(t) which together contain all the information in s(t). Conventionally, a(t) consists of the even (odd) bits and b(t) the odd (even) bits of

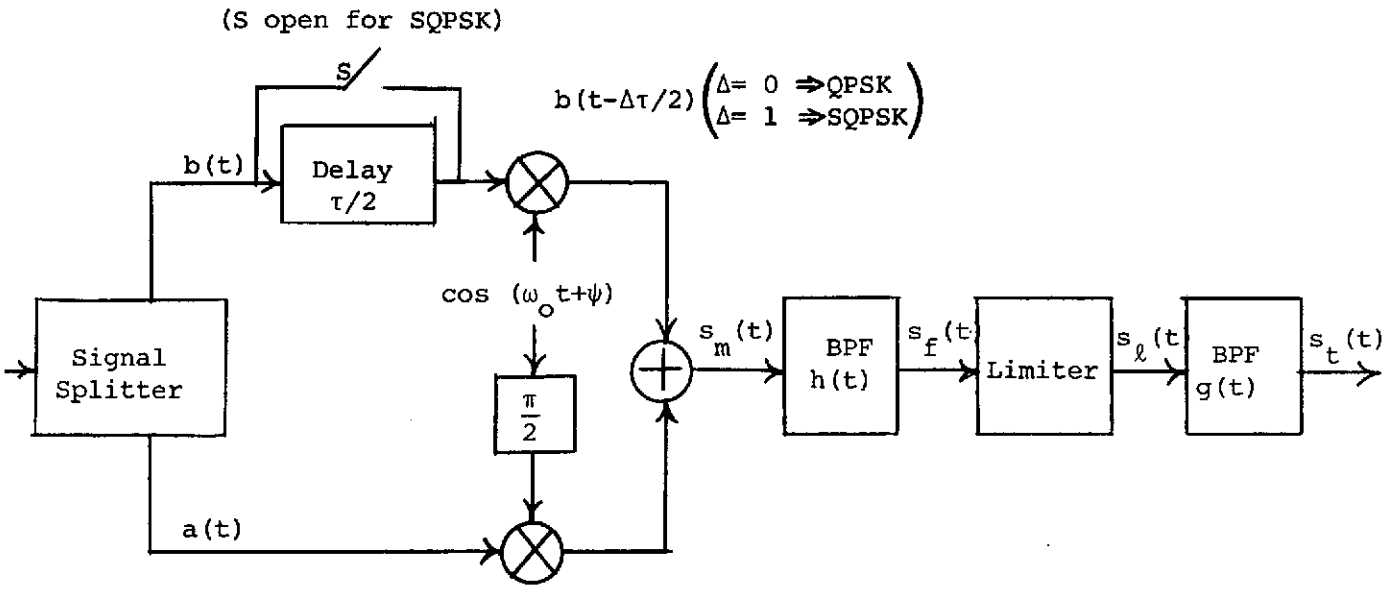

FIGURE 10.2 SIMPLIFIED TRANSMITTER BLOCK DIAGRAM FOR QPSK AND SQPSK

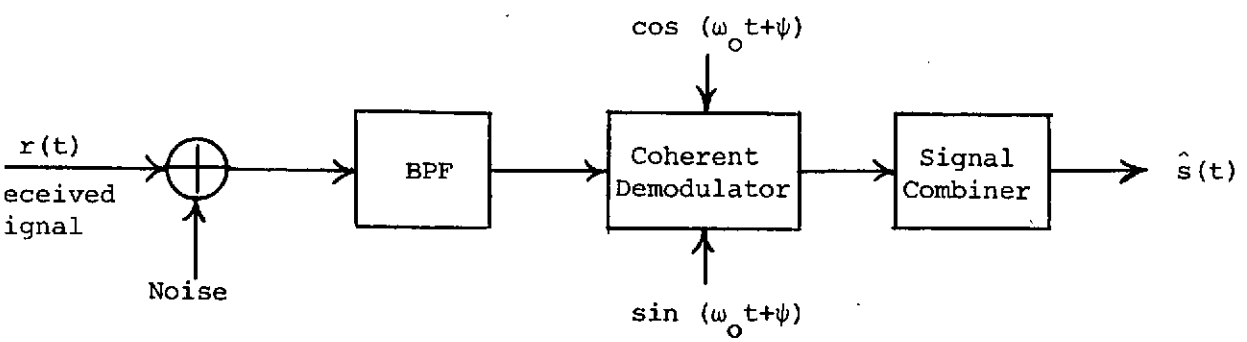

FIGURE 10.3 SIMPLIFIED RECEIVER BLOCK DIAGRAM FOR QPSK AND SQPSK

s(t). Also the pulses of a(t) and b(t) are of width τ, twice the width of s(t). This signal is filtered to decrease sideband energy yielding $s_f(t)$ which is then amplitude limited by the power output amplifier of the transmitter. (The power output amplifier is usually operated in a saturated mode to gain maximum efficiency.) Limiting may also occur prior to the power amplifier but we will lump the effects into one block on the diagram designated 'limiter.' The limited signal, $s_\ell(t)$, may undergo more filtering, g(t), before being transmitted to eliminate excessive sideband transmission produced by the limiting action.

The received signal r(t) is combined with additive white Gaussian noise n(t), bandpass filtered and coherently detected. This yields baseband signals $\hat{a}(t)$ and $\hat{b}(t)$ which are then combined yielding a statistical estimate of s(t), $\hat{s}(t)$.

In order to compare QPSK with BPSK, we assume the same transmitted power and rate of transmitted information. Also we note that BPSK results from letting b(t) = 0. The power spectrum of $s_m(t)$ for BPSK is given in Appendix 10.A, equation (10.A.17), as

$$S_{s_m}(\omega^+) = \frac{\pi}{4} S_a(\omega-\omega_o)^* \qquad \text{(BPSK)} \qquad (10.7)$$

and the power spectrum for QPSK is given by one half of equation (10.A.21) (for equal power) as

$$S_{s_m}(\omega^+) = \frac{\pi}{8} \{S_a(\omega-\omega_o) + S_b(\omega-\omega_o)\} \quad \text{(QPSK)} \qquad (10.8)$$

We assume that a(t) and b(t) have the same autocorrelation function (this will usually be true since a(t) and b(t) are usually derived from a single bit stream) and therefore the power spectrum $S_a(\omega)$ and $S_b(\omega)$ of a(t) and b(t) respectively will be the same. Therefore

---

* ω^+ implies $\omega>0$. The power spectrum for negative frequencies will be a mirror image of $S_{s_m}(\omega^+)$ since $S_{s_m}(\omega)$ is even.

(10.8) becomes

$$S_{s_m}(\omega^+) = \frac{\pi}{4} S_a(\omega-\omega_o) \qquad \text{(QPSK)} \qquad (10.9)$$

$S_a(\omega)$ for QPSK is half as wide as for BPSK since the pulse of a(t) for QPSK has twice the width of a(t) for BPSK, i.e.,

$$S_a(\omega)_{QPSK} = S_a(2\omega)_{BPSK} \qquad (10.10)$$

It follows that the modulated signal $s_m(t)$ for QPSK has half the bandwidth of BPSK for the same total bit rate. This also applies to the filtered signal $s_f(t)$.

In considering the effect of limiting we assume that the filter h(t) does not produce intersymbol interference. Also it is assumed that the limiter is a hard limiter. With these assumptions, it is shown in Appendix 10.A (equations (10.A.20) and (10.A.27)) that hardlimiting completely restores the sideband energy which was suppressed by h(t). Therefore the power spectrum of the hardlimited signal, $s_\ell(t)$, for BPSK and QPSK is given within a proportionality constant by (10.7) and (10.9) respectively.

The previous important result implies that the bandpass filter h(t) has no effect whatsoever on the spectrum of $s_\ell(t)$. Also we note that although BPF g(t) can eliminate some of the unwanted sideband energy generated by the hardlimiter, the hardlimiter (in this case the power output amplifier) will be relatively inefficient since it is dissipating power which is not being transmitted. Herein lies the major disadvantage of QPSK. It will be shown in the next section that QPSK overcomes this disadvantage while maintaining the attributes of QPSK over BPSK. Probability of bit error will also be considered in the next section on SQPSK.

10.2.3 Staggered Quadriphase Shift Keying (SQPSK)

SQPSK was developed in order to at least partially eliminate the effect of the limiter restoring the high frequency sidebands which were reduced by the bandpass filter. Intuitively, we note that since QPSK allows phase transitions of $\pm\pi$ in addition to $\pm \pi/2$ that such polarity changes when filtered introduce amplitude distortion which is subsequently converted to phase modulation by a hard limiter.[2] This phase distortion recreates the high frequency sidebands. Of course bandpass filtering after hardlimiting can again reduce these sidebands to a minimum but since the final power amplifier (TWT) performs hard-limiting this effectively decreases the efficiency of the power amplifier. SQPSK overcomes this disadvantage by allowing only phase transitions of $\pm \pi/2$. For a bandlimited signal, even transitions of $\pm \pi/2$ will result in some restoration of the high frequency sidebands after hard-limiting but it turns out that the effect is not nearly as severe as for QPSK especially if the type of bandpass filtering is carefully chosen.

Referring to Figure 10.2, switch S is open for SQPSK allowing $b(t)$ to be delayed in time by half its pulse width or $\tau/2$. Comparing $a(t)$ and $b(t-\tau/2)$ as in Figure 10.4, we note that the maximum phase transition at any given time is limited to $\pm \pi/2$ and herein lies the major difference between QPSK and SQPSK. The rest of the transmitter and receiver is essentially the same as for QPSK.

The power spectrum of the modulated signal, $s_m(t)$, is given by (10.8) and since a time shift does not effect the power spectrum it follows that (10.9) is also applicable to SQPSK again assuming $a(t)$ and

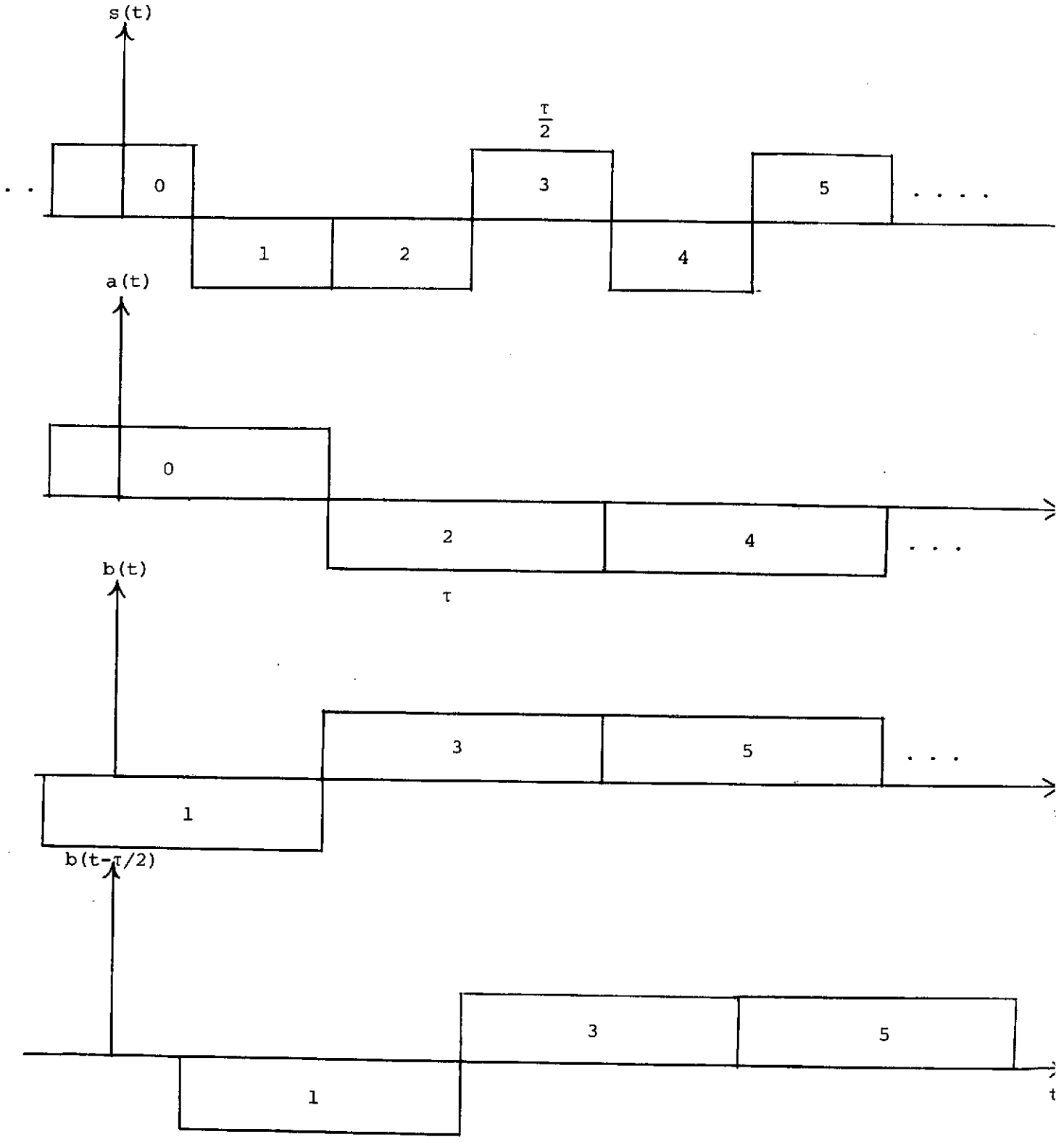

FIGURE 10.4 BASEBAND SIGNAL WAVEFORMS FOR QPSK AND SQPSK

b(t) have the same autocorrelation function. Therefore the power spectrum of $s_m(t)$ for SQPSK is given by

$$S_{s_m}(\omega^+) = \frac{\pi}{2} S_a(\omega-\omega_o) \qquad \text{(SQPSK)} \qquad (10.11)$$

It follows, as in QPSK, that

$$S_{s_m\,SQPSK}(\omega^+) = S_{s_m\,BPSK}[2(\omega-\omega_o)] \qquad (10.12)$$

i.e., the modulated signal $s_m(t)$ for QPSK has half the bandwidth of BPSK for the same total bit rate; this result also applying for $s_f(t)$.

The output of the hardlimiter, however, does depend on the filtering action of h(t) as shown in Appendix 10.A and Appendix 10.B. In Appendix 10.A an equivalent pulse $p_\ell(t) \longleftrightarrow P_\ell(f)$ (equation 10.A.34 and 10.A.36) is defined at the output of the hardlimiter. If the baseband input pulses to the limiter are rectangular then the equivalent output pulses are rectangular yielding an output spectrum of the form $Sa(\alpha\omega)$.* If the baseband input pulses to the limiter are raised cosine or Gaussian, then the equivalent output pulses are given in Appendix 10.B. For both the raised cosine and Gaussian, the equivalent output pulse is more rectangular than the input pulse thereby giving rise to more high frequency energy. The output power spectra for raised cosine and Gaussian inputs does not decay as rapidly as the input spectra; however, the output spectra decays more rapidly as compared with QPSK which always yields a $Sa(\alpha\omega)$ output spectrum. Therefore, at least for the raised cosine and Gaussian case, SQPSK is superior to QPSK in relation to excessive sideband energy at the output of the limiter. This implies more efficient operation of the power output amplifier, less interference

---

* $Sa(\beta) = \sin \beta/\beta$

due to spurious radiation and less filtering required by the transmitter output filter. The increase in complexity as compared to QPSK is minimal as can be seen by referring to Figure 10.2 and 10.3.

We now consider the bit error rate of QPSK/SQPSK as compared to BPSK. It was previously shown that QPSK/SQPSK can transmit the same information as BPSK but utilizing half the bandwidth. It will now be shown that the total bit error rate for QPSK and SQPSK is the same as BPSK under the constraint that the transmitted and received power be the same for both modulation schemes. From (10.7) and (10.9) we see that the baseband pulse amplitude of QPSK/SQPSK must be $1/\sqrt{2}$ that of BPSK in order to maintain equal power outputs. From Figure 10.4, however, we note that since the baseband pulse widths of QPSK/SQPSK are twice that of BPSK, the received pulse energy in both cases is the same. Normalizing the pulse energy to 1, Figure 10.5 shows the signal space diagrams for both cases. For QPSK/SQPSK, however, the coherent quad demodulator (assumed ideal) will yield two individual signals each having the same signal space diagram as BPSK. Since the probability of bit error is a function of the distance between the signals on the diagram, which is the same in all cases, the bit error probability is the same for BPSK and QPSK/SQPSK. It follows that the probability of error for white Gaussian noise is given by equations (10.14) and (10.15) as in the BPSK case.

FIGURE 10.5 SIGNAL SPACE DIAGRAMS FOR BPSK AND QPSK/SQPSK

SQPSK has other advantages to QPSK in addition to the one previously discussed. For example, it has been shown that under certain conditions SQPSK offers approximately a 3 dB advantage over QPSK in the presence of receiver oscillator phase jitter.[3] Also, the improvement of SQPSK over QPSK for small amounts of jitter is shown to be proportional to the excess bandwidth allowed in transmission with little or no improvement available for a minimum bandwidth system. However, the performance of SQPSK is in no case inferior to QPSK in relation to phase jitter. It follows that SQPSK is most advantageous in relation to phase jitter in systems which do not track out the jitter and have excess bandwidth available.

Another advantage of SQPSK over QPSK arises for the case where the orthogonality between the channels is destroyed in part by nonideal conditions. It was previously shown that both QPSK and SQPSK have detection performances identical to BPSK if orthogonality is preserved. In this case, however, the detection performance of SQPSK can be shown to fall between BPSK and QPSK.[4] In fact, for equally likely modulating pulses, the probability of bit error is the average of the probability of bit errors for BPSK and QPSK and it follows that the detection performance on SQPSK is as good or better than QPSK.

In order to gain maximum power efficiency, a reference carrier is rarely transmitted in phase shift keying. Therefore the reference carrier must be derived from the modulated signal at the receiver for proper synchronization. For BPSK, a squaring loop can perform this function but the desired reference will have a twofold phase ambiguity of 0 or π radians. QPSK, on the other hand, requires a fourth order multiplier which has a fourfold ambiguity of 0, $\pm \pi/2$ or π. SQPSK,

however, requires only a multiplier of order two as in BPSK and therefore the reference has only a two state ambiguity. Also since fourth order multiplication results in a larger loss than second order, SQPSK achieves better synchronization performance than QPSK expecially for low SNR.[5]

10.3 SUMMARY

It has been shown that SQPSK is superior to QPSK in at least four ways. The first advantage is decreased spurious sideband energy at the transmitter output amplifier resulting in higher output amplifier efficiency and less out of band interference. Also, SQPSK is more immune to receiver oscillator instability, offering in some cases approximately a 3 dB advantage over QPSK. In addition SQPSK offers a detection performance which is as good or better than QPSK. For suppressed carrier transmission, SQPSK also has the advantage of less phase ambiguities and better synchronization performance as compared with QPSK. Therefore it appears that SQPSK will be used in present and future systems since it requires little additional complexity and yet offers many advantages over QPSK.

10.4 REFERENCES

(1) J. Wozencraft and Irwin Jacobs, Principles of Communications Engineering, New York:Wiley, 1967, pp. 82-83.

(2) S. A. Rhodes, "Effects of Hardlimiting on Bandlimited Transmission with Conventional and Offset QPSK Modulation," in 1st IEEE Conf. Telecommun., Houston, Tex., Dec. 1972.

(3) R. D. Gitlin, "The Performance of Staggered Quadrature Amplitude Modulation in the Presence of Phase Jitter," IEEE Trans., COM-23, pp. 348-352 (March, 1975).

(4) S. A. Rhodes, "Effect of Noisy Phase Reference on Coherent Detection of Offset-QPSK Signals," IEEE Trans., COM-22, pp. 1046-1055 (August 1974).

(5) S. A. Rhodes, "Carrier Synchronization Techniques for Offset-QPSK Signals," NTC, San Diego, Calif., Dec. 1974.

(6) R. K. Kwan, "Effects of Filtering and Limiting a Double-Binary PSK Signal," paper presented at Canadian IEEE Symposium on Communications, Montreal, Nov. 7, 1968.

APPENDIX 10.A

POWER SPECTRUM OF BPSK, QPSK AND SQPSK

This appendix derives the power spectrum of BPSK, QPSK and SQPSK before and after filtering and after hardlimiting. The relevant signals with their appropriate notation are shown in Figure 10.A.1.

The modulated signal, $s_m(t)$, is given by*

$$s_m(t) = a(t) \cos \omega_o t + b(t) \sin \omega_o t \tag{10.A.1}$$

where

$$a(t) = \sum_k a_k \, p(t-k\tau) \tag{10.A.2}$$

$$b(t) = \sum_k b_k \, p(t-k\tau-\Delta\tau/2); \qquad \Delta = 0 \text{ for QPSK}, \quad \Delta = 1 \text{ for SQPSK} \tag{10.A.3}$$

The coefficients a_k and b_k are independent binary random variables which take on values of ± 1 with equal probabilities, and $p(t)$ is given by

$$p(t) = g\left(-\frac{\tau}{2}, \frac{\tau}{2}\right) \tag{10.A.4}$$

where the gate function $g(\alpha,\beta) = \begin{cases} 1 & \text{for } \alpha \le t \le \beta \\ 0 & \text{otherwise} \end{cases}$

The filtered signal, $s_f(t)$, is given by

$$s_f(t) = u(t) \cos \omega_o t + v(t) \sin \omega_o t \tag{10.A.5}$$

or

$$s_f(t) = \sqrt{u^2(t) + v^2(t)} \cos (\omega_o t + \theta(t)) \tag{10.A.6}$$

where

$$u(t) = a(t) * h(t) \tag{10.A.7}$$

$$v(t) = b(t) * h(t) \tag{10.A.8}$$

Hereafter we will be assuming that the filtered pulses will be essentially disjoint, i.e., $\begin{cases} u(t-k\tau)u(t-\ell\tau) = 0 \\ v(t-k\tau)v(t-\ell\tau) = 0 \end{cases}$ for $k \neq \ell$ and for all t.

---

* For simplicity we are assuming the arbitrary phase angle ψ is zero.

After hardlimiting we have

$$s_\ell(t) = x(t) \cos \omega_o t + y(t) \sin \omega_o t \tag{10.A.9}$$

where

$$x(t) = \frac{u(t)}{\sqrt{u^2(t) + v^2(t)}} \tag{10.A.10}$$

$$y(t) = \frac{v(t)}{\sqrt{u^2(t) + v^2(t)}} \tag{10.A.11}$$

We now derive the general power spectrum equation. Let $s(t)$ be given by

$$s(t) = \alpha(t) \cos \omega_o t + \beta(t) \sin \omega_o t \tag{10.A.12}$$

where $\alpha(t)$ and $\beta(t)$ are random binary pulse streams with pulse widths τ. It can be shown that the power spectrum $S_s(\omega)$ of $s(t)$ is given by

$$S_s(\omega) = \frac{\pi}{4} \{S_\alpha(\omega+\omega_o) + S_\beta(\omega+\omega_o) + S_\alpha(\omega-\omega_o) + S_\beta(\omega-\omega_o) + 2\text{Im } S_{\beta\alpha}(\omega+\omega_o) + 2\text{Im } S_{\beta\alpha}(\omega-\omega_o)\} \tag{10.A.13}$$

where

$$S_\alpha(\omega) = \frac{1}{\tau} |P_\alpha(\omega)|^2 \qquad \text{(Power spectrum of } \alpha(t)) \tag{10.A.14}$$

$$S_\beta(\omega) = \frac{1}{\tau} |P_\beta(\omega)|^2 \qquad \text{(Power spectrum of } \beta(t)) \tag{10.A.15}$$

$$S_{\beta\alpha}(\omega) = \frac{1}{\tau} P_\beta(\omega) P_\alpha^*(\omega) \qquad \text{(Cross power spectrum of } \beta(t) \text{ and } \alpha(t)) \tag{10.A.16}$$

$P_\beta(\omega)$ and $P_\alpha(\omega)$ are the Fourier transforms over one pulse interval of $\beta(t)$ and $\alpha(t)$ respectively.

Let us apply these results to BPSK, i.e., $b(t) \triangleq 0$. Using (10.A.13), the power spectra $S_{s_m}(\omega)$ and $S_{s_f}(\omega)$ of $s_m(t)$ and $s_f(t)$, respectively, are given by

$$S_{s_m}(\omega) = \frac{\pi}{4}\{S_a(\omega+\omega_o) + S_a(\omega-\omega_o)\} \quad \text{(BPSK)} \qquad (10.A.17)$$

$$S_{s_f}(\omega) = \frac{\pi}{4}\{S_u(\omega+\omega_o) + S_u(\omega-\omega_o)\} \quad \text{(BPSK)} \qquad (10.A.18)$$

where $S_a(\omega)$ and $S_u(\omega)$ are the power spectra of a(t) and u(t) respectively.

After hardlimiting, the power spectrum is

$$S_{s_\ell}(\omega) = \frac{\pi}{4}\{S_x(\omega-\omega_o) + S_x(\omega+\omega_o)\} \quad \text{(BPSK)} \qquad (10.A.19)$$

Using (10.A.10), x(t) can be written as

$$x(t) = \frac{u(t)}{|u(t)|} = a(t) \quad \text{(BPSK)} \qquad (10.A.20)$$

Therefore $S_{s_\ell}(\omega) = S_{s_m}(\omega)$ for BPSK and it follows that hardlimiting has eliminated the effect of bandpass filtering.

Consider now the QPSK case. Some equations below will also apply to SQPSK. Since a(t) and b(t) are assumed independent, it follows that for $\omega > 0$ (designated ω^+) the power spectra $S_{s_m}(\omega^+)$ and $S_{s_f}(\omega^+)$ of $s_m(t)$ and $s_f(t)$ respectively can be written as

$$S_{s_m}(\omega^+) = \frac{\pi}{4}\{S_a(\omega-\omega_o) + S_b(\omega-\omega_o)\} \quad \text{(QPSK/SQPSK)} \qquad (10.A.21)$$

$$S_{s_f}(\omega^+) = \frac{\pi}{4}\{S_u(\omega-\omega_o) + S_v(\omega-\omega_o)\} \quad \text{(QPSK/SQPSK)} \qquad (10.A.22)$$

The power spectrum for $S_{s_\ell}(\omega^+)$ is given by

$$S_{s_\ell}(\omega^+) = \frac{\pi}{4}\{S_x(\omega-\omega_o) + S_y(\omega-\omega_o) - 2\,\mathrm{Im}\,S_{xy}(\omega-\omega_o)\} \quad \text{(QPSK/SQPSK)} \qquad (10.A.23)$$

It is easily shown that x(t) can be written as

$$x(t) = \frac{1}{\sqrt{2}} \frac{\sum_k a_k\, p(t-k\tau)}{\sum_k p(t-k\tau)} \quad \text{(QPSK)} \qquad (10.A.24)$$

or

$$x(t) = \frac{1}{\sqrt{2}} \sum_k a_k \, g(t-k\tau) \qquad \text{(QPSK)} \qquad (10.A.25)$$

where $g(t) = g(-\frac{\tau}{2}, \frac{\tau}{2})$ as defined in (10.A.4).

Similarly

$$y(t) = \frac{1}{\sqrt{2}} \sum_k b_k \, g(t-k\tau) \qquad \text{(QPSK)} \qquad (10.A.26)$$

It follows from (10.A.25) and (10.A.26) for QPSK that $S_{yx}(\omega) = 0$. Also we note that (10.A.25) and (10.A.26) are the same as (10.A.2) and (10.A.3) except for the scale factor $1/\sqrt{2}$. It follows that within a scale factor $S_{s_\ell}(\omega^+)$ and $S_{s_m}(\omega^+)$ are identical. The effect of hardlimiting has therefore completely eliminated the effect of bandpass filtering as in the BPSK case. Or in other words the power spectrum of the hard-limited signal, $s_\ell(t)$, is independent of the characteristics of the bandpass filter and it follows in the QPSK case that $S_{s_\ell}(\omega^+)$ can always be written as

$$S_{s_\ell}(\omega^+) = k \frac{\sin^2[(\omega+\omega_o)\,\tau/2]}{[(\omega+\omega_o)\,\tau/2]^2} \qquad \begin{matrix}\text{(QPSK)} \\ \text{(k = constant)}\end{matrix} \qquad (10.A.27)$$

Lastly let us apply the equations to SQPSK after it has been hard limited. Let $\tilde{P}(t) \triangleq P(t)*h(t)$. For SQPSK, it can be shown that $x(t)$ and $y(t)$ can be written in the following manner,

$$x(t) = \sum_k a_k \, \tilde{P}_x(t-k\tau) \qquad (10.A.28)$$

$$y(t) = \sum_k b_k \, \tilde{P}_y(t-k\tau) \qquad (10.A.29)$$

where $\tilde{P}_x(t)$ and $\tilde{P}_y(t)$ are given by

$$\tilde{P}_x(t) = \frac{g(-\frac{\tau}{2}, \frac{\tau}{2})}{\left[1+\left\{\frac{\tilde{p}(t+\tau/2)}{\tilde{p}(t)}\right\}^2 + \left\{\frac{\tilde{p}(t-\tau/2)}{\tilde{p}(t)}\right\}^2\right]^{1/2}} \qquad \text{(SQPSK)} \qquad (10.A.30)$$

$$\tilde{P}_y(t) = \frac{g(0,\tau)}{\left[1+\left\{\frac{\tilde{p}(t)}{\tilde{p}(t-\tau/2)}\right\}^2 + \left\{\frac{\tilde{p}(t)}{\tilde{p}(t-\tau/2)}\right\}^2\right]^{1/2}} \qquad \text{(SQPSK)} \qquad (10.A.31)$$

We can use (10.A.23) which also applies to SQPSK in determining $S_{s_\ell}(\omega^+)$. It follows from (10.A.28) and (10.A.29) that $S_{yx}(\omega^+) = 0$. Also since $\tilde{P}_y(t) = \tilde{P}_x(t-\tau/2)$, we conclude that $S_x(\omega) = S_y(\omega)$. We can therefore write (10.A.23) as

$$S_{s_\ell}(\omega^+) = \frac{\pi}{2\tau}\left|\tilde{P}_x(\omega-\omega_o)\right|^2 \qquad \text{(SQPSK)} \qquad (10.A.32)$$

where $\tilde{P}_x(\omega)$ is the Fourier transform of (10.A.30), i.e.,

$$\tilde{P}_x(\omega) = \int_{-\tau/2}^{\tau/2} \frac{e^{-j\omega t}dt}{\left[1+\left\{\frac{\tilde{p}(t+\tau/2)}{\tilde{p}(t)}\right\}^2 + \left\{\frac{\tilde{p}(t-\tau/2)}{\tilde{p}(t)}\right\}^2\right]^{1/2}} \qquad (10.A.33)$$

(SQPSK)

If $\tilde{p}(t)$ is even, which we will assume hereafter, (10.A.33) reduces to

$$\tilde{P}_x(\omega) = \tilde{P}_\ell(\omega) = 2\int_0^{\tau/2} \frac{\cos \omega t\, dt}{\{1+q(t)\}^{1/2}}; \qquad \tilde{p}(t) \text{ even} \qquad (10.A.34)$$

where

$$q(t) = \left\{\frac{\tilde{p}(t-\tau/2)}{\tilde{p}(t)}\right\}^2 \qquad (10.A.35)$$

After limiting, then, the equivalent pulse in the time domain is

$$p_\ell(t) = \frac{1}{\{1+q(t)\}^{1/2}}: \qquad \tilde{p}(t) \text{ even} \qquad (10.A.36)$$

It follows from the previous results that for SQPSK $S_{s_\ell}(\omega)$ does depend on the characteristics of the bandpass filter in contrast with the results for QPSK.[6]

APPENDIX 10.B

EQUIVALENT PULSES AFTER HARDLIMITING FOR SQPSK

In Appendix 10.A it was shown that, in contrast to BPSK and QPSK, the power spectrum of SQPSK after bandpass filtering and hard-limiting is dependent on the actual characteristics of the bandpass filter. The exact relationship between $S_{s_\ell}(\omega)$ and $p(t)$ (in this appendix $p(t)$ will be any pulse, i.e., not just rectangular) is given by (10.A.32), (10.A.34), and (10.A.35) of Appendix 10.A. We can expand (10.A.35) by the binomial theorem to yield

$$P_x(\omega) = 2\left\{\frac{\tau}{2}\ \mathrm{Sa}(\omega\ \pi/2) - \frac{1}{2}Q^{(1)}(\omega) + \frac{3}{8}Q^{(2)}(\omega) - \frac{5}{16}Q^{(3)}(\omega) + \ldots.\right\} \tag{10.B.1}$$

where

$$\mathrm{Sa}(\alpha) = \frac{\sin\alpha}{\alpha} \tag{10.B.2}$$

$$Q(\omega) = \int_0^{\tau/2}\left\{\frac{p(t-\ /2)}{p(t)}\right\}^2 \cos\omega t\ dt \tag{10.B.3}$$

and

$$Q^{(n)}(\omega) = \underbrace{Q(\omega)*Q(\omega)*\ldots*Q(\omega)}_{n\ \text{times}}\ ; \qquad * \text{ denotes convolution} \tag{10.B.4}$$

Since in general convolving $Q(\omega)$ with itself results in a function which is more spread in frequency, we conclude that successive terms in (10.B.1) represent wider bandwidth terms. Also we can see from (10.B.1) that in order to conserve bandwidth we desire that $Q(\omega)$ fall

off in frequency as rapidly as possible. This conclusion gives us a clue to the signal design of p(t). Ideally p(t) should be Gaussian or some other time pulse which has a Fourier transform which decays rapidly in frequency. Unfortunately, q(t) and therefore $Q(\omega)$ can be shown to be restricted to a much smaller class of functions than p(t) and it follows that we cannot arbitrarily pick q(t) (i.e., as Gaussian) and expect to be able to find a corresponding p(t) by solving (10.A.35) in Appendix 10.A. In fact, q(t) must be carefully chosen to satisfy certain conditions in order for p(t) to exist. Without going into detail one condition on q(t) is that

$$q(\tfrac{\tau}{2} - t) = q^{-1}(t) \text{ for } q(t) \text{ even and defined over } (-\tfrac{\tau}{2}, \tfrac{\tau}{2}) \tag{10.B.5}$$

A way of determining the pulse p(t) which is least affected by bandfiltering and hardlimiting is to determine $P_x(\omega)$ for different input pulses and compare the results. This will be done in the following sections for a raised-cosine and Gaussian pulse.

Let p(t) be a raised cosine pulse given by

$$p(t) = (\cos^2 \pi t/\tau) g(-\tfrac{\tau}{2}, \tfrac{\tau}{2}) \tag{10.B.6}$$

This pulse is shown as the solid curve in Figure 10.B.1 for $\tau = 1$. The Fourier transform P(f) of p(t) is given by

$$P(f) = \frac{\pi\tau}{2} \left[2\mathrm{Sa}(\omega\ \pi/2) + \mathrm{Sa}\{(\omega - 2\pi/\tau)\tau/2\} + \mathrm{Sa}\{(\omega + 2\pi/\tau)\tau/2\}\right] \tag{10.B.7}$$

(We note that the first term in (10.B.1) and (10.B.7) are the same except for a constant factor.)

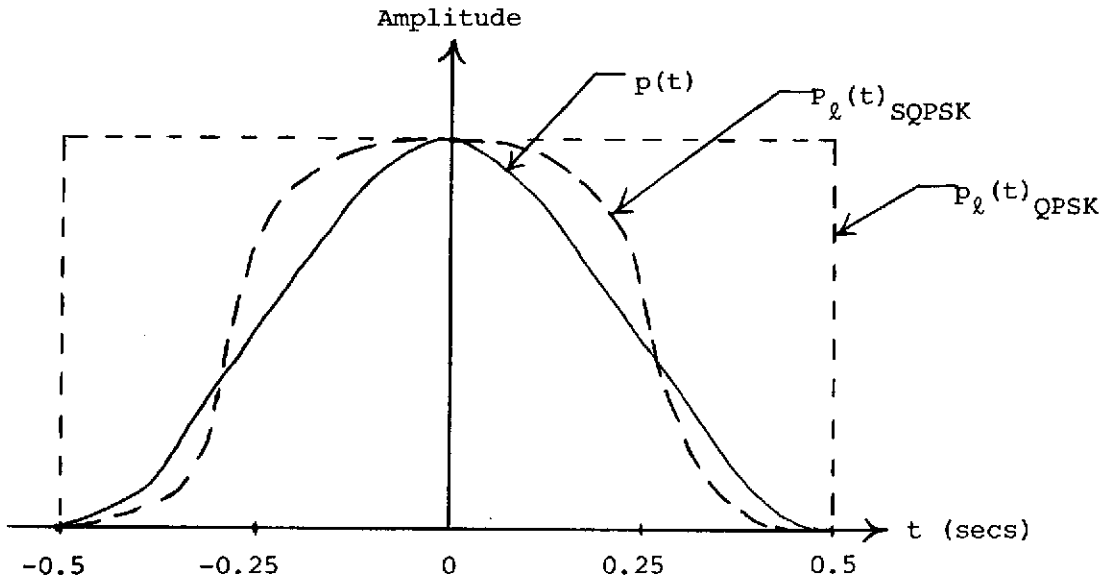

FIGURE 10.B.1 A RAISED COSINE AND EQUIVALENT PULSES FOR QPSK AND SQPSK

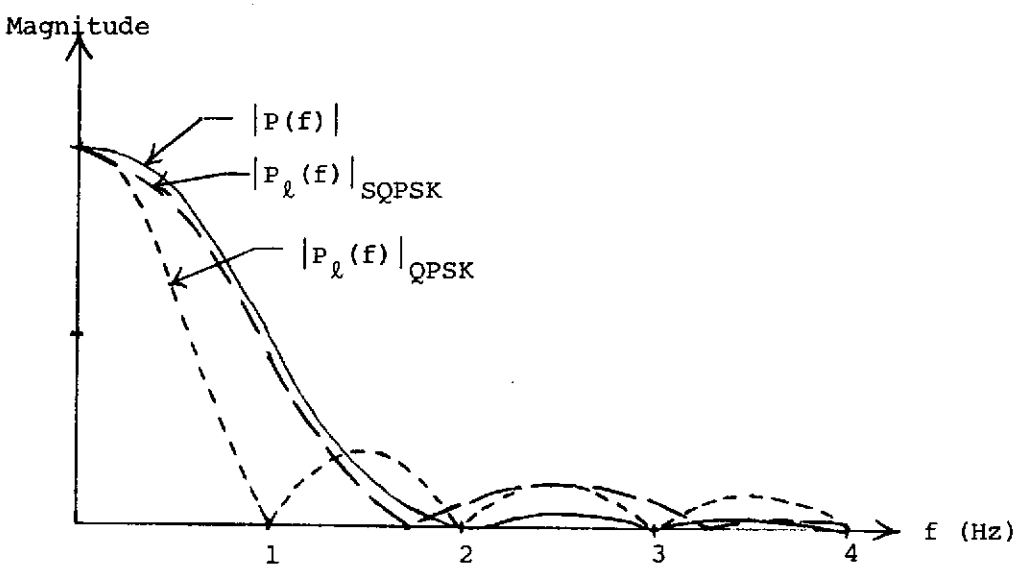

FIGURE 10.B.2 MAGNITUDE OF FOURIER TRANSFORM FOR PULSES IN FIGURE 10.B.1

The equivalent time pulse $p_\ell(t)$ for SQPSK and after hard-limiting is given by (10.A.36) in Appendix 10.A. For the case of the raised cosine $p_\ell(t)$ is given by

$$p_\ell(t) = \frac{g(-\frac{\tau}{2}, \frac{\tau}{2})}{\sqrt{1 + \tan^4 \pi(t)/\tau}} \tag{10.B.8}$$

This pulse for $\tau = 1$ is plotted in Figure 10.B.1 as the curve designated $p_\ell(t)_{SQPSK}$. It is obvious for the raised cosine case that the effect of hardlimiting is to broaden the pulse and give it a more rectangular shape. This tends to restore some of the sideband energy which was filtered out prior to hardlimiting. However the effect is not as pronounced as in the QPSK case where the equivalent pulse $p_\ell(t)_{QPSK}$ is always rectangular as shown in Figure 10.B.1.

The Fourier transform $P_\ell(\omega)$ of $p_\ell(t)$ can be determined from (10.B.1) and (10.B.3) in this Appendix or (10.A.34) in Appendix 10.A. Unfortunately the integrals in both cases are difficult to evaluate for our particular pulse and we therefore choose to find $P_\ell(\omega)$ by using a Fast Fourier Transform (FFT) on (10.B.8). The magnitude of the result, $|P_\ell(f)|_{SQPSK}$, is shown in Figure 10.B.2 along with $|P_\ell(f)|_{QPSK}$ and $|P(f)|$ the magnitude of Equation (10.B.7).

Comparing $|P(f)|$ and $|P_\ell(f)|_{SQPSK}$, we note that limiting has restored some undesirable sideband energy, but we are still better off than with QPSK which has appreciable energy even at 4 Hz.

Consider the Gaussian pulse p(t) shown in Figure 10.B.3 and given by

$$p(t) = e^{-12t^2} \tag{10.B.9}$$

The normalized equivalent pulse is given by

$$P_{\ell}(t) = \frac{\sqrt{2}}{\sqrt{1+e^{-6}e^{24t}}} \qquad (10.B.10)$$

The equivalent pulse as shown in Figure 10.B.3 is again more rectangular in shape than the original pulse. The magnitude of the Fourier transforms $|P(f)|$ and $|P_{\ell}(f)|_{SQPSK}$ is shown in Figure 10.B.4. The magnitude for $f = 0$ has been normalized to 1 in both cases. Again we note that the output of the limiter for SQPSK exhibits more sideband energy than before limiting; however, in comparison with QPSK (see Figure 10.B.2), we are better off.

From the preceding results for QPSK and SQPSK we note that at least in the cases of a raised cosine and Gaussian pulses the unwanted sideband energy is appreciably reduced for SQPSK with little added system complexity. This implies more efficiency from the power output amplifier and less filtering required by the output filter.

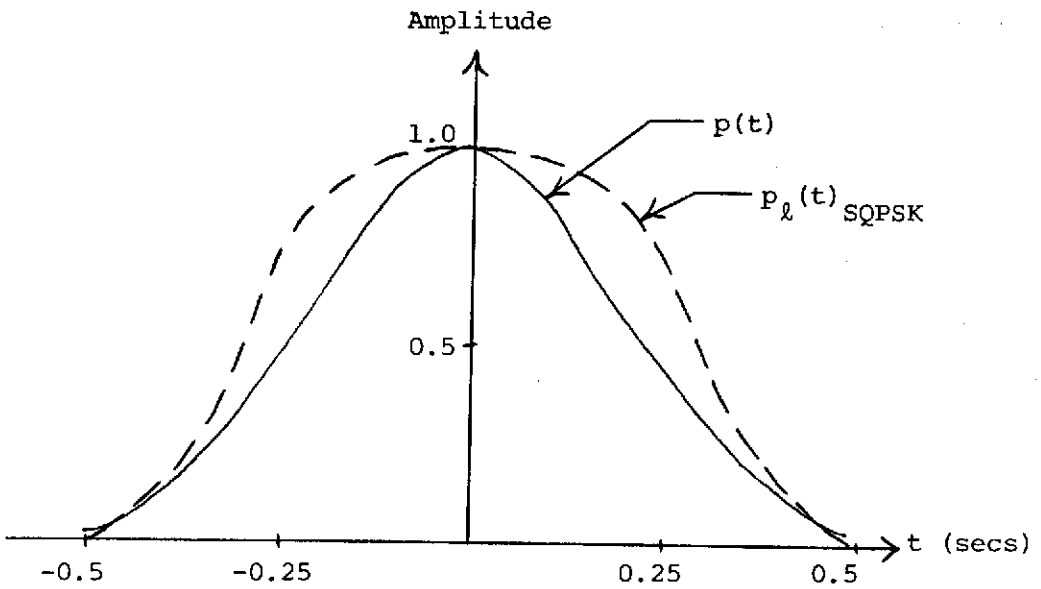

FIGURE 10.B.3 A GAUSSIAN AND EQUIVALENT PULSE FOR SQPSK

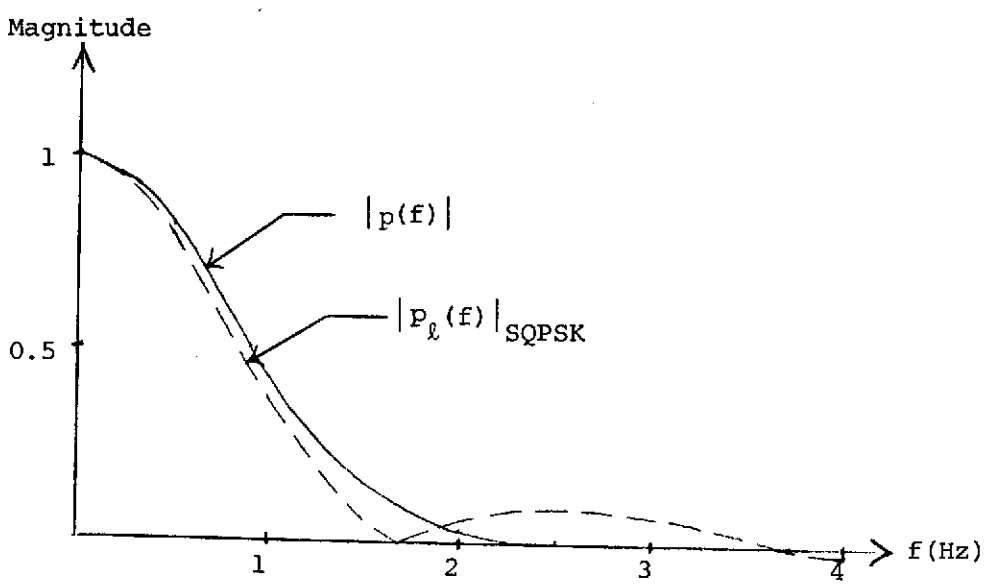

FIGURE 10.B.4 MAGNITUDE OF FOURIER TRANSFORM FOR PULSES IN FIGURE 10.B.3

11.0 ORBITER REENTRY COMMUNICATIONS

Communications blackout during manned spacecraft reentry continues to be a perplexing problem. With lifting reentry vehicles, such as the Shuttle Orbiter, and the associated longer periods for which such vehicles are in a "blackout" condition the problem is even greater. There has been much analysis of the effects of ionization induced interference on reentry vehicles of the ballistic type,[1] but very little analysis has been found with regard to the glide reentry vehicle. These vehicles typically glide with a high angle of attack and the region behind the shock wave on the lower surface of the vehicle can be a region of severe ionization.

The purpose of this investigation is to estimate the plasma attenuation effects for a reentering Orbiter. The communications link of interest is upward from the Orbiter to the proposed Tracking and Data Relay Satellite (TDRSS).

11.1 PROPAGATION IN AN IONIZED MEDIUM

The Orbiter, upon reentering the atmosphere, will be subjected to a shock wave forming in front of the vehicle causing the surrounding air to be compressed and have an increased temperature. As a result of this increased temperature, air molecules become disassociated and ionized. This ionized layer enveloping the spacecraft is referred to as the reentry plasma sheath.

11.1.1 Reentry Plasma

In general the sheath surrounding a glide reentry vehicle is comprised of regions as shown in Figure 11.1. These regions are:

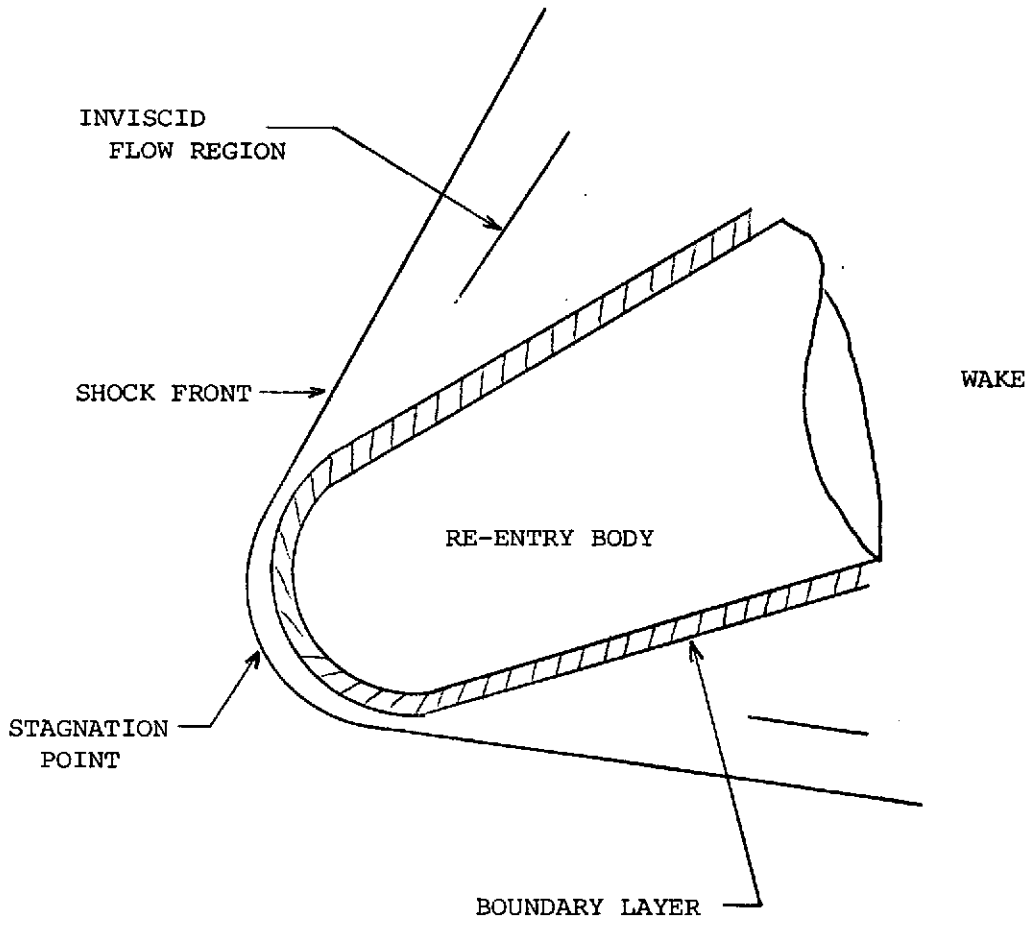

FIGURE 11.1 HYPERSONIC FLOW REGIONS AROUND A RE-ENTRY VEHICLE

a) Shock Front: this is the boundary between disturbed and undisturbed air and characterized by sharp increases in temperature and pressure.

b) Stagnation Point: at this point the velocity of free stream air relative to the vehicle is reduced to zero. The most severe plasma and temperature conditions occur at this point and immediately beyond.

c) Inviscid Flow Region: this is sometimes referred to as the intermediate region which is in a state of chemical nonequilibrium. The plasma conditions at this region are not as severe at the stagnation point but are responsible for communications blackout for most systems.

d) Boundary Layer: this layer, comprised of large velocity and temperature gradients, exists at the surface of the reentry vehicle. For most flight parameters the effects of inviscid flow region dominate those of the boundary layer.

e) Wake Region: this is the region of electron ion recombination usually occurring behind the vehicle.

11.1.2 Electromagnetic Wave Propagation Through A Plasma

If a uniform plasma having an electron density of n electrons per unit volume the a.c. current J which flows in the plasma as the result of an electric field $\overline{E} = e^{j\omega t}$ applied to the plasma is

$$\overline{J} = \frac{ne^2\overline{E}}{m(\omega_c+j\omega)} = \sigma\overline{E} \qquad (11.1)$$

where

n = number of electrons per unit volume

e = electronic charge

m = electronic mass

ω_c = electron collision frequency

$\overline{E}$ = electric field strength

σ = conductivity of the plasma = $ne^2/m(\omega_c+j\omega)$

According to Maxwell's EMF equation

$$\nabla \times \bar{H} = \bar{J} + \frac{\partial}{\partial t}(\varepsilon_o \bar{E}) \qquad (11.2)$$

$$= j\omega\varepsilon_o \bar{E} + \sigma\bar{E}$$

$$= j\omega\varepsilon_o K\bar{E}$$

where

ε_o = free space permitivity

$\varepsilon_o \bar{E}$ = electric displacement

K = effective dielectric coefficient

The effective dielectric coefficient K can be written as

$$K = 1 - \frac{ne^2}{m\varepsilon_o\omega^2} \quad \frac{1 + j(\omega_c/\omega)}{1 + (\omega_c/\omega)^2} \qquad (11.3)$$

and plasma frequency, ω_p, is defined as

$$\omega_p = \sqrt{\frac{ne^2}{m\varepsilon_o}} \qquad (11.4)$$

If it is assumed that the environment is not a vacuum so that the collision frequency will never be zero, the effective dielectric constant is a complex quantity of the form $K = K_r + jK_i$, where

$$K_r = 1 - \left(\frac{\omega_p}{\omega}\right)^2 \frac{1}{1 + (\omega_c/\omega)^2} \qquad (11.5a)$$

$$K_i = -\left(\frac{\omega_p}{\omega}\right)^2 \frac{\omega_c/\omega}{1 + (\omega_c/\omega)^2} \qquad (11.5b)$$

The variation in the real and imaginary parts of the dielectric coefficient, each as a function of ω_c and ω_p, is presented graphically in Figures 11.2 and 11.3 respectively, and the magnitude of the effective dielectric constant is shown in Figure 11.4. Observation of these curves and equation (11.5) leads to the conclusion that for $\omega_c/\omega = 1$, K_i is a maximum. Furthermore, $K = 1$, only when $\frac{\omega_p}{\omega} = 0$ (i.e., zero plasma

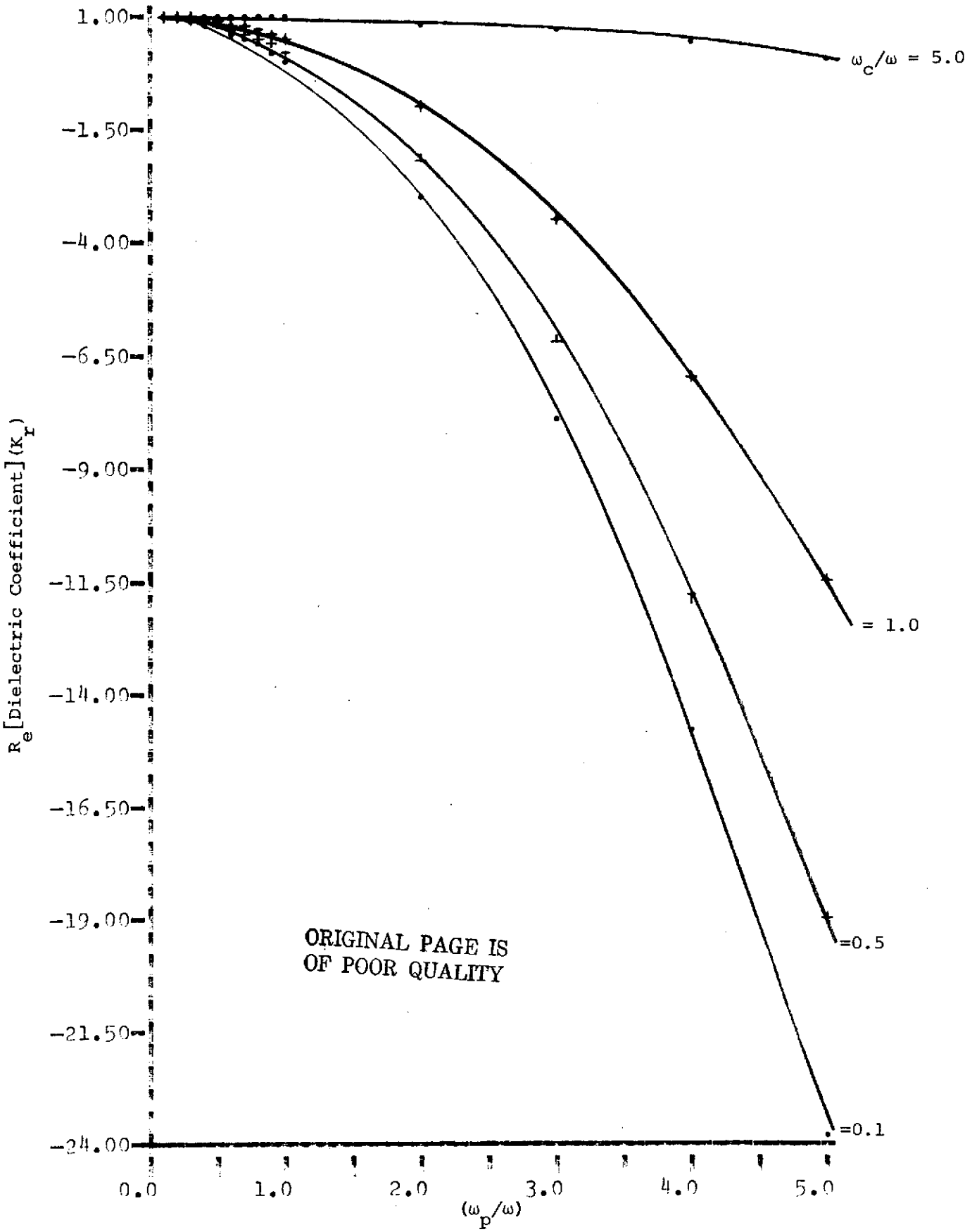

FIGURE 11.2 REAL PART OF DIELECTRIC COEFFICIENT AS A FUNCTION OF (ω_p/ω)

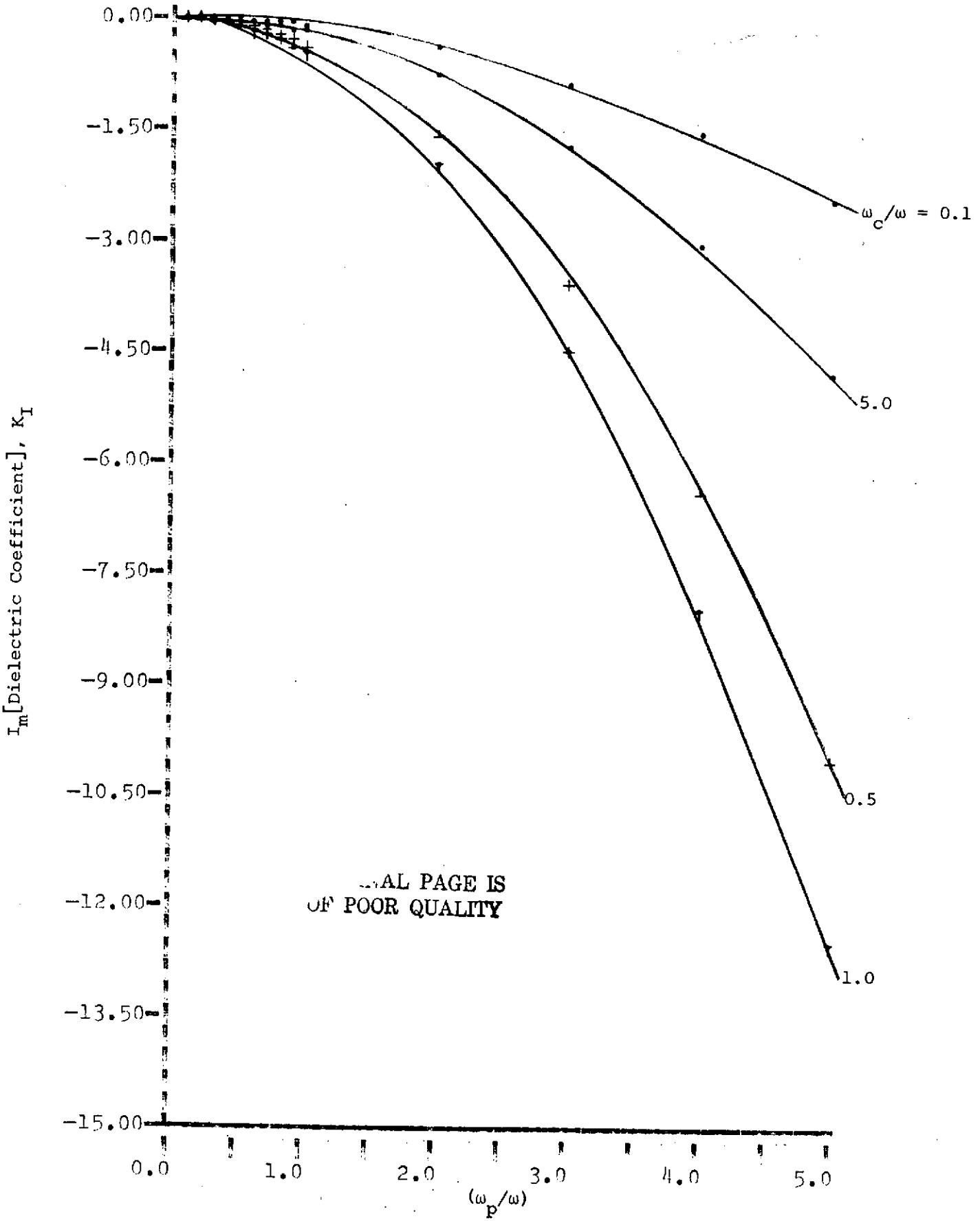

FIGURE 11.3 IMAGINARY PART OF DIELECTRIC COEFFICIENT AS A FUNCTION OF (ω_p/ω)

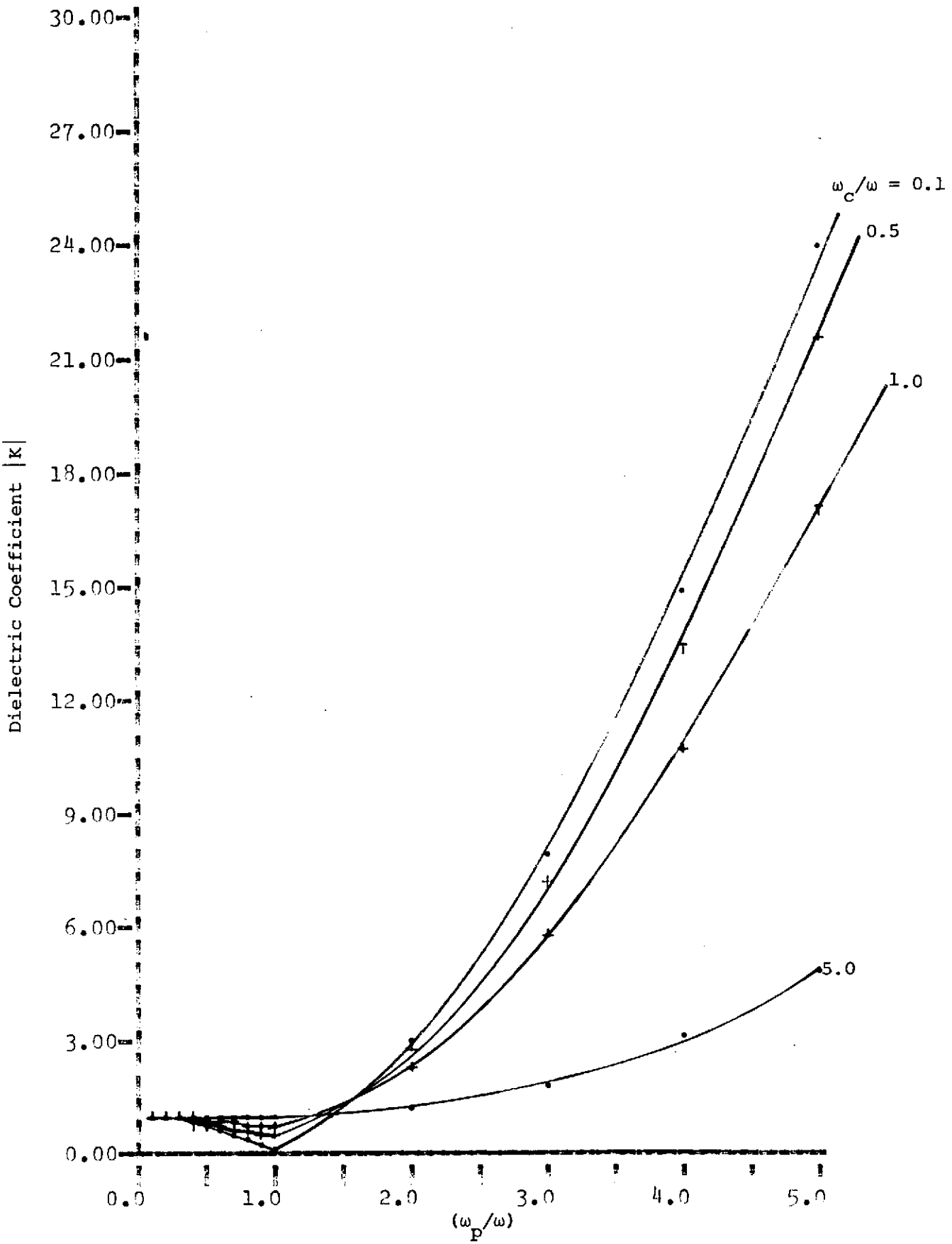

FIGURE 11.4a MAGNITUDE OF DIELECTRIC COEFFICIENT AS A FUNCTION OF (ω_p/ω)

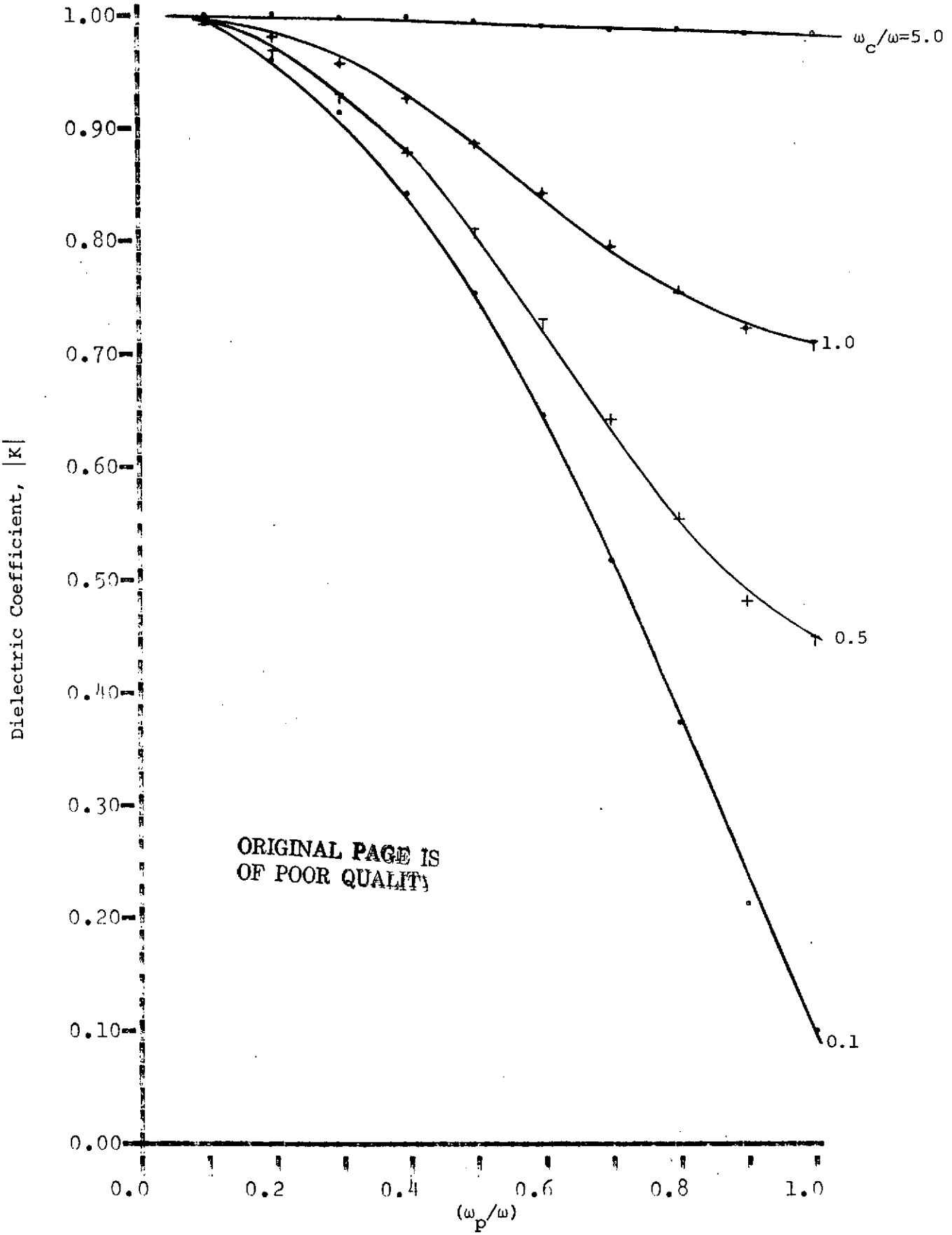

FIGURE 11.4b EXPANDED SCALE FOR DIELECTRIC COEFFICIENT AS A FUNCTION OF (ω_p/ω)

frequency), however for the case when $\omega >> \omega_p$ the effective dielectric constant $K \approx 1$. It is this latter case that one tries to achieve when selecting a propagation frequency to overcome the effects of the plasma sheath.

It has been shown[1] that the plasma can be considered to be a medium with permeability μ_o, permittivity ε_o, and complex conductivity σ. The wave equation satisfied by the electric field vector $\bar{E}$ is then

$$\nabla^2 \bar{E} + \mu_o \varepsilon \omega^2 \bar{E} = 0 \tag{11.6}$$

The one dimensional plane wave solution of (11.6) is of the form

$$\bar{E} = \bar{E}_o \exp(\pm \gamma x) \tag{11.7}$$

where

$\gamma = jkK^{\frac{1}{2}} = \alpha + j\beta$

α = attenuation constant

β = phase constant

$k = \omega/c = 2\pi/\lambda$

λ = free space wavelength

We can then define the phase and attenuation constants to be

$$\beta = k\left[\frac{|K| - K_r}{2}\right]^{\frac{1}{2}} \tag{11.8}$$

$$\alpha = k\left[\frac{|K| + K_r}{2}\right]^{\frac{1}{2}} \tag{11.9}$$

Plots of the normalized phase and attenuation constants as a function of ω_p/ω and ω_c/ω are presented in Figures 11.5 and 11.6 respectively.

The total attenuation of a wave propagating through a homogeneous layer of thickness d may be written as follows:

$$L = 20 \log \exp(\alpha d)$$

$$= 8.686\ \alpha d \ \text{(dB)} \tag{11.10}$$

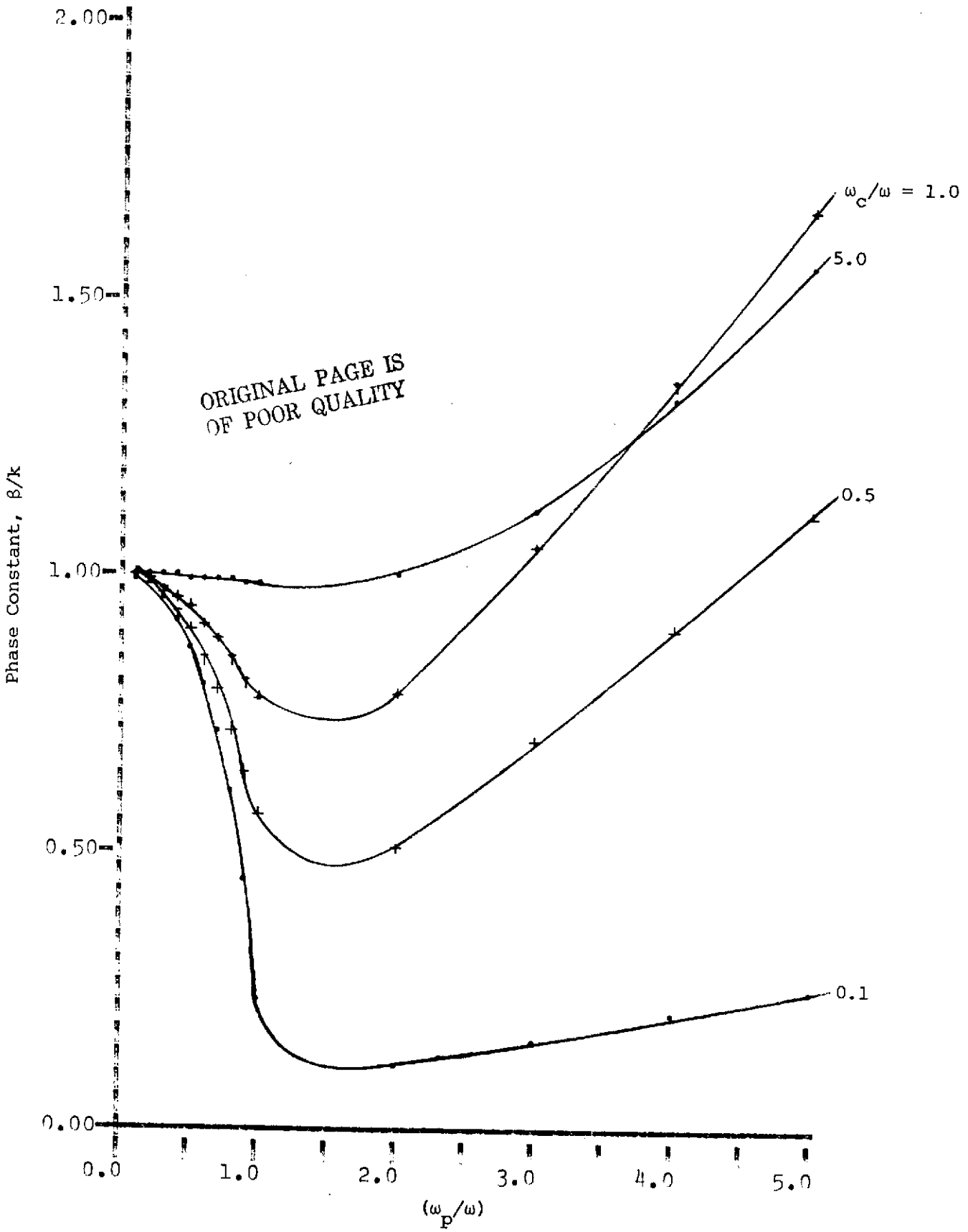

FIGURE 11.5 NORMALIZED PHASE CONSTANT AS A FUNCTION OF ω_p/ω

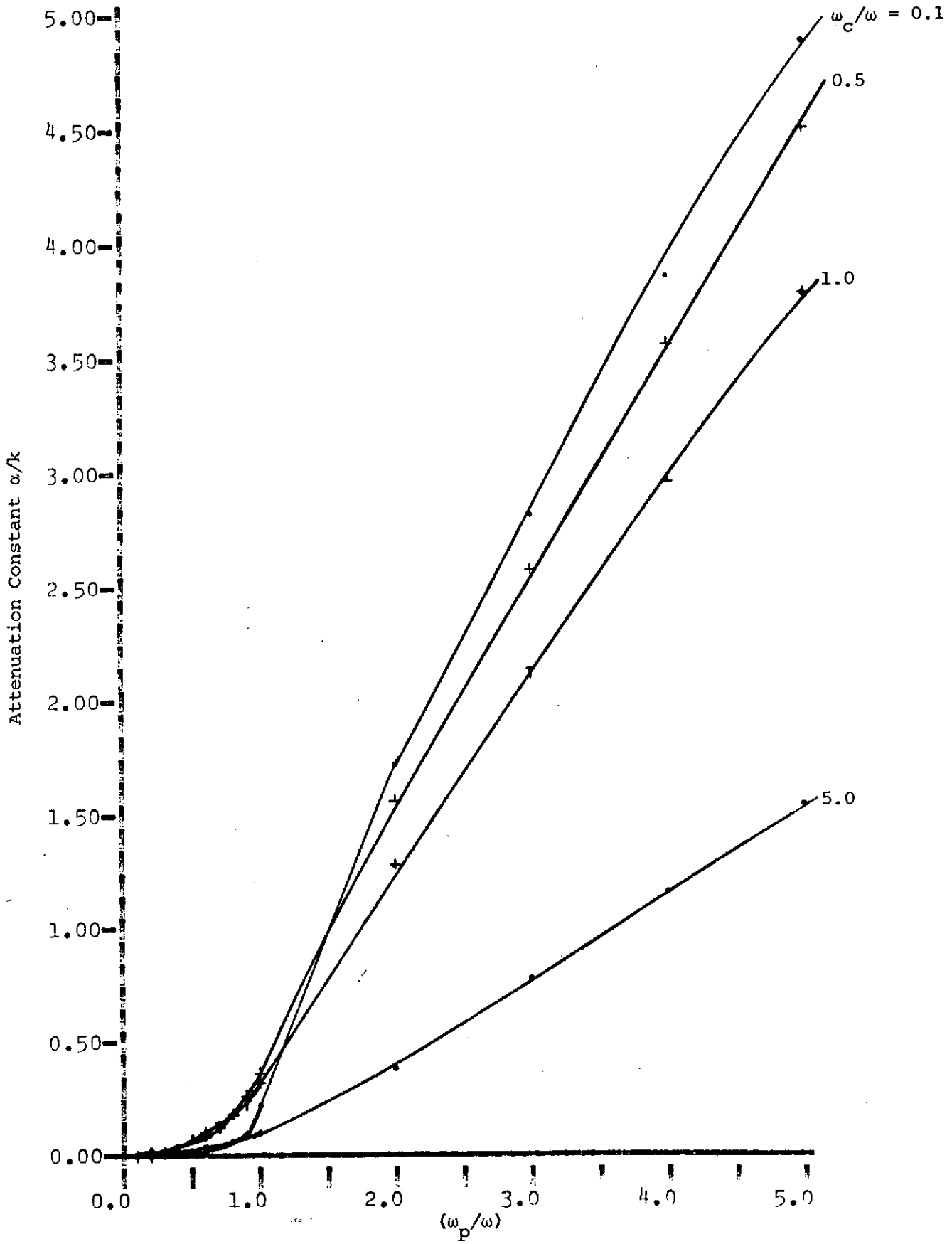

FIGURE 11.6a NORMALIZED ATTENUATION CONSTANT AS A FUNCTION OF ω_p/ω

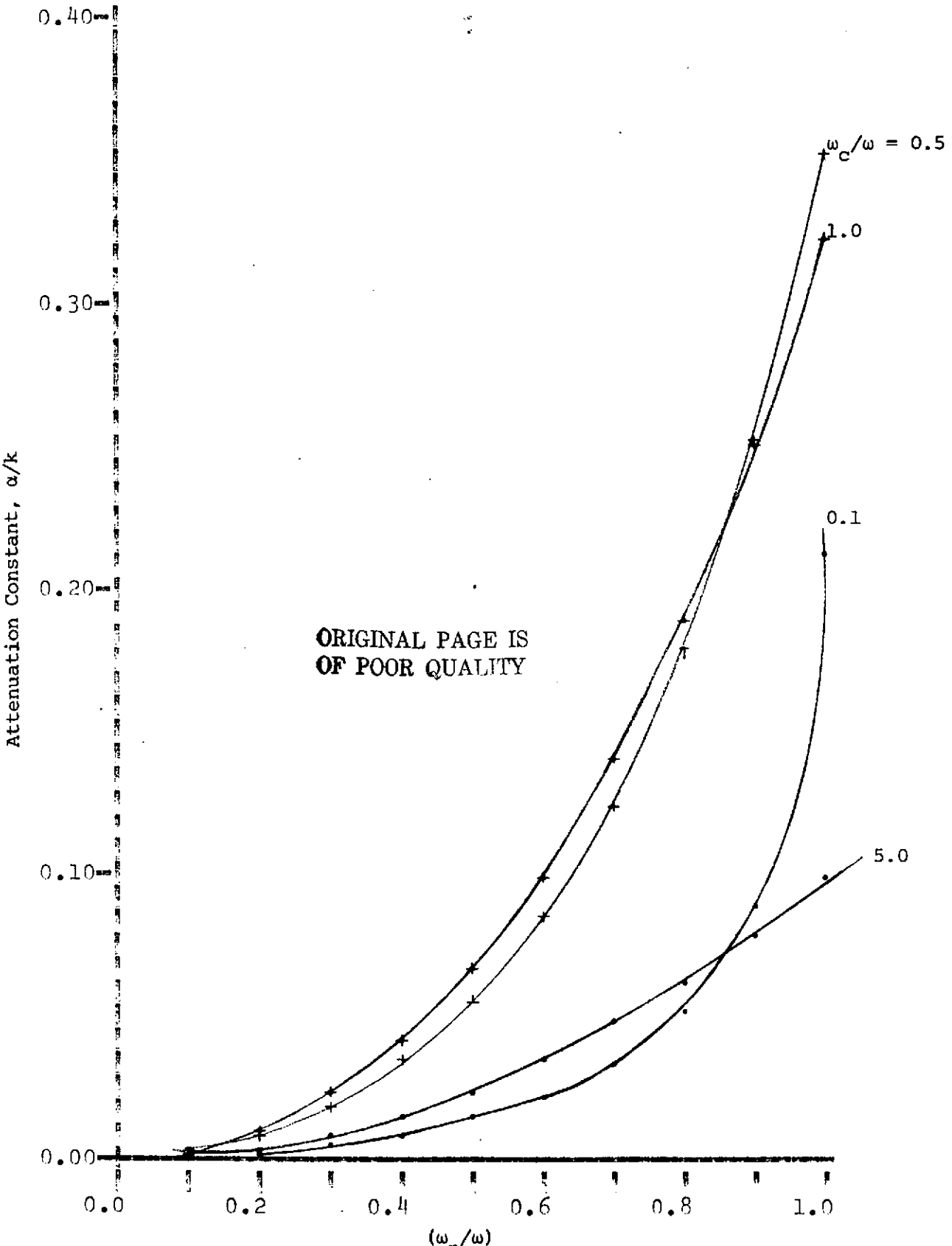

FIGURE 11.6b EXPANDED ATTENUATION CONSTANT AS A FUNCTION OF ω_p/ω

11.2 ESTIMATES OF HYPERSONIC SHOCK EFFECTS OF THE ORBITER DURING REENTRY

Reentry vehicles of the lifting body type, such as the Shuttle Orbiter, consist in part of a lower surface which approximates a flat plate. To minimize the effects of aerodynamic heating the leading edge of most reentry vehicles is blunted. The Orbiter, as shown in Figure 11.7, can be looked upon, then as a vehicle consisting of a small blunt nose followed by a rather large afterbody such as an inclined flat plate.

McCabe and Stolwyk[2] have developed a methodology by which the effects of radio communications interference may be estimated when only the vehicle trajectory and body configuration are known. Simple shapes such as inclined flatplate, conic, and blunt body have been analyzed regarding plasma effects on propagation (the idea being that actual vehicle shapes can be synthesized by combinations of the more elemental forms). For the case of the Shuttle Orbiter the blunt body/ inclined flat plane appears to provide the best approximation.

11.2.1 Inclined Flat Plane

The flow conditions of a flat plate during reentry have been modeled and the plasma and collision frequencies computed as shown in Figures 11.8 and 11.9 respectively as a function of angle of attack. In the figures M sin θ_δ is referred to as the hypersonic similarity parameter which determines the component of velocity normal to the surface of the plate. M_1 is the free stream Mach number and θ_δ is the angle of attack. The depth of the shock region behind the stagnation point may

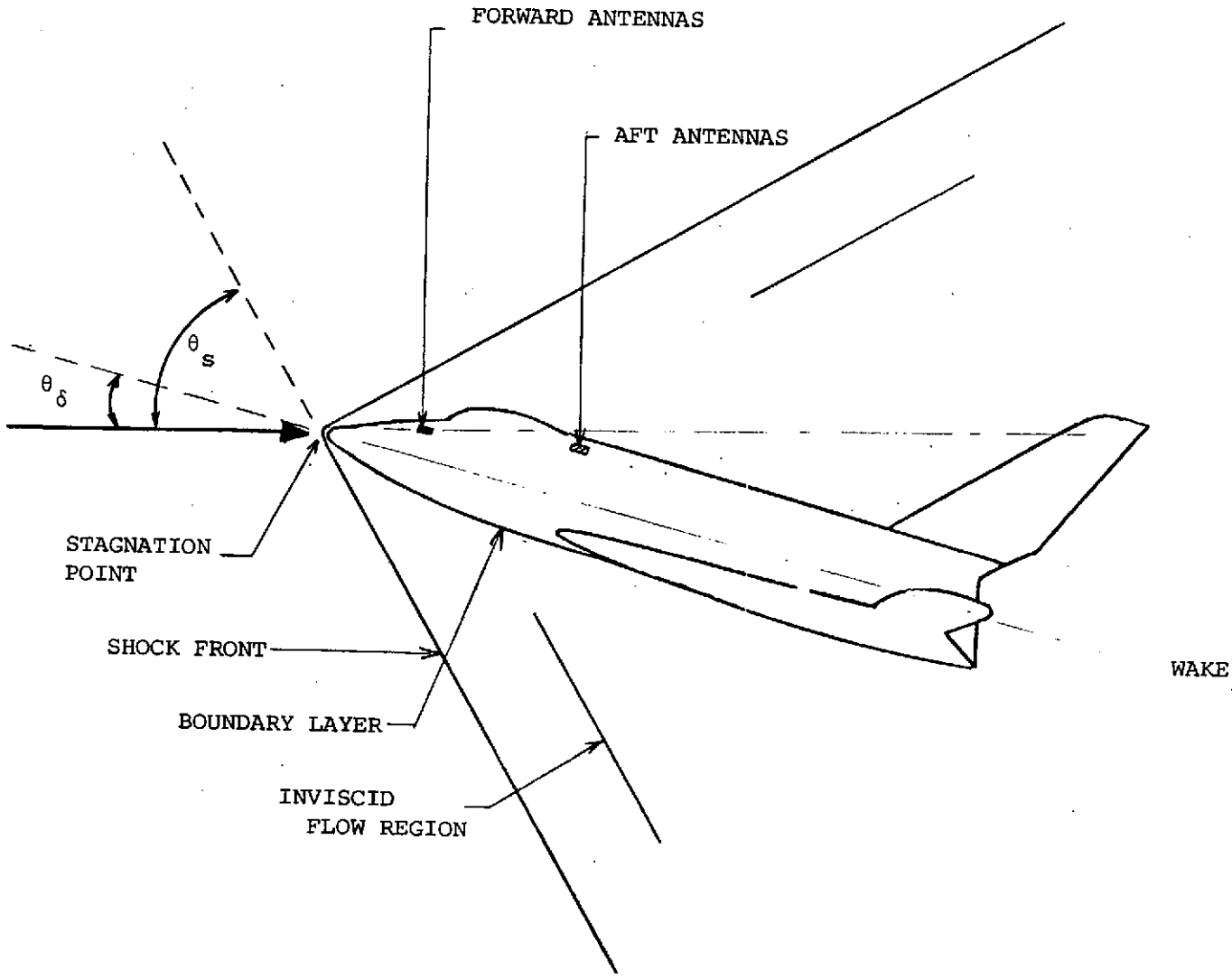

FIGURE 11.7 HYPERSONIC FLOW AROUND A RE-ENTRY SHUTTLE ORBITER

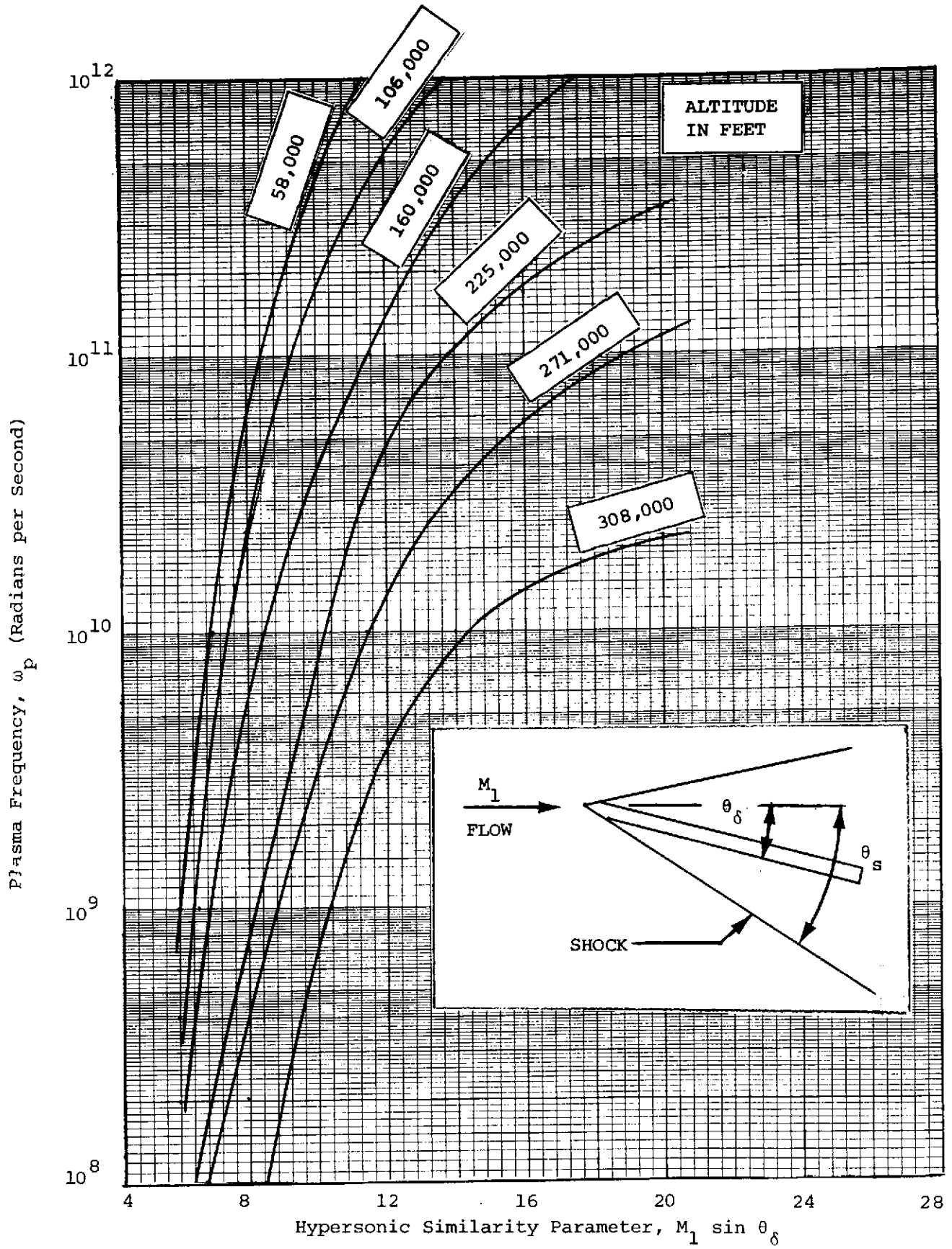

FIGURE 11.8 FLAT PLATE INVISCID FLOW PLASMA FREQUENCY

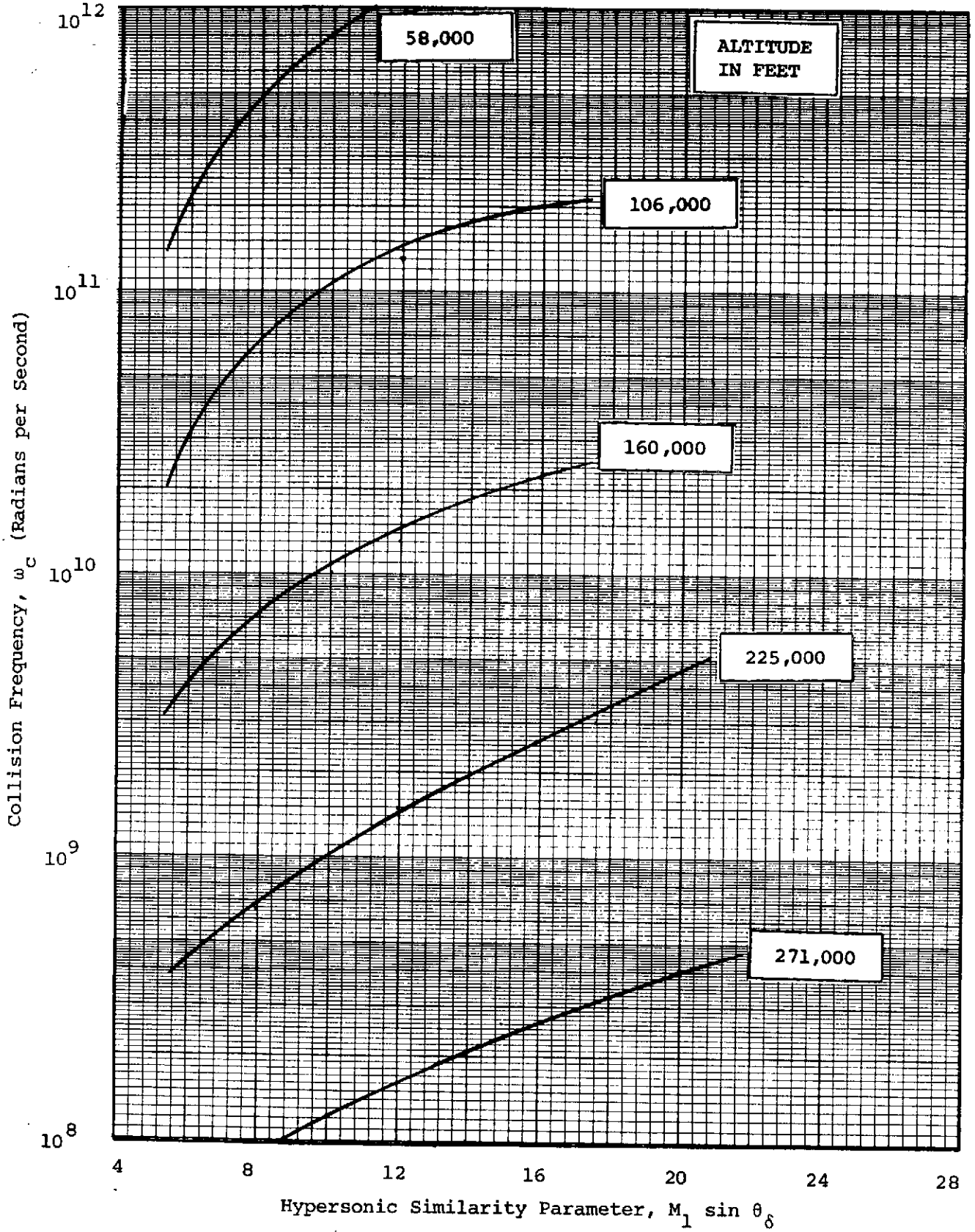

FIGURE 11.9 FLAT PLATE INVISCID FLOW COLLISION FREQUENCY

be estimated from Figure 11.10 which relates the shock angle θ_s to angle of attack θ_δ. To evaluate attenuation characteristics when propagating from the surface of the plate one assumes that the inviscid region is homogeneous with the size of the region increasing with increasing distance from the leading edge.

11.2.2 Blunt Body

As mentioned the blunt leading edge of a reentry vehicle is designed to reduce the effects of aerodynamic heating; there is, however, a corresponding increase in ionization at the stagnation point. McCabe and Stolwyk[2] have computed the plasma and collision frequencies at the stagnation point as a function of vehicle velocity. These curves are presented in Figures 11.11 and 11.12 respectively with vehicle altitude as a parameter. Conditions of propagation throughout this region are constant if the stagnation layer is assumed to be homogeneous and have a uniform thickness δ.

11.2.3 The Orbiter Communications Problem

In this section estimates of the Orbiter plasma and collision frequencies as a function of the flight profile of Figure 11.13 will be obtained. This information will be used to develop attenuation bounds and the corresponding communications performance between the Orbiter and the TDRSS.

Using the Orbiter flight profile in Figure 11.13, approximations to plasma and collision frequencies in both the inviscid flow and stagnation region were made using the data in Figures 11.8 through 11.12. Presented in Figure 11.14 is an indication of the envelope of plasma frequencies expected for the Orbiter reentering at an angle of

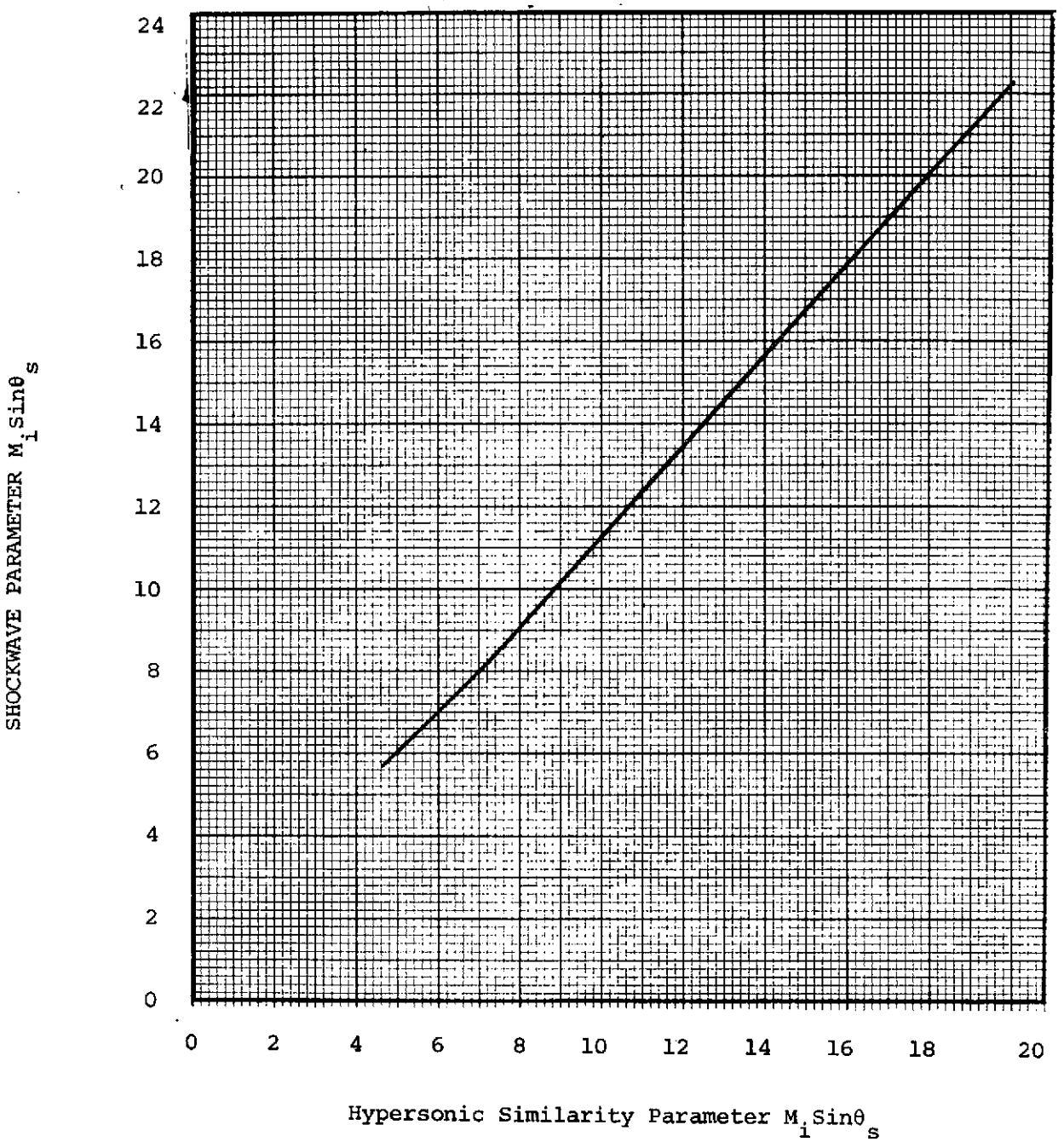

FIGURE 11.10 FLAT SHOCKWAVE PARAMETER

ORIGINAL PAGE IS
OF POOR QUALITY

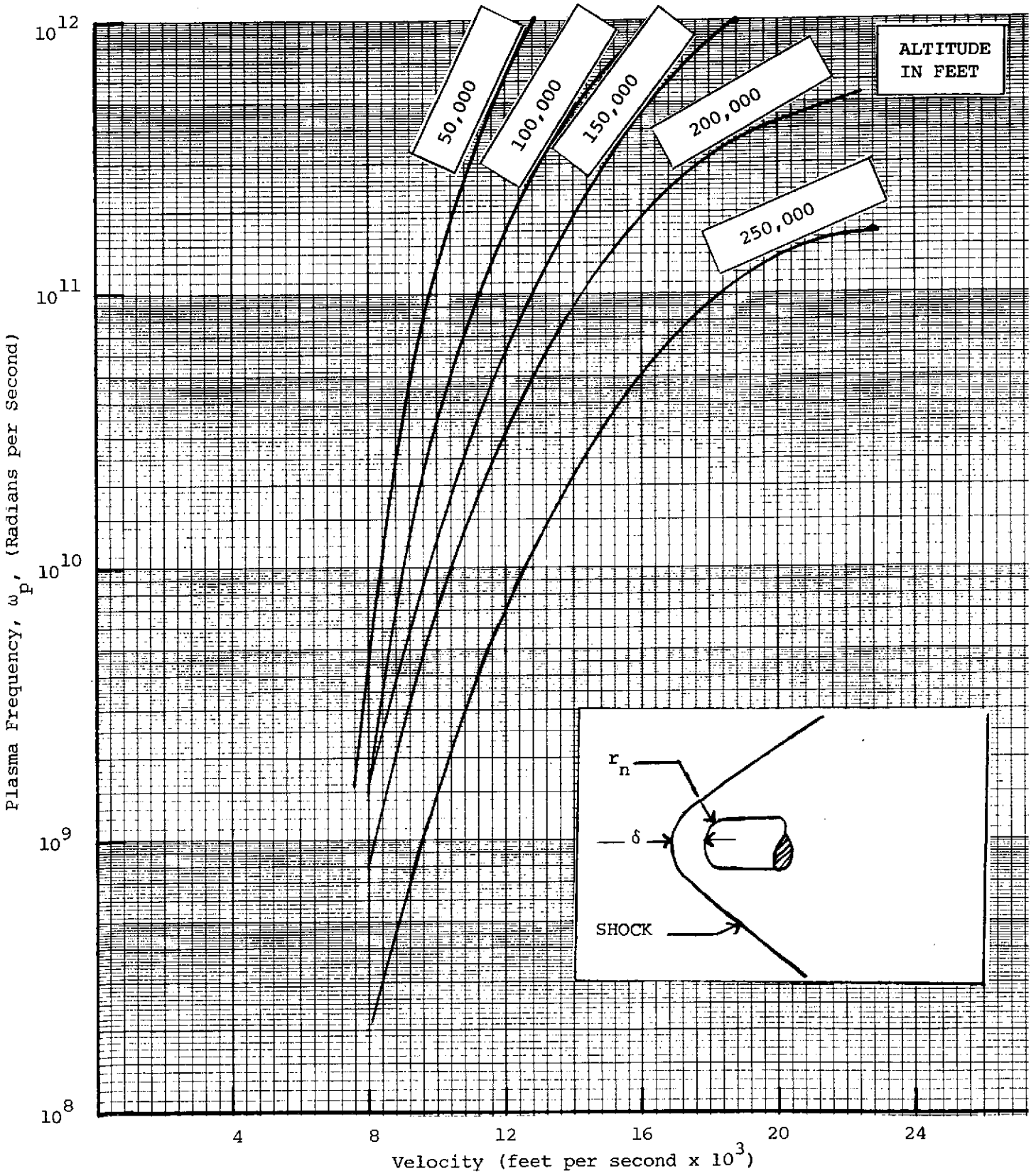

FIGURE 11.11 STAGNATION POINT PLASMA FREQUENCY

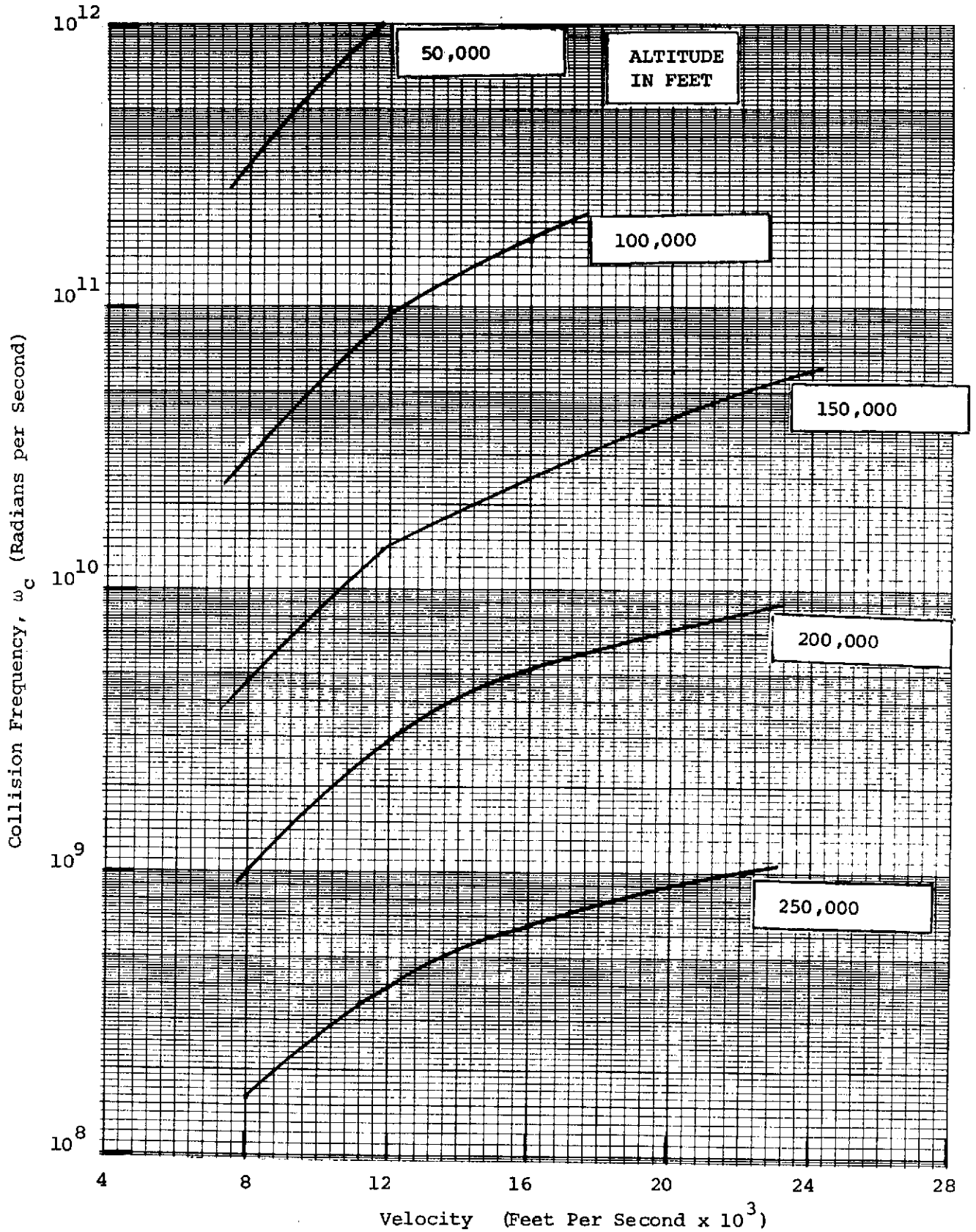

FIGURE 11.12 STAGNATION POINT COLLISION FREQUENCY

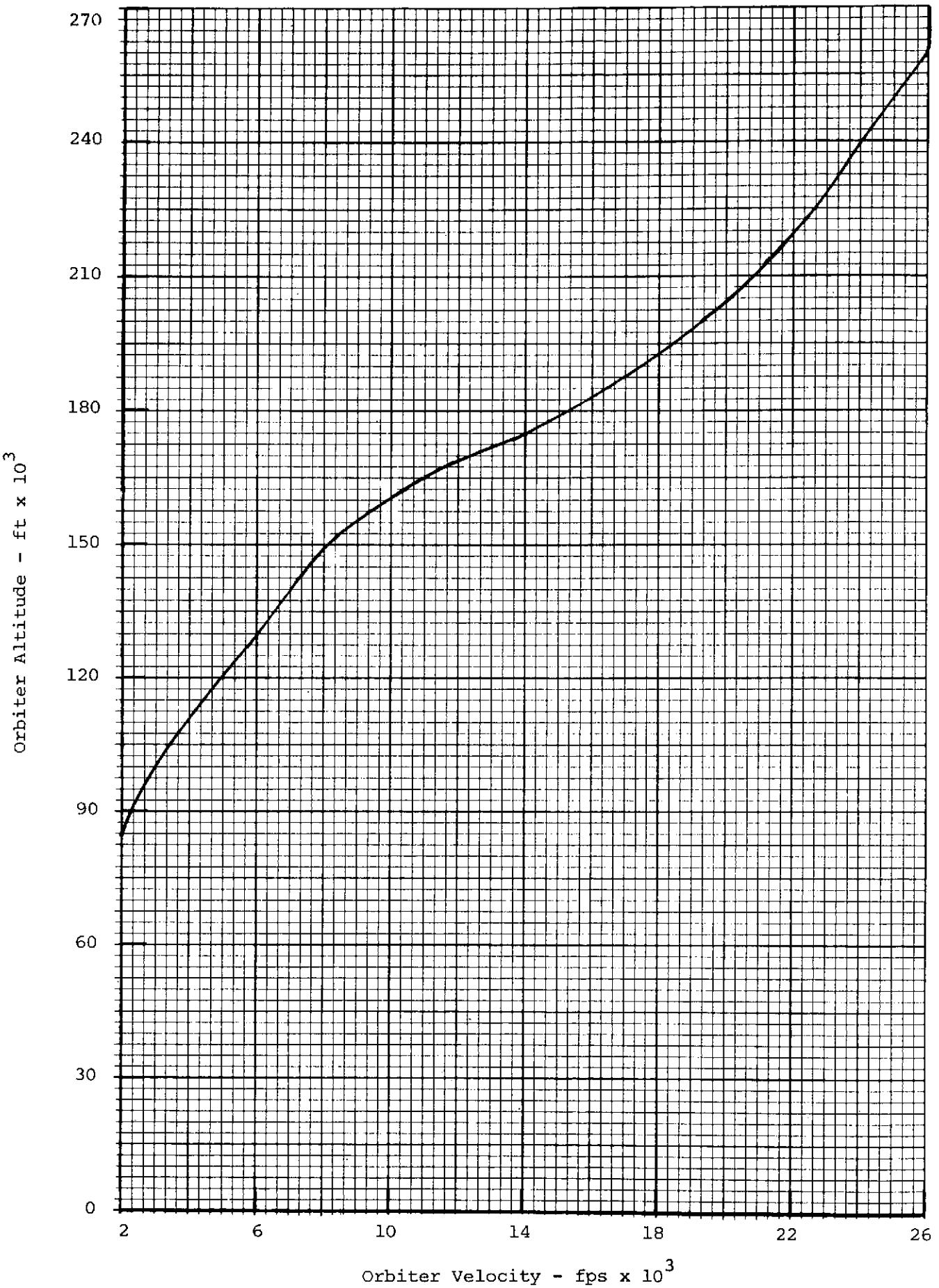

FIGURE 11.13 ORBITER FLIGHT REENTRY PROFILE

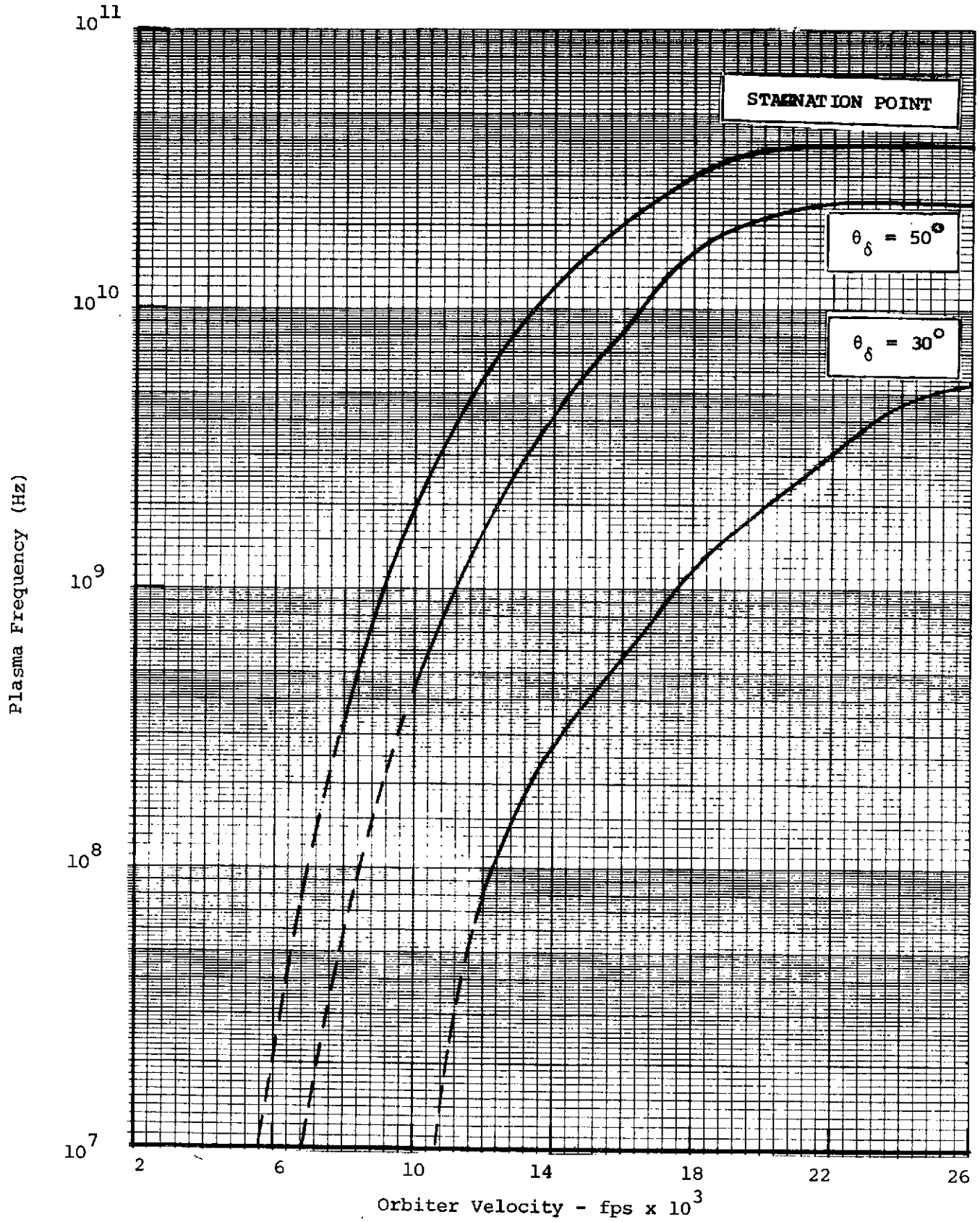

FIGURE 11.14 ORBITER PLASMA FREQUENCY IN THE INVISCID FLOW AND STAGNATION REGIONS

attack between 30° and 50°. Also shown in the figure is the plasma frequency in the stagnation region. Likewise a similar set of curves have been calculated for the estimated collision frequencies and is presented in Figure 11.15. Observation of these curves indicates that plasma frequencies in excess of 20 GHz are estimated for the initial phases of reentry.

Since the TDRSS operating frequencies are only at S-Band (≈2 GHz) and Ku-Band (≈15 GHz), if the Orbiter communications signal is to penetrate the plasma region one of these frequencies must be used. Attenuation factors for 2 GHz and 15 GHz propagation frequencies have been computed and are presented in Figures 11.16 and 11.17 respectively.

From Figures 11.16 and 11.17 one can determine the worst case attenuation (which occurs at an angle of attack of 50°). Some typical values for worst case attenuation are presented in Table 11.1.

TABLE 11.1

TYPICAL "WORST CASE" ATTENUATION VALUES

Orbiter Velocity fps	Plasma Frequency Hz	Attenuation Factor (m^{-1})	
		2 GHz	15 GHz
22×10^3	2.5×10^{10}	> 100	≈100
18×10^3	1.5×10^{10}	≈ 100	≈100
14×10^3	4×10^9	≈ 15	≈10
10×10^3	$< 10^9$	< 1	< 1

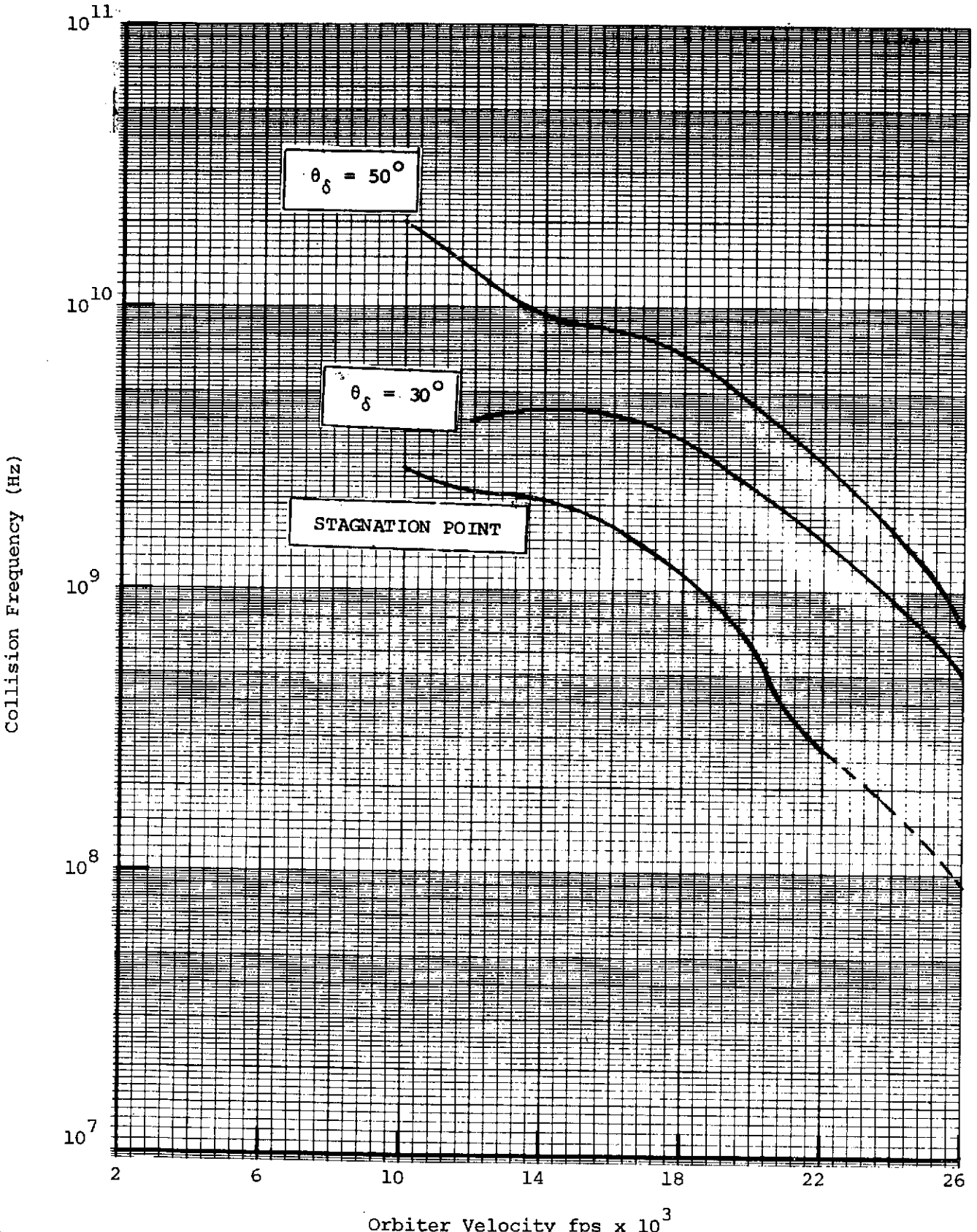

FIGURE 11.15 ORBITER COLLISION FREQUENCY IN THE INVISCID FLOW AND STAGNATION REGIONS

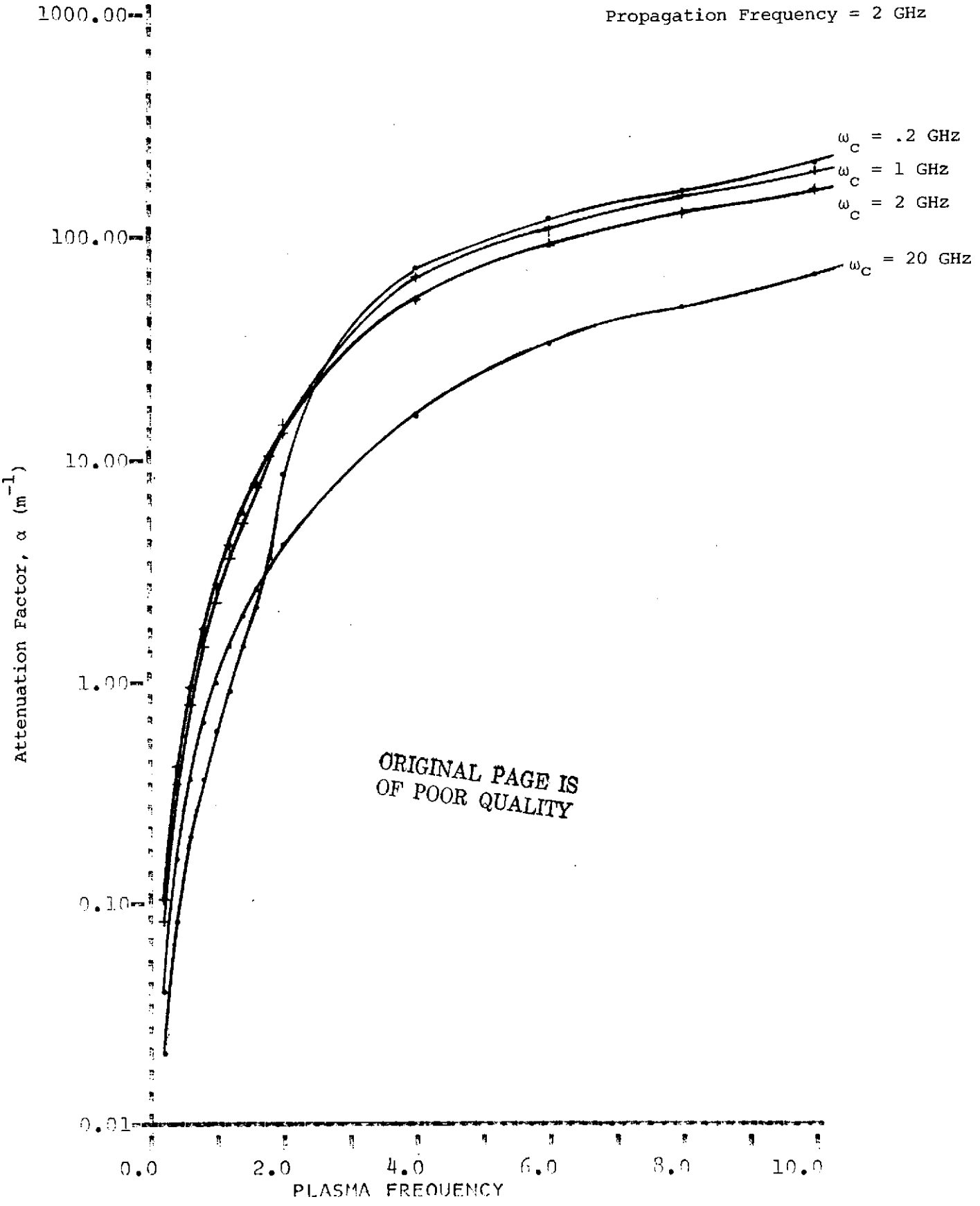

FIGURE 11.16 ATTENUATION AT S-BAND FACTORS FOR ORBITER COMMUNICATIONS

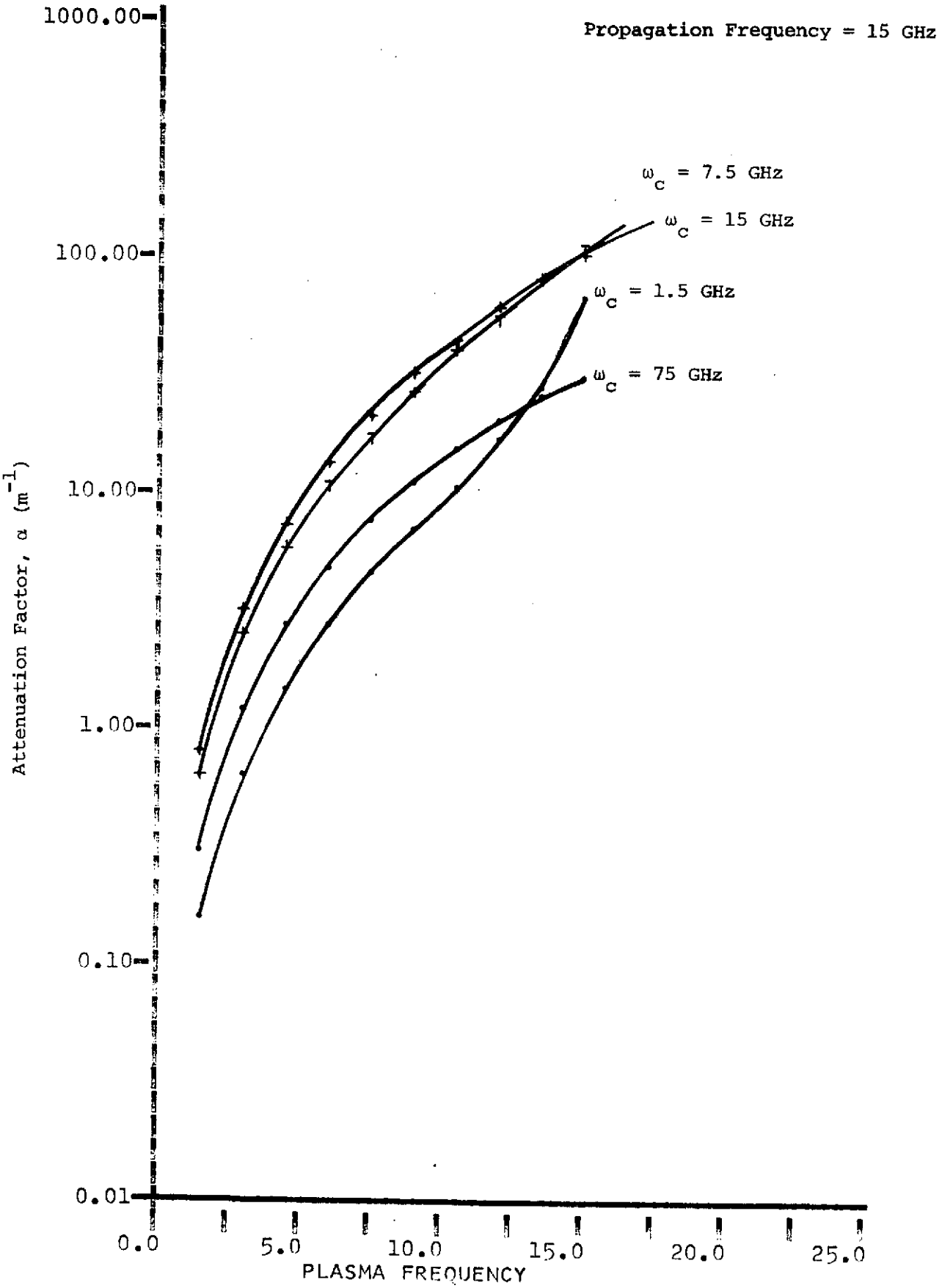

FIGURE 11.17 ATTENUATION FACTORS FOR ORBITER COMMUNICATIONS AT KU-BAND

Estimates of attenuation per meter are presented in Figure 11.18 as a function of Orbiter reentry velocity with frequency and angle of attack as parameter.

If one further assumes that the forward and aft antennas are mounted approximately 4 meters (13.2 ft.) and 14 meters (46.2 ft.) respectively behind the nose of the spacecraft, then estimates of the thickness of the shock wave at the antenna location can be calculated by use of Figure 11.10. Results of these estimates are presented in Table 11.2. Using Equation (11.10) the propagation loss due to the plasma effects can be calculated for the two frequencies of interest, with angle of attack and antenna location as parameters.

TABLE 11.2

ESTIMATES OF SHOCK WAVE THICKNESS AT ORBITER ANTENNAS

θ_δ (degrees)	θ_s (degrees)	$\theta_\delta - \theta_s$ (degrees)	Shock Wave Thickness, d (meters)	
			Antenna at 4m	Antenna at 14m
30	33	3	0.2	0.7
35	39	4	0.27	0.97
40	45	5	0.31	1.1
45	51	6	0.38	1.3
50	57	7	0.47	1.63

As an example of the degree of attenuation that may be encountered during reentry, consider the case where the communications antenna is located 4 meters (13.2 ft.) behind the nose of the Orbiter. Estimates of the total propagation loss due to plasma effects have been computed for this case and are presented in Figure 11.19 with transmission frequency and angle of attack as parameters. The curves indicate the propagation loss is directly proportional to angle of attack and inversely proportional to transmit frequency; therefore, with an angle of attack of 30° and a transmit frequency at Ku-Band the plasma propagation loss is negligible.

Indications are, however, that the angle of attack will be closer to 50°, thereby increasing the propagation loss by nearly two orders of magnitude. Moreover, there are no Ku-Band surface antennas planned for the Orbiter at this time, so that one is forced to use the loss estimate of the upper most curve (i.e., the worst case condition). The estimates indicate that losses that are considered tolerable (i.e., less than 10 dB) will not be realized until the Orbiter has attained a decent velocity of approximately 15,000 feet per second which corresponds to an altitude of 180,000 feet.

11.3 CONCLUSIONS

The Orbiter will be subjected to a highly ionized plasma sheath upon reentry. Estimates have been made of the attenuation due to reentry velocity as a function of angle of attack and Orbiter transmission frequency.

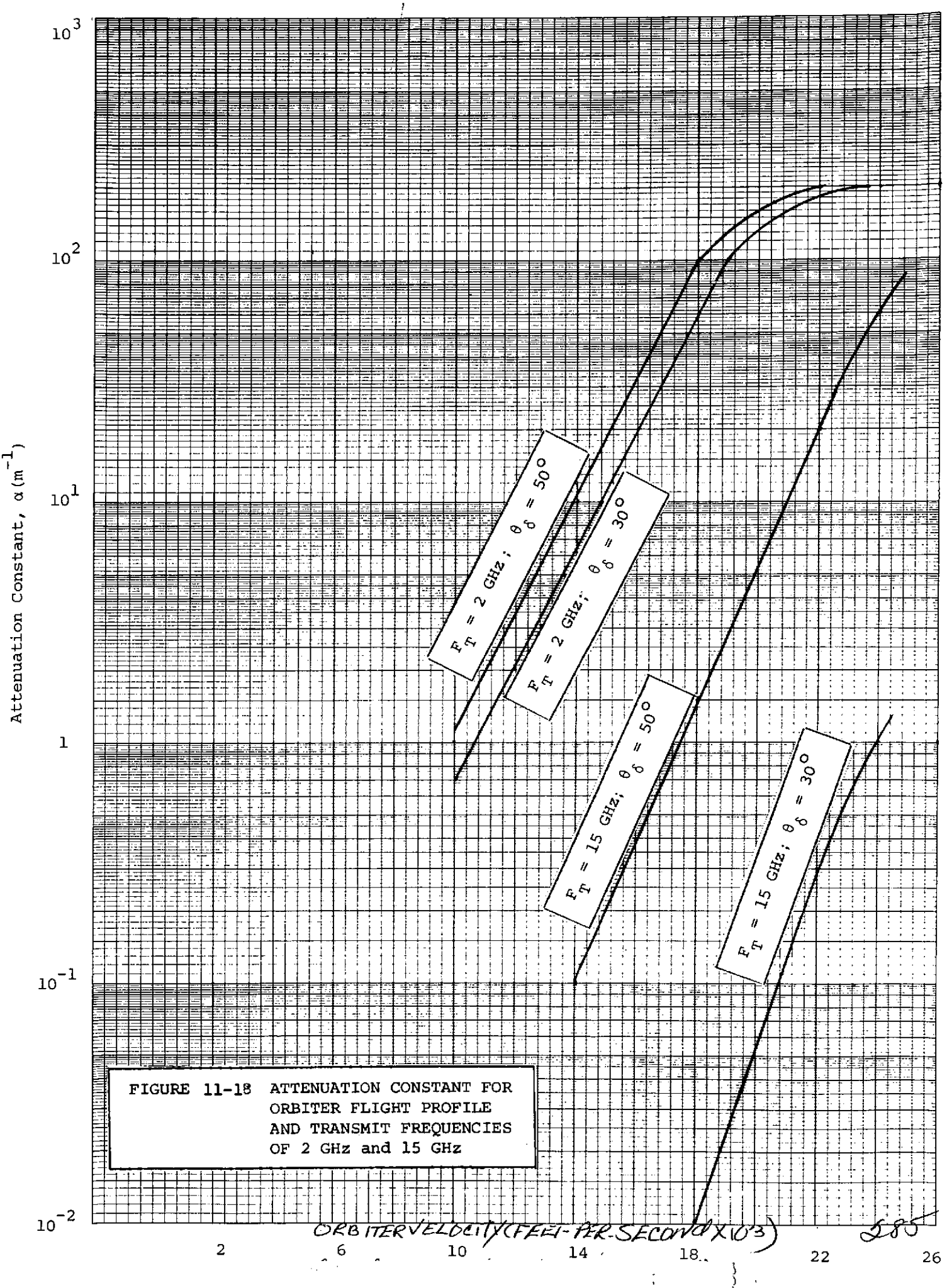

FIGURE 11-18 ATTENUATION CONSTANT FOR ORBITER FLIGHT PROFILE AND TRANSMIT FREQUENCIES OF 2 GHz and 15 GHz

285

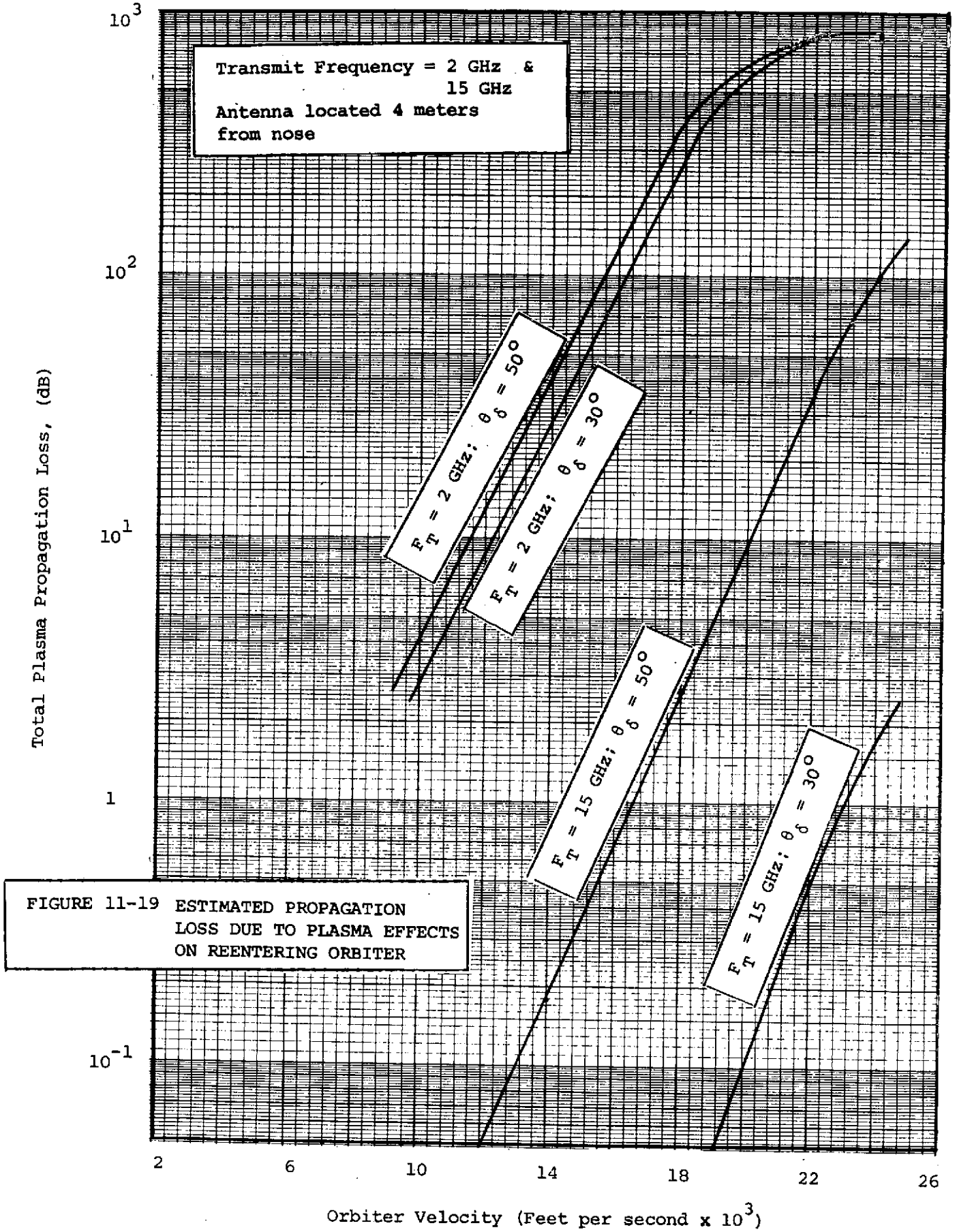

FIGURE 11-19 ESTIMATED PROPAGATION LOSS DUE TO PLASMA EFFECTS ON REENTERING ORBITER

ORIGINAL PAGE IS
OF POOR QUALITY

The foregoing analysis indicates that the outlook for an Orbiter-TDRSS link to overcome the reentry communications blackout problem is pessimistic. One must consider, however, that the analysis is most valid for the region beneath the Orbiter. If the flow conditions on the upper surface are reduced in severity by an order of magnitude, communication via the TDRSS may indeed be realizable even at S-Band. Moreover, if a Ku-Band surface antenna (e.g., cavity-back planar spiral) were installed losses can be reduced even further.

11.4 REFERENCES

(1) Ryback, James P. and Churchill, R. J., "Progress in Reentry Communications," IEEE Trans. Aerospace and Elect. Sys., Vol. AES-7, No. 5, pp. 879-894, Sept. 1974.

(2) McCabe, William M., and Stolwyk, Carl F., "Electromagnetic Propagation Through Shock Ionized Air Surrounding Glide Re-Entry Spacecraft," IRE Trans. of Space and Electron. Telemetry, pp. 257-266, December 1962.